NUREG/CR-6511, Vol. 2
ANL-97/3

Steam Generator Tube Integrity Program

Annual Report
August 1995 - September 1996

Manuscript Completed: November 1997
Date Published: February 1998

Prepared by
D. R. Diercks, S. Bakhtiari, K. E. Kasza, D. S. Kupperman,
S. Majumdar, J. Y. Park, W. J. Shack

Argonne National Laboratory
9700 South Cass Avenue
Argonne, IL 60439

J. Muscara, NRC Project Manager

Prepared for
Division of Engineering Technology
Office of Nuclear Regulatory Research
U.S. Nuclear Regulatory Commission
Washington, DC 20555-0001
NRC Job Code W6487

Steam Generator Tube Integrity Program: Annual Report August 1995-September 1996

by

D. R. Diercks, S. Bakhtiari, K. E. Kasza, D. S. Kupperman,
S. Majumdar, J. Y. Park, and W. J. Shack

Abstract

This report summarizes work performed by Argonne National Laboratory on the Steam Generator Tube Integrity Program from the inception of the program in August 1995 through September 1996. The program is divided into five tasks: (1) Assessment of Inspection Reliability, (2) Research on ISI (in-service-inspection) Technology, (3) Research on Degradation Modes and Integrity, (4) Tube Removals from Steam Generators, and (5) Program Management. Under Task 1, progress is reported on the preparation of facilities and evaluation of nondestructive evaluation techniques for inspecting a mock-up steam generator for round-robin testing, the development of better correlations between failure pressure and leak rate with eddy current (EC) signals, the inspection of sleeved tubes, workshop and training activities, and the evaluation of emerging NDE technology. Under Task 2, results are reported on closed-form solutions and finite-element electromagnetic modeling of EC probe responses for various probe designs and flaw characteristics. Under Task 3, facilities are being designed and built for the production of cracked tubes under aggressive and near-prototypical conditions and for the testing of flawed and unflawed tubes under normal operating, accident, and severe accident conditions. In addition, crack behavior and stability are being modeled to provide guidance for test facility design, develop an improved understanding of the expected failure behavior of tubes with circumferential cracks, and predict the behavior of flawed and unflawed tubes under severe accident conditions. Task 4 is concerned with the acquisition of tubes and tube sections from retired steam generators for use in the other research tasks. Progress on the acquisition of tubes from the Salem and McGuire 1 nuclear plants is reported.

DISCLAIMER

Contents

Figures

Tables

Executive Summary

Assessment of Inspection Reliability

As part of the assessment of in-service inspection (ISI) of steam generator (SG) tubes, a SG mock-up will be used for round robin (RR) tests and as a resource to assess new technology. The mock-up will contain 400 tube openings, each with a 3.66-m (12-ft) length of tubing. Tubes will include a variety of defects and artifacts. Eddy current (EC) and ultrasonic testing (UT) techniques are being evaluated as a means to characterize the defects in the mock-up tube bundle. Twenty Alloy 600 tube specimens, prepared under laboratory conditions, were provided for this evaluation. Ultrasonic depth and length characterizations, obtained by high-frequency diffraction and Lamb wave and amplitude drop methods, were applied to these tubes by various researchers. Estimates of eddy current depth and length were also acquired by using pancake-coil, multicoil-array, and polarized-probe (Zetec +Point) methods, and applying neural-network algorithms to multiparameter EC data. A clear trend is evident. The UT techniques overestimate the depth of the crack in most cases and particularly when cracks are shallow. The results of neural-network analysis of EC data are better, and significant improvements in correlation of data are expected when optimized training sets are used. Results with the +Point probe were best for estimating the depth of ID cracks.

Preliminary estimates from longitudinal outer- and inner-diameter cracks, circumferential outer- and inner-diameter cracks, and intergranular attack (IGA) suggest that no one technique is superior for characterizing all types of defects. Intergranular attack is particularly difficult to size. The +Point probe was very effective for estimating the depth of the three ID cracks. It is somewhat easier to measure crack length than crack depth. Length estimates obtained with EC probes are generally expected to be shorter than those obtained by UT techniques, because the threshold for detecting a crack is higher with EC methods. However, the data presented in this report do not necessarily support this idea.

Ultrasonic techniques provide better spatial resolution than EC techniques and, as a result, cracks that appear segmented on ultrasonic interrogation may not be resolved with EC analysis. In addition, ultrasonic Lamb waves can be used to provide a good image of the extent of circumferential defects, but can not be used for depth estimates.

Data on tube failure pressure and leak-rate exhibit substantial scatter when correlated with EC voltage amplitude. Improvements in signal analysis (e.g., application of neural-network and multivariate regression algorithms) are being explored in this program to find a more accurate method for relating failure pressure and leak rate to EC data.

An NEA Workshop on Steam Generator Tube Integrity in Nuclear Power Plants was held at Oak Brook, IL, October 30-November 2, 1995. The present capability of EC and UT techniques to detect circumferential cracking was compared during this workshop.

Many aspects of ISI that may improve the technology are being reviewed in this program. It may be possible to improve neural networks and multivariate regression to the point where they are better than conventional pattern recognition techniques in the area

of data analysis and interpretation. Neural-network technology has been applied to the analysis of EC data with good results, even with limited samples. It is possible that defects can be reconstructed from EC data but the reconstruction depends on the diffusion equation rather than a wave equation as used for ultrasonic modeling. Thus, one must rely on indirect algorithmic approaches to solve the inverse problem to determine the geometry of a defect. That is, one can not simply reconstruct to origin of an EC signal from what is detected. The altermnative "solution" to the inverse problem for EC techniques is to use pattern recognition algorithms to interpret the signals.

Advances in digital signal processing may dramatically improve our capability to extract information from an EC probe. It may be possible to use sophisticated digital filters to solve problems that are now approached with multifrequency techniques such as the elimination of signals from tube support plates.

Research on ISI Technology

The objective of this task is to evaluate advanced NDE and signal analysis techniques for reliable ISI of original and repaired SG tubes. Improved correlations between EC results and flaw morphology, leak rate, and failure pressure will be evaluated. The implementation of degradation-specific management requires detailed knowledge about the specific nature and severity of flaws. Improved techniques (EC and others) are needed for more reliable inspection and interpretation of flaws. The reliability and accuracy of the techniques must be quantified so that plugging criteria and the consequences of degraded tubes that remain in service after inspections can be evaluated. Furthermore, the robustness of EC measurement parameters and techniques need to be evaluated with respect to their range of applicability.

The research on improved EC inspection of SG tubes is focusing on four primary areas: (1) evaluation of analytical methods for the prediction of EC responses as a function of probe design, flaw characteristics, and material properties; (2) assessment of effective signal analysis procedures; (3) assessment of flaw imaging and display methods for simple and accurate flaw characterization; and (4) evaluation of improved probe designs that use directional arrays so that axial and circumferential defects can be examined simultaneously. The reliability and effectiveness of improved inspection techniques will be evaluated through laboratory testing of SG tubes that contain various flaws and the SG tube bundle mock-up. Final validation will utilize in–service-degraded SG tubing.

Better analytical models will help us understand the relationship between signal characteristics and the presence of defects. Reliable computational electromagnetic (EM) models are important for researchers and practitioners in EC-related NDE applications. To date, at Argonne National Laboratory (ANL), various modeling approaches to the application of EC probe response to NDE of SG tubing have been evaluated. The approaches consisted of closed-form, volume integral, and finite element solutions, with the finite element method (FEM) being the most elaborate and computationally intensive technique and the method that was adopted by and is currently being used at ANL. The software in use is a general-purpose three-dimensional (3-D) FEM-based computational code that is a versatile research tool capable of precise modeling of the complex geometries that are often encountered in ISI of SG tubing. Simulations have been carried

out to model calibration standard defects and axial notches with and without ligaments. Ultimately, the code will be used to model other defect geometries of interest, such as cracks and IGA. The elaborate computer-aided-design-based mesh-generating preprocessor of the software allows incorporation of various material property variations (e.g., presence of magnetite and copper deposits), as well as modeling of complex geometrical variations (e.g., defect-prone areas, such as baffle plates, and roll-expanded and crevice regions).

A series of FORTRAN programs, originally developed at Oak Ridge National Laboratory (ORNL) and used for the design and analysis of EC SG problems have also been modified so they are compatible with the available platforms at ANL. To process and display the outcomes of these programs, computation and visualization software is currently utilized. Because of the specific problem geometries that can be treated and the underlying assumptions in the formulation method, programs that are based on closed-form EM solutions can run with minimal computational resources. They can be used to simulate the impedance response of several standard differential and absolute EC probes to axisymmetric geometries. These codes will be used both to check the results of computationally intensive FEM solutions that can better simulate realistic flaw geometry and as a tool to analyze and determine EC probe and test parameters for general test case scenarios.

Efforts in this task have also focused on evaluation of advanced signal analysis techniques as applied to NDE of original and repaired SG tubes to help establish improved correlations between EC indications and flaw morphology, leak rate, and failure pressure. Certain elements play a critical role in achieving this goal. In particular, evaluation of modern signal analysis techniques to extract relevant features from EC ISI measurement data, identification of an optimal set of features that are most significant in determining flaw characteristics, and implementation of suitable architecture and learning algorithms (neural network, multiparameter regression, etc.). To date, a neural network (NN) code originally developed at ORNL for EC estimation of defect depth in SG tubing has been made operational on the HP-UX platforms at ANL. The code has been examined and a summary of the outcomes is reported here. Work is currently underway on implementation of more modern algorithms that further incorporate feature extraction techniques to help develop improved correlations among EC data, SG tube flaw characteristics, and failure pressure.

Research on Degradation Modes and Integrity

The objective of this task is to evaluate and experimentally validate models that will predict potential degradation modes, progression rates, leak/rupture behavior, failure pressures, and leak rates for SG tubes and for repaired tubes under normal operating, accident, and severe accident conditions. Initial efforts have concentrated on the design and construction of experimental facilities for the production of flawed tubing and the pressure and leak-rate testing of flawed and unflawed tubing under a wide range of conditions. The facilities under design and construction are an autoclave system in which tubes will be cracked under accelerated (chemically aggressive) conditions; a Pressure Leak-Rate Test Facility in which failure-pressure and leak-rate tests will be conducted under simulated SG operating conditions; a model boiler facility where tubes will be

cracked under more nearly prototypical conditions; a high-temperature, severe-accident, tube-failure facility; and a high-pressure tube-rupture and leak-rate test facility.

Alloy 600 tubing for initial testing purposes has been obtained from two sources. Two hundred feet of 19.05-mm (0.750-in.)-diam tubing was purchased in 0.9-m (3-ft.) lengths from Valinco in the as-fabricated ("cold-worked") condition, and ≈110 m (360 ft.) of 22.23-mm (0.875-in.)-diam tubing in 3.7-m (12-ft.) lengths was obtained from Pacific Northwest National Laboratory (PNNL). Both sets of tubing conform to the chemical analysis specifications for ASTM B 163 (Alloy 600). Room-temperature tensile tests have determined that although the ultimate tensile strengths of the two tubing samples are comparable, the ductility and yield strength of the 22.23-mm tubes are significantly greater than that of the 19.05-mm tubes. In addition, the room-temperature hardness of the 22.23-mm-diam tubing is slightly greater than that of the 19.05-mm-diam tubing. Optical metallography indicates that the grain boundaries of both tubing materials are sensitized and that the grain size is ASTM 8.0 for the 19.05-mm-diam tubing and 8.6 for the 22.23-mm-diam tubing. Present plans call for the purchase of a larger quantity of 22.23-mm-diam tubing to serve as the principal test material for the present program.

The first autoclave testing facility has been designed and constructed and will be used to crack tubes under accelerated (chemically aggressive) conditions for use in subsequent tube-rupture and leak-rate tests and for the evaluation of NDE equipment and techniques. In this system, six tubular specimens may be simultaneously exposed at pressurized water reactor (PWR) SG operating temperatures to aggressive secondary-water chemistries at the outer surface. The tube specimens are plugged at the bottom and pressurized from the top by an independent refreshed primary-water system to provide internal pressure loading. Individual valving of the six specimens permits continuation of a given run after one or more of the specimens have developed a leaking crack. Following assembly and shakedown, initial tube cracking tests were performed with eight Alloy 600 tube specimens. The second autoclave system will be assembled after enough experience is accumulated with the first system.

A model boiler multi-tube corrosion cracking facility is being designed to closely simulate SG thermal-hydraulic and chemistry conditions of the tube/crevice geometry. In particular, heat transfer conditions across the tube wall from the primary water side to the secondary side will be maintained in this facility to cause chemical concentration of impurity species in secondary-side crevices and thereby produce SCC on the outside of the tube. This facility will permit the production of cracked tubes under nearly prototypical conditions. These cracked tubes will be used in leak-rate/failure tests and characterization by NDE at ANL.

Initially, a single-tube boiler concept was evaluated. However, an assessment of the overall long range needs of the program indicated the production of a larger number of prototypical flawed tubes was required. For this reason, the design was changed from a single-tube to a seven-tube boiler. Tubes will be cracked at nominal temperatures and pressures of 338°C (640°F) and 14.2 MPa (2060 psi) on the primary, and 288°C (550°F) and 7.24 Mpa (1050 psi) on the secondary side. Corrosion enhancement of secondary-side water by the addition of NaOH to the deionized water and increased primary-side temperatures and pressures will be used to accelerate cracking and explore the influence

of these parameters. Prototypical tube heat fluxes in the range of 160,000-320,000 W/m^2 (50,000-100,000 BTU/hr-ft^2) are achievable in the boiler. The facility uses a primary-side reflux boiler to create heat transfer across seven shortened steam generator tubes and a secondary-side natural convection loop with condenser to maintain constant-boiling conditions on the outside of the tube. A crevice simulator is used on each of the seven tubes to promote localized chemical hideout and cracking.

A primary-to-secondary-side heat transfer model has been developed for predicting tube heat transfer and crevice chemical hideout. The model simulates the coupled falling-film condensation heat transfer within the tube from the reflux-boiler-generated steam, the heat conduction through the tube and crevice wall, and the boiling that occurs on the outside of the tube. The heat transfer is analyzed as a function of primary and secondary thermal-hydraulic conditions and crevice design. It has been demonstrated that by controlling the primary reflux boiler and the secondary condenser, a wide range of crevice region heat transfer conditions can be achieved, including prototypical tube wall temperatures.

Detailed design of the model boiler multi-tube corrosion cracking facility has been completed. Detailed hardware specification for all of the components have been completed and vendor price quotes have been received. Work continues on refining the boiler performance prediction code, studying operational characteristics, and developing facility operation procedures.

The Pressure and Leak-Rate Test Facility will be used to obtain data on failure pressures, failure modes, and leak rates of flawed tubing at temperatures up to 343°C (650°F), pressures of 21 MPa (3000 psi), and pressurized-water flow rates up to 760 L/min (200 gal/min). The facility incorporates several features that are necessary to obtain more prototypical data under stable, controlled conditions, including a large blowdown vessel water inventory to ensure high, stable flow rate capability and permit full-range testing of initially stable leaking cracks to instability; piping and valves of a size appropriate to minimize pressure drop in the supply line to a flawed tube and thereby permit high flow rates; the use of a downstream back-pressure regulator valve to control tube secondary-side pressure, thereby minimizing nonprototypical two-phase flow from entering the tube; and a computer feedback valve control to allow programmed ramps of the pressure differential across the tube.

The design of the Pressure Leak-Rate Test Facility has been completed, and technical specifications for all components have been formulated. A formal ANL safety review of the facility has been conducted, and approval has been granted for facility construction. Purchase order contracts have been issued for all components, instrumentation, and controls. Modifications to the laboratory area are completed, an existing computer control room has been upgraded, and a new computer has been installed. All procurements have been delivered except for the long-lead-time pressure vessels and the gas pressurization system, which are currently being manufactured. Installation of instrumentation and control cabinets is ≈60% completed, and the steam muffler has been installed.

It is of interest to the present program to determine flow rates through subcritical throughwall cracks at high pressures. Therefore, a third tube-rupture and leak-rate test

facility is being constructed to perform tests at pressures up to 52 MPa (7,500 psi) and flow rates up to 45.4 L/min (12 gal/min). The system utilizes a high-pressure positive-displacement triplex pump to supply water at pressures up to 52 Mpa (7,500 psi), and a fixed flow rate of 45.4 L/min (12 gal/min). A test control valve will be used to apportion the flow from the pump either to the specimen or around a bypass loop. These components have been procured, but construction of the system has not yet begun.

The failure pressures of flawed and unflawed tubes at very high temperatures under severe-accident conditions are also of interest in the present program, and a high-temperature facility has been constructed. The facility basically consists of a length of SG tube placed in a furnace, closed off at one end, and connected to a high-pressure nitrogen gas bottle by suitable valving at the other end. Design and construction have been completed, and the system has been used to conduct a series of constant-pressure tests on flawed tubes with temperature ramps that correspond to those predicted for various severe-accident scenarios. In addition, pressure ramp tests have been conducted to establish flow/stress behavior. The results of these tests are summarized below.

Analytical studies were performed to estimate critical crack sizes, leak-before-burst behavior, and expected leak rates for axial and circumferential cracks of various lengths and depths to help assure that the Pressure Leak-Rate Test Facility has sufficient capacity to study leakage and failure behavior under normal and design-basis accident conditions. The studies showed that cracks less than ≈15 mm (0.6 in.) long will never become unstable under any normal or design basis accident scenario. For cracks less than ≈51 mm (2 in.) long, only deep cracks (>75% throughwall) could break through and leak under a main-steamline break (MSLB). Throughwall cracks longer than ≈56 mm (2.2 in.) would be unstable even under normal operating pressures. Estimates of the leak rates through cracks with geometries in the range of interest were then obtained to ensure that the flow capacity of the facility was adequate. The maximum flow through the crack and maximum pressure that the tube can withstand without the crack becoming unstable and growing rapidly were calculated as a function of crack length. Once a crack becomes unstable, it is impossible to predict the leak area, and the resulting flow rates could be close to those for a double ended rupture, i.e., ≈1,720 and 2,460 L/min (455 and 650 gal/min) for tubing with ODs of 19 and 22 mm (0.75 and 0.875 in.) respectively. Because cracks longer than ≈56 mm (2.2 in.) would be unstable under normal operating conditions, the maximum flow rate through any stable crack will be ≈300 L/min (80 gal/min) under single–phase flow.

The literature has a large number of models and a large amount of experimental data on the rupture of SG tubing with axial flaws. However, the literature on the problem of circumferential cracks in tubing is much more limited, although a large literature on the failure of piping exists. Limit load analyses for throughwall and part–through circumferential cracks have been reviewed. A model that was originally developed in Japan for pipe bending and uses an empirical correction to account for the difference in stress level between the remaining ligament of the part–through crack and the remainder of the pipe cross section was modified to give results that are in better agreement with the limited data in the literature on the failure of circumferential cracks in tubing.

Free bending is a limiting failure mode for circumferentially cracked tubing. If the lateral deflection of the tube is completely restrained and the tube deforms only axially,

another limiting failure mode with much higher failure pressures occurs. It appears that, in most cases, lateral constraint (e.g., by tube support plate) is sufficient to give failure pressures that are much closer to those that correspond to complete restraint than to those expected for the free bending case. Finite-element analyses are being conducted to verify these results and to more accurately characterize the effects of lateral constraint on failure pressure and crack-opening area. A simple beam model to describe the effect of lateral constraint on the failure of tubes with a circumferential crack has also been developed.

During design basis accidents, the temperature of the SG tubing is <350°C. In this temperature range, creep effects in Alloy 600 are negligible. However, in severe accidents, much higher temperatures are possible. At these higher temperatures, plastic deformation is likely to be much more extensive than at normal reactor operating temperatures, and creep effects may no longer be negligible. Most previous analyses of the behavior of flawed SG tubing during severe accidents have assumed that failure of flawed SG tubing in severe accidents can be predicted by a flow stress model by taking the flow stress to be a function of temperature. In contrast, the failure of unflawed tubing and other components, such as the surge line nozzle, is described in terms of creep damage failure.

Results from recent tests conducted at ANL, which are reported here, have shown that pressure and temperature ramp rates significantly influence failure pressure and failure temperature. Therefore, a creep rupture model for predicting failure of flawed and unflawed tubes was developed. For high-temperature tests with a variety of loading histories, predictions based on this model are in much better agreement with the test results than predictions based on flow stress models. However, for completeness, the flow stress models are also discussed in this report.

Both the flow stress and creep rupture models depend upon an empirical factor m_p, a hoop stress magnification factor that accounts for the effect of the crack. Past studies have developed a variety of expressions for m_p. Based upon previous tests at normal reactor operating temperature at PNNL and the current high–temperature tests at ANL, we have developed a new expression for m_p, which is better agreement with the available data over a wide range of crack geometries, including very deep cracks. The new correlation is also supported by the results of detailed finite-element analysis of cracked tubing.

Available data on the creep rupture properties of Alloy 600 was compiled. A least–squares bilinear best fit, along with estimated 95% confidence limits, was developed in terms of the Larson–Miller parameter and the stress. The present best–fit curve for the Larson–Miller parameter was compared with that currently used in SCDAP. Although the SCDAP correlation is a reasonable fit to the data, there clearly is a change in slope at the high stress levels of interest to the analysis of flawed tubes that is not reflected in the correlation. Creep-rupture properties of Type 316 stainless steel and A508, Class 2 low-alloy steel were also analyzed.

Several techniques have been used to determine the length and depth of electro-discharge-machined (EDM) flaws introduced into specimens tested under simulated severe-accident conditions. An accurate determination of the flaw depth in particular, is critical when calculating the expected failure pressure of the tube. The first technique

used for the severe-accident test specimens was posttest fractography, in which the fracture surfaces of the failed specimen are photographed, and the contrast between the machined portion of the fracture surface and the region of subsequent ductile fracture is used to estimate flaw depth. The second technique we employed to measure flaw depth was replication of the premachined flaws prior to testing. This technique offers the advantage that the flaw geometry is preserved in time, and reexamination of the flaw is possible even after the test is completed. A third technique, developed later in the test series, was direct measurement of the flaw depth prior to testing by using a traveling optical microscope with a digital readout of the x, y, and z positions of the objective lens. This technique is highly accurate, but the measurements cannot be rechecked after the specimen has been tested. A fourth technique, used occasionally, is destructive metallography of the flawed tube. This technique is also quite accurate, but the depth is determined at only one position per section along the flaw length and the specimen is destroyed and cannot be tested subsequently.

Flaw depths were determined by one or more of these techniques for all of the specimens tested in the severe-accident test series. In addition, the posttest fractography technique was used to verify the EDM flaw depths in SG tube specimens tested at PNNL in the late 1970s. Using the values obtained, we reanalyzed the PNNL tube failure data in conjunction with our experimental and analytical study of tube failure behavior under severe-accident conditions.

To validate the creep rupture model, several types of tests were conducted on both flawed and unflawed SG tubes. Several types of load histories were examined, including isothermal constant-pressures, isothermal constant pressure ramps, constant-temperature ramp under constant pressure, and two time/temperature histories that have been calculated for an accident sequence that involves total station blackout with a stuck-open SG secondary-side atmospheric dump valve, resulting in loss of feedwater and secondary-side depressurization. The experimental results are in much better agreement with the predictions of the creep rupture model than with those of a simple rate-independent flow stress model and confirm the idea that the effect of flaws on failure can be characterized by the m_p approach.

Tube Removals from Steam Generators

The objective of this task is to remove and obtain tubes and sections from retired SGs for use in the other research tasks of this program. The work to be performed under this task can be divided into three activities: (1) review of inspection records and other plant data to determine which tubes to remove, (2) arranging for necessary on-site support services, such as radiation control, health physics support and monitoring, and area power, and (3) arranging for access to the tubes, the actual cutting and removal of tubes and sections that contain tubes and portions of the tube sheet and tube support plates, and packaging and shipment of the removed tubes and sections to ANL.

Discussions have been held with four electrical utilities about the possible acquisition of tubes from SGs scheduled to be retired from service within the next year. The Salem Units 1 and 2 steam generators have been scheduled for replacement in late 1996 and early 1997, but Public Service Electric and Gas (PSE&G) has decided to dispose of the SGs

by burial at Barnwell, and tube sampling is not possible at that site. Other options are currently being explored with respect to these SGs. Duke Power Company has indicated a willingness to permit on-site sampling of tubes from one of the McGuire 1 SGs, which are to be replaced between January and May of 1997, and the details of a possible agreement are currently being negotiated. Contacts have also been made with Florida Power and Light about recovery of tubes from the Combustion Engineering SGs being replaced at St. Lucie, and with South Carolina Electric and Gas about obtaining tubes from the Westinghouse D-3 units at Virgil Summer. All of these discussions are at an early stage at present, and no commitments have been made.

Acknowledgments

The authors acknowledge the contributions of D. E. Busch, J. E. Franklin, L. Knoblich, E. R. Koehl, C. F. Konicek, W. Lawrence, D. R. Perkins, and C. W. Vulyak to the experimental work described in this report. The authors also thank R. Kurtz (PNNL), A. Diaz (PNNL), T. Gomm (INEEL), C. Dodd, V. Cecco (Atomic Energy of Canada, Ltd.), M. Brook (ABB AMDATA), and J. Cox (Zetec) for their contributions to Task 1 and X. Kong of Northern Illinois University for his contributions to Task 2. The contributions of Dr. J. Muscara of the Office of Nuclear Regulatory Research, U.S. Nuclear Regulatory Commission, to the development and guidance of the program are also acknowledged.

Acronyms and Abbreviations

ABB	ASEA Brown-Boveri
AECL	Atomic Energy of Canada, Ltd.
ANL	Argonne National Laboratory
ASME	American Society of Mechanical Engineers
ASTM	American Society for Testing and Materials
AVB	antivibration bars
BC	bobbin coil
BCL	Battelle Columbus Laboratories
CIDSCC	circumferential inner-diameter stress corrosion crack/cracking
CNRA	Committee on Nuclear Regulatory Activities
CODSCC	circumferential outer-diameter stress corrosion crack/cracking
CSF	conjugate spectrum filter
CSNI	Committee on the Safety of Nuclear Installations
DAS	data acquisition system
DE	destructive examination
DSF	defect sensitivity factor
EC	eddy current
ECT	eddy current testing
EdF	Electricité de France
EDM	electro-discharge machining
EM	electromagnetic
EPRI	Electric Power Research Institute
FEM	finite-element method
FM	flow meter
ID	inner diameter
IGA	intergranular attack
IGSCC	intergranular stress corrosion cracking
INEL	Idaho National Engineering Laboratory
ISI	in-service inspection
LFCC	linear-fit correlation coefficient
LIDSCC	longitudinal inner-diameter stress corrosion crack/cracking
LMP	Larson-Miller parameter
LODSCC	longitudinal outer-diameter stress corrosion crack/cracking
LOOT	leave-one-out training
MRPC	motorized rotating pancake coil
MS DOS	Microsoft™ disk operating system
MSLB	main-steamline break
NDE	nondestructive evaluation
NN	neural network
NRC	U.S. Nuclear Regulatory Commission
OD	outer diameter
ODSCC	outer-diameter stress corrosion crack/cracking
ORNL	Oak Ridge National Laboratory
OS	operating system
PC	(IBM) personal computer; pancake coil

PISC	Program for Inspection of Steel Components
PNNL	Pacific Northwest National Laboratory
POD	probability of detection
PSE&G	Public Service Electric and Gas Company
PWR	pressurized water reactor
PWSCC	primary-water stress corrosion cracking
RFEC	remote-field eddy current
RMS	root mean square
RPC	rotating pancake coil
RR	round robin
SCC	stress corrosion cracking
SCF	standard cubic feet
SG	steam generator
SS	stainless steel
TOF	time of flight
TR	transmit-receive
TW	throughwall
UT	ultrasonic testing
WRSM	Water Reactor Safety Information Meeting

1 Introduction

The objective of this program is to provide the experimental data and predictive correlations and models needed to permit the U.S. Nuclear Regulatory Commission (NRC) to independently evaluate the integrity of steam generator (SG) tubes as plants age and degradation proceeds, new forms of degradation appear, and new defect-specific management schemes are implemented. The areas addressed by the program include assessment of procedures and equipment used for in-service inspection (ISI) of SG tubes, and recommendations for criteria and requirements to improve the reliability and accuracy of ISI; validation and improvement of correlations and models that are used to evaluate integrity and leakage of degraded SG tubes; and validation and improvement of correlations and models that predict the generation and progression of degradation in SG tubes as a function of aging, including the effects of the operational environment such as temperature, dry-out and concentration conditions, stresses, and primary- and secondary-side water chemistry.

The studies in this program focus primarily on Alloy 600 SG tubing in the mill-annealed condition, because this is the tubing material that is (and will be) present in plants where SGs have not been replaced and because it is more susceptible to cracking than replacement materials such as thermally treated Alloy 600 or 690. Although most SGs that use mill-annealed Alloy 600 will probably require eventual replacement, the behavior of this material will be of concern for many more years. Thermally treated Alloy 600 and 690 will also be tested. Although these alloys are expected to be much less susceptible to degradation than mill-annealed Alloy 600, it is still necessary that we be able to predict their behavior.

The bulk of the materials used in the program will be exposed to simulated operating conditions and environments during laboratory testing. Because some of the laboratory testing environments represent accelerated conditions and because service degradation, tubing conditions, and in-service operating and inspection conditions cannot always be faithfully represented in laboratory conditions and specimens, this program will seek and use service-degraded tubing and perform in-situ inspections of generators removed from service for correlation with and validation of experimental data, integrity and degradation predictive models, and inspection capability. Comparisons will be made with the morphology and character of service-degraded flaws to help ensure that the flaws produced in the laboratory and used for studies on inspection reliability, pressurization, and leak testing will be as realistic as possible. The reliability of flaw detection and accuracy of flaw sizing data by typical ISI personnel, procedures, and equipment will also be assessed.

This program is divided into four technical and one management task:

Assessment of Inspection Reliability

Research on ISI Technology

Research on Degradation Modes and Integrity

Tube Removals from Steam Generators

Program Management

This annual report describes activities from the inception of the program in August 1995 through September 1996.

2 Assessment of Inspection Reliability (D. S. Kupperman and S. Bakhtiari)

The objective of the inspection task is to evaluate and quantify the reliability of current and emerging inspection technology for current-day flaws, i.e., establish probability of detection (POD); correlate nondestructive evaluation (NDE) parameters with structural integrity; and establish the capability to size cracks. The reliability and accuracy of the techniques must be quantified so that plugging criteria and the consequences of degraded tubes that remain in service after inspection can be evaluated. Eddy current (EC) and other NDE techniques that are currently used for ISI of SG tubes are being evaluated with respect to the probability of flaw detection and accuracy of sizing so the consequences of degraded tubes that remain in service after inspections can be evaluated. The methods and test parameters under investigation are those currently used for various forms (and locations) of degradation. The results of the NDE will be validated by inspection and destructive evaluation of service-degraded tubing.

This program will require an evaluation of results of a round-robin (RR) test that will be conducted by commercial ISI teams. The RR test will include both EC and ultrasonic test (UT) methods. Teams will report the flaw types, sizes, and locations, as well as other commonly used parameters such as voltage responses from the EC tests. Much of this testing will be performed on the SG tube bundle mock-up with laboratory-degraded tubes developed at Pacific Northwest National Laboratory (PNNL) under contract to Westinghouse. This mock-up will be assembled at Argonne National Laboratory (ANL), where it will be set up for RR testing and assessment of emerging technology. Information on the methodology and flaws used, as well as data and results obtained during the Program for Inspection of Steel Components (PISC III) RR testing of SG tubes, will be obtained and compared with the results obtained in the RR testing performed under this program.

2.1 Technical Progress

2.1.1 Mock-Up

The SG mock-up to be used for RR testing and as a resource for assessing new technology will contain 400 tube openings, each with a 3.66-m (12-ft) length of tubing (Fig. 1). The mock-up was partially assembled at PNNL and is now at ANL for final assembly. As part of the effort to assess ISI technology, a field eddy current (EC) system has been assembled. The ANL system includes Zetec's MIZ-30-8 Data Acquisition Unit, 4D Pusher-Puller, PM-1 Probe Motor Control, Stand-Alone Controller, Acquire 30d software

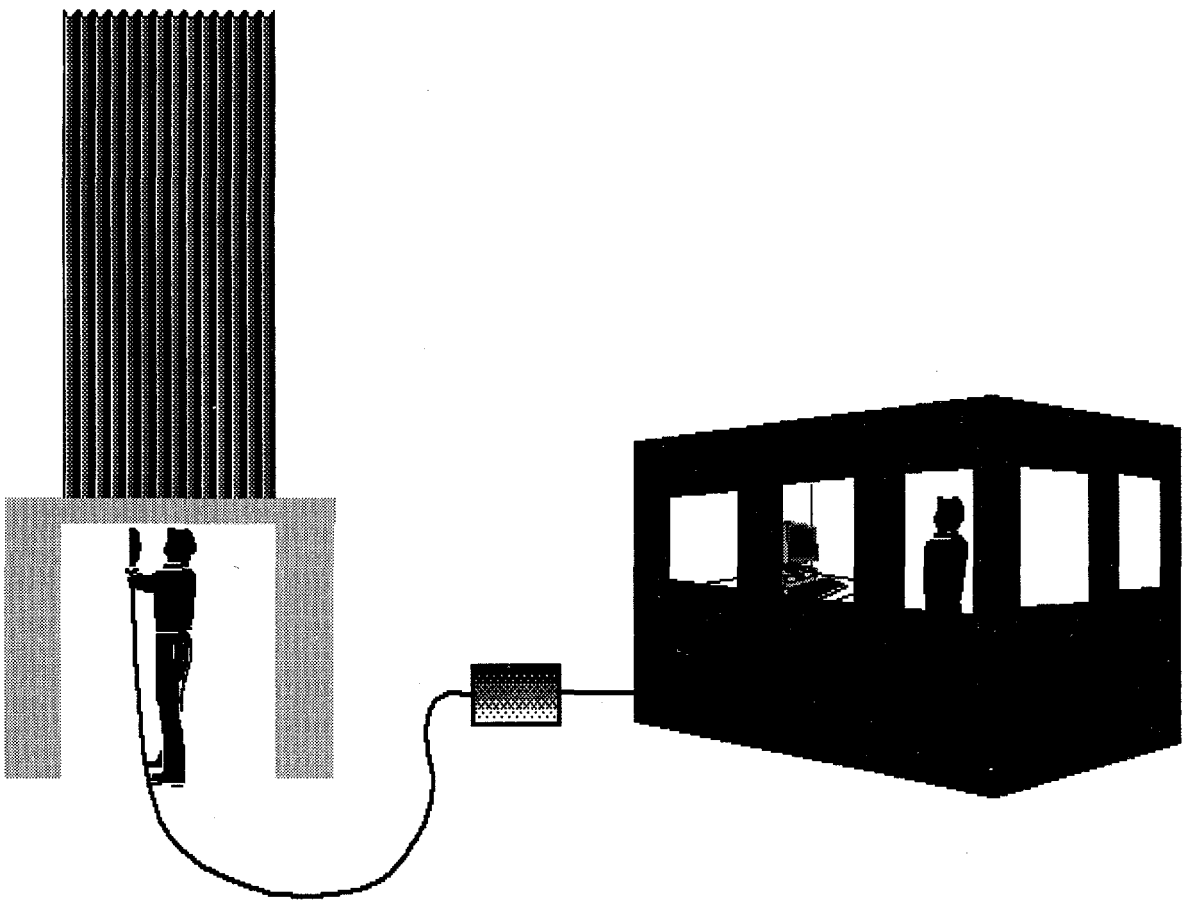

Figure 1. Schematic representation of SG mock-up facility

for data acquisition, and Eddynet95 software for data analysis, which includes c-scan imaging capability. The computer system used for data acquisition and analysis is a Hewlett Packard 700 series system with 128 Mb ram, 2 Gb hard drive, and rewriteable 650 Mb, 1.3 Gb, and 2.6 Gb magneto-optical drives.

This system hardware and software were first tested on an as-fabricated Alloy 600 tube, 3.66 m (12 ft.) long and 22.2 mm (0.875 in.) in diam, positioned vertically on the mock-up support frame and inserted into one of the simulated tube sheet sections provided by PNNL. The probe was fed to the tube via a standard conduit fixed to the bottom of the simulated tube sheet. Various artifacts were positioned on the tube OD to evaluate the ability to determine the axial and circumferential positions of tube flaws and to assess the accuracy of repositioning the probe in the tube. Flaw like indications were evaluated to assess the potential for generating spurious indications.

One possibility for a flaw simulation in the tubes of the mock-up bundle is a laser-cut slot. Although a laser-cut slot does not accurately represent a crack, it may be more

representative of a crack than an electro-discharge machining (EDM) notch. Laser-cut slots are tapered and their entry widths can be as small as 10 μm (0.4 mils). Bridging across the faces of the slot is also possible, making detection somewhat more difficult with a laser-cut slot than with an EDM notch of the same depth. Laser-cut slots 20% deep could be extremely difficult to detect and have responses that lie between detecting and measuring a field-induced crack and an EDM notch. Laser cut slots may be useful for expanding the EC data set.

2.1.2 Evaluation of NDE Techniques for Characterizing Flaws in the Mock-Up

Eddy current and UT techniques are being evaluated as a means to characterize the defects in the mock-up tubes. A subset of twenty 22.2-mm (7/8-in.)-diam tubes taken from the tubes to be used in the mock-up were used for blind testing. The tube specimens exhibit longitudinal inner-surface stress corrosion cracks, longitudinal outer-surface stress corrosion cracks, circumferential inner-surface stress corrosion cracks, circumferential outer-surface stress corrosion cracks, and intergranular attack (IGA). The tubes were subjected to ultrasonic depth and length characterization by high-frequency diffraction and Lamb waves. Eddy current depth and length were estimated by a pancake coil, multi-coil arrays, a polarized probe (Zetec Plus Point), and neural-network algorithms applied to multiparameter EC data. After the tubes were inspected they were metallographically analyzed to establish the actual depth, length, and profiles of the cracks. The analysis of the results will allow the best techniques to be used for characterizing the defects in the mock-up tubes.

2.1.2.1 Ultrasonic Evaluation at High Frequency

A. Diaz at PNNL and T. Gomm at the Idaho National Engineering Laboratory (INEL) collaborated to carry out ultrasonic inspections of the 20 tubes to assess this technique as a method for inspecting tubes before they are integrated into the mock-up SG. The size, shape, and location of the flaws are required so that blind inspection results can be interpreted correctly. High-frequency, longitudinal, and shear waves in a focused, pulse echo mode were used with waves incident at 0 and 45° (for both axial and circumferentially oriented cracks). All of the PNNL/INEL inspections were carried out from the outside of the tube. High-frequency backscatter and frequency analysis was used to characterize IGA. A, B, and C scans were used to characterize all of the cracks and the IGA. Time-of-flight (TOF) data were used to estimate depth when a crack tip echo was detectable; otherwise a 14-dB-drop method with signal movement was used to estimate depth.

Frequencies of 20-50 MHz were employed in an immersion tank. However, because of the attenuation in Alloy 600, the peak in the frequency spectrum is ≈30 MHz for propagation through the wall thickness and back (in pulse echo mode).

Two calibration tubes were used. The first tube contained two sets of outer-surface saw cuts. The first set included four axial cuts 0.25-1.02 mm (0.010-0.040 in.) deep and 5.08-9.78 mm (0.200-0.385 in.) long. The second set contained five circumferential cuts 0.127-1.016 mm (0.005-0.040 in.) deep and 2.16-6.86 mm (0.085-0.270 in.) long. A second tube contained outer-surface saw cuts (axial and circumferential) and EDM notches

on the inner and outer surfaces. The saw cuts are 0.25-1.02 mm (0.010-0.040 in.) deep and 3.43-9.53 mm (0.135-0.375 in.) long. The EDM notches are nominally 0.51 mm (0.020 in.) deep and 6.35 mm (0.250 in.) long.

2.1.2.2 Ultrasonic Evaluation with Lamb Waves

The 20 SG tube samples were also inspected by M. Brook at ABB AMDATA with an ultrasonic probe that propagated Lamb waves in the tube wall; Lamb waves are unaffected by a roll transition. These waves propagate in a free tube wall and are capable of detecting inner or outer-surface circumferential cracks. Although axial cracks are not detectable with this probe unless circumferentially oriented branches are present, it is possible in principle to make a Lamb wave probe that could detect axial cracks. The probe for the data reported here is used in a scan mode that covers a range of 140 mm (5.5 in.). There may not be enough information present in the Lamb wave echo signal to determine the depth, but estimates can be made by measuring the echo amplitude. The length of the defect is accurately estimated by observing the drop in signal amplitude as the defect is scanned. Intergranular attack has been called correctly because the echo signals are generated over a large area of the tube.

Calibration was carried out with a tube that contained circumferential EDM notches with throughwall depths of 20, 40, and 60% and arc lengths of 20, 40, and 60°. The signal from the 20%-throughwall (TW), 60-degree arc notch was set to 80% of full screen height. The probe was moved axially 1.3 mm (0.05 in.) for every 360° scan. A, B, and C scans were generated. The probe was operated at a frequency of ≈5 MHz. A PC-based Intraspect ultrasonic system was used to collect the data.

2.1.2.3 Evaluation with an Eddy Current Array Probe

The 20 tubes were inspected with an EC C5/HD array probe by V. Cecco et al. at Atomic Energy of Canada, Ltd. (AECL). The probe consists of three parts. Two parts contain differential transmit-receive (TR) pancake coil arrays whereas the third contains a bobbin coil that was used simultaneously in differential and absolute modes. Each pancake array consisted of eight independent TR units. The coils in the two arrays are rotated relative to each other to completely cover the entire circumference. Thus, each unit "sees" an arc of 22.5°. The sensitivity to axial and circumferential cracks was comparable. Data could be displayed in Zetec Eddynet c-scan and clip-plot formats. The data from the absolute channels of the bobbin coil were useful in detecting long axial cracks. The amplitude from the bobbin coil was useful in distinguishing axial cracks from IGA. The tubes were also examined with a 24-probe array, each covering a 15° arc to see if more coils would lead to improvements. This data will be analyzed at a later date. The data presented in this report were collected with a Zetec MIZ-30 interfaced with a Hewlett Packard 700 series workstation. Data acquisition and analysis were carried out with Zetec Eddynet software. A standard Zetec 4D probe driver with Zetec PM-1 motor controller was used to pull the probe through the tube at a constant speed of 0.30 m/s (12 in./s).

Calibration was carried out with a standard ASME tube, a tube supplied by PNNL that contained axial and circumferential outer-surface notches, and a Westinghouse-supplied calibration tube that contained a 20% outer-surface axially symmetrical EDM notch, a dent,

and 1.6-mm (0.060-in.)-diam throughwall holes. Lack of calibration tubes with inner-surface notches and limited outer-surface notches severely restricted the ability to estimate the depth of the cracks. Data were collected as the probe was pulled back through the specimen and then through the calibration tubes. The frequencies used were 45, 90, 180, and 400 kHz. The dent was used to adjust the phase angle while the dent signal was oriented horizontally. The vertical component of the 20% outer-surface notch groove signal was set to 10 V. Frequency dependence of the Lissajous-figure orientation and frequency dependence of the vertical component of the signal amplitude were used to distinguish outer-surface from inner-surface flaws and to determine whether the defect was deep or shallow. The expansion transition caused some problems with signal interpretation. If a flaw was detected with the array but not with the bobbin coil, it was called circumferential. If the flaw was detected by both array and bobbin coil, it was identified as axial or IGA.

2.1.2.4 Neural-Network Analysis of Eddy Current Data

Using 16 pancake coils (two rings of eight coils each), C. Dodd carried out a neural-network analysis of the EC data collected for the 20 tubes. The EC coils were ≈4.6 mm (0.180 in.) in diam. Data were acquired with the standard Zetec MIZ-30 acquire program. Manipulation of data was required to convert the neural net training with a single pancake coil to the 16 individual coils of the array. Training of the neural net was carried out with tube standards and 23 metallographically sectioned samples with axial and circumferential outer-surface stress corrosion cracks and IGA. A complication in this effort was a lack of training data for inner-surface defects and only one training sample with a roll transition. Standards that were used contained 360° circumferential notches 20, 40, 60, and 80% throughwall. Lift-off of 0.1 and 0.2 mm (0.004 and 0.008 in.) was also part of the calibration tube and was used to set the phase shift so the lift-off signal was horizontal. The standard also contained a 100%-deep groove and axial notches.

2.1.2.5 Sizing with +Point EC Probe

A standard Zetec, three coil, surface riding, motorized rotating pancake coil (MRPC) probe was used to estimate the depth of cracks. This probe contains +Point (cross polarized), high-frequency-shielded, and pancake coils. Phase analysis of data from the +Point coil was carried out to estimate flaw depth. The +Point coil is sensitive to both axial and circumferential cracks. Calibration was carried out with EDM notches and grooves. In the setup procedure, the Lissajous figure for a 20%-deep OD axial notch was set for a small positive angle.

2.1.2.6 Experimental Results

Figure 2 shows estimated crack depth determined by high-frequency UT examination and by a neural-network algorithm applied to multiparameter EC data vs. the maximum crack depth determined by metallographic analysis of the tubes. The UT technique overestimates the depth of the crack in most cases and particularly in the case of shallow cracks. The main problem for the ultrasonic interrogation was the difficulty in detecting the echo from the crack tip that is used to estimate the depth. The results from neural-

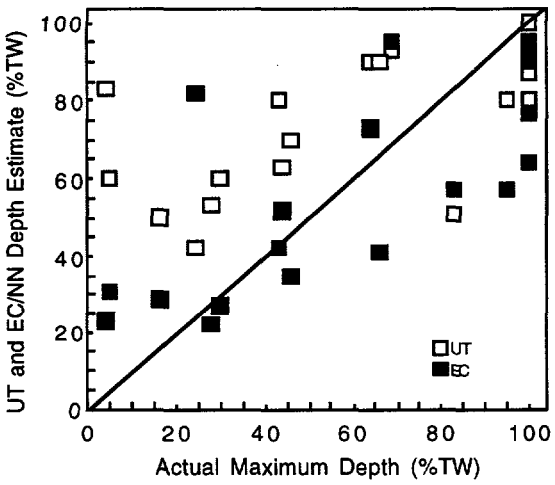

Figure 2.
Preliminary depth estimates (% throughwall) obtained at PNNL and INEL with high frequency ultrasonic waves (open squares) and estimated depth from a neural network (NN) algorithm (C. Dodd) applied to EC data (black squares) vs. the maximum depth (% throughwall) of the crack from metallographic analysis (PNNL) of the set of 20 SG tube specimens.

network analysis of EC data are better and are particularly encouraging, because a proper training data set was not available for this analysis. Significant improvements in the correlation are expected when optimized training sets are used with this neural-network algorithm. Despite the less-than-desirable UT results, the cracked tubes to be installed as part of the mock-up SG will be characterized by high-frequency UT, with improvements in the technique implemented where feasible, and with eddy current neural network analysis.

UT and EC neural-network results are shown in Fig. 3. The depth estimated by the UT technique is consistently greater than that predicted by the neural-network algorithm applied to the EC data.

To better understand the problems that are encountered while estimating depths, data from the 20 tubes have been analyzed in several ways. For example, the data presented in Fig. 4 show the neural-network results of depth predictions for tubes with and without a roll transition. No dramatic difference in depth measuring capability can be observed when EC data are used in conjunction with the neural-network algorithm.

Some estimates of flaw depth were also made with an ultrasonic probe from the inner-surface of the tube (from PNNL report on ultrasonic examination). The results of estimating depth from the inner surface are, on the average, noticeably lower than those obtained from the outer surface. This difference could be the result of differences in probe design but may also be the result of tube curvature effects. Waves incident on the tube inner wall are somewhat focused, whereas waves incident on the outer surface are spread out as they enter the tube wall. Estimates of crack depth obtained by ultrasonic wave inspection on inner and outer surfaces of 20 tubes are presented in Fig. 5, along with neural-network EC results.

The results of applying a neural-network algorithm to EC data are presented as a function of flaw type in Fig. 6. Preliminary estimates from longitudinal outer- and inner-surface cracks circumferential outer-and inner-surface cracks and IGA are separated. No

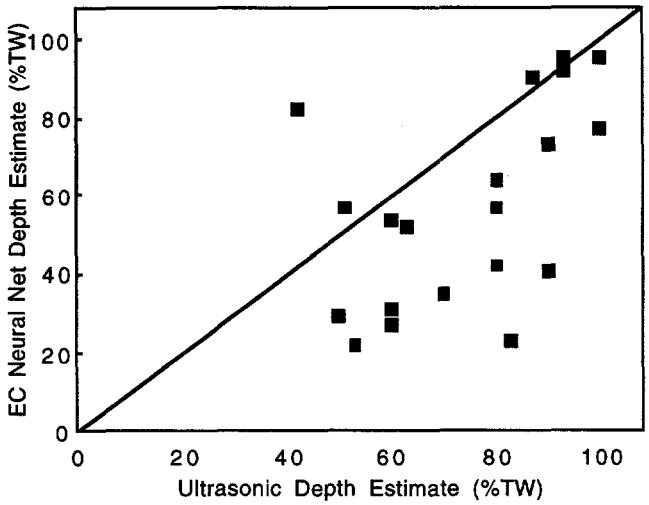

Figure 3.
Flaw depth estimates (% throughwall) from a high frequency ultrasonic wave technique (PNNL/INEL) and a neural network (NN) algorithm applied to multiparameter EC data (C. Dodd).

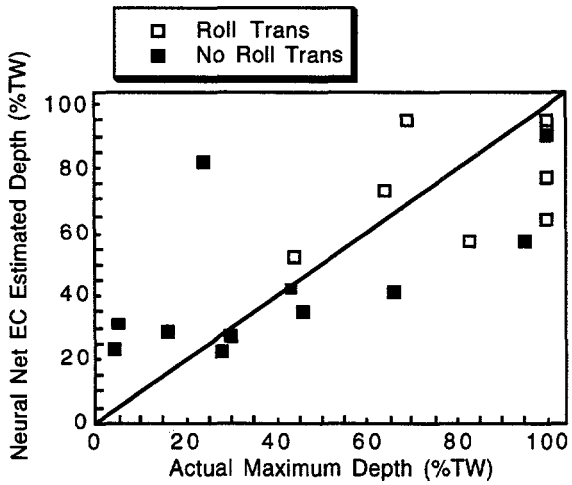

Figure 4.
Estimated depth obtained by applying neural network (NN) algorithm to EC data (C. Dodd) for tubes with and without roll transition.

one defect appears dramatically easier to characterize than any other, although the correlation coefficient from a linear fit to data restricted to outer-surface axial and circumferential cracks is a respectable 0.9. Similar data, obtained by high-frequency ultrasonic diffraction techniques, are shown in Fig. 7.

Estimating depth appears possible with neural network analysis of EC data if proper training-set data are available. However, the result presented in Fig. 6 was limited to a small data set; when upper and lower 95% confidence limits are calculated, the need for larger data sets to judge the effectiveness of neural net analysis becomes apparent. For estimates of OD crack depth only, the upper and lower confidence limits for the mean and individual (i.e., additional) points can be seen in Fig. 8. The range of upper and lower confidence limits is rather large. For example, if a new point were added to the data for an

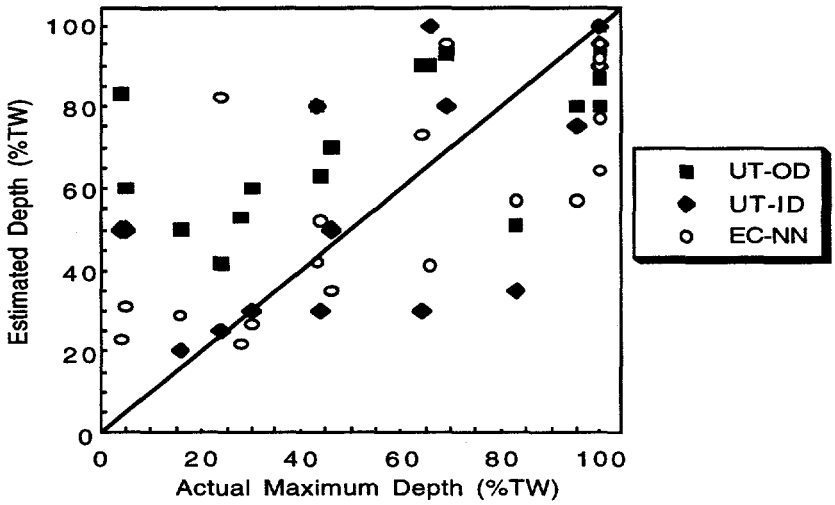

Figure 5. Estimates of crack depth obtained by UT wave inspection of inner (Westinghouse/PNNL) and outer (PNNL/INEL) surfaces (ID and OD, respectively) of 20 tubes, along with preliminary EC neural-network (NN) results (C. Dodd) vs. actual maximum depth

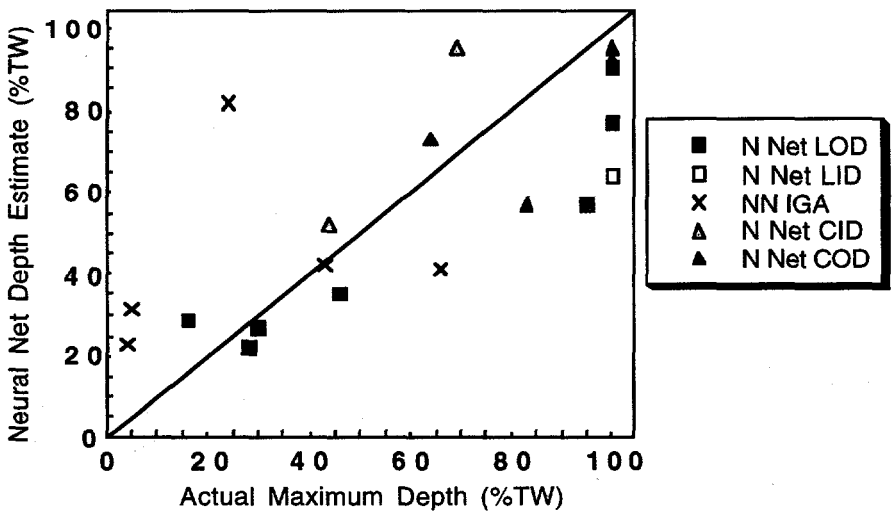

Figure 6. Results obtained by applying a neural network algorithm to EC data are presented as a function of longitudinal OD cracks, longitudinal ID cracks, circumferential OD cracks, circumferential ID cracks and IGA. No one defect appears dramatically easier to characterize than any other.

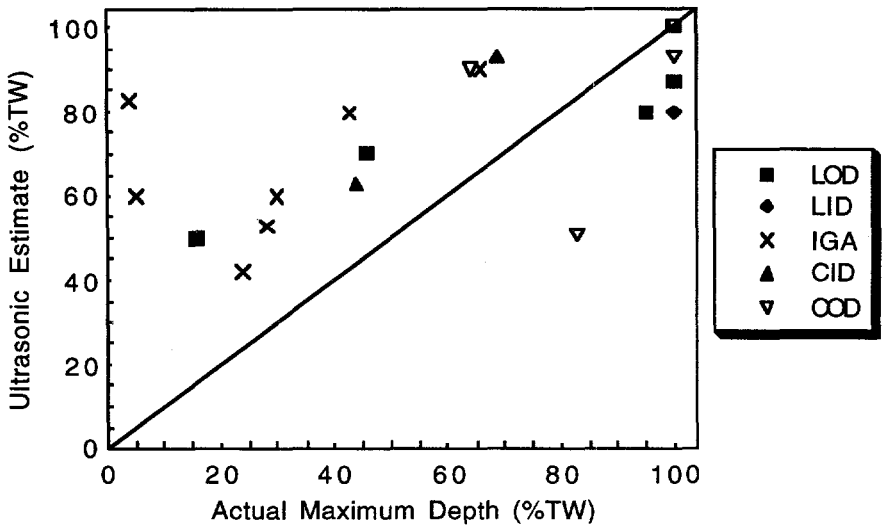

Figure 7. Depth estimates (PNNL/INEL) obtained from high frequency ultrasonic diffraction, for longitudinal OD cracks, longitudinal ID cracks, circumferential OD cracks, circumferential ID cracks and IGA. No one defect appears easier to characterize than any other.

actual maximum depth of 50%, there is a 95% probability that the estimated depth will fall between 15 and 75%, while the mean will still lie between 35 and 55%.

Analysis of EC data from the 20-tube set has been carried out with a phase shift analysis of +Point data acquired at Zetec. The analysis of the data was carried out at ANL with Eddynet95 software. Phase analysis was used to estimate the depth of cracks. Calibration was carried out with a series of EDM notches in calibration tubes. The results are reasonable, particularly if restricted to the cracks that do not represent IGA. Figure 9 compares the results of the analysis of +Point data with those obtained by destructive examination. The correlation coefficient is ≈0.75 for a linear fit to all of the data. Figure 10 shows +Point data with 95% confidence limits. Again, the range of the upper and lower confidence limits is very large because of the small size of the data set. Figure 11 presents the depth estimate results from +Point, neural net, and high frequency UT analysis vs. destructive analyses.

The possibility of combining results of various NDE methods to improve sizing accuracy has been examined. For example, the estimates of depth from the +Point probe are best for the three inner-wall stress corrosion cracks. The application of neural network analysis to data taken from the outer-wall circumferential stress corrosion cracks is better than results from other EC or UT methods. The UT data can be corrected somewhat to account for the oversizing of the reported results. For this report, the empirically corrected UT estimate for depth of longitudinal outer-diameter stress corrosion cracks was determined from

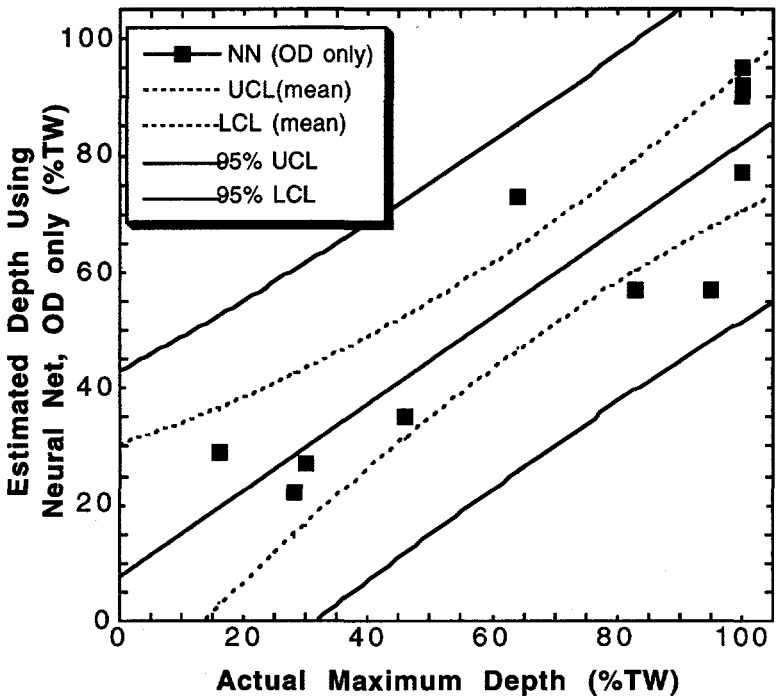

Figure 8. Upper and lower 95% confidence limits (UCL and LCL) for mean and individual (i.e. additional) points for OD depth estimates determined by neural network (NN) analysis. For example, if a new point were added to the data for an actual maximum depth of 50% there is a 95% probability that the estimated depth will fall between 15 and 75%, while the mean will still lie between 35 and 55%.

CDE = -78 + (1.92)RDE,

where CDE is the corrected depth estimate and RDE is the reported depth estimate, with depths in percent throughwall. The results for cracks, excluding the very-difficult-to-characterize IGA, are shown in Fig. 12. This figure indicates how the ability to estimate depth can be improved by basing the NDE method selected on the type of degradation encountered. The linear correlation coefficient for this data is 0.95, better than that obtained with any NDE technique alone. The upper and lower 95% confidence limits are also shown and are better than those for a single method. Improvements in estimating depth are clearly still needed, and means to better estimate depth could include UT from the ID and EC analysis that combines phase and amplitude information. Improvement in the training set for the application of neural networks can also lead to better depth estimates, particularly if there are separate training sets for each type of flaw. Application of signal processing techniques could lead to improved signal-to-noise ratios for EC data and an increase in the accuracy of depth estimates.

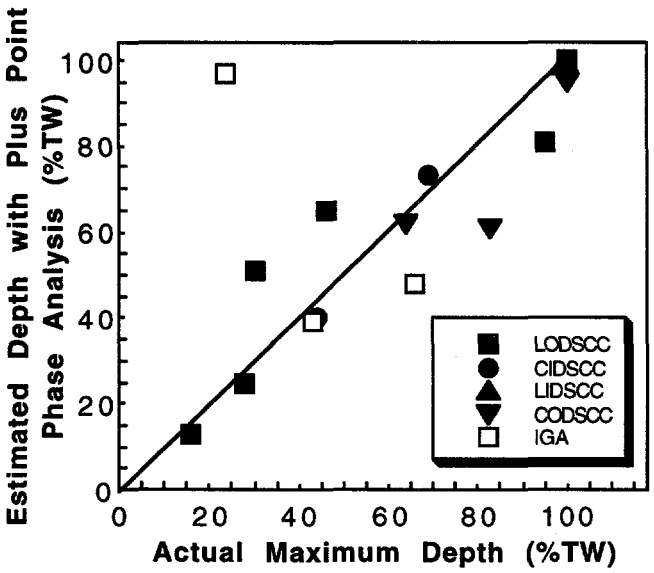

Figure 9.
Crack depth estimates from EC data for 20 tubes by phase shift analysis of +Point data. The analysis was carried out at ANL with Eddynet95 software. Calibration was carried out with a series of EDM notches in calibration tubes. The correlation coefficient is ≈0.75 for a linear fit to all the data, though sizing of the ID cracks is very good. LODSCC, CODSCC = longitudinal and circumferential outer-diameter stress corrosion crack; LIDSCC, CIDSCC = longitudinal and circumferential inner-diameter stress corrosion crack.

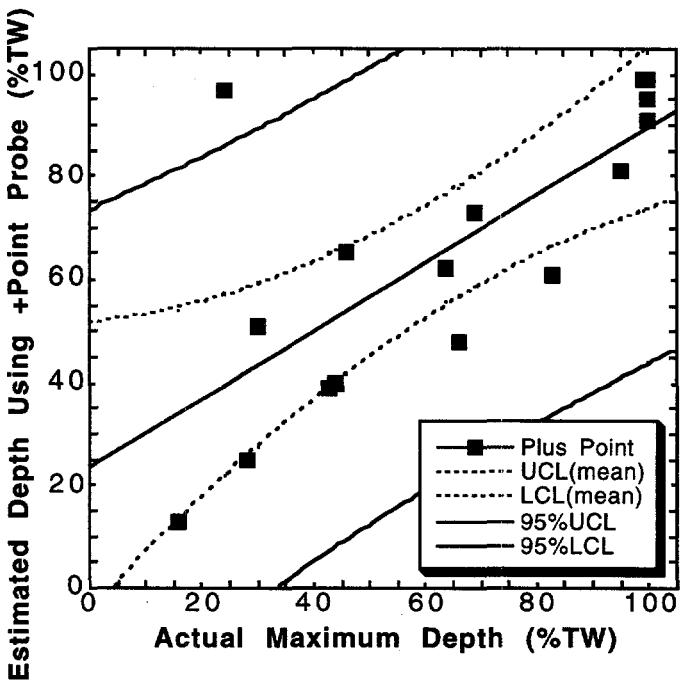

Figure 10. Depth estimates from +Point data with 95% upper and lower confidence limits for mean and additional points. Range of upper and lower confidence limits is very large because of small size of data set.

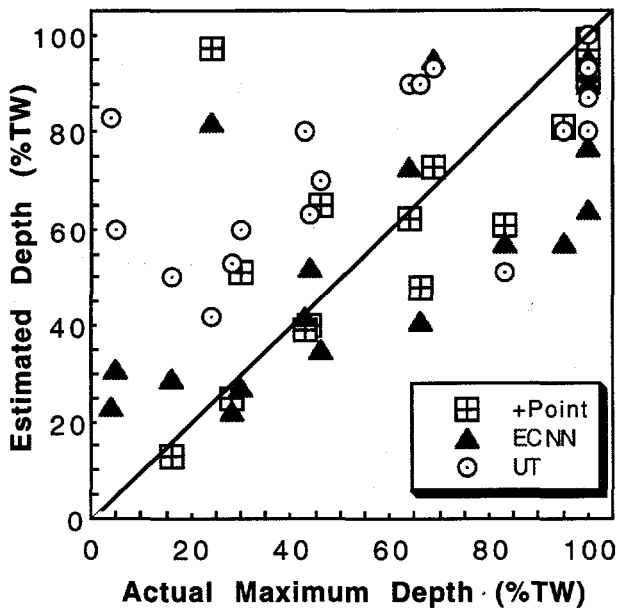

Figure 11.
Depth estimated by +Point, eddy current neural net (ECNN), and high-frequency ultrasonic (UT) analysis vs. actual depths obtained by destructive analyses.

Crack length is somewhat easier to measure than crack depth. A comprehensive characterization of crack length was also carried out with a Zetec +Point probe. Crack lengths estimated from the data were compared with lengths estimated by destructive examination (DE) carried out by PNNL. The data were acquired at Zetec and analyzed at ANL with Eddynet95 software in the c-scan mode; the results are shown in Fig. 13. For complicated crack structures revealed by DE, the full extent of cracking was compared with the estimated length. If a well-defined, deep crack was found among a series of shallow cracks, the length of the deep crack was compared with the EC-determined length. The results for circumferential cracks (0.99 linear-fit correlation coefficient [LFCC]) are better than results for axial cracks (0.90 LFCC). It is difficult to define the ends of the crack because the EC signal does not drop sharply at the edges. Subjective judgment is therefore required when estimating circumferential or axial crack lengths. The lengths of inner wall cracks may be much easier to determine than the lengths of outer wall cracks because the EC signal is defined better (0.99 LFCC for ID cracks versus 0.92 LFCC for OD cracks).

An alternative to characterizing crack length with ECs is the use of ultrasonic techniques. One possibility is to use ultrasonic guided or Lamb waves that are launched from the inside of the tube and propagate axially in the tube wall. An ultrasonic Lamb wave image (from ABB-AMDATA) of a laboratory-grown CODSCC in one of the Alloy 600 SG tubes is shown in Fig. 14. This image suggests six crack segments, five at the same axial location and one offset axially, with an arc length of 50°. The total arc length that was indicated ultrasonically is 130°. The DE showed a crack with an arc length of 160° that contained a segment with an arc length of 60°, axially offset from the larger segment by ≈0.05 in. While the DE of the lower part of the crack shown in this figure does not reveal well-

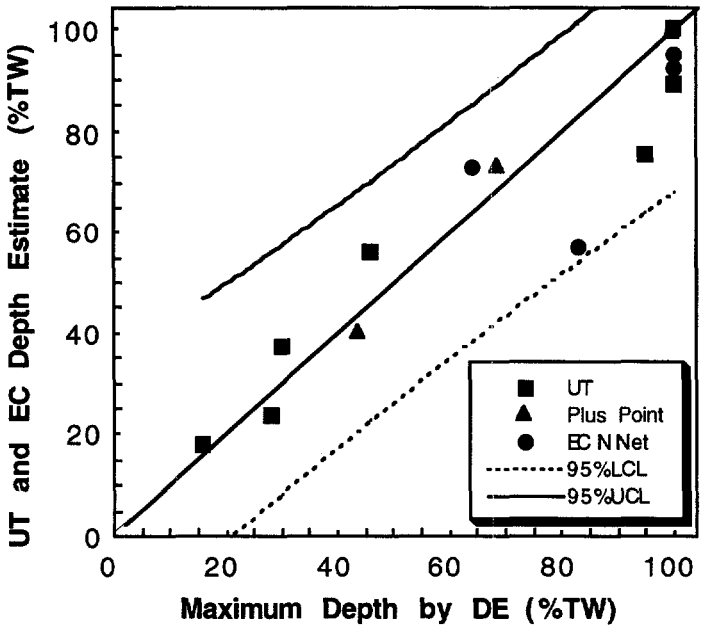

Figure 12. Estimated maximum crack depth vs. maximum depth obtained by destructive examination (DE). Depths from ID cracks were determined from phase analysis with a +Point EC probe (triangles). Depths for circumferential OD cracks were estimated from neural network analysis of EC pancake coil data (circles). Depths for longitudinal OD cracks were estimated from high-frequency ultrasonic data (UT) corrected empirically for systematic over-calling of depth (squares).

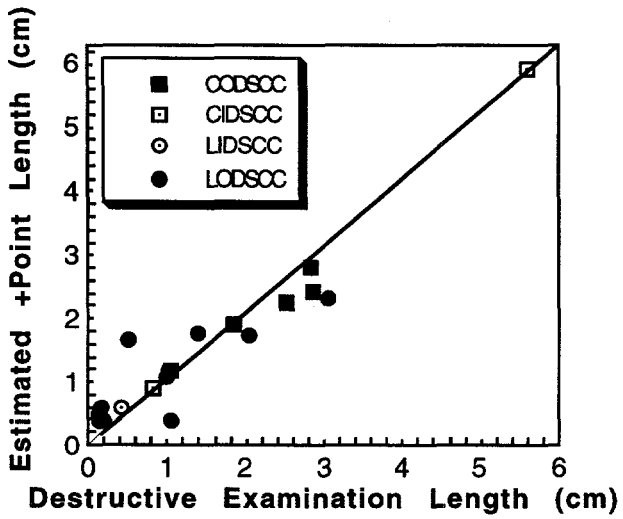

Figure 13.
Estimated crack length vs. destructive-examination (DE) crack length from 20-tube set. Estimates were generated from +Point EC data acquired at Zetec and analyzed at ANL with Eddynet95 software. For complicated crack structures revealed by DE, full extent of cracking was compared with estimated length. If a well-defined deep crack was found among a series of shallow cracks, length of deep crack was compared with EC-determined length.

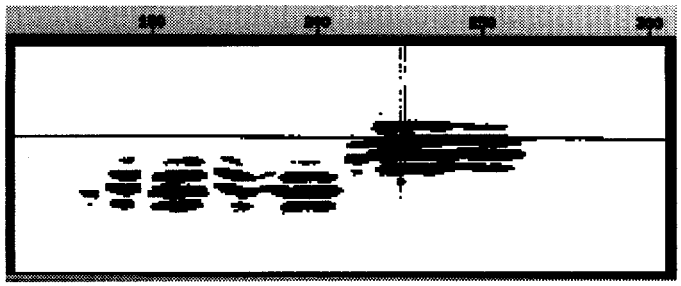

Figure 14. Ultrasonic Lamb wave image (from ABB-AMDATA) of laboratory-grown circumferential inner-diameter stress corrosion crack in Alloy 600 SG tube. Image suggests six segments, five at the same axial location and one offset axially with an arc length of 50°. Total arc length indicated ultrasonically is 130°. Destructive examination showed a crack with total arc length of 160°, containing a segment with an arc length of 60° axially offset from the larger segment by about ≈1.3 mm (0.05 in.). While destructive examination of lower part of crack shown in this figure does not reveal well-defined segments, the DE does show widely varying depths for this part of crack. Segments indicated ultrasonically are result of low-amplitude signals from shallower parts of continuous crack.

defined segments, the DE does show widely varying depths for this part of the crack. The segments indicated ultrasonically are the result of low-amplitude signals from the shallower parts of the continuous crack.

A second UT method for characterizing the cracking pattern is to use high-frequency normal-incidence longitudinal waves launched in water. A high-frequency ultrasonic image of a stress corrosion crack is shown in Fig. 15. The image shows the intersection of a complicated crack with the outer surface of the Alloy 600 tube. The image shows the roll transition as a dark horizontal line across the center of the image, along with circumferentially and axially oriented crack segments. The axial segments are up to 8 mm (0.3 in.) in extent. A 50-MHz normal-incidence longitudinal focused beam in water was used to create this image at INEEL.

Examples of crack length estimates obtained by UT and EC techniques for selected tubes are shown in Figs. 16-20. The primary emphasis in this set of figures is on circumferential cracks. The data were obtained by ultrasonic TOF diffraction and amplitude drop at PNNL and INEL, by Lamb waves at ABB AMDATA for circumferential cracks, and by several EC probes, including conventional array analysis at AECL, neural-network algorithm applied to EC data by Dodd, and +Point at ANL. The results obtained by UT techniques exhibit better resolution, and as a result, cracks that may appear segmented on ultrasonic interrogation may not appear segmented with EC probes. Although Lamb waves were not especially useful for measuring crack depth, inspection with Lamb waves appears to be useful for detection of circumferential cracks and length estimates. Lamb waves can also be used to detect axial cracks if they contain circumferential components and exhibit IGA. If they are used in a scanning mode, Lamb waves can be used to provide a good image of a defect. In addition, Lamb waves are not affected by the roll transition. The locations of cracks may vary considerably with the technique used. When symbols are

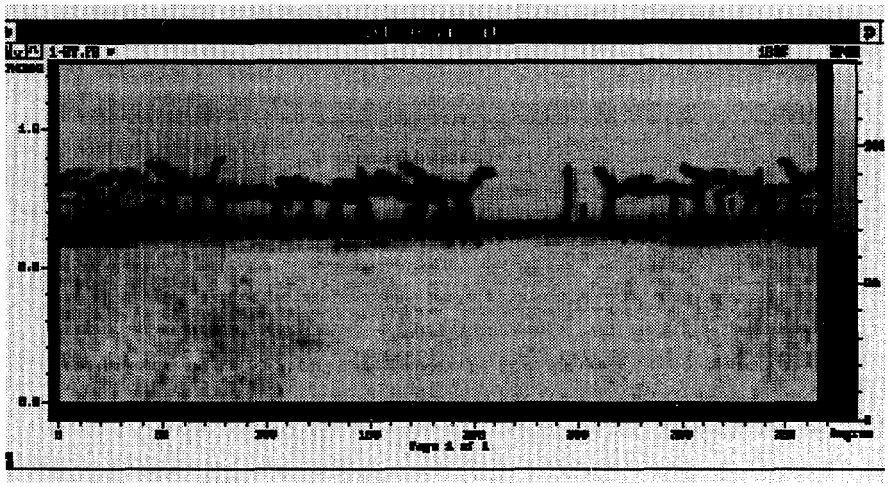

Figure 15. High-frequency ultrasonic image of a stress corrosion crack. Image shows intersection of complicated cracks with Alloy 600 tube outer surface. Roll transition appears as a horizontal dark line across center of image, along with circumferentially and axially oriented crack segments. Axial segments are up to 7.6 mm (0.3 in.) in extent. INEL used a 50 MHz normal-incidence, longitudinally focused beam in water was used to create this image (INEL).

observed between the ends of a line segment that represents the length of cracks in Figs. 16-20, the segment has "structure" and the location of the symbols indicates the location of signal peaks in the data.

Normal-incidence high-frequency ultrasonic and Lamb wave evaluation of the crack length in Tube 401 (with roll transition) correlated well with DE of this circumferential OD crack, the maximum depth of which was 83% TW (Fig. 16). No EC data were available for this tube. Estimates of crack length and location in tube 406 (with roll transition) and an OD circumferential crack, partly throughwall, were good for both UT and EC (Fig. 18). Lengths of the circumferential OD, partly-throughwall crack were correctly predicted by EC and UT for Tube 410 (with roll transition) although the locations were not (Fig. 19). Again, high-frequency UT and Lamb wave ultrasonics correctly identified the segmentation of the crack.

Tube 206 (no roll transition) contained axially oriented OD cracks, partly throughwall. The estimates from the EC array were short for two of the three cracks revealed by DE (Fig. 20). For two of the three cracks revealed, the high-frequency UT and the +Point techniques estimated the lengths and locations correctly. However, the +Point and high frequency UT probes (but not the EC array) indicated the presence of a crack not revealed by DE.

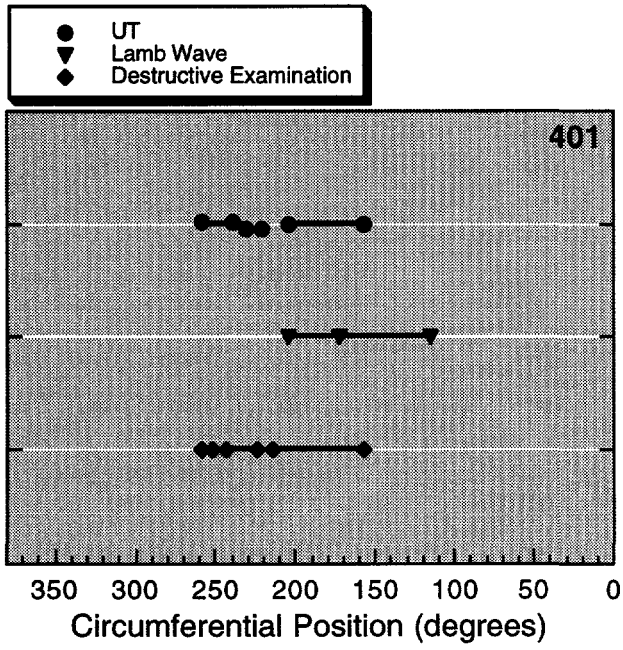

Figure 16.
Length of circumferential outer-diameter crack in 22.23-mm (0.875-in.)-diam Alloy 600 tube predicted by high-frequency ultrasonic wave (incident to outer surface of tube) (PNNL/INEL) and by Lamb wave (ABB). No EC array data are available for this tube. Symbols between ends of crack representation indicates segmented structure; location of symbols indicates location of signal peaks in data.

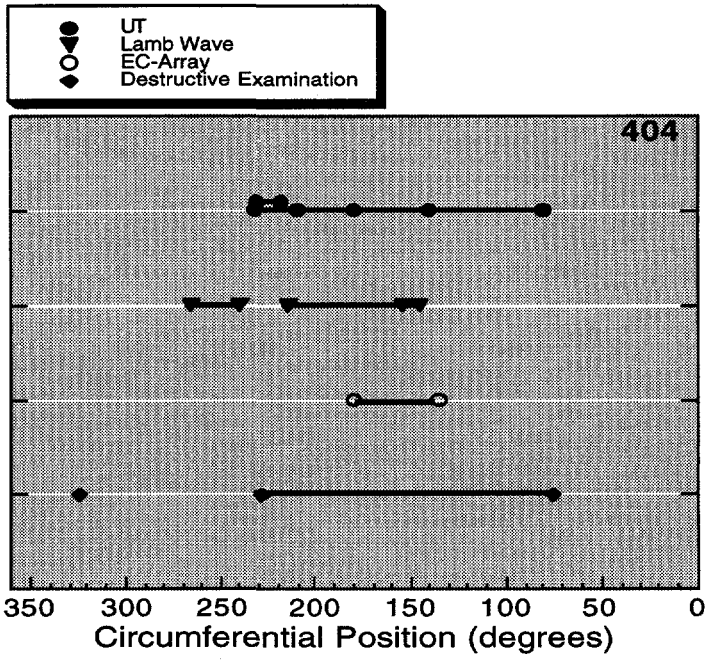

Figure 17. Length of circumferential inner-diameter stress corrosion crack predicted by high-frequency ultrasonic wave (incident to outer surface of tube) (PNNL/INEL), Lamb wave (ABB), and C5/HD EC array (AECL). Symbols between ends of crack representation indicate somewhat segmented structure; location of symbols indicates location of signal peaks in data.

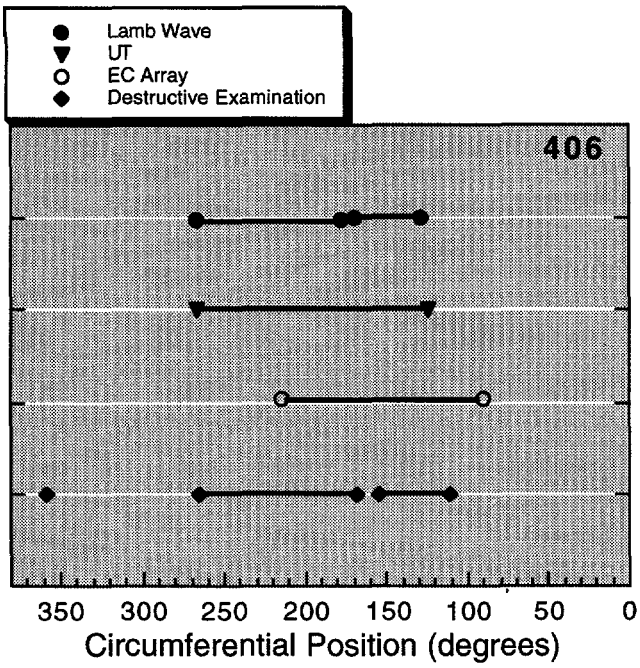

Figure 18.
Length of circumferential inner-diameter crack in 22.23-mm (0.875-in.)-diam Alloy 600 tube predicted by high-frequency ultrasonic wave (incident to outer surface of tube) (PNNL/INEL), Lamb wave (ABB), and C5/HD EC array (AECL); location of symbols indicates location of signal peaks in data.

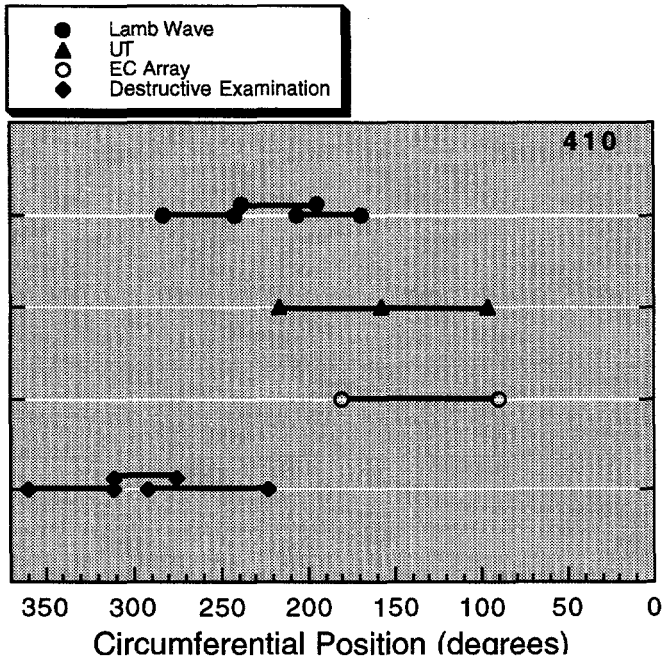

Figure 19.
Length of circumferential inner-diameter crack in 22.32-mm (0.875-in.)-diam Alloy 600 tube, predicted by various methods. Location of symbols indicates location of signal peaks in data.

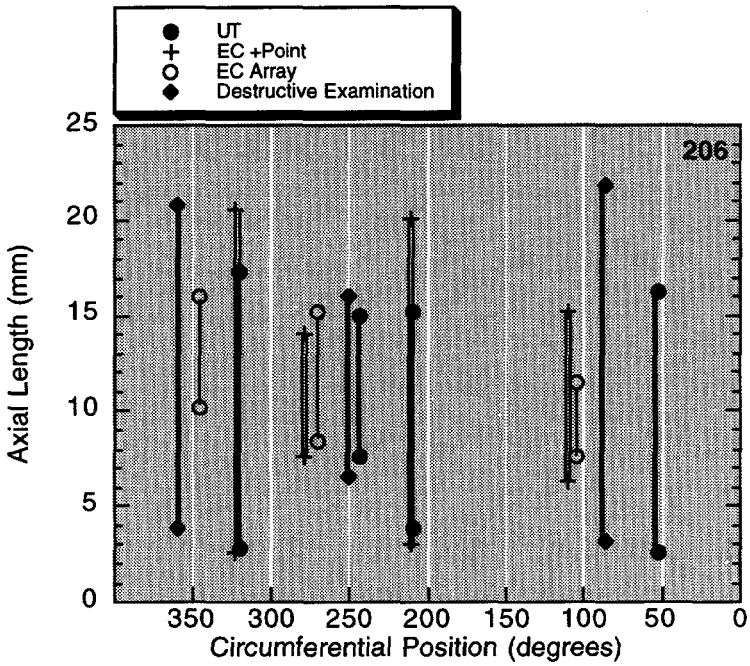

Figure 20.
Length of axial outer-diameter crack in 22.23-mm (0.875-in.)-diam Alloy 600 tube predicted by high-frequency ultrasonic wave (incident to outer surface of tube) (PNNL/INEL), +Point probe (ZETEC/ANL), and C5/HD EC array (AECL). Location of symbols indicates location of signal peaks in data.

2.1.3 Determination of Leak Rate and Failure Pressure

Scatter in single parameter correlations between failure pressure and EC voltage has led to an effort to improve the correlation through multivariate parameter correlations. Substantial scatter is observed in tube failure pressure (more for pulled tubes than model boiler tubes) and leak-rate data when correlated with EC voltage amplitude, as can be seen schematically in Figs. 21 and 22.

Improvements in signal analysis (e.g., application of neural-network algorithms) are being explored in this program to find a better correlation between failure pressure and leak rate with EC signals. The work planned will be presented in the next report.

2.1.4 Inspection of Sleeved Tubes

Two primary problems are associated with sleeved tubes: the large expansion and the distortion in signal from ferromagnetic material produced by welding procedures. Transmit-receive probes have an advantage over bobbin coils for inspection of sleeves.

Dobbeni et al.[2] assessed the application of ISI technology to sleeved tubes that were repaired with hybrid expansion joints in 1993 and 1994. Deep circumferential primary-water stress corrosion cracks (PWSCCs) were found in the parent material. Laser-welded sleeves were used in 1994. Cecco 3 (C3) and +Point probes were selected to detect circumferential and axial cracks, respectively, in sleeved tubes. Large permeability variations were found if the C3 probe was used without a magnetic bias, which reduced these variations. Based on C3 and +Point probe inspection data, tubes were pulled that showed axial and circumferential cracks in laser-welded sleeves (weld and hydraulic

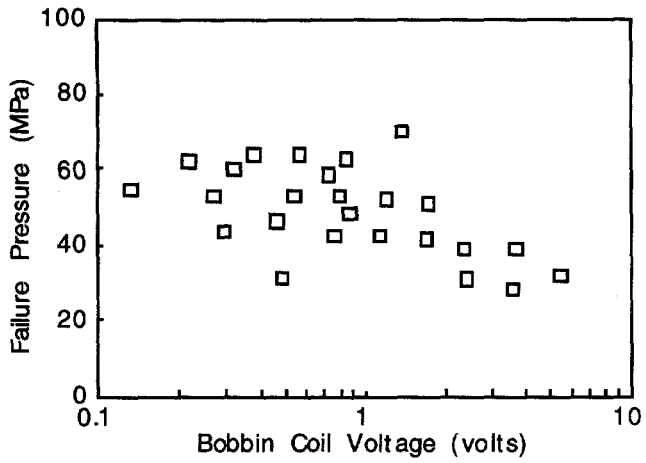

Figure 21.
Schematic semi-log plot of failure pressure vs. bobbin coil voltage for pulled tubes.

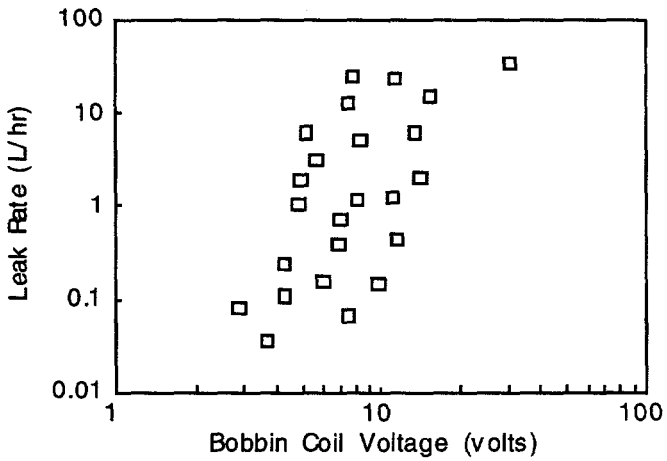

Figure 22.
Schematic log-log plot showing leak rate vs. bobbin coil voltage for 19.05-mm (0.750-in.)-diam pulled tubes and model boiler tests (ΔP= 16.1 MPa [2335 psi]).

transitions) and circumferential cracks and wastage in hybrid expansion joints (parent tube and hydraulic transition). A false call was also present in the transition. This effort of Dobeni et al. showed that a good correlation can be obtained between EC data and defects in sleeved tubes if the cracks are deep (>90% throughwall). Permeability variations create significant problems for analysis. The +Point probe provides good imaging except in the weld area and experienced analysts are required to interpret data from the C3 probe.

2.1.5 Program for Inspection of Steel Components III

Round-robin testing to evaluate techniques used to inspect SG tubing ended in 1993. The experimental evaluation of test procedure performance was carried out for a tubesheet, tube support plate, antivibration bars (AVB), and U bends. Approximately 100 defects (but very few cracks) were evaluated; stress corrosion cracking including axial SCC, IGA, spark-eroded axial and circumferential narrow slots, pitting, and wastage. USA organizations involved with the RR testing were, Allen Nuclear Tech, Conam, PNNL, Zetec, Westinghouse, and Oak Ridge National Laboratory (ORNL).

Although analysis of the RR tests has not yet been released, some teams performed consistently better than others. As a result, there is a need to determine what the teams that performed better did to attain higher scores. The best results were associated with the UT techniques, but not all defects were examined by UT and thus any claims of superiority of UT techniques must be qualified. In addition, speed and cost are other factors that must be considered when comparing EC and UT techniques. Nevertheless, detection of the circumferential defects was relatively easy with UT. Combining EC with UT techniques did not seem to provide an overall advantage and there is no clear indication from this study that defects <40% deep can be detected. The correlation between the NDE signal and a defect is much better if the flaw is >40% deep. Another conclusion of this study is that there is a need to analyze each type of defect to establish the best NDE method for its detection.

Because the defects were not field induced, there is concern about how well the laboratory-grown cracks represent field cracks, particularly circumferential cracks. Furthermore, the sample of defects consisted of 90 notches and only 7 cracks. Questions have been raised about the argument that the probability of detection (POD) for cracks and notches by EC is approximately the same and thus the use of notches is appropriate. The value of the results of this study is questionable because the number of cracks was limited and inspection procedures varied.

2.2 Workshops

A committee on Nuclear Regulatory Activities/Committee on the Safety of Nuclear Installations (CNRA/CSNI) Workshop on Steam Generator Tube Integrity in Nuclear Power Plants was held at Oak Brook, IL on October 30-November 2, 1995. One of the panel sessions addressed inspection issues. One of the "products" of the workshop is Table 1, which presents the circumferential-crack inspection procedures that are used by research teams in nine countries.

2.3 Emerging Technology

Many aspects of ISI technology can be improved. Some potential improvements are discussed below, including some that have already been implemented. Faster EC data analysis is possible through fiber optic and satellite links. Raw EC data files can be transferred from an optical disc at a data acquisition location to a hard disc at the data analysis location via a fiber optic link, thus eliminating a delay of ≈4 h that would otherwise be experienced because of the need to physically transfer the optical disc to an off-site location for analysis. Digital satellite communication can also be used to connect off-site and on-site analysis. A transportable earth satellite station can be installed at a plant site while a permanent earth station can be established at the location where the analysis will take place. Cost savings and faster inspections can be realized with this communication option.[3]

Remote-field EC (RFEC) inspection, which employs low-frequency AC to inspect tubes from the inside, is a throughwall inspection technique. A solenoid coil generates the EC while detectors are axially displaced from the exciter by two or more tube diameters and

Table 1. International comparison of circumferential crack inspection

Country	Technique	Detection Limit (minimum depth)	Sizing	Scope	Future Actions
USA	EPRI guidelines are employed. Use RPC (+Point, Pancake) and array probes (Cecco).	Limit is plant specific. Detection threshold is 40-50% through-wall, from ID and OD.	No qualified sizing techniques expected until 1996. Current method for length is based on RPC. Phase and amplitude used for depth while +Point appears best for length.	Scopes are plant dependent. In general, 20% of tubes are inspected.	Qualified sizing by EPRI guidelines is expected. More tubes to be pulled for performance-based qualification. Alternate repair criteria and better probes and software needed.
France	RPC (absolute and differential) using EdF Procedures. Qualification based on pulled tubes.	The threshold is 50% throughwall for OD cracks.[a]	No depth sizing. OD circ. length not accurate. Only ID crack lengths are sized. (RPC accuracy is approximately ±30°).	Inspect 100% of 600MA tubes (hot leg) in roll trans. with RPC each year (OD). For 600TT tubes, inspect 100% sludge pile, and 25% at random. Nothing done for 690 tubes.	Qualifying UT equipment but no plans for industrial use. Improve OD circumferential crack detection (determination of size is not a primary objective). Automated analysis.
Japan	Detection with 8 x 1 probes.	50% throughwall for ID cracks.	No data.	100% at mechanical expansion using 8 x 1 (hot leg).	New probe for faster inspection (rotating-field probe). Automated analysis and double manual analysis for future.
Finland	Bobbin coil for general inspection, with RPC on tube sheet. No crack-ing problems.	Not applicable	No sizing.		Assess single-pass probe for detection.

Table 1. International comparison of circumferential crack inspection (cont'd.)

Country	Technique	Detection Limit (minimum depth)	Sizing	Scope	Future Actions
Canada	Cecco-3 is used for detection and sizing (amplitude based). Technique qualified on pulled tubes. Qualification based on lab samples.	40-50% throughwall for OD cracks.	Use Cecco data from Bruce pulled tubes, estimate ±15% of throughwall depth, 5 mm length for OD cracks.	Inspection 100% with active known degradation. 20% for plausible degradation. Only small samples for I-800 SGs.	Auto analysis of CECCO probe data. Improved analysis using c-scan plots. Work on UT probe development and qualification. Validation program with lab/pulled tubes.
Germany	Bobbin coil and RPC but no cracks.	Not applicable	Not applicable	10% every 4 yr with bobbin coil, covering 100% of length.	No need
Belgium	RPC + UT and +Point used for inspections. Techniques qualified on EDM notches and pulled tubes.	30-40% throughwall for OD cracks using EC + UT.	Estimation of degraded cross-sectional area from raw UT and TOF data.	100% in plants with cracks (all hot leg tubes, some cold leg).	Continue to improve EC and UT technique. Continue to develop sleeve inspection technique. Assess new transmit/receive probes.
Spain	RPC with qualification on lab samples and pulled tubes.	50% throughwall for OD cracks.	No sizing.	100% of plants with cracks (hot leg) and 3% of others, except 0% for I-800 tubes.	Replace SGs that have circ. cracks. Use +Point and RPC for detection.
Switzer-land	Use bobbin coil and RPC on crevice, tube sheet, etc. If nothing seen with bobbin coil then no RPC is used. No formal technique qualification required.	50% throughwall.	Use reference notches, but change of length is most important for OD and ID cracks. Length criteria is 13 mm.	3% of I-800 and I-690 tubes and 100% for I-600 tubes (hot leg).	Assess new multielement probes to be tried for fast screening. Need for better understanding of growth rate and undefined signals.

[a] Based on 72 pulled tubes, the POD is 95% for outer-surface cracks that over 35% of the cross-sectional area of the tube (at least part of the crack exceeded the detection threshold), and 95% for inner-surface cracks that cover 29% of the cross-sectional area.

may be oriented to measure any component of the flux density. The tube acts as a waveguide. The pickup coil senses mainly the indirect electromagnetic (EM) coupling. In contrast to conventional EC systems, in RFEC inspection, the field on the outside of the tube wall is much greater than the field on the inside. The field is mainly due to energy that is diffusing back inward from the outside. Defects cause the amplitude and phase of the signal to change. Impedance plane diagrams are used for signal analysis. In general, the angle of the defect trace on the monitor is used to characterize the anomaly, but amplitude is also used. Unlike the conventional impedance plane, the RFEC voltage plane is not restricted to the first quadrant. Points on the RFEC plot represent amplitude and phase of through-transmission signals. Remote-field EC signals cause almost no phase change and are well separated from liftoff, but separation of the different types of defects is relatively difficult. The technique might be useful for characterizing outer-surface defects.[4]

As indicated in this report, neural-networks have the potential for improvement over conventional pattern recognition techniques in the area of data analysis and interpretation. Neural-network technology has been applied to the analysis of EC data and is reported in this and other documents.[5] Good results have been achieved with limited samples, and neural-networks show promise as a data analysis scheme. The neural network processes and classifies raw data with good results for defect detection using four frequencies (100, 200, 400, 800 kHz).

It is possible that defects can be reconstructed from EC data, but the reconstruction depends on the diffusion equation and one has to rely on indirect algorithmic approaches to solve the inverse problem.[6] Eddy current analysis differs from radiographic or ultrasonic techniques, where the reconstruction of defects is possible because the physical phenomena are governed by the wave equation. The time reversal nature of the wave equation permits the use of procedures such as holography and tomography for defect reconstruction. The "solution" to the inverse problem for EC techniques is to use pattern recognition algorithms to interpret the signals. The variations in shape of the trajectories of the signal in the impedance plane are used in the pattern recognition schemes. Significant additional effort is needed to optimize this method of signal analysis.

Other researchers have explored the possibility of using neural networks to analyze EC data for systems other than SG tubing. Mann et al.[7] used neural networks for the inversion of EC data to obtain flaw sizes. A back-projection algorithm with a uniform-field EC probe was used in their work. The flaws of Mann et al., consisted of five semi-elliptical EDM notches and two fatigue cracks in Ti-Al-4V. When a 1000-pair training set (representing ≈1% of the possible flaws) was used, the correlation between predicted and actual depth was very good (within ±10%) and probably could be improved even more with a larger training set. In their study, the researchers suggest that the depth of a crack can be estimated reasonably well with neural-networks, even when the system is trained on EDM notches.

The application of a three-dimensional (3-D) EC analysis to EC signals has been carried out for SG tubes.[8] A reasonable correlation between experimental and theoretically predicted results has been achieved. Finite-element and boundary-element methods were applied to the EC problem. Experimental and calculated probe impedance trajectories for 100 and 400 kHz are presented for four 50% external slits with a width of 0.25 mm (0.010

in.), that were 90° apart. The agreement between calculation and experiment (differential bobbin coil) is satisfactory. Because the computer time required to perform 3-D calculations is very long, simplified two-dimensional (2-D) analyses have been examined. Two- and 3-D analyses of EC signals from 50 and 100% throughwall cracks in SG tubes, with 100 and 400 kHz frequencies were compared with experimental measurements. The results are qualitatively similar, but, quantitatively, the 3-D analysis appears significantly better (2-D results were ≈1/2 of the experimental value). The problem with the 2-D analysis may be due to the lack of information about the volume of the crack. Other efforts to reconstruct 3-D images from EC signals (the inverse problem) are found in Refs. 7 and 8.

Advances in digital signal processing may dramatically improve our capability to extract information from an EC probe. It may be possible to use sophisticated digital filters to solve problems that are now approached by multifrequency techniques, such as the elimination of signals from the tube support plates. Stepinski and Maszi[9] address the problem of detection and classification of material defects during an EC inspection. They consider algorithms for detecting and characterizing flaws and propose a new type of filter for classifying EC data. The new 2-D conjugate spectrum filters (CSFs) are sensitive to both phase angle and shape of the EC response. They transform all of the EC patterns into straight lines and thereby simplify the decision-making process. If digitized EC data sampled at a frequency synchronized with the inspection speed is available, CSFs could be used with SG tubing.

Rose et al.[10] describe a method for inspecting SG tubing with guided ultrasonic waves. The advantage of this concept is the absence of a moving probe and 100% coverage of the tube. Launching of guided waves with sufficient energy to inspect a long length of tubing is very difficult and sensitive to ultrasonic frequency, but theoretical considerations have significantly helped to optimize probe design. The ultrasonic wave is injected at the top of the tubing and travels the length of the tube with little attenuation. Echoes that return to the transmitting probe indicate the presence of defects in the tube. Defects that are only 10% of the total cross-sectional area have been detected in tubes nearly 17 m (55 ft.) long. Tests have shown that guided waves can travel at least 49 m (160 ft.). Although ultrasonic guided waves may be useful for inspection of SG tubing, satisfactory characterization of a detected flaw may not be possible for a fixed-probe configuration, because of the distortion of the ultrasonic wave as it propagates in the tube wall. The use of guided waves as part of a scanner, as described in Section 2.1.2.6, may be more effective for detecting circumferential cracks.

3 Research on ISI Technology (S. Bakhtiari and D. S. Kupperman)

The objective of this task is to evaluate advanced NDE and signal analysis techniques for reliable ISI of original and repaired SG tubes. Improved correlations between EC results and flaw morphology, leak rate, and failure pressure will be assessed. Eddy current ISI methods have not always proved reliable for detection, classification, and sizing of flaws, especially cracks. The implementation of degradation-specific management requires detailed knowledge about the specific nature and severity of flaws. Improved techniques (EC and others) are needed for more reliable inspection and interpretation of flaws. The reliability and accuracy of the techniques must be quantified so that plugging criteria and the consequences of leaving degraded tubes in service after inspection can be evaluated. Furthermore, the robustness of the voltage parameter and of other EC parameters and techniques must be evaluated with respect to their range of applicability.

The research on improved EC inspection of SG tubes will focus on four primary areas: (1) application of analytical methods for the prediction of EC response as a function of probe design, flaw characteristics, and material properties; (2) evaluation of effective signal analysis procedures; (3) evaluation of flaw imaging and display methods for simple and accurate flaw characterization; and (4) assessment of improved probe designs that use directional arrays so axial and circumferential defects can be examined simultaneously. The reliability and effectiveness of improved inspection techniques will be demonstrated through laboratory testing of SG tubes that contain various flaws and the SG tube bundle mock-up. Final validation will utilize in-service-degraded SG tubing.

3.1 Analytical/Computational Electromagnetic Modeling

Because the interaction of the induced EC coil field with heterogeneous media is a complex phenomenon, it is vitally important to have a reasonably accurate a-priori knowledge of the probe response to interpret the measured data and to optimize parameters for better probe design. One must distinguish between real defect signals and those due to background signals, such as those due to tube support plates, probe wobble (liftoff), material inhomogeneities, thickness variations, etc. Reliable computational EM models are important to the researchers and practitioners in EC NDE applications for providing such information.

In this work, three EM modeling approaches to the simulation of EC probe response for NDE of SG tubing were initially evaluated. The approaches were closed-form integral solutions (by C. V. Dodd[11]), volume integral formulation (VIC-3D software by Sabbagh Associates), and a finite element method (ELEKTRA interface module by Vector Fields). The closed-form solution (relaxation method) is based on Burrow's point defect theory, wherein the underlying assumption is that a point defect has an infinitesimal volume. Although calculations with this approach can be performed reasonably quickly, the solutions are accurate only for small defects with uniform cross section. The solution accuracy degrades when larger, complex-shaped defects are modeled. VIC-3D software uses a volume integral EM formulation in conjunction with a moment method numerical solution technique, which suggests a more computationally intensive calculation when compared with the previous method. The model is capable of taking into account more

complex defect geometries for axisymmetric problems. The ELEKTRA package, which is currently in use at ANL, is a general-purpose 3-D FEM-based computational code that may be used to treat steady-state and transient-field calculations. This software can be utilized as a research tool to design and analyze a wide range of EM-based systems. A brief description of these three modeling codes is given below.

FORTRAN programs that were originally developed under NRC sponsorship at ORNL and used for the design and analysis of EC SG problems[11] were modified and made compatible with the platforms available at ANL. A listing of these programs, along with a brief description of their purpose, is provided in Appendix A. To process and display the outcomes of these programs, computation and visualization software, MATLAB, is currently used at ANL. Because of their treatment of specific problem geometries and the underlying assumptions in the solution method, these programs can run with minimal computational resources. They can be used to simulate impedance responses to defects that are exhibited by four types of probes: pancake, reflection, circumferential boreside, and circumferential encircling. Both absolute and differential coils may be modeled for circumferential boreside and encircling probes. The defects can be treated as point defects, as point defects averaged over the depth of the actual defects, or as point defects averaged over the volume of the defects. In general, the solution accuracy is inversely proportional to defect size. For general test case scenarios, these codes will be used to check the results of computationally intensive FEM solutions, which can better simulate realistic flaw geometry, and as a tool for analysis and determination of EC probe response and test parameters.

VIC-3D software, developed by the Sabbagh associates uses a volume-integral formulation to model EC probe response and computes flaw/field interactions in conjunction with a moment method solution technique. The objective of such integral equation methods is to cast the solution for the unknown current density, which is induced on the scatterer, in the form of an integral equation where the unknown induced current density is part of the integrand. The integral equation is then solved for the unknown induced current density by numerical techniques such as the moment method. VIC-3D software can model absolute and differential probes (with or without ferrite cores), simulate layered materials with planar and tubular geometries, model cracks and flaws due to manufacturing defects, corrosion pitting, or other destructive processes. A general axisymmetric model allows the description of tubes with tube supports, rolled-expansion transition zones, or welded sleeves. The model also allows consideration of linear ferromagnetic materials. The flaw library includes holes, axially oriented thin cracks, user-defined flaws such as IGA, and various axisymmetric artifacts. Typical simulation of EC probe response to a crack would consist of specifying probe coil dimensions and number of turns, modeling of test material by specifying intrinsic EM properties, specifying flaw conductivity and dimensions, and, finally, specifying operating frequency and scan positions. The results can be presented in both tabular and graphic form: 2- and 3-D plots; strip charts; and impedance-plane formats, which simulate the display of an NDE instrument. This software is available for PC (MS DOS), as well as for workstation environments such as Sun OS, HP-UX, UNIX, etc.

The ELEKTRA software module from Vector Fields uses a discrete finite-element model to solve the partial differential equations that govern the behavior of a system and

includes the EM finite element pre- and postprocessor OPERA-3D. The preprocessor is used to form a mesh that is discretized into elements. A 2-D grid is created initially and swept through space to create a 3-D model. The sweep operation includes facilities for rotation, projection and translation. The mesh primitive blocks are assigned orientations and material characteristics. Upon enforcement of the appropriate boundary conditions, the resulting input is fed into the analysis module. The 3-D time-varying field equations are subsequently solved. The time variation can either be transient or steady state. In addition, the effects due to motion can be computed. The problem space is defined such that total and reduced magnetic scalar potentials are used in nonconducting media; this reduces the solution costs and corrects the cancellation errors associated with the simple reduced-potential approach. In conducting media, the software uses magnetic vector and electric scalar potentials, which are directly coupled with the potentials in the exterior medium. The postprocessing environment provides facilities to display the results of the analysis in several ways, including 3-D viewing of the model from any angle; graphs; histograms; contour maps of the solutions; contour components of the results on any surface; calculation of fields; forces, and energy; and user-defined functions. Although a PC version of this software is available, the full version for 3-D analysis and display, necessary to model and analyze nonplanar EC field distributions is primarily intended to run on platforms that range from workstations to mini and mainframe computers.

Modeling of EM NDE sensors poses some specific challenges for 3-D FEM formulations. The desired solutions (e.g., change in the EC coil's primary magnetic field that is due to a small defect in a tube) are often variations that are orders of magnitude smaller than the calculated total fields. To accurately model a scanning probe, several initial trials are often required to achieve an acceptable convergence as well as computationally efficient solutions. In general, details of the impedance locus that require accurate impedance calculations are of interest. This suggests that finely discretized regions under the coil may have to be moved for each new coil position. Several iterations of the mesh design are usually required to obtain a satisfactory mesh for the first coil position, from which the others can then be derived. Three-dimensional FEM-based models could be a reliable means to achieve reasonably accurate solutions for EC NDE problems with complex model geometries and awkward defect boundaries.

3.1.1 Sample Calculations: Closed-Form Solutions

Using the closed-form solution method, sample calculations were performed for a differential bobbin coil and an absolute pancake coil. The calculations are generic, i.e., the parameters used for the simulation, such as coil diameter, height, number of turns, and current density, do not represent any particular industry standard probe. The results here are given in terms of the defect sensitivity factor (DSF) for a lattice of point defects at various axial and radial positions within the tube wall, modeled as a flat layer for the pancake coil simulations. The DSF at a point in a conductor is proportional to the coil voltage produced by a point defect at that location. For all cases, the tube OD was 19.1 mm (0.750 in.) with a tube wall thickness of 1.27 mm (0.050 in.). A resistivity value of ρ = 100 $\mu\Omega$-cm was used for the tube material, which represents Alloy 600. The lower and upper frequency limits of f = 100 kHz and f = 500 kHz that were used in these calculations are typical for inspection with standard probes. An arbitrary liftoff distance (the coil-to-tube inner-wall separation) of L_1 = 0.25 mm (0.010 in.) was assumed for this case.

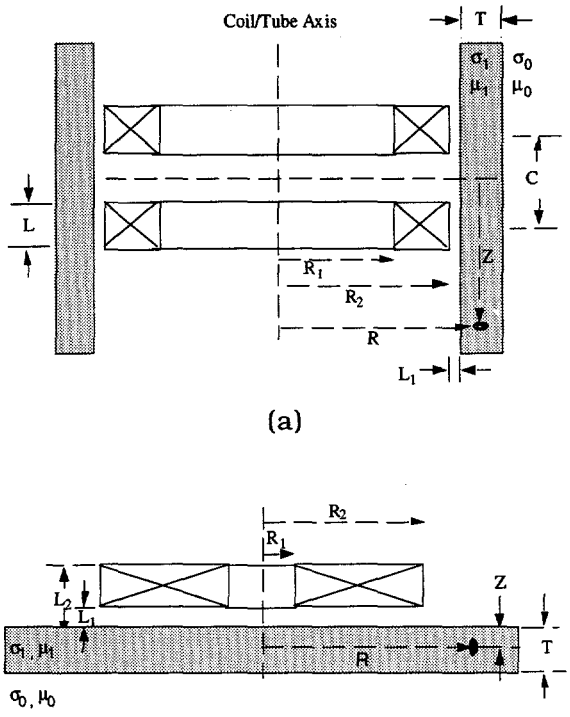

Figure 23. Cross-sectional view of (a) differential bobbin coil, and (b) absolute pancake coil inside a tube, along with model parameters

Figures 23a and b show cross-sectional views of two types of coils inside a tube, along with the model parameters. Amplitude and phase variations of the DSF for a lattice of point defects located at various axial and radial positions within the tube wall (obtained with a bobbin coil operating at a frequency of 100 and 500 kHz, respectively) are shown in Figs. 24 and 25. Comparison of the two figures clearly indicates the fact that lower frequencies allow for greater depth of penetration. Nevertheless, better sensitivity is achieved at higher frequencies, if the signal loss due to skin depth attenuation does not completely eliminate the defect signal. For the same coil size, the greater depth of penetration achieved at lower frequencies generally implies diminished resolution and lack of measurement sensitivity to small variations.

Figures 26 and 27 are the simulation results for a pancake probe. Here, a small pancake coil with inner radius R_1 = 1.27 mm (0.05 in.) and outer radius R_2 = 3.18 mm (0.125 in.) was modeled. The other simulation parameters were the same as in the previous test case with the bobbin coil probe. The effect of frequency is similar to that observed for the bobbin coil. When compared with the bobbin coil, the results indicate a smaller penetration depth for the pancake coil, i.e., the depth of penetration is dependent not only on the operating frequency but also on the coil geometry.

3.1.2 Finite-Element-Method Simulations

Finite-element calculations with the 3-D FEM-based code ELEKTRA describe the response of an EC bobbin probe to simulated SG tubing artifacts. Such calculations could

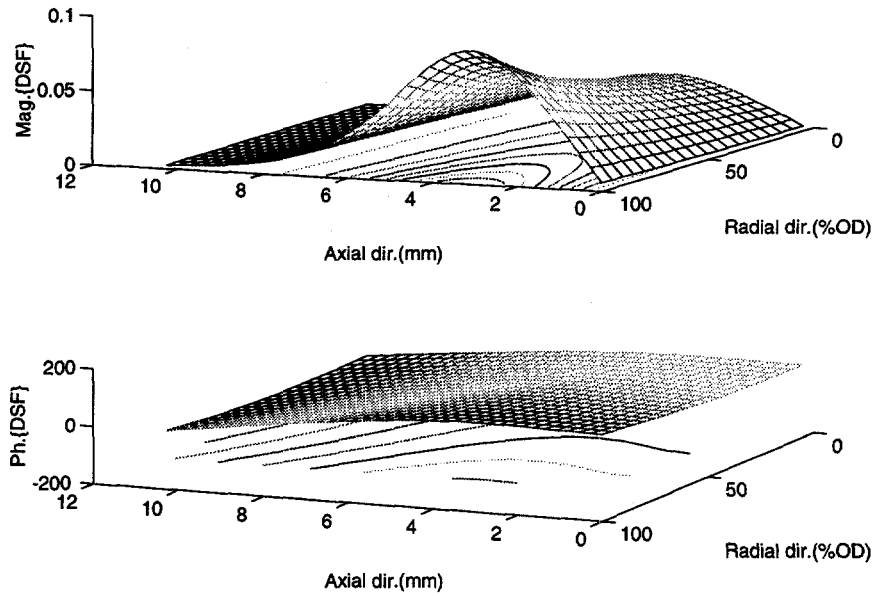

Figure 24. (a) Amplitude and (b) phase of DSF for a differential bobbin coil inside Alloy 600 tubing material for a lattice of point defects at various axial and radial positions, where f = 100 kHz, wall thickness = 1.27 mm (0.050 in.).

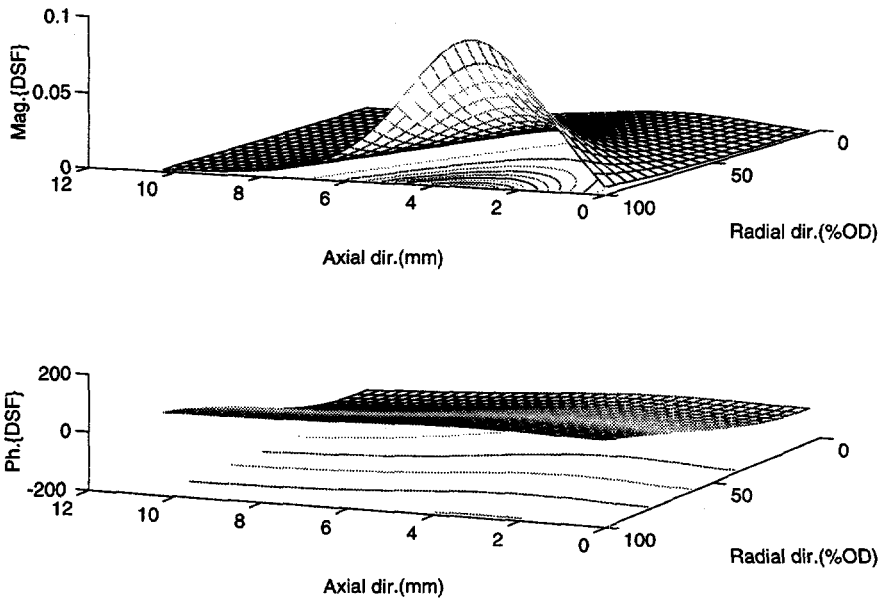

Figure 25. (a) Amplitude, and (b) phase of DSF for differential bobbin coil inside Alloy 600 tubing material for a lattice of point defects at various axial and radial positions, where f = 500 kHz, wall thickness = 1.27 mm (0.050 in.).

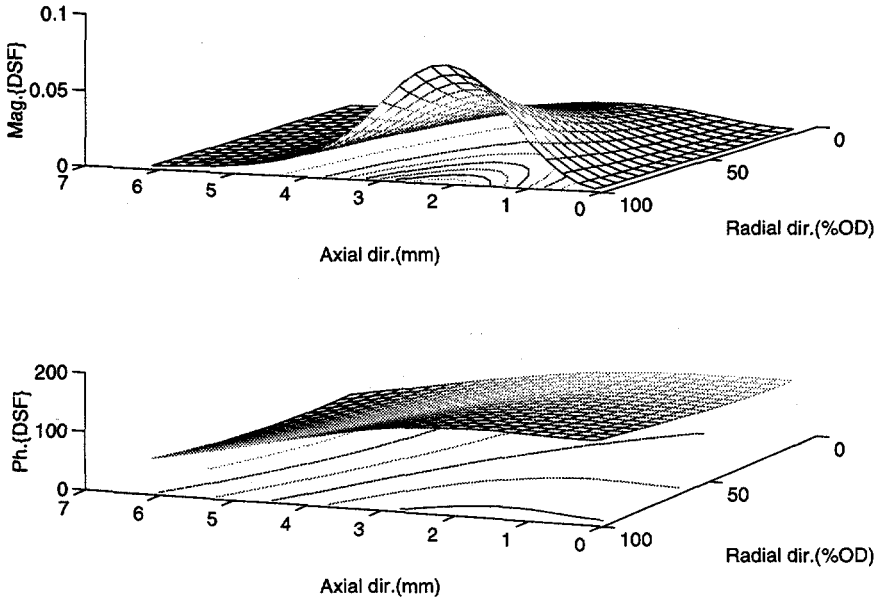

Figure 26. (a) Amplitude and (b) phase of DSF for an absolute pancake coil on Alloy 600 tubing material for a lattice of point defects at various axial and radial positions, f *= 100 kHz, wall thickness = 1.27 mm (0.050 in.).*

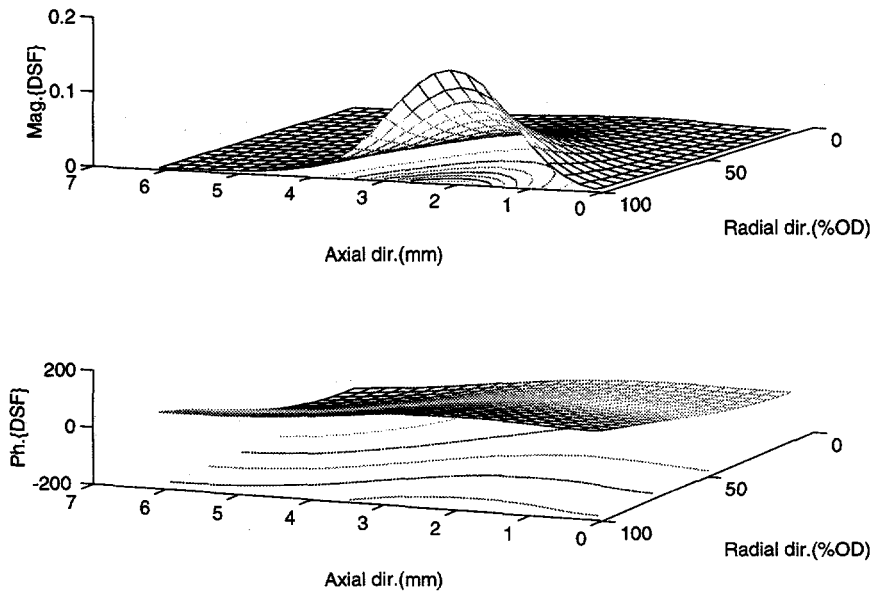

Figure 27. (a) Amplitude and (b) phase of DSF for an absolute pancake coil on Alloy 600 tubing material for a lattice of point defects at various axial and radial positions, where f *= 500 kHz, wall thickness = 1.27 mm (0.050 in.).*

be very helpful in understanding and interpreting the response of an EC probe to complex tube/defect geometries associated with the ISI of SG tubing. To establish the validity of the model, theoretical and experimental responses of an absolute bobbin probe to two types of calibration standard defects are compared. Modeling results from a theoretical study of the effect of length, width, and ligament size in axial cracks on EC indications with conventional ISI bobbin probes are also presented.

In the FEM model, governing EM field equations in terms of magnetic-vector and electric-scalar potentials in conducting media and reduced or total scalar potentials in nonconducting regions are solved by using finite-element discretization. A more detailed analysis can be found in the proceedings of the 24th Water Reactor Safety Information Meeting (WRSM).[12] Probe impedance is determined through energy and power calculations. The signal trajectory in the impedance plane, due to probe motion, is determined by calculating the response at discrete points along the tube axis. Representative test cases that simulate steady-state solutions with both differential and absolute bobbin coils are presented here.

3.1.2.1 Numerical and Experimental Results

A series of test case simulations was initially carried out to verify the accuracy of the FEM solutions by comparing the results with detailed experimental measurements. The experimental EC data, supplied by C. V. Dodd, formerly of ORNL, were obtained using a large aluminum tube that contained throughwall holes and axial slits. Measurements were made at three frequencies with a Hewlett-Packard impedance analyzer and a specially constructed absolute bobbin coil (SN480A). Here, we compare the experimental data for a throughwall hole and an axial slit with the FEM calculations. The results are expressed in terms of both calculated impedance variations as a function of probe position inside the tube and impedance-plane plots that simulate conventional EC instrument display.

Figure 28 shows the lumped element equivalent circuit for the probe and test sample (tube) interaction modeled as primary and secondary sides of a transformer circuit. Also shown, within the dashed rectangle, is the part of the circuit modeled by the FEM problem space. It should be noted that, in this figure, the final solutions are normalized to eliminate explicit dependence of the parameters on the coil/cable resistance R_0. These normalized parameters are experimentally determined as

$$X_n = \frac{X}{X_0} \tag{1}$$

and

$$R_n = \frac{R - R_0}{X_0}, \tag{2}$$

where

$$X_0 = \omega L_0 \tag{3}$$

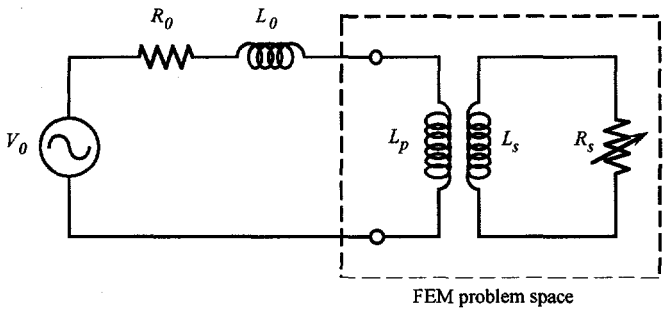

Figure 28.
Lumped element equivalent circuit of EC probe and sample with region of problem space modeled by FEM shown within the dashed rectangle.

represents the coil reactance in air. By using the normalized variables (Eqs. 1 and 2), R_0 can be ignored. This normalization allows direct comparison of the theoretical and experimental data.

3.1.2.2 Verification of Computational Results

Figure 29 depicts the aluminum tube standard used in the measurement. The tube contains three sets of four axially symmetrical (repeated every 90° around the tube circumference) artifacts. Eddy current probe readings are the average of nine measurements, each made in a different circumferential orientation. The values of resistance and reactance (in ohms) were determined with a Hewlett-Packard impedance analyzer. In Fig. 30, which shows a cross section of the tube-and-coil geometry, the tube has an inner radius r_i^t = 38.86 mm (≈1.53 in.) and an outer radius r_o^t = 44.45 mm (≈1.75 in.). The diameter D^h of the through-wall hole artifact is 11.18 mm (≈0.44 in.). The length of the slit l^g is 36.0 mm (1.42 in.) and the width w^g is 0.38 mm (0.015 in.). The coil has an inner radius r_i^c = 31.75 mm (1.25 in.), an outer radius r_o^c = 38.0 mm (1.50 in.), a width $w = r_o^c - r_i^c$ = 6.25 mm (0.25 in.), and length l = 6.60 mm (0.26 in.). A measured resistivity value of $\rho = 3.88\,\mu\Omega - cm$ was used to simulate the aluminum tube material. The coil was wound over a Teflon™ form with #36 gauge wire.

The computed results are given in terms of both current density distribution over the tube surface and calculated impedance components. In the FEM model, all materials were assumed to be nonmagnetic (i.e., relative permeability μ_r = 1). The coil represents N = 1836 turns, carrying a unit current density (A/mm^2). Figures 31a and b depict the tube/coil geometry, along with the distribution of the current density $|\bar{J}|$ at f = 0.5 kHz for the two artifacts modeled here. The coil center in these figures coincides with the defect center in the axial direction. Because the geometry is symmetrical, only 1/8 of the problem was modeled in both cases. Results are displayed for the case in which the probe is positioned at z = 0 mm (center of the defect is at z = 0 mm).

The FEM solution for the distribution of current density on the aluminum tube with a throughwall hole and an absolute bobbin coil operating at f = 0.5 kHz is shown in Fig. 31a. Current distribution for the slit is shown in Fig. 31b. The distribution on the tube outer surface at 0.5 kHz shows the distortion along the path of circumferentially induced currents due to presence of throughwall artifacts. It can be observed that the lowest test frequency chosen here allows detection of outer-surface artifacts for the highly conducting

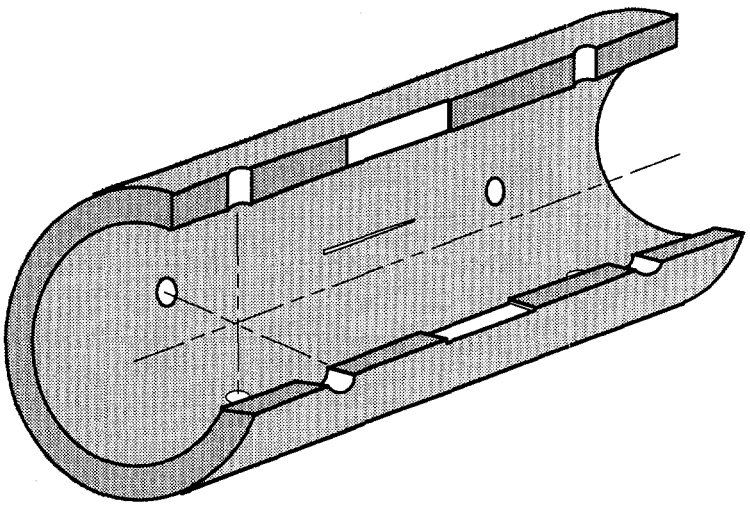

Figure 29. Geometry of aluminum tube standard with throughwall hole and axial slit artifacts placed symmetrically (90° apart) around the circumference.

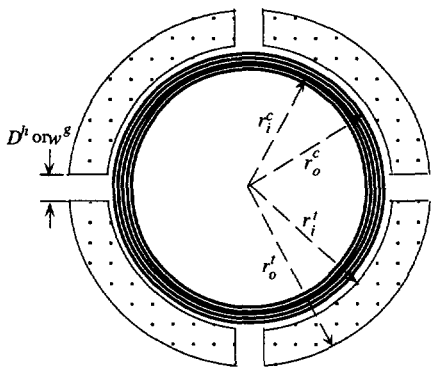

Figure 30.
Cross-sectional geometry of the absolute bobbin coil inside the aluminum tube with one set of throughwall artifacts 90° apart around the circumference.

aluminum material. On the other hand, attenuation at the highest measured frequency, f = 7.5 kHz, would allow detection of only near inner-surface artifacts that correspond to the shallow skin depth.

Figures 32 and 33 show theoretical and experimental results for the variation of coil resistance and reactance as a function of the axial position along the tube and the impedance-plane plot of the same data. The results show close agreement between theory and measurement both for the simulated throughwall hole and the axial slit. Agreement for the throughwall hole is not as good at the highest frequency. This could be associated with operating the coil near the coil/cable resonance and the effect of inner winding capacitance at higher frequencies for coils with thick gauge wire. Better consistency between theory and measurement is generally expected at frequencies away from the resonance where probe sensitivity to such parameters is minimal. The 3-D FEM computations correctly predict the variation of the EC bobbin probe signal in the presence of axisymmetrical artifacts.

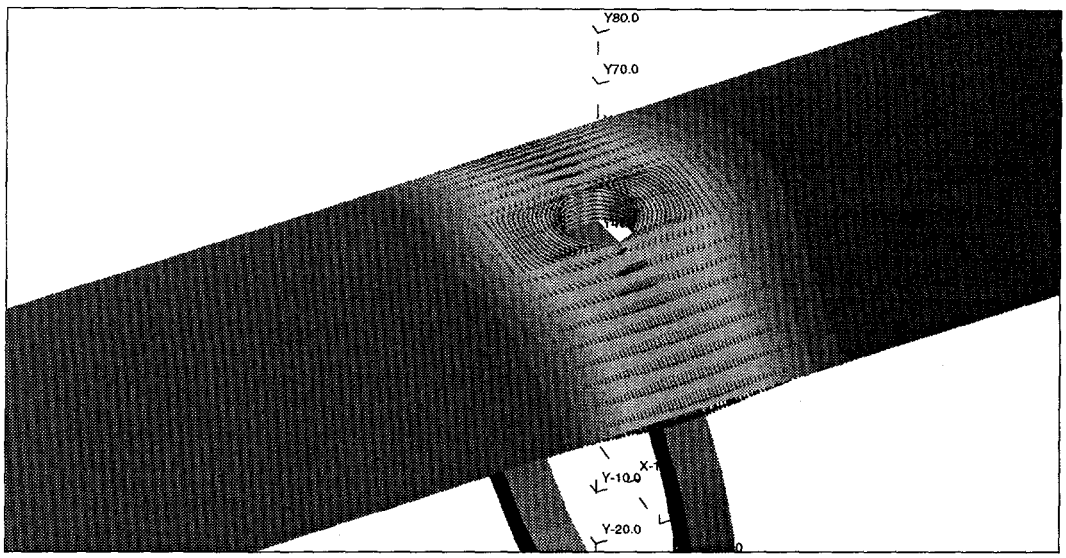

(a)

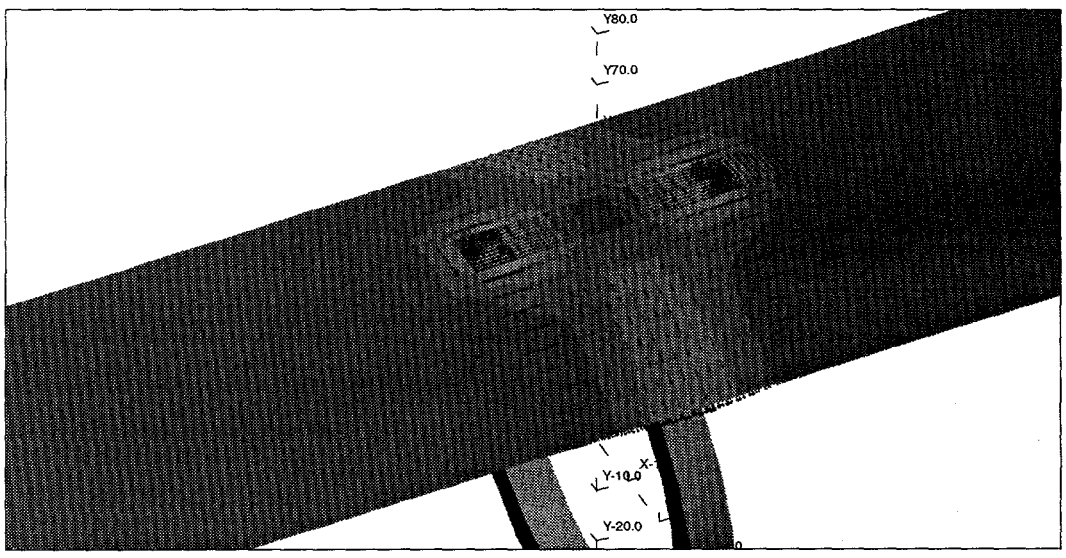

(b)

Figure 31. Finite-element solution for distribution of current density due to absolute bobbin coil at f = 0.5 kHz on aluminum tube with (a) throughwall hole and (b) axial slit.

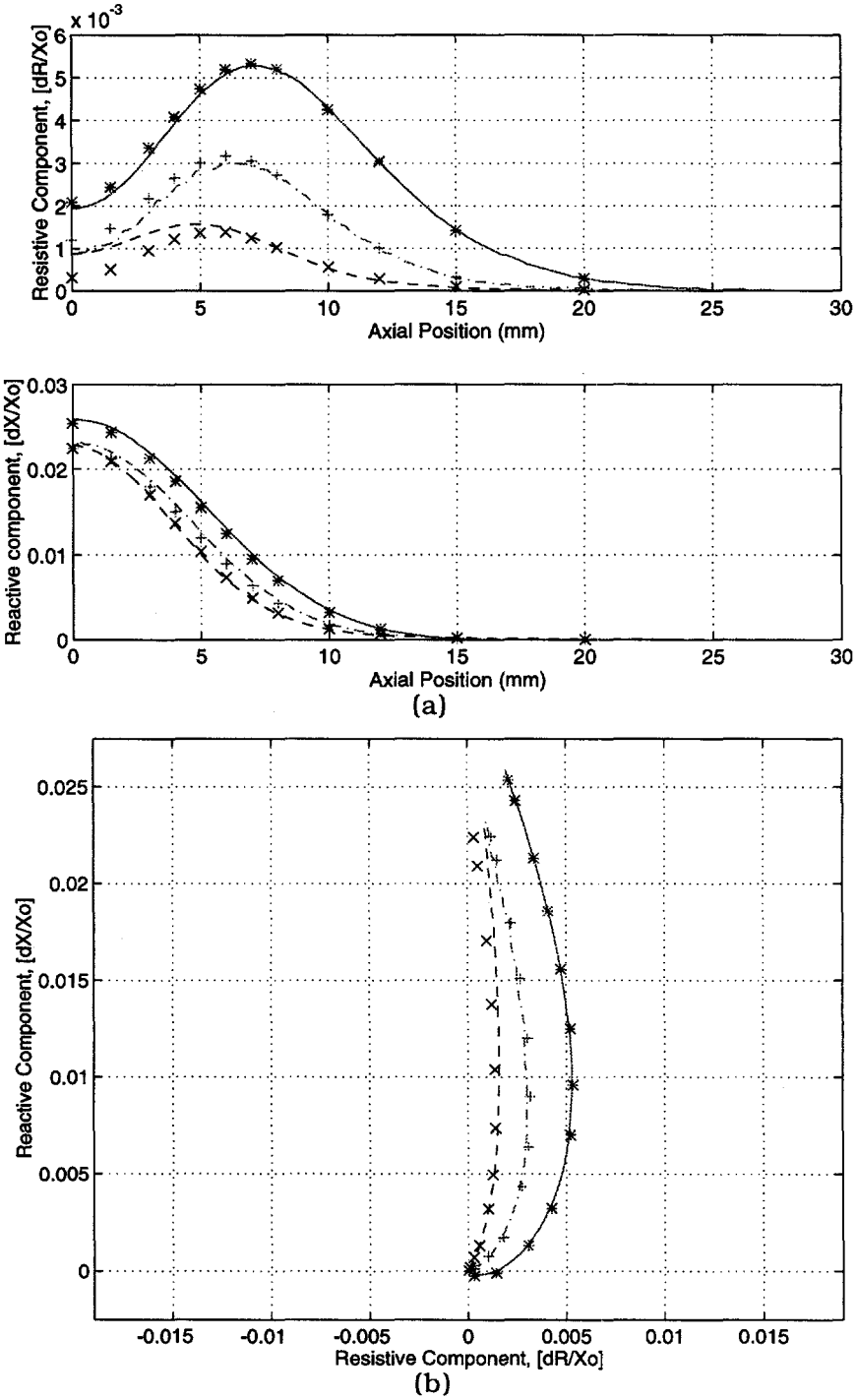

Figure 32. Experimental (-, -·, --) and theoretical (, +, x) values of (a) resistance and reactance as a function of position of absolute bobbin coil, and (b) impedance-plane signal trajectory, at f = 0.5, 1.2, and 7.5 kHz. Artifacts are four axially symmetric throughwall holes (90° apart around tube circumference).*

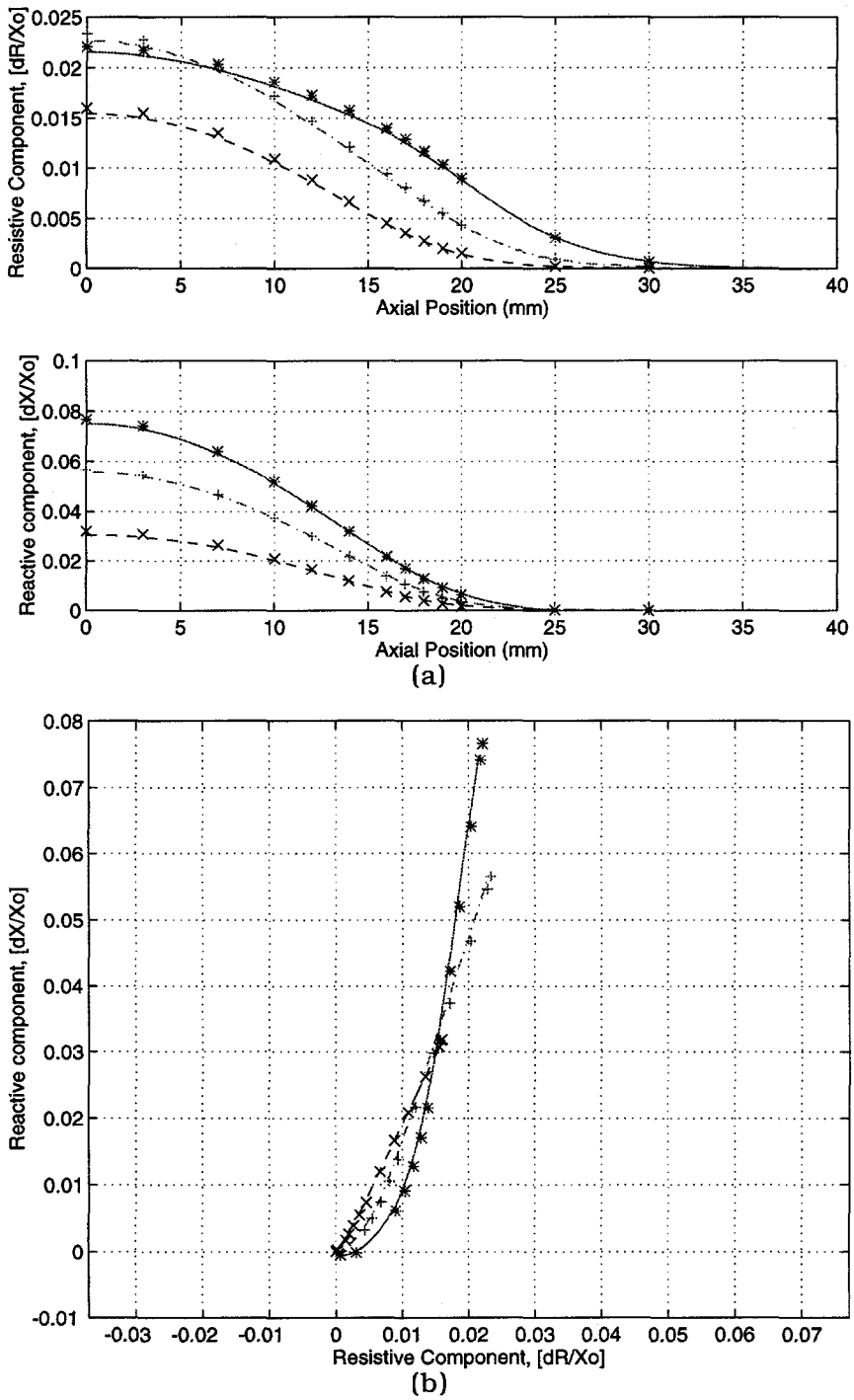

Figure 33. Experimental (-, -·, --) and theoretical (, +, x) values of (a) resistance and reactance as a function of position of absolute bobbin coil, and (b) impedance-plane signal trajectory, at f = 0.5, 1.2, and 7.5 kHz. Artifacts are four axially symmetric slits (90° apart around the tube's circumference).*

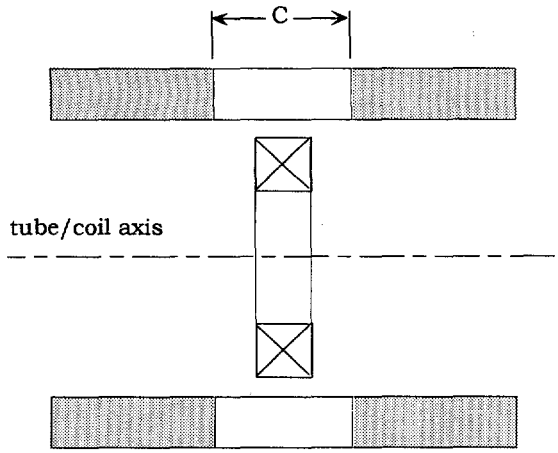

Figure 34.
Cross-sectional geometry of absolute bobbin coil inside a tube with four symmetrical axial slits of length C.

The above results indicate a substantial difference in the EC signal amplitudes associated with the two artifacts modeled here. Bobbin probe signal amplitude alone cannot generally be regarded as an absolute indication of the volumetric extent of defects when comparing differing flaw geometries. This can be observed by comparing the probe impedance responses, which are linearly proportional to the probe output voltage, for the two defect geometries modeled here. Although the volume of the through-wall hole is much greater than that of the axial groove, it results in a smaller perturbation of the coil impedance. In a conducting medium, eddy currents always flow through the path of least resistance. The discontinuity (infinite resistance) introduced by the thin but long axial groove forces the currents to take a contour around the defect; this, in turn, gives rise to a larger impedance mismatch for the probe.

3.1.2.3. Effect of Length on Bobbin Probe Indication of Axial Cracks

Electromagnetic modeling results on the effect of crack length on absolute-bobbin-coil signal amplitude are presented next. These test cases pertain to simulation of absolute-bobbin probe response to axial slits, 100% through-wall, on 22.23-mm (0.875-in.)-OD Alloy 600 tubing with a nominal wall thickness of 1.27 mm (0.05 in.) and a conductivity of $\rho = 100.0\ \mu\Omega - cm$. The modeled probe was a conventional 18.3-mm (0.72-in.)-OD absolute bobbin coil. Simulations were carried out at frequencies of f = 100 and 400 kHz. Computed solutions are displayed both as current distribution along the tube and also in terms of change in the magnitude of the probe impedance, which is linearly proportional to its output voltage (i.e., related by a constant multiplier that is proportional to the coil current density).

Figure 34 depicts the cross-sectional geometry of an absolute bobbin coil located symmetrically under a 100% throughwall axial slit. For all of the test cases considered here, the width of the slit was arbitrarily chosen to be 0.127 mm (0.005 in.), and the length C was varied from 0.25 to 50 mm (0.010 to 2 in.). The coil was initially positioned symmetrically in the middle of the slit and the coil's length and height were taken to be 1.27 and 1.525 mm (0.050 and 0.060 in.), respectively.

Figure 35a and b show the distribution of current density at f = 100 kHz on a 45° section of the tube that contained four 100% throughwall slits of two differing lengths. For

the results shown in Fig. 35, the coil was positioned in the middle of the axial slit at $z = 0$. Current distributions in Figs. 35a and b show that the narrow crack forces circumferentially induced currents to take a flow contour around the defect. Consequently, the longer crack should result in larger perturbation of the induced current density.

Finally, to examine the effect of crack length on absolute-bobbin-coil response, a series of computations was carried out by placing the coil symmetrically under the artifact and then varying the defect length. The geometry of the model is depicted in Fig. 34.

Figure 36 shows the result of the analysis at frequencies of 100 and 400 kHz for a 100% throughwall slit. Calculated values are displayed as percent change in probe signal amplitude as a function of crack length. These values were determined from the relation

$$\% \text{ Change of } |Z| = 100 * \left(\frac{|Z_{wo}| - |Z_w|}{|Z_{wo}|} \right), \tag{4}$$

where Z_{wo} and Z_w represent the probe impedance without and with defects in the tube, respectively. Calculated results at both frequencies indicate a nonlinear relationship between crack length and EC voltage amplitude that is also dependent on frequency. The perturbation of the EC absolute-bobbin-coil signal is small for approximate defect lengths that are <2 mm (0.08 in.). Furthermore, the slope of the curve decreases with increase in defect length. For example, at 100 kHz, the percent variation in the signal amplitude for an increase in crack length from 5 to 25 mm (0.2 to 1 in.) is more than five times that of the change in length from 25 to 50 mm (1 to 2 in.).

3.1.2.4 Effect of Width on Bobbin Probe Indication of Axial Cracks

Results of EM modeling of the effect of crack width on the amplitude of the absolute-bobbin-coil signal are presented here. Once again, Fig. 34 depicts the cross-sectional geometry of an absolute bobbin coil located symmetrically under a 100% throughwall axial slit. For all test cases considered here, crack length C was taken to be 25.0 mm (1 in.) and the width W varied from 0.015 mm (0.0006 in.) to 1.0 mm (0.04 in.). Other coil and tube parameters were taken to be the same as those for simulations carried out in the previous section.

Figure 37a and b show the distribution of current density on a 90° section of the tube that contained four 100% throughwall slits at f = 400 kHz for W = 0.125 and 1 mm, respectively. For the results shown in Fig. 37, the coil was positioned in the middle of the axial slit at $z = 0$. Current distributions shown in Figs. 37a and b display contours of circumferentially induced currents that are forced to flow around the defect. Results shown here indicate minimal variation of current distribution due to the change in crack width.

To examine the effect of crack width on absolute-bobbin-coil response, a series of computations was carried out by placing the coil symmetrically under the artifact and varying the defect width. Figure 38 shows the results of this analysis at frequencies of 100

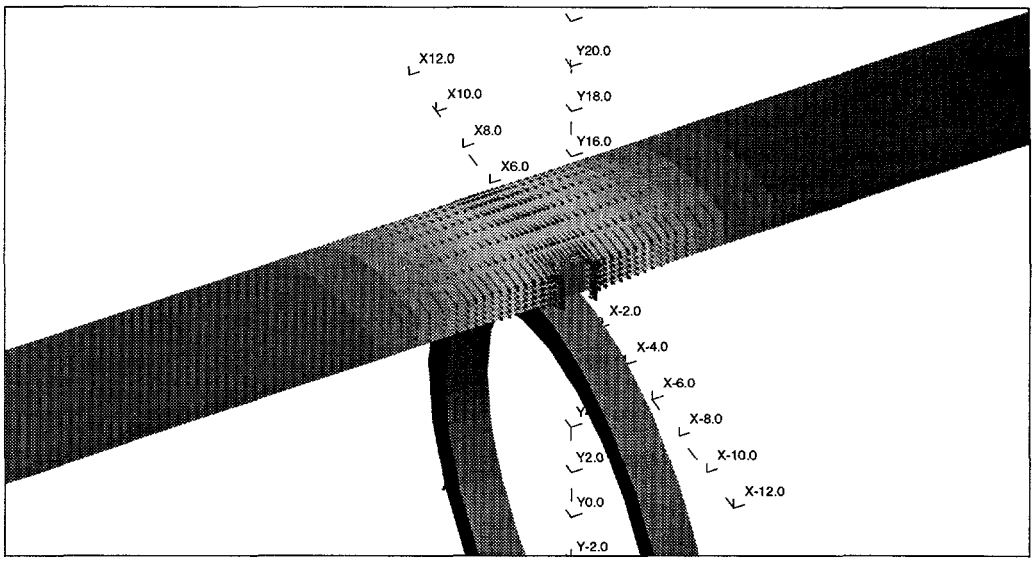

(a)

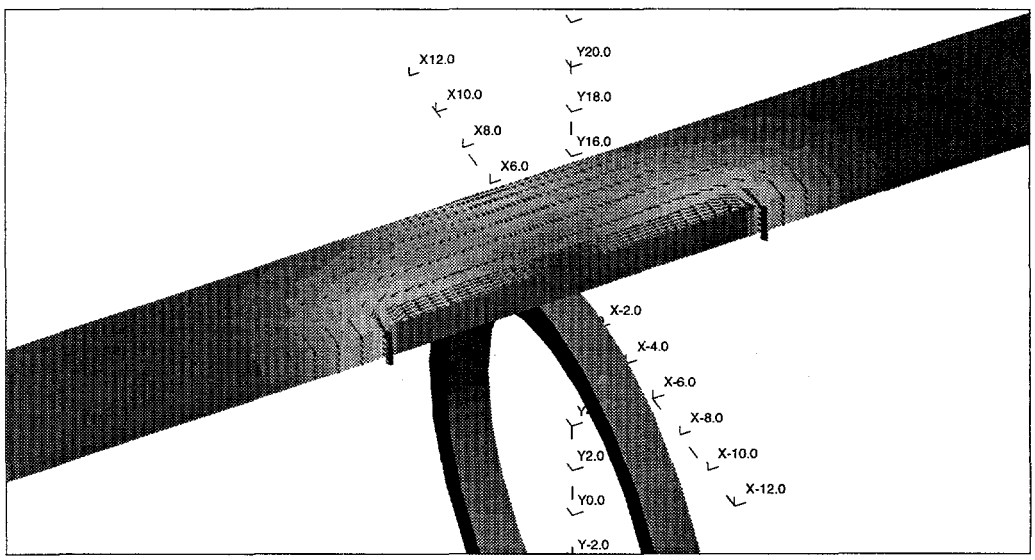

(b)

Figure 35. Finite-element solution for distribution of current density with an absolute bobbin coil at f = 100 kHz on Alloy 600 tube with 0.127-mm (0.005-in.)-wide 100% throughwall axial slits having lengths of (a) C = 1 mm (0.04 in.) and (b) C = 13 mm (0.5 in.).

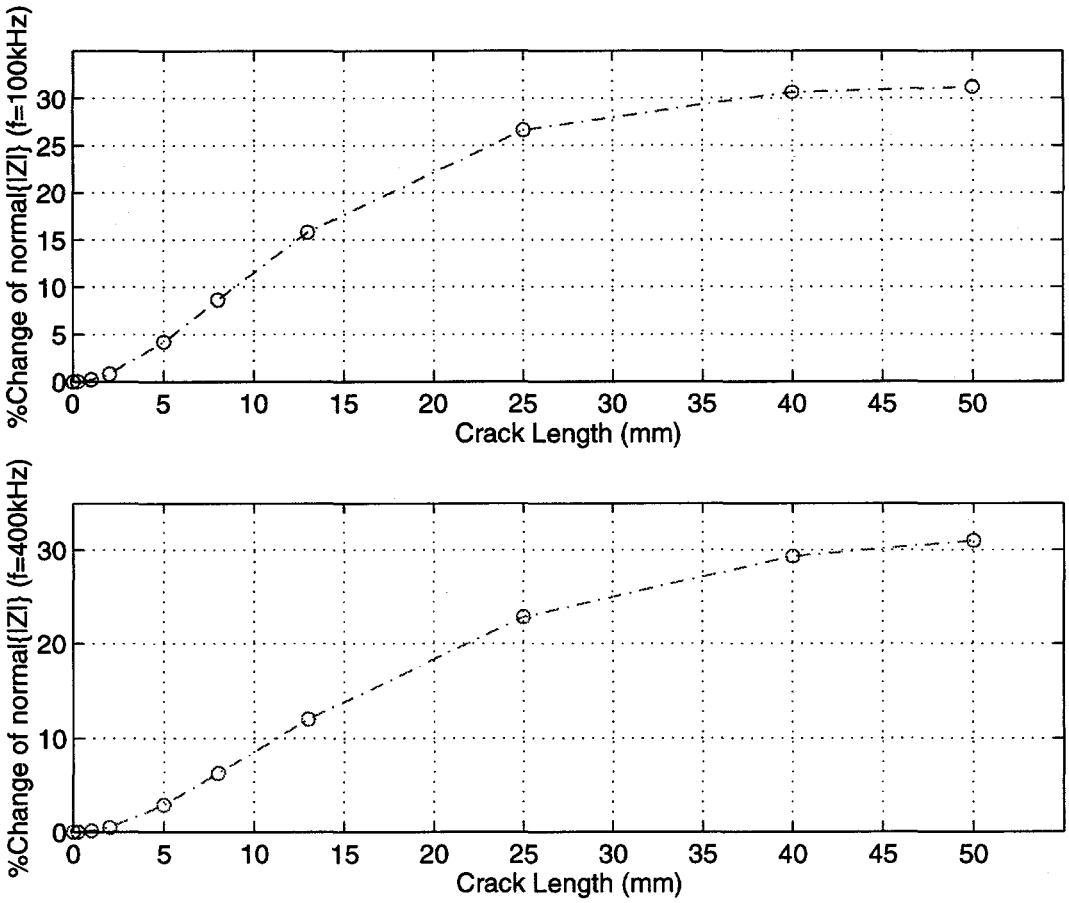

Figure 36. Plot of change in absolute probe signal amplitude as a function of 100% throughwall crack length at (a) f = *100 kHz and (b)* f = *400 kHz.*

and 400 kHz. Calculated values are displayed as percent change in probe signal amplitude as a function of *W*. This relative change was calculated in accordance with Eq. 4.

Comparison of the profiles shown in Figs. 38a and b indicates that, although the results obtained at higher frequency show slightly larger variation of the signal amplitude, the variation of the EC voltage amplitude as a function of crack width over the range of 0.015 to 1 mm (0.0006 to 0.04 in.) is relatively small at both frequencies. This finding is in agreement with the concept that conduction loss is proportional to the path length of EC flow, which is a frequency-dependent parameter.

3.1.2.5 Theoretical Analysis of Axial Groove With Ligament

Results obtained by modeling the effect of ligaments in axial grooves on bobbin coil signals are presented below. The test cases pertain to simulation of the probe response to axial grooves, 100 and 75% throughwall, on 22.23-mm (0.875-in.)-OD Alloy 600 tubing with a nominal wall thickness of 1.27 mm (0.05 in.) and conductivity of $\rho = 100.0\ \mu\Omega - cm$. The modeled probes were conventional 18.3-mm (0.72-in.)-OD differential and absolute bobbin coils, and the simulation frequencies were f = 100 and 400 kHz, typical frequencies

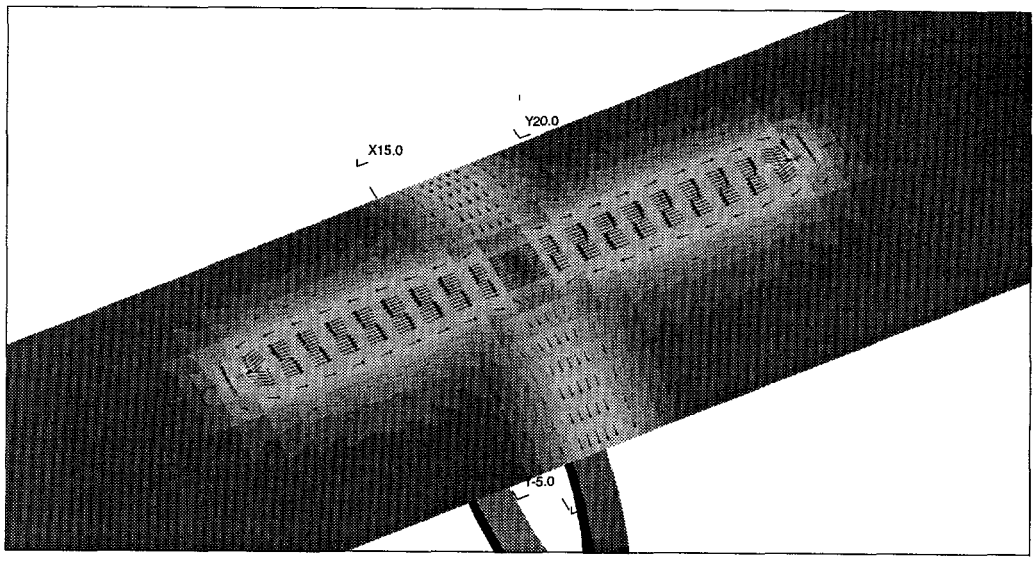

(a)

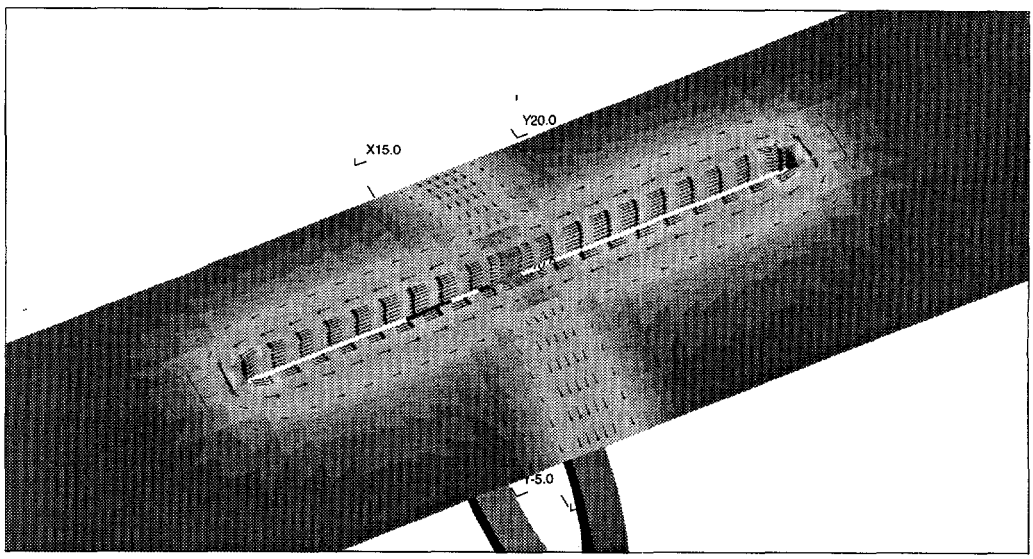

(b)

Figure 37. Finite-element solution for distribution of current density on Alloy 600 tube with four symmetrical 25-mm (1 in.)-long 100% throughwall axial slits having width of (a) W = 0.125 mm (0.005 in.) and (b) W = 1 mm (0.040 in.). The probe is an absolute bobbin coil at excitation frequency of f = 400 kHz.

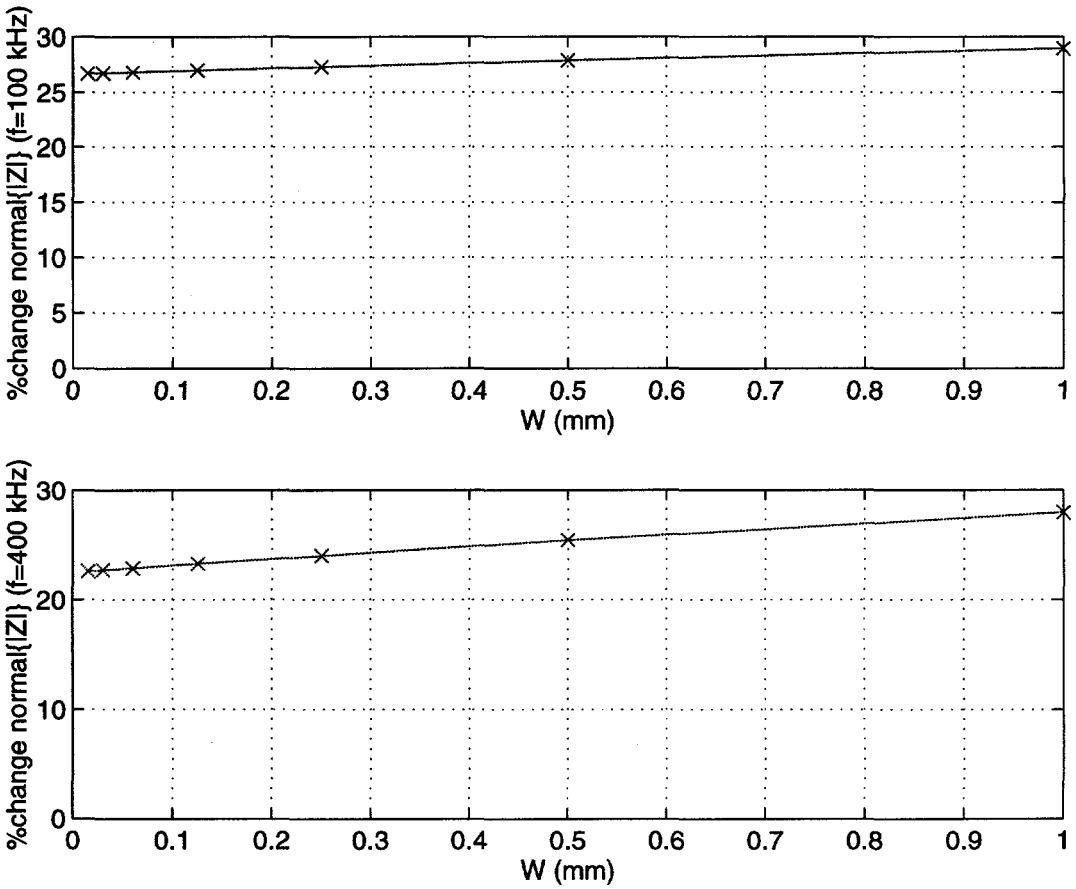

Figure 38. Plot of relative change in the amplitude of the absolute bobbin probe signal as a function of defect width for 100% throughwall axial cracks at (a) f = *100 kHz and (b)* f = *400 kHz.*

used for multifrequency ISI of SG tubes. Once again, the results are given in terms of both current distribution along the tube and computed resistance and reactance values as a function of probe position. Finally, simulation results are presented to show the expected normalized variation in the amplitude of an absolute-bobbin-probe signal at two frequencies as a function of ligament size in axial grooves that were 100 and 75% throughwall.

Figure 39 depicts the cross-sectional geometry of an absolute bobbin coil located symmetrically under an axial slit with a ligament. For all test cases considered here, slit length C was arbitrarily chosen to be 25.4 mm (1 in.), and unless otherwise specified, the ligament length L was taken to be 0.127 mm (0.005 in.). The width of the slit was also taken to be 0.127 mm (0.005 in.). The ligament was positioned symmetrically in the middle of the slit. Coil length and height were taken to be 1.27 and 1.525 mm (0.05 and 0.06 in.), respectively. For the differential bobbin probe, the coil spacing was taken to be 1.525 mm (0.06 in.).

Figures 40a and b show the distribution of current density due to the presence of a ligament, at f = 100 kHz for a differential and absolute-bobbin probe, respectively. To simultaneously display the inner and outer distribution of currents, two 45° top and bottom

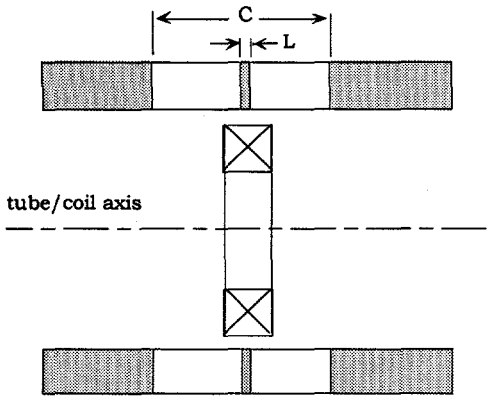

Figure 39.
Cross-sectional geometry of absolute bobbin coil inside a tube with four symmetrical axial slits of length C and ligaments of length L.

sections of the tube are shown. In Fig. 40a, the lagging coil of the differentially wound probe is positioned under the defect at z = 1.5 mm (0.06 in.). For the results shown in Fig. 40b, the absolute coil was positioned in the middle of the axial slit at z = 0. Comparison of the current distributions shown in Fig. 40 with the distribution shown earlier in Fig. 37a for the axial groove without ligament clearly reveals that the small ligament creates a path for the circumferentially induced currents to flow across the slit, and, consequently, the amplitude of the probe signal is reduced. Similar results are shown in Fig. 41 for a 75% OD throughwall groove of the same ligament size. Examination of these results also reveals similar trends, except that the presence of a thin layer of normal tubing material under the groove causes currents to flow primarily underneath the artifact and, again, the result is a reduction of signal amplitude relative to the case in which the artifact is 100% throughwall.

Figures 42 and 43 are plots of the calculated impedance response of the absolute-bobbin probe for the slit, with and without the ligament, at f = 100 and 400 kHz, respectively. In both cases, the presence of the ligament significantly changes the probe signal variation. Impedance-plane plots for the differential coil for the same defect geometry are shown in Fig, 44. Figure 45 shows the computed response for the absolute coil at f = 100 kHz, for the 75% OD slit with and without a ligament. As expected, the presence of the ligament produces a significantly smaller change in coil response than the change obtained for a 100% throughwall slit because of the presence of ID tubing material under the defect. The presence of this material allows the currents to flow primarily underneath the OD artifact. Figure 46 shows impedance variations for the same test case geometry and at the same frequencies, except that a differential coil was modeled. For the most part, the results show only small changes in the impedance-plane trajectory due to the presence of the ligament, relative to the changes for the 100% throughwall slit.

Finally, to examine the effect of the size of a ligament in a long axial groove on the absolute bobbin coil response, a series of computations was carried out by placing the coil symmetrically under the artifact and then varying the ligament length. The geometry of the model is depicted in Fig. 39. Figure 47a shows the result of the analysis at frequencies of 100 and 400 kHz for the 100% throughwall slit. Calculated values are displayed as percent change in probe signal amplitude as a function of ligament length. Similar

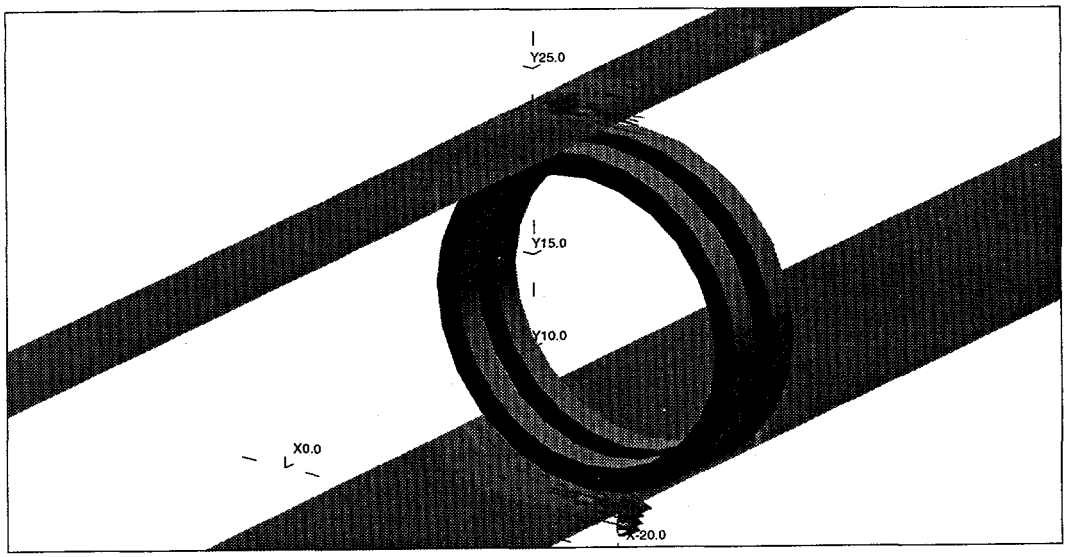

(a)

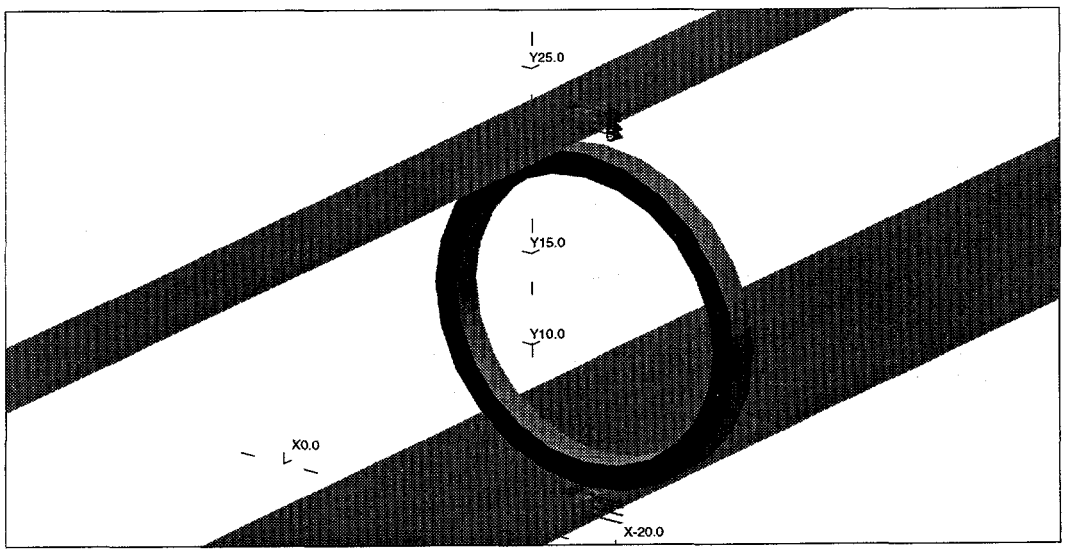

(b)

Figure 40. Finite element solution for distribution of current density due to (a) differential and (b) absolute bobbin coil, at f = 100 kHz, on Alloy 600 tube with 25.4-mm (1-in.)-long, 0.127-mm (0.005-in.)-wide axial 100% throughwall slit with 0.127-mm (0.005-in.)-long ligament in center.

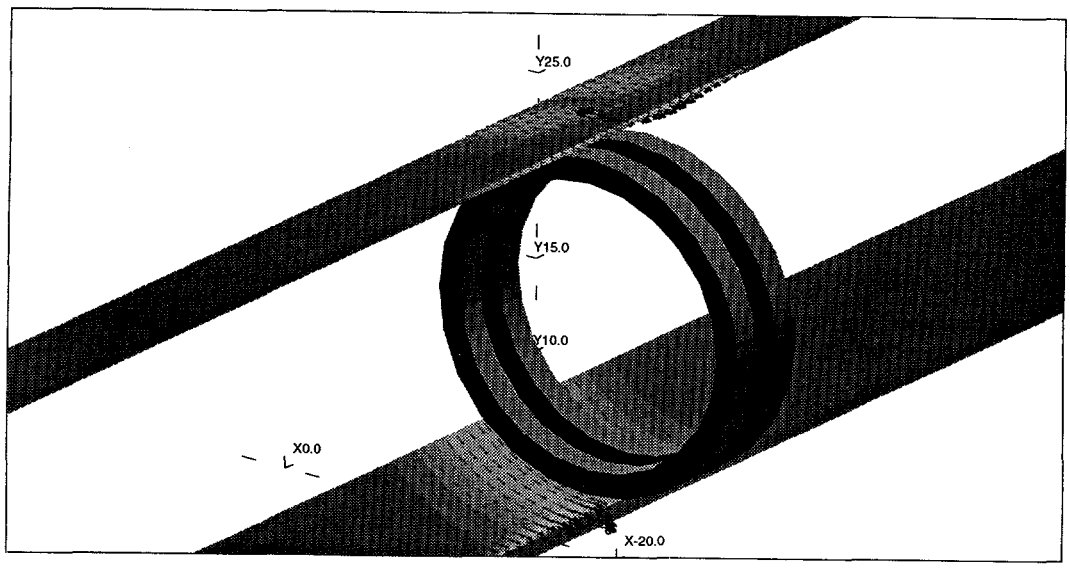

(a)

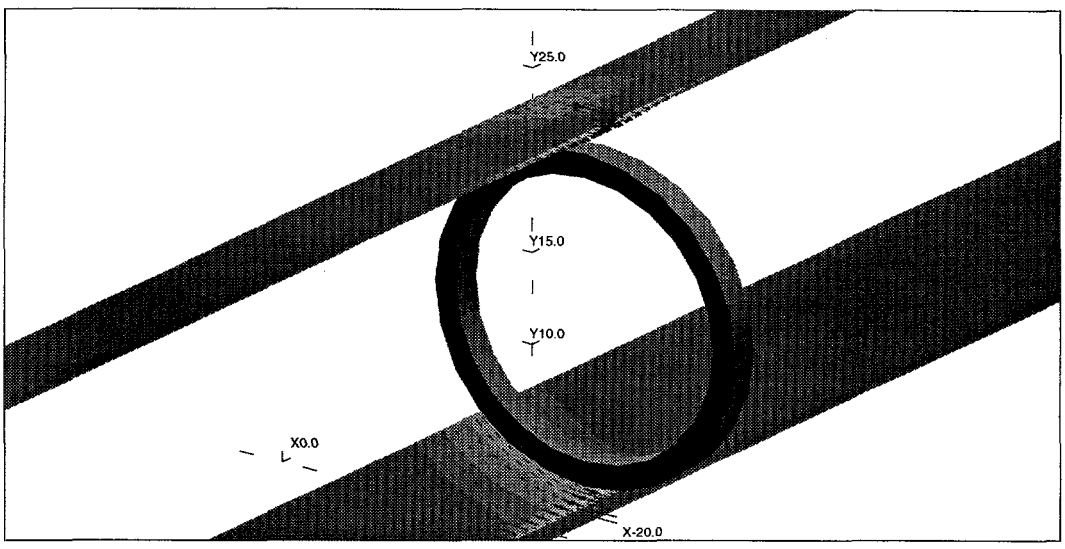

(b)

Figure 41. Finite element solution for distribution of current density due to (a) differential and (b) absolute bobbin coil on Alloy 600 tube with 25.4-mm (1-in.)-long, 0.127-mm (0.005-in.)-wide 75% outer diameter axial groove with 0.127-mm (0.005-in.)-long ligament in center, at f = *100 kHz.*

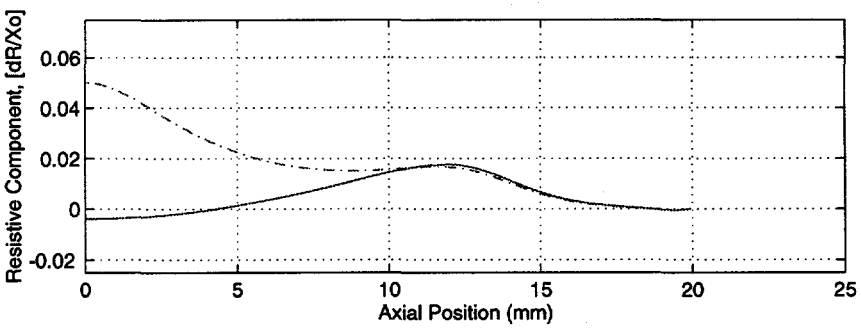

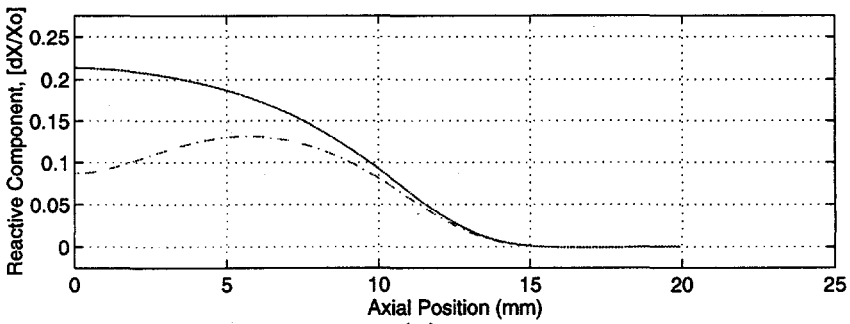

(a)

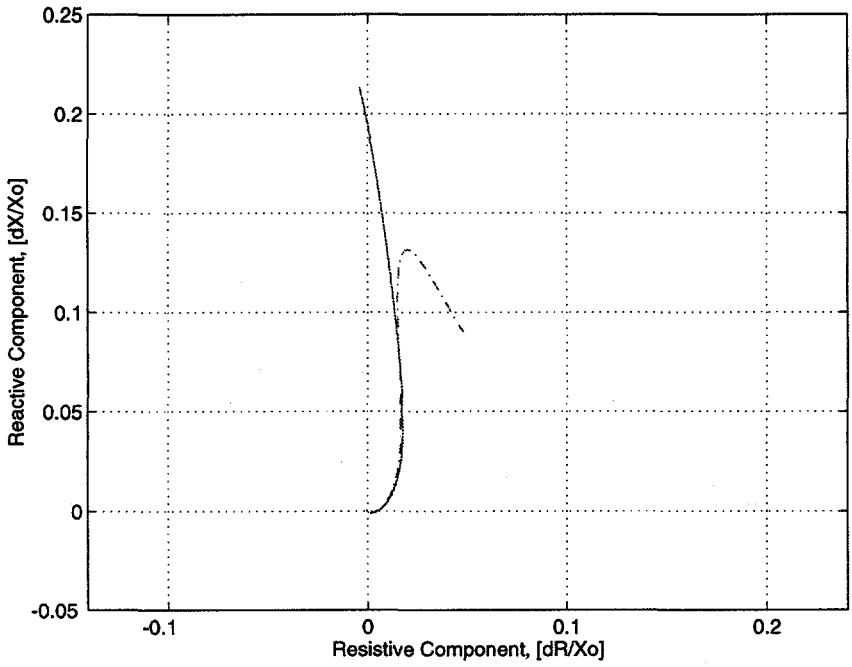

(b)

Figure 42. Calculated (a) resistance and reactance as a function of position, and (b) impedance-plane signal trajectory for absolute bobbin coil, at f = 100 kHz. Artifacts are four axially symmetrical 100% throughwall slits, without (solid line) and with (dashed line) ligament.

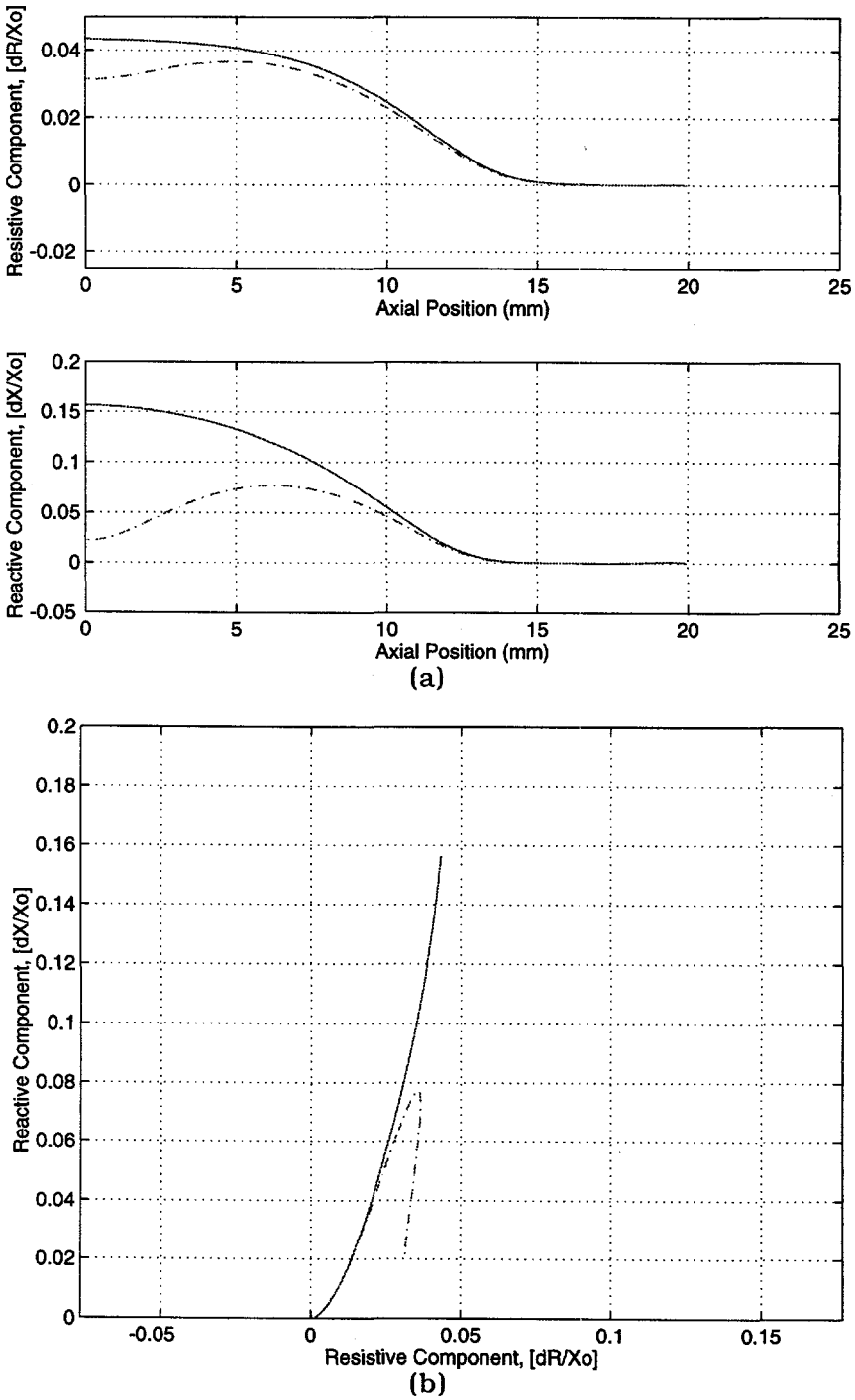

Figure 43. Calculated (a) resistance and reactance as a function of position, and (b) impedance-plane signal trajectory for absolute bobbin coil, at f = 400 kHz. Artifacts are four axially symmetrical 100% throughwall slits, without (solid line) and with (dashed line) ligament.

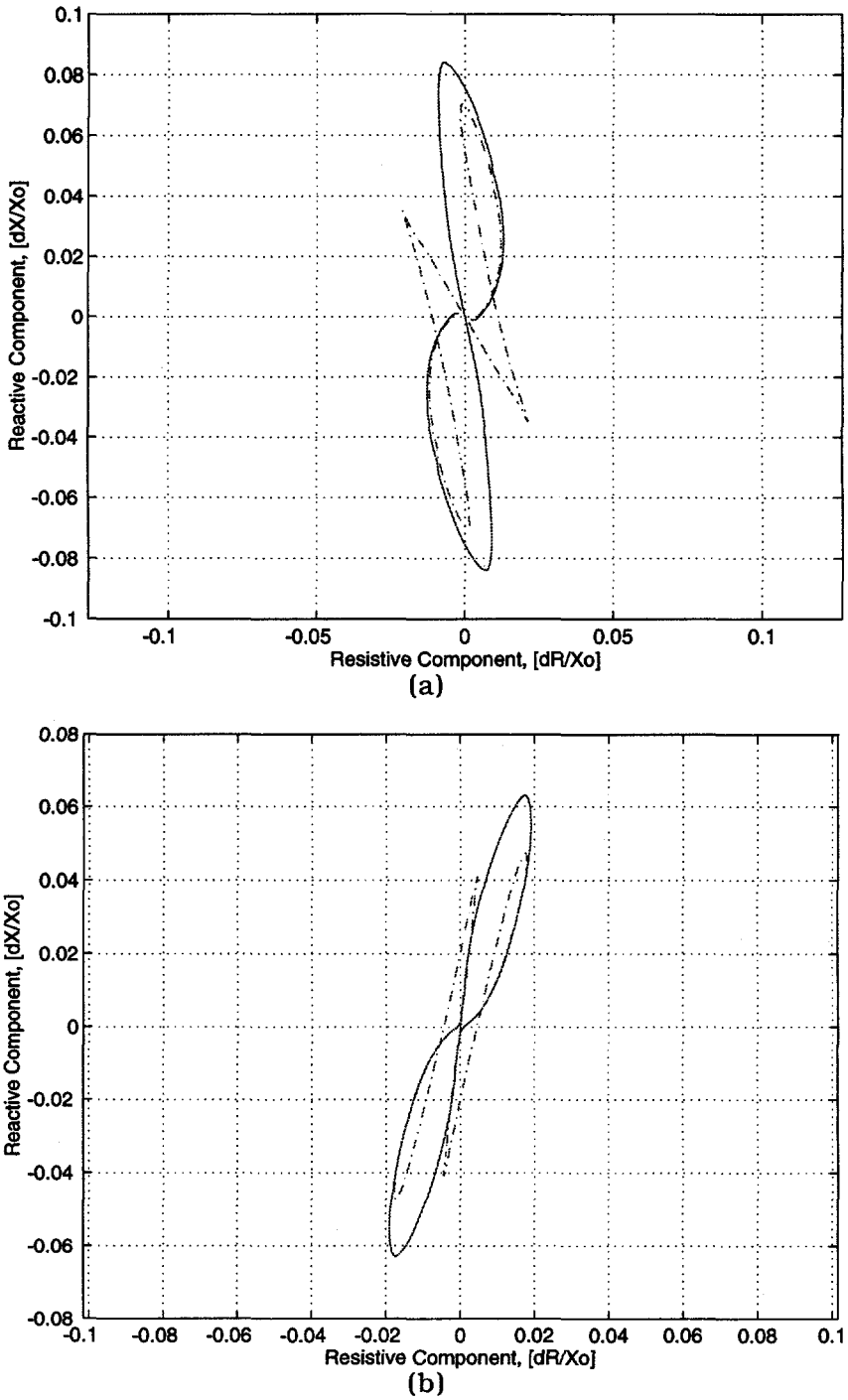

Figure 44. Calculated impedance-plane signal trajectory for differential bobbin coil, at (a) f = 100 kHz and (b) f = 400 kHz. Artifacts are four axially symmetrical 100% throughwall slits without (solid line) and with (dashed line) ligament.

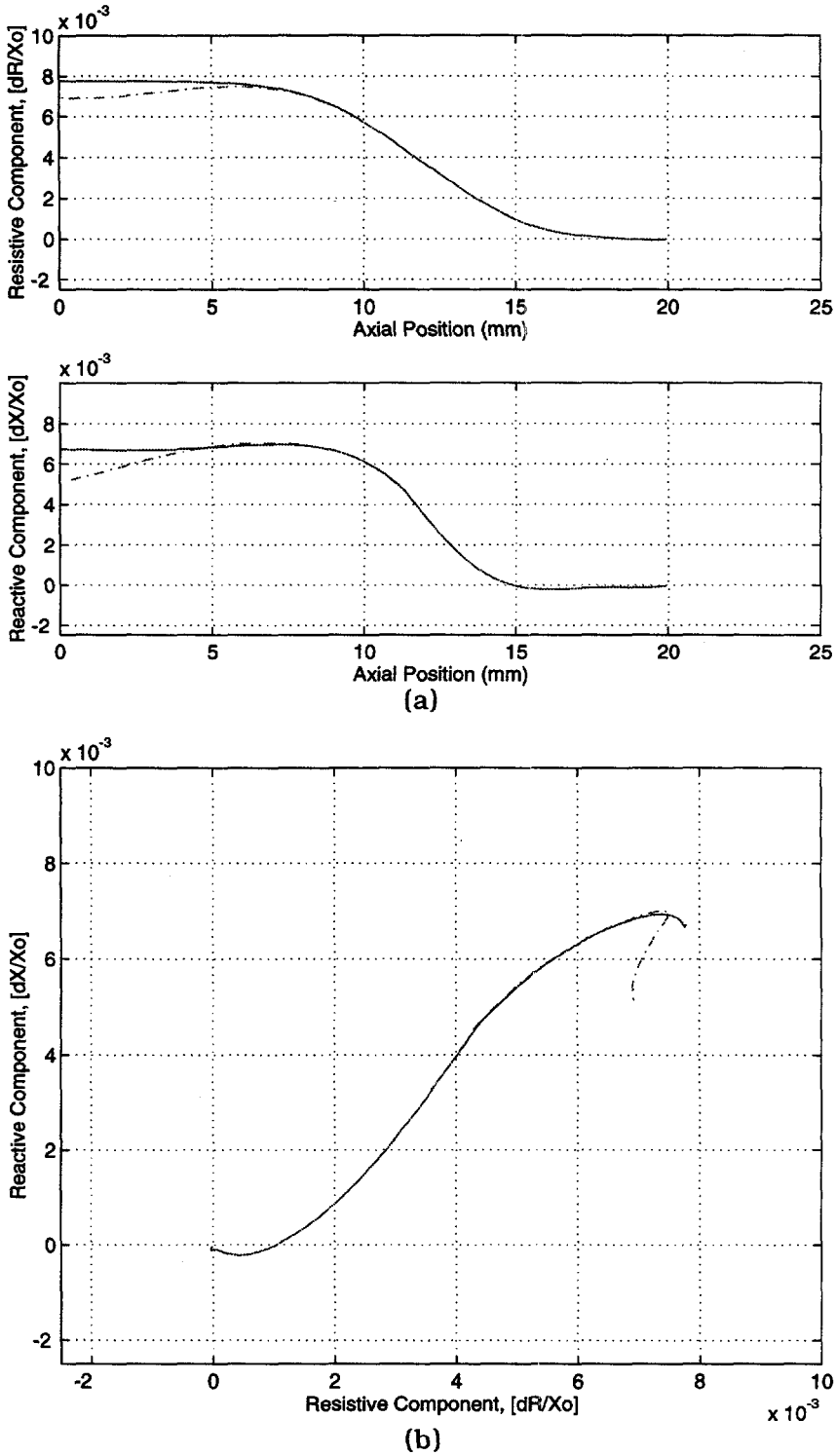

Figure 45. Calculated (a) resistance and reactance as a function of position, and (b) impedance-plane signal trajectory for absolute bobbin coil, at f = 100 kHz. Artifacts are four axially symmetrical 75% OD slits, without (solid line) and with (dashed line) ligament.

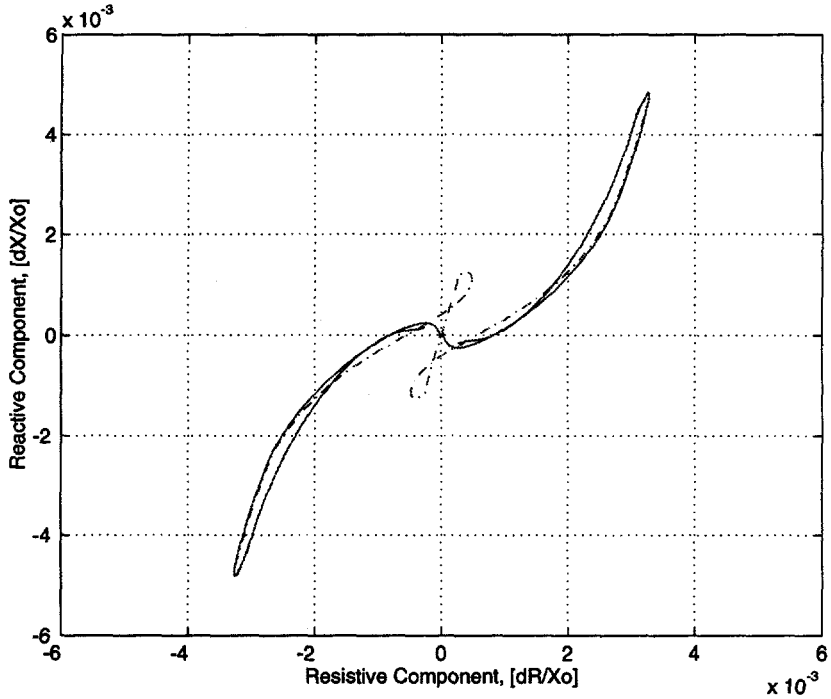

(a)

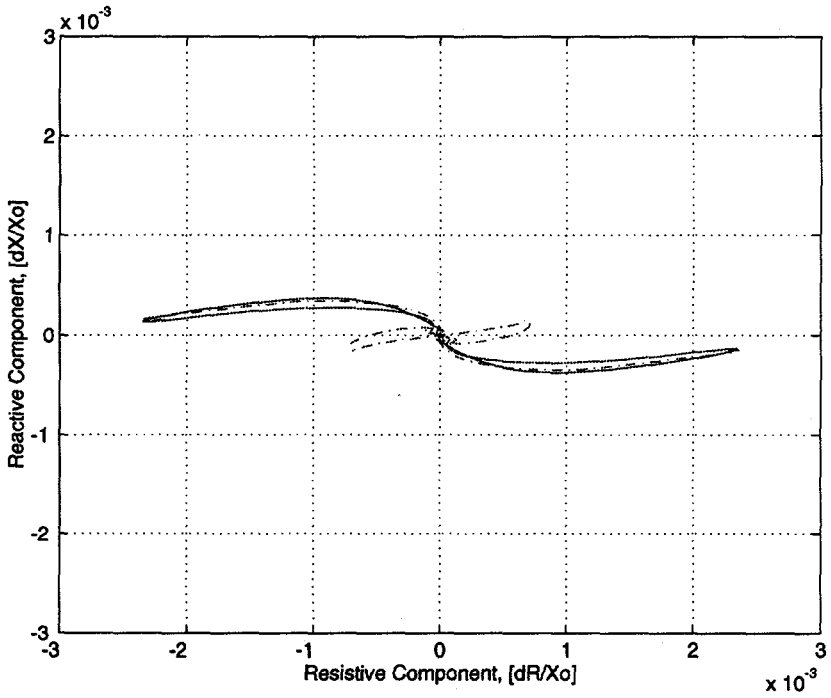

(b)

Figure 46. Calculated impedance-plane signal trajectory for differential bobbin coil at (a) f = 100 kHz and (b) f = 400 kHz. Artifacts are four axially symmetrical 75% outer-diameter grooves without (solid line) and with (dashed line) ligament.

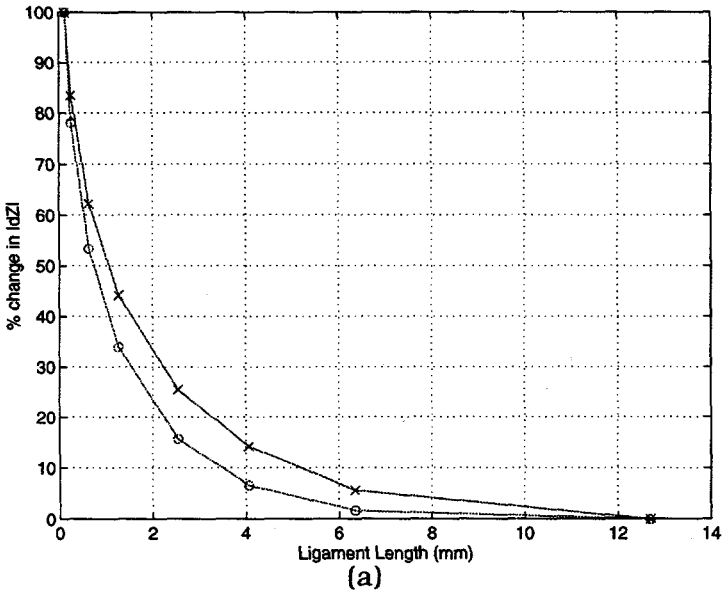

(a)

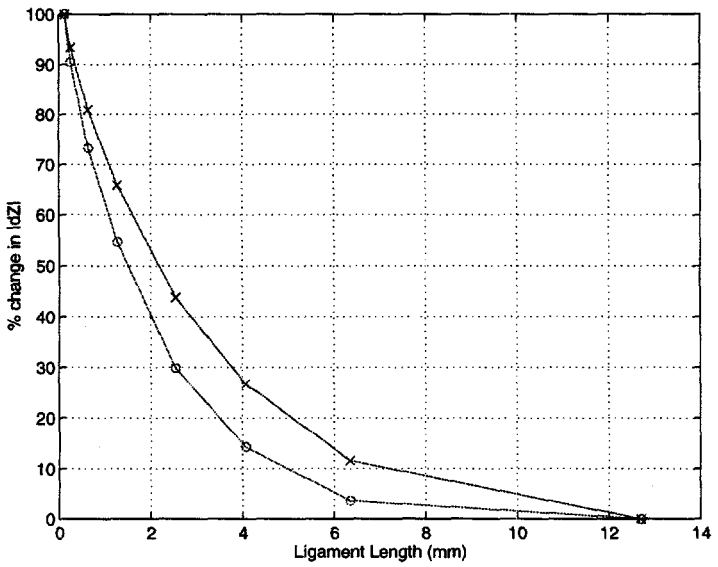

(b)

Figure 47. Plot of change in absolute bobbin probe signal amplitude as a function of ligament length at f = 100 (solid line) and 400 (dashed line) kHz for (a) 100% throughwall, and (b) 75% outer-diameter axial groove.

calculations are shown in Fig. 47b for the 75% OD throughwall groove. In both cases, the change in amplitude of the bobbin coil signal quickly drops with increase in ligament length and approaches the abscissa, which represents no defect.

3.2 Signal Processing and Analysis

The objective of this endeavor is to evaluate advanced signal processing and data analysis techniques when applied to NDE of SG tubing for more reliable ISI of original and repaired SG tubes. In particular, the following elements play an important role in achieving such a goal:

Evaluation of modern signal analysis techniques for extraction of relevant features from EC ISI measurement data.

Identification of an optimal set of features that are most significant in determining flaw characteristics.

Implementation of suitable architecture and learning algorithms (neural network, multiparameter regression, etc.) to establish a reliable correlation between EC indications and flaw morphology, leak rate, and failure pressure.

3.2.1 Evaluation of ORNL's Neural Network Algorithm

In collaboration with Dr. X. Kong[†], a neural network code *bpnd.c*, which was originally developed at ORNL for EC defect depth estimation in SG tubes was modified to run on the HP-UX platforms at ANL.[13] The algorithm and its implementation are evaluated and the initial results are summarized below.

3.2.1.1 Neural Network Algorithm

The neural network algorithm used to predict defect depth is briefly described first in terms of its structure, learning rule, and the training samples used to obtain the neural network weights.

3.2.1.2 Neural-Network Structure and Initialization

A standard backpropagation neural-network structure with momentum is used to predict defect depth from EC measurements. The structure of the neural network is chosen as follows:

Nine input nodes (Layer 1). One node is connected to a constant input to provide a bias term for the neural network. The other eight inputs correspond to the eight EC components: real and imaginary parts at four frequencies: 60, 180, 260, and 520 kHz. The number of input nodes may need to be adjusted according to the EC test configuration,

Twelve hidden nodes (Layer 2). The number of hidden nodes is largely determined by the size of training samples and the number of output classes. Although estimations can be made beforehand on the proper number of hidden layer nodes, the optimum choice is often achieved through some trial and error.

Two output nodes (Layer 3). Currently, only one node is used to output the predicted defect depth.

The weight vector for the neural network is initialized randomly in the range -0.5–0.5. The parameters for the standard backpropagation with momentum are chosen as follows:

[†] Xuan Kong, Department of Electrical Engineering, Northern Illinois University, DeKalb, ANL 1996 summer research faculty.

learning parameter, 0.1; momentum, 0.5. The training data were presented to the neural network in a random order and the amount of the training was measured by epoch. Each epoch corresponds to 1,000,000 random presentations of training samples. After each 100 epochs of training, the neural network weights were saved. A total of 500 epochs of training were carried out for a typical training session. On an HP 9000/735 workstation, the training took more than ten hours to complete. it should be noted that once the training stage is completed, predictions could be carried out in real time.

3.2.1.3 Presentation of Training Samples

Calibrated EC data are presented to the neural network as inputs and the defect depth (in percentage of the tube wall thickness) as the desired outputs. The training data set is determined by the evaluation method. Samples in the training set are presented to the neural network in random order and they may be presented more than one time. To calibrate the EC inputs, a portion of each tube that contains no defects is identified and the EC baseline values are recorded. Subsequently, the baseline values are subtracted from the raw EC data for that tube. Each measurement point is then rotated by the phase angle of the probe that is determined from liftoff indications inside the tube (i.e., rotated so that liftoff signal is horizontal).

The data base consisted of 23 tubes with metallographic data and EDM notch standards. The 23-tube set, fabricated from Alloy 600, with a tube OD of 22.23 mm (0.875 in.) and a wall thickness of 1.27 mm (0.05 in.), all with outer-surface tubing defects, was furnished by PNNL. Most of the tubes in this set contained axial ODSCC defects, five tubes contained circumferential ODSCC defects, and three tubes exhibited IGA. The EDM notch standards contained circumferential and axial notches. Nominal notch depths were 20, 40, 60, 80, and 100% for both standards. The data were recorded at four frequencies of 65, 130, 260, and 520 kHz, every 0.8 mm (0.03 in.) along the tube with a P90 rotating pancake probe. Readings were recorded every 22.5° around the circumference of the tube, simulating a 16-coil array.

The neural network was first trained, at ANL, with data from the SG tube sample data base.[11] Five (out of 32) data sets were not used in the training set so that the trained network could be evaluated for its ability to predict defect depth from independent EC measurements. The remaining 27 data sets provide 33,868 training pairs, representing the EC measurement vs. the actual defect depth. The actual defect depth from metallography measurements may be zero for the portions of the sample tubes that contain no defects. Ultimately, a leave-one-out (LOOT) training procedure was used to predict the maximum depth for all artifacts available in the entire data sets.

3.2.1.4 Forward Computation

Let a training sample pair be denoted as *[X(n), D(n)]*, with the input vector *X(n)* applied to the input nodes and the desired response vector *D(n)* presented to the output nodes. The activity level $v_j^{(l)}(n)$ for neuron j in layer l is

$$v_j^{(l)}(n) = \sum_{i=0}^{p} w_{ji}^{(l)}(n) y_i^{(l-1)}(n), \qquad (5)$$

where $y_i^{(l-1)}(n)$ is the function signal of neuron i in the previous Layer l-1 at iteration n and $w_{ji}^{(l)}(n)$ is the weight of neuron j in layer l that is fed from neuron i in Layer l-1. The function signal follows the sigmoidal nonlinearity:

$$y_j^{(l)}(n) = \frac{1}{1+e^{-v_j^{(l)}(n)}}. \tag{6}$$

At the input layer,

$$y_j^{(l)}(n) = x_j(n), \tag{7}$$

where $x_j(n)$ is the jth element of the input vector $X(n)$. If neuron j is in the output layer,

$$y_j^{(3)}(n) = o_j(n). \tag{8}$$

Hence, the error signal can be computed as

$$e_j(n) = d_j(n) - o_j(n), \tag{9}$$

where $d_j(n)$ is the jth element of the output vector $D(n)$.

3.2.1.5 Backward Computation or Weight Update

By going backward layer by layer, the local gradient δ can be obtained for the output layer neuron j from:

$$\delta_j^{(3)}(n) = e_j^{(3)}(n) o_j(n)[1 - o_j(n)], \tag{10}$$

and for the hidden-layer neuron j from:

$$\delta_j^{(2)}(n) = y_j^{(2)}(n)[1 - y_j^{(2)}(n)] \sum_k \delta_k^{(l+1)}(n) W_{kj}^{(l+1)}(n). \tag{11}$$

The adjustment of the weights in layer l can be made as follows:

$$w_{ji}^{(l)}(n+1) = w_{ji}^{(l)}(n) + \alpha[w_{ji}^{(l)}(n) - w_{ji}^{(l)}(n-1)] + \eta \delta_j^{(l)} y_j^{(l-1)}(n), \tag{12}$$

where η is the learning-rate parameter and α is the momentum constant.

3.2.1.6 Iterations

Randomly selected training pairs are presented to the neural network, and forward calculation and weight update are then performed. The process repeats itself until satisfactory results (e.g., sufficiently small errors in defect depth prediction) are obtained or a predetermined number of iterations is completed. In the program, each epoch consists of one million iterations and the training is normally performed for several hundred epochs.

3.2.2 Eddy Current Test Data Base

3.2.2.1 Test Set One

It was stated in the original ORNL report[11] that the first set of test data consists of 2 standard test tubes, 16 tubes with axial outer-diameter stress-corrosion-cracks, 5 tubes with circumferential outer-diameter stress-corrosion-cracks, and 3 tubes with IGA. Although EC measurements for all of the tubes are available, the actual defect depth information is not available for all of the tubes. In addition, there are 12 sets of eddy current measurement data for a standard test tube (tube vbm), and they are labeled as vbm001–vbm012. The data base contains 39,290 input-output pairs for a total of 32 different sets. The exact number of usable data pairs (EC measurements and defect depth) is listed in Table 2.

3.2.2.2 Results of Defect Depth Prediction

Five sets of neural network weights were initially used to evaluate the accuracy of the defect depth prediction for the five tube samples not used in the training set. The defect depth is given in terms of the percentage of the tube wall thickness. The results are summarized in the Table 3. From the table, it can be concluded that the results obtained here are fairly close to those obtained by Dodd, as outlined in the ORNL report.[11] The large discrepancy in the prediction result of tube 4-11 may be due to the following: the training sample size for the circumferential ODSCC flaws was significantly smaller than that of the longitudinal ODSCC flaws, and the neural network weights were skewed towards longitudinal ODSCC defects. Therefore, the depth prediction for the circumferential ODSCC defects are not as accurate as the prediction for the longitudinal ODSCC defects. One may overcome this problem by training more than a single neural network, with each network being dedicated to a specific type of defect.

Another preliminary conclusion that can be drawn from the above results is that the training time may be reduced without any reduction in prediction accuracy, which can lead to a more computationally efficient training process. Thus, with respect to Table 3, the training time of 500 epochs may be reduced considerably because the neural network did not improve its performance significantly from 100 to 500 epochs.

3.2.2.3 Data Analysis Results

To further evaluate the performance of neural networks for defect depth prediction, the following training and analysis procedure was employed:

(1) The weight vector of a neural network of fixed structure (9 inputs, 12 hidden nodes, and 2 outputs) was initialized randomly. The training parameters are given as follows: learning parameter η = 0.1 and momentum constant α = 0.5.

(2) The neural network was trained with available data on 31 out of 32 files, leaving out the one to be evaluated later by the trained neural network.

Table 2. Summary of usable sample sizes of test tubes in Set One.

Tube Name	Defect Type	Total Points	Usable Points
vbs003d.dat	Standard	625	625
vbm001.dat	Standard	575	575
vbm002.dat	Standard	575	575
vbm003.dat	Standard	575	575
vbm004.dat	Standard	575	575
vbm005.dat	Standard	575	575
vbm006.dat	Standard	575	575
vbm007.dat	Standard	575	575
vbm008.dat	Standard	575	575
vbm009.dat	Standard	575	575
vbm010.dat	Standard	575	575
vbm011.dat	Standard	575	575
vbm012.dat	Standard	575	575
5-01	IGA	4,900	2,573
5-14	IGA	4,900	2,130
4-11	CODSCC	800	685
w-23-03	CODSCC	4,900	2,875
w-23-09	CODSCC	4,900	1,215
w-40-07	CODSCC	4,900	2,796
2-05	LODSCC	800	302
b-10-02	LODSCC	4,900	2,045
b-10-10	LODSCC	6,533	1,433
b-30-02	LODSCC	4,900	990
b-45-06	LODSCC	4,900	875
b-49-05	LODSCC	4,900	798
b-49-09	LODSCC	6,533	102
b-55-08	LODSCC	6,533	3,057
b-59-10	LODSCC	4,900	2,557
b-62-09	LODSCC	6,533	1,380
b-63-07	LODSCC	6,533	83
e-13-06	LODSCC	12,964	2,646
1-14-06	LODSCC	6,533	3,257
TOTAL		105,365	39,290

Table 3. Defect depths (% throughwall) predicted by neural network (NN) and actual depth obtained by metallography.

Tube Name	Defect Type	Defect Depth Predicted by NN after Epoch[a] 100	200	300	400	500	Actual Depth[b]	ORNL Results
4-11	CODSCC	142[c]	152[c]	165[c]	175[c]	184[c]	100	91
B-10-10	LODSCC	41	44	44	44	44	46	43
B-63-07	LODSCC	62	59	60	57	56	69	77
E-13-06	LODSCC	6	6	7	7	7	0	[d]
vbm005	standard	72	72	75	72	71	75	[e]

[a] ANL results.
[b] The actual defect depth refers to the metallography depth.
[c] NN depth estimates >100 imply a throughwall defect.
[d] This tube was documented as having a defect depth of 73%; however, the actual depth data embedded in the original code show a depth of zero.
[e] The defect depth for this tube was not predicted in the ORNL report.[13]

(3) Each epoch of training consisted of 1,000,000 iterations by using sample points from the training set repeatedly. The weight vectors obtained after 100, 200, 300, 400, and 500 epochs were saved.

(4) The trained neural network was then used to predict the defect depth of the data set that was not used in the training stage.

The above procedure was repeated for each of the 32 data sets, and the results are summarized in Table 4.

The capability of the neural network to generalize was also tested by training the network with only the data for the standard tube and using the trained network to predict defect depth of the 21 tubes with longitudinal and circumferential ODSCC types of defects. The results are summarized in Table 5. When compared with the results presented in Table 4, in which the training consisted of all defect forms available, the results in Table 5 show a reduction in accuracy of the estimated defect depths. This test further indicates that a complete training data set is important for more reliable neural-network-based predictions. The training data set should incorporate sufficient information on all defect types that are being analyzed.

Table 4. Defect depth (% throughwall) predicted by the trained neural network and actual depth obtained by metallography. The training method is LOOT (leave-one-out training), and the prediction shown is the maximum defect depth.

Tube Name	Defect Type[a]	Predicted Defect Depth After Training Epoch[c]					Actual Depth[d]
		100	200	300	400	500	
vbs003d	Standard	67.76	80.86	85.41	87.07	87.04	100.00
vbm001	Standard	76.15	78.00	79.33	77.10	78.13	74.91
vbm002	Standard	77.09	80.25	79.50	79.92	76.69	74.91
vbm003	Standard	73.64	79.01	79.50	76.73	77.09	74.91
vbm004	Standard	74.12	72.14	68.40	69.92	68.80	74.91
vbm005	Standard	74.56	73.34	71.16	70.43	69.86	74.91
vbm006	Standard	69.64	78.02	80.75	76.40	75.88	74.91
vbm007	Standard	74.12	78.78	73.95	72.90	75.86	74.91
vbm008	Standard	69.78	74.33	71.45	75.29	72.16	74.91
vbm009	Standard	71.52	73.69	71.97	69.79	71.72	74.91
vbm010	Standard	72.16	71.95	69.26	70.68	80.28	74.91
vbm011	Standard	72.13	73.60	76.50	77.75	77.75	74.91
vbm012	Standard	70.97	75.37	76.71	75.01	74.02	74.91
5-01	IGA	6.41	8.74	8.44	8.36	8.73	18.00
5-14	IGA	35.85	38.00	40.01	41.78	39.60	47.00
4-11	CODSCC	23.93	13.18	13.34	13.86	10.08	100.00
w-23-03	CODSCC	105.19	118.43	122.39	140.94	144.15	100.00
w-23-09	CODSCC	73.96	90.11	85.42	90.52	88.70	100.00
w-40-07	CODSCC	98.15	96.88	97.41	96.89	97.10	98.80
2-05	LODSCC	33.50	48.50	52.20	55.96	56.89	62.00
b-10-02	LODSCC	19.78	18.09	18.30	16.79	17.06	43.00
b-10-10	LODSCC	43.34	45.40	49.13	46.97	47.10	46.00
b-30-02	LODSCC	5.80	5.70	6.06	7.32	8.23	45.00
b-45-06	LODSCC	46.46	49.11	50.85	51.18	51.97	40.00
b-49-05	LODSCC	20.01	22.64	21.04	22.97	23.44	33.00
b-49-09	LODSCC	93.62	111.30	105.48	103.08	106.01	50.00
b-55-08	LODSCC	59.81	56.39	59.88	57.09	57.87	59.00
b-59-10	LODSCC	7.75	7.22	7.55	8.94	8.95	20.00
b-62-09	LODSCC	70.18	67.06	61.87	62.11	66.22	58.00
b-63-07	LODSCC	56.92	57.09	56.77	55.49	54.11	69.00
e-13-06	LODSCC	6.81	6.81	8.60	7.77	8.73	0.0
1-14-06	LODSCC	61.70	60.68	61.31	63.28	61.46	100.00

[a] CODSCC = circumferential outer-diameter stress corrosion crack
LODSCC = longitudinal outer-diameter stress corrosion crack

[b] Depth estimates >100% imply a throughwall crack.

[c] Refers to the depth obtained by metallography.

Table 5. Generalization capability of neural network (NN) as measured by defect depths (% throughwall) predicted by the trained NN after specific number of epochs. The training data used were from the 13 sets of measurements made on the two tube standards. The values shown are the predicted maximum defect depth.

Tube Name	Defect Type[a]	Predicted Defect Depth After Training Epoch[b] 100	200	300	400	500	Actual Depth[c]
5-01	IGA	16.19	30.98	16.49	22.32	26.71	18.00
5-14	IGA	81.72	68.95	64.64	59.81	46.91	47.00
4-11	CODSCC	315.5	434.8	521.2	487.7	444.2	100.00
w-23-03	CODSCC	240.3	291.9	331.1	326.7	313.9	100.00
w-23-09	CODSCC	242.4	308.9	331.3	328.5	323.7	100.00
w-40-07	CODSCC	46.84	39.84	63.53	77.51	89.41	98.80
2-05	LODSCC	68.97	79.39	81.00	69.05	51.30	62.00
b-10-02	LODSCC	37.71	41.16	55.01	57.65	51.77	43.00
b-10-10	LODSCC	45.38	48.93	50.39	55.37	57.19	46.00
b-30-02	LODSCC	16.71	17.14	18.09	18.86	19.19	45.00
b-45-06	LODSCC	52.34	61.24	70.17	77.85	81.93	40.00
b-49-05	LODSCC	28.87	28.01	26.43	26.05	26.16	33.00
b-49-09	LODSCC	233.0	255.9	234.1	241.1	130.0	50.00
b-55-08	LODSCC	104.6	104.3	117.8	133.6	127.4	59.00
b-59-10	LODSCC	12.61	12.88	15.83	17.79	18.83	20.00
b-62-09	LODSCC	169.6	194.6	162.5	163.9	148.1	58.00
b-63-07	LODSCC	56.86	60.27	64.34	69.54	72.46	69.00
e-13-06	LODSCC	21.01	14.40	13.35	18.55	22.45	0.0[d]
1-14-06	LODSCC	84.42	70.01	90.36	83.95	86.75	100.00

[a] CODSCC = circumferential outer-diameter stress corrosion crack
LODSCC = longitudinal outer-diameter stress corrosion crack

[b] Depth estimates >100% imply a throughwall crack.

[c] Refers to the depth obtained by metallography.

[d] This tube was documented as having a defect depth of 73% in the ORNL report. However, the data embedded in the original code show a depth of zero.

4 Research on Degradation Modes and Integrity (D. R. Diercks, K. E. Kasza, S. Majumdar, J. Y. Park, and W. J. Shack)

The objective of Task 3 is to evaluate and experimentally validate models that will predict potential degradation modes, progression rates, crack evolution, leak/rupture behavior, failure pressures, and leak rates for SG tubes and for repaired tubes under normal operating, accident, and severe accident conditions.

Deterministic and probabilistic models for predicting leak rates from degraded tubes under normal operating and accident conditions in SGs have been formulated and used in previous investigations. These models have often been generated from limited data and/or data and correlations from laboratory work wherein the flaw morphology and tube conditions did not necessarily represent in-service conditions representative of current degradation modes. Work is being performed under this task to update and validate these models and correlations and, as required, produce new correlations for flaw types of current interest.

Previous investigations have also focused on normal operating conditions and design basis accidents. Questions have arisen about failure pressures and leak rates from degraded tubes subjected to severe accident conditions. Material flow (creep) and crack opening may be greater under higher temperature conditions than under normal operating temperatures, and the leak rates may be higher, while failure pressure may be lower.

Initiation of environmentally assisted cracking, crack growth rates, and crack arrest and reinitiation are not well predicted or quantified for cracks in current operating SG tubes. Crack initiation times, crack growth rates, and changes in morphologies can be quite variable. Furthermore, the factors that influence the nature of crevices and crevice corrosion cracking are not well understood. To evaluate the continued integrity of currently unaffected and of degraded SG tubes left in service, a better and quantitative understanding of the above phenomena and their variability is needed.

Efforts under Task 3 during the first year of the program have concentrated on the design and construction of experimental facilities for the production of flawed tubing, and for the rupture and leak-rate testing of flawed and unflawed tubing under a wide range of conditions. The facilities under design and construction include an autoclave system for producing cracks in tubes under accelerated (chemically aggressive) conditions; a model boiler facility to produce cracks in tubes under more nearly prototypic conditions; a Pressure Leak-Rate Test Facility for conducting tube failure and leak-rate tests under simulated SG operating conditions; a high-temperature severe accident tube testing facility; and a high-pressure pressurization and leak-rate test facility. The capabilities of the latter three test facilities are summarized in Table 6.

In addition, effort has been devoted to the analysis and modeling of stability for various flaw geometries and loading conditions. A series of tube pressurization tests has also been conducted under postulated severe-accident conditions, and the results of these tests have been successfully analyzed and modeled.

Table 6. Summary of capabilities of SG tube rupture and leak-rate test facilities under design and construction

Facility	Maximum Pressure (MPa)	Maximum Temp. (°C)	Maximum Flow Rate (L/min)	Pressurizing Medium
Pressure Leak-Rate Test Facility	21	320	760	water/ steam
High-Temperature (Severe Accident) Facility	≈28	1000	-	N_2
High-Pressure Facility	52	R.T.[a]	46	water

[a] R.T. = room temperature

4.1 Acquisition and Characterization of Alloy 600 Tubing

Alloy 600 tubing for initial testing purposes has been obtained from two sources. Two hundred feet of 19.05-mm (0.750-in.)-diam tubing was purchased in 0.9-m (3-ft.) lengths from Valinco in the as-fabricated ("cold-worked") condition (Heat NX8524), and ≈110 m (360 ft.) of 22.2-mm (0.875-in.)-diam tubing in 3.7-m (12-ft.) lengths was obtained from PNNL. PNNL was unable to identify the heat number for the latter tubing, but the tubing was labeled "EX-82-1/3675" on all but one piece, which was labeled "HT #9829/1L-102." Heat analyses were provided for the Valinox tubing, and a check chemical analysis was performed on a sample from the PNNL tubing. These analyses are shown in Table 7. In all cases, the tubing conforms to specification ASTM B 163 for Alloy 600.

Room-temperature tensile tests were conducted on the 19.05 and 22.23-mm (0.750 and 0.875-in.) Alloy 600 tubes by an outside vendor. The results, summarized in Table 8, show that, although the ultimate tensile strengths are comparable, the ductility and yield strength of the 22.23-mm (0.875-in.) tubes is significantly greater than that of the 19.05-mm (0.750-in.) tubes.

The room-temperature hardnesses of the Alloy 600 tubing from Valinco (19.05-mm [0.750-in.]-diam, Heat NX8524) and PNNL (22.23-mm [0.875-in.]-diam, ID EX-82-1/2675) were determined to be VH 173±8 and VH 184±9, respectively. Thus, the 22.23-mm (0.875-in.)-diam tubing is slightly harder than the 19.05-mm (0.750-in.)-diam tubing. Optical metallography of an etched (10% oxalic acid) cross section of the tubing shows that the grain boundaries of both tubing materials are sensitized (Fig. 48). The grain size is ASTM 8.0 (average linear intercept 20 μm) for the 19.05-mm (0.750-in.)-diam tubing and ASTM 8.6 (average linear intercept 16 μm) for the 22.23-mm (0.875-in.)-diam tubing.

Present plans call for the purchase of a larger quantity (≈460 m or 1500 ft.) of 22.23-mm (0.875-in.)-diam tubing from Valinco to serve as the principal test material for the present program. Valinco has agreed to supply this tubing with the heat treatment specified by ANL, and experiments are currently underway on tubing samples to determine this optimum heat treatment. Smaller quantities of tubing representing other heat chemistries and heat treatments will be also be acquired as a part of this program.

Table 7. Elemental analysis of Alloy 600 tubing material. The 19.05-mm (0.750-in.)-diam tubing was purchased from Valinco (Heat NX8524) and the 22.23-mm (0.875-in.)-diam tubing was acquired from PNNL (ID EX-82-1/2675).

Element	Chemical analysis (wt. %)			
	3/4-in.-diam		7/8-in.-diam[a]	Alloy 600
	Top of ingot	Bottom of ingot	Check analysis	Specifications[b]
Ni	74.66	74.95	75.05	72.0 min.
Cr	15.21	14.84	15.21	14.0–17.0
Fe	9.16	9.11	8.30	6.0–10.0
Mn	0.20	0.20	0.18	1.0 max.
Cu	<0.01	0.01	0.17	0.5 max.
C	0.022	0.023	0.035	0.15 max.
S	<0.001	<0.001	0.001	0.015 max.
Si	0.20	0.17	0.23	0.5 max.
Al	0.24	0.22	0.15	-
Ti	0.29	0.35	0.18	-
Co	0.01	0.02	0.03	-
P	0.003	0.005	0.009	-
B	0.004	0.002	0.002	-
N	<0.01	<0.01	0.004	-

[a] Average of four samples.
[b] From ASTM B 163.

Table 8. Room-temperature tensile properties of Alloy 600 tubing obtained from Valinco (19.05-mm [0.750-in.]-diam, heat NX8524) and PNNL (22.23-mm [0.875-in.]-diam, ID EX-82-1/2675)

Spec. No.	Diam (mm)	σ_y (MPa)	Ave. σ_y (MPa)	σ_u (MPa)	Ave. σ_u (MPa)	ε_t (%)	Ave. ε_t (%)
6-1	19.05	295.6		678.8		25.50	
6-2	19.05	313.9		681.7		25.50	
6-3	19.05	314.6	308.0	681.7	680.7	24.50	25.17
15-1	22.23	356.5		689.0		44.00	
15-2	22.23	356.5		681.0		44.50	
15-3	22.23	358.0	357.0	678.4	682.8	41.00	43.17

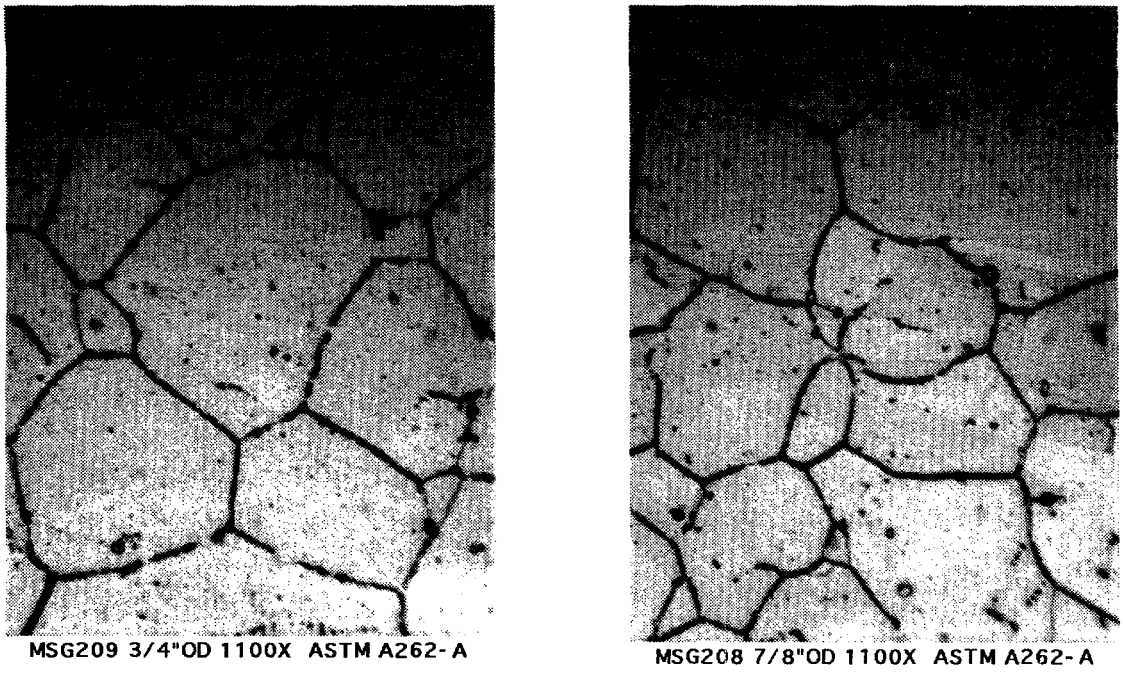

Figure 48. Optical Metallography of cross section of Alloy 600 Tubing: 19.05-mm (0.750-in.)-diam (left) and 22.23-mm (0.875-in.)-diam (right).

4.2 Autoclave Testing Facility

Because cracked tubing from operating or retired SGs is difficult and expensive to obtain and the availability of such tubing is limited, it is necessary to produce prototypical cracks in tubes as a part of this program. These tubes will be used for subsequent pressurization and leak-rate tests and for the evaluation of NDE equipment and techniques. Under the present program, two facilities are being designed to produce cracked tubes. The first of these, the autoclave facility described here, will be used to produce cracks under accelerated aggressive conditions. The second facility, the model boiler described in Section 4.3, will be used to produce cracks under more prototypical conditions that simulate those in SGs.

4.2.1 Description of Autoclave Facility

An autoclave system for the production of cracked specimens was constructed. The design of this system, which is based on a previously described concept,[14] is shown in Fig. 49. Six tubular specimens, each ≈0.30 m (12 in.) long, in a hexagonal array, may be simultaneously exposed at PWR SG operating temperatures (or slightly higher to accelerate cracking) to aggressive secondary-water chemistries at the outer surface under slowly refreshed (≈1 cm^3/min) flow conditions. The tube specimens are plugged at the bottom and pressurized from the top by an independent, refreshed primary-water system to provide internal pressure loading. Individual valving of the six specimens will permit continuation of a given run after one or more of the specimens has developed a leaking

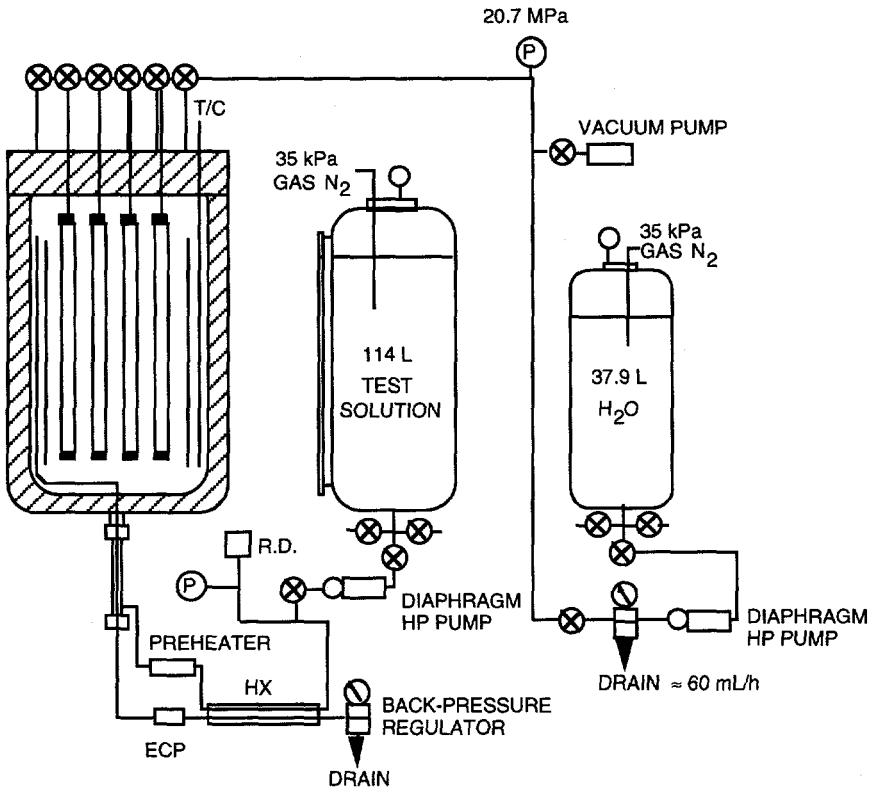

Figure 49. Schematic diagram of autoclave test specimen cracking facility.

crack. Present plans call for the use of high-purity water on the primary side, but it may be possible to modify the chemistry of this water to induce PWSCC failures on the inner surface.

The key component in this system is an 8-L (2-gal) Hastelloy C-276 autoclave that is used to contain the specimens and the aggressive solutions that are used to induce cracking. The secondary-water solution presently being used contains as much as ≈60% NaOH, plus CuO and copper, all of which are known to induce stress corrosion cracking in Alloy 600. Hastelloy C-276 was selected as the construction material for the autoclave because of its high resistance to SCC. Other components in the facility that operate in contact with the aggressive secondary-water chemistry are fabricated of Hastelloy C-276 or stainless steel (SS), depending on temperature.

During operation, deionized deaerated primary water stored in a 38-L (10-gal) tank under nitrogen cover gas is used to pressurize the closed-end tube specimens with a high-pressure (≈21 MPa [3000 psi]) diaphragm pump. The primary water is refreshed at a rate of ≈1 cm^3/min. On the secondary side of the specimens, the aggressive secondary solution is slowly pumped through the autoclave at 8.3 MPa (1200 psi) by a similar pump after preheating to ≈300°C (570°F). The pressure differential across the specimen wall is selected to correspond to ≈60% of its yield strength. Those portions of the specimens where SCC is not desired will be masked using Ni plating or other means, since shrinkable Teflon™ tubing has been found to be unsatisfactory, as discussed below. A throughwall crack in a given tube is indicated by depressurization of the primary side, and the leaking tube can be valved off to permit continuation of the run to crack the remaining tubes.

The autoclave is rated for a maximum pressure of 13.1 MPa (1900 psi) at 350°C (662°F) and is ASME Code stamped. The pressure in the autoclave is controlled with a back-pressure regulator, and a rupture disk is installed for additional protection.

4.2.2 Program Status

All of the components for the two autoclave systems have been ordered and delivered, and the first system has undergone shakedown tests. The secondary side of the autoclave system was tested for leaks at 8.27 MPa (1200 psi) at room temperature and at 300°C, with high purity water and the caustic test solution. The primary side of the system was tested at 20.68 MPa (3000 psi). Several Hastelloy Conax™ fittings that were exposed to the caustic test solution cracked because of high fitting stresses. The system was disassembled to remove the cracked fittings, and it was redesigned to move the Hastelloy Conax™ fittings outside the autoclave. The heater, temperature, and other control systems functioned satisfactorily. Attempts to mask the test specimen surface with heat shrinkable Teflon™ proved to be unsatisfactory. Other techniques, such as nickel plating, will be used. Initial tube cracking tests were performed on eight Alloy 600 tube specimens in the caustic test solution. The results of the initial tests are described in the next section. Tube cracking tests will be continued to obtain optimum test conditions for axial and circumferential cracks in 19.05-mm (0.750-in.)- and 22.23-mm (0.875-in.)-diam tubes. A second autoclave system will be assembled after enough experience is accumulated with operation of the first system.

4.2.3 Initial Test Results

Eight 19.05-mm (0.875-in.)-diam Alloy 600 specimens (Heat NX8524) were tested in an aqueous caustic solution (NaOH 600 g/l, CuO 6 g/L, and Cu 0.1 g/L) at 300°C. The tests were in two groups, with three specimens (Specimens SG0001, SG0002, SG0003) tested in the first group and the remaining five specimens (Specimens SG0004, SG0006, SG0007, SG0008, and SG0009) in the second group (Table 9). The ID of the specimens was pressurized with high purity water to a hoop stress equal to ≈62% of the yield strength of the material. Specimen SG0003 developed several axial cracks and one 360° circumferential throughwall crack in an accumulated test time of 30 h. Figure 50 shows a portion of the fracture surface of the 360° throughwall circumferential crack. Stress corrosion cracking is present near the outer surface, and ductile shear failure is present at the inside surface. Figure 51 is a magnified view of the fracture surface near the outer surface, where the intergranular nature of the cracking is evident. Branching and axial components of the circumferential cracking are also seen in Figs. 50 and 51. Specimen SG0008 developed two axial cracks. Figure 52 shows a 12.7-mm (0.5-in.)-long axial crack on Specimen SG0008; minor branching of the crack is also seen. There was no evidence of cracking in Specimens SG0001 and SG0002 after a 30-h test. All of the other specimens developed axial cracks in accumulated test times of 144–240 h. However, the cracks were at the end-cap welds. The Alloy 600 test tubes were in the as-received condition. Figure 53 is an optical photomicrograph of an etched cross section of the material, showing grain boundaries with some degree of sensitization. The grain size is ASTM 8.0, with an average linear intercept of 0.02 mm (0.0008 in.).

Table 9. Summary of autoclave cracking test results for 19.05-mm (0.750-in.)-diam Alloy 600 tube specimens (Heat NX8524)

Test Batch No.	Specimen ID	Test Time (h)	Results
1	SG0001	30	no crack
1	SG0002	30	no crack
1	SG0003	30	circumferential and axial cracks
2	SG0004	144	leak at the end-cap weld
2	SG0006	192	leak at the end-cap weld
2	SG0007	192	leak at the end-cap weld
2	SG0008	240	axial cracks
2	SG0009	240	leak at the end-cap weld

Figure 50. Scanning electron photomicrograph of fracture surface of circumferential crack at 21X magnification.

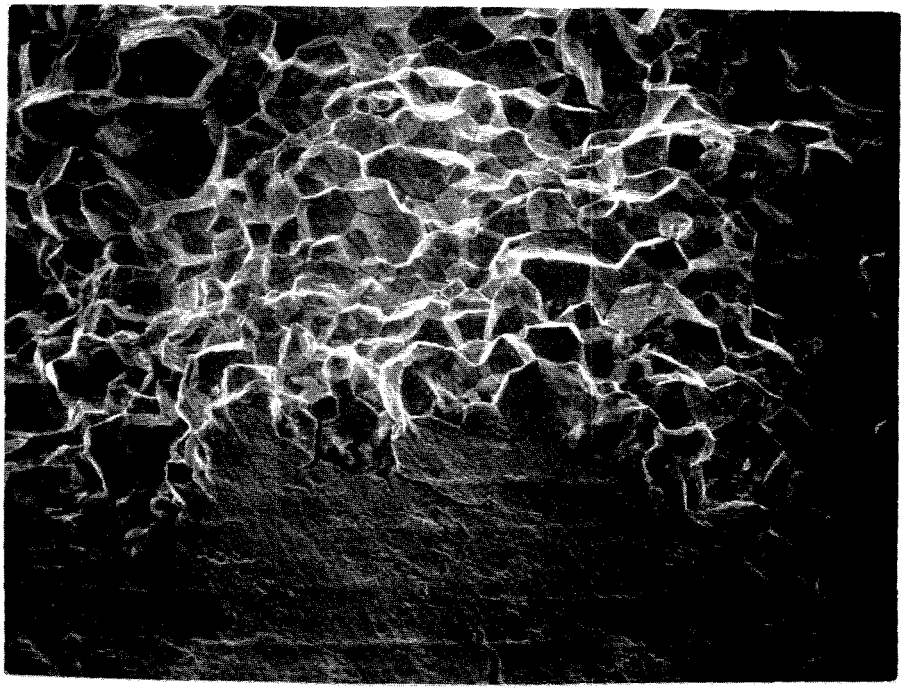

Figure 51. Scanning electron micrograph of fracture surface of circumferential stress corrosion crack at 150X magnification.

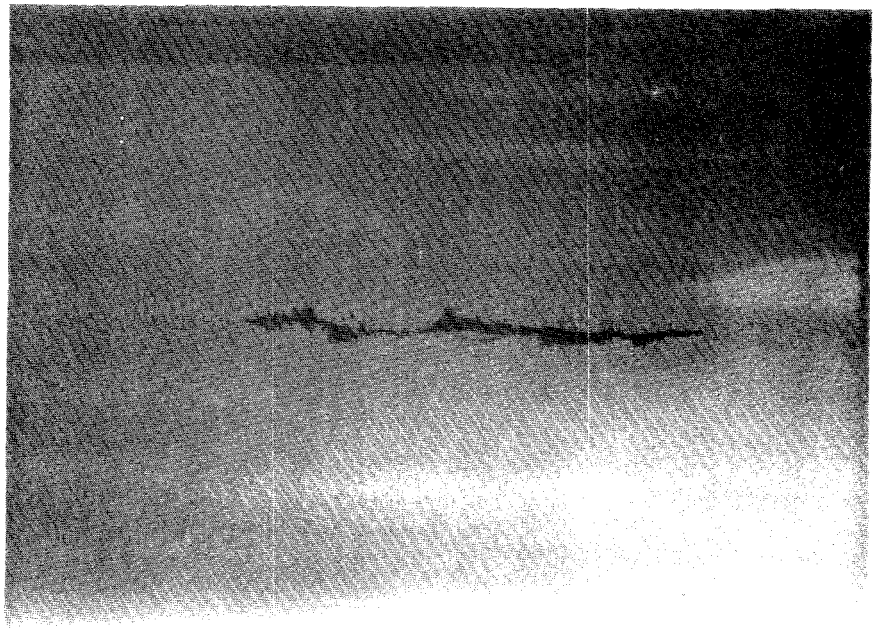

Figure 52. Axial crack, 12.7 mm (0.5 in.) long developed in test specimen SG0008. Magnification = 4X.

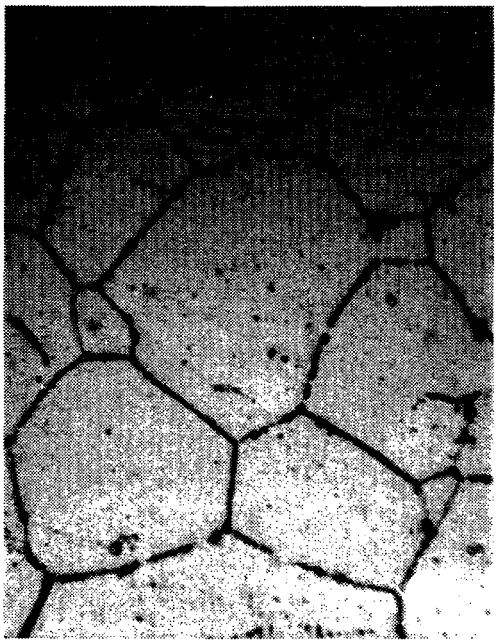

Figure 53.
Optical photomicrograph of cross-section of 19.05-mm (0.750-in.)-diam Alloy 600 Tube (Heat No. NX8524).

4.3 Model Boiler Tube Cracking Facility

Secondary-side steam generator tube SCC is a major aging degradation mechanism in nuclear power plant SGs. A model boiler multi-tube corrosion cracking facility (Fig. 54) is being designed to closely simulate SG thermal-hydraulic and chemistry conditions for the tube/crevice geometry. In particular, heat transfer conditions across the tube wall from the primary-water side to the secondary side will be maintained in this facility to cause chemical concentration of impurity species in secondary side crevices and thereby produce SCC at the outside of the tube. This facility will permit the production of cracked tubes under nearly prototypical conditions, in contrast to the highly aggressive accelerated conditions used to crack tubes in the autoclave system described in Section 4.2. These cracked tubes will be used in leak-rate/failure tests and NDE characterization at ANL.

In the early stages of the design of this facility, a single-tube boiler concept was evaluated. However, an assessment of the overall long-range needs of the program indicated the need for increased production of prototypical flawed tubes. For this reason, the design was changed from a single tube configuration to the seven-tube boiler that is currently being developed.

Tube cracking will be accomplished at nominal temperatures and pressures of 338°C (640°F) and 14.2 Mpa (2060 psi) on the primary side and 288°C (550°F) and 7.24 Mpa (1050 psi) on the secondary side. Enhancement of secondary-side water corrosion by additions of sodium hydroxide (NaOH) to the deionized water at concentrations up to 5 mg NaOH/kg H_2O and by primary-side elevated temperatures and pressures as high as 360°C (680°F) and 18.7 MPa (2710 psi) will be used to accelerate cracking and explore the influence of these parameters. Prototypical tube heat fluxes in the range of 160,000–320,000 W/m^2 (50,000–100,000 Btu/h-ft^2) are achievable in the boiler.

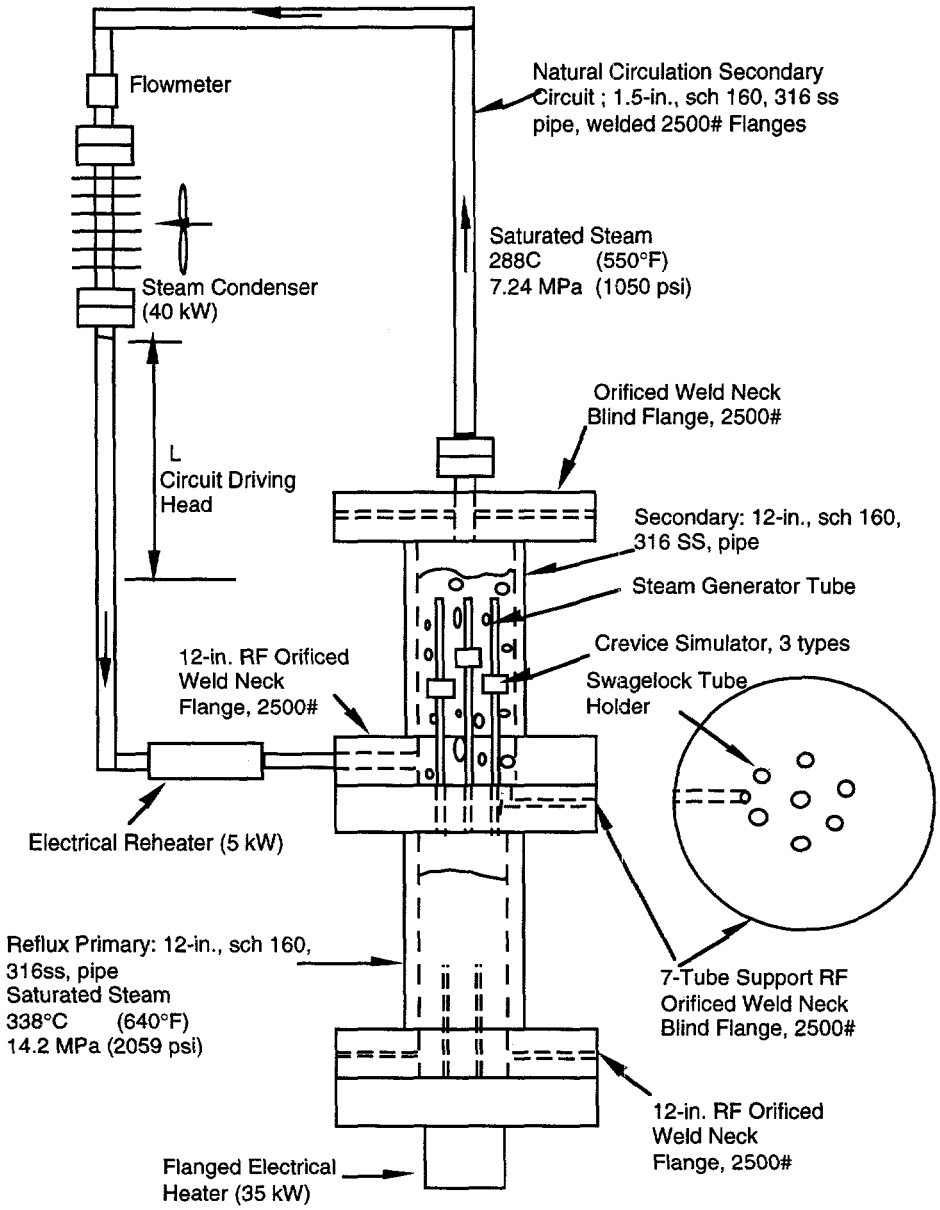

Figure 54. Steam generator multitube corrosion cracking facility

The primary consideration in the design of this facility was the ability to achieve prototypical boiling conditions on the secondary side of an SG tube, in the crevice area formed by the tube and its interface with a crevice simulator. Both tube and crevice simulators are made of prototypical materials, and the crevice region is subject to prototypical temperatures, pressures and heat fluxes. The secondary-side water chemistry can be varied to simulate typical PWR operating conditions, and the impurity levels can be increased to accelerate cracking and permit the evaluation of the effects of impurity level. The apparatus is designed to offer excellent control over thermal conditions that influence boiling, thereby permitting the study of the influence of thermal conditions on the corrosion of SG tubes.

The ANL model boiler is a simplified version of the more conventional designs that have been used in the past. In the ANL facility, a primary side reflux boiler is used to create heat transfer across seven shortened SG tubes to a secondary-side natural convection loop that contains a condenser to maintain constant boiling conditions on the outside of the tube. A crevice simulator is used on each of the seven tubes to promote localized chemical hideout and cracking. Facility simplicity, which is the result of the absence of complicated pumped primary and secondary loops, reduces costs over earlier designs that were used in other programs, and improves flexibility in simulating the wide range of conditions needed to develop an improved data base on SG tube integrity.

The facility is designed for unattended operation and will run continuously for two-to-five-week periods, which is the estimated time range within which various degrees of SCC occur. The entire facility will be designed to meet the ASME Code for a maximum allowable working pressure of 20.7 MPa (3000 psi) and a maximum temperature of 360°C (680°F).

4.3.1 Equipment Features

A schematic diagram of the model boiler multi-tube corrosion cracking facility concept is shown in Fig. 54. The primary consideration in the design of this facility was the ability to achieve nominally prototypical boiling conditions and crevice superheat on the secondary side of the tubes in the crevice area formed by the crevice simulator. The primary side of the SG tube is subjected to nominally prototypical saturated steam pressures and temperatures of 14.2 Mpa (2060 psi) and 338°C (640°F). Temperatures up to 360°C (680°F) and the corresponding steam saturation pressure are possible. These conditions can be varied by controlling the electrical heat input to a reflux boiler. The reflux boiler generates steam, which condenses on the primary (inside) surfaces of the seven tubes to achieve prototypical temperatures and heat fluxes across the tube wall/crevice simulators. The design of the facility does not permit the study of corrosion on the primary side. The heat transfer through the tube wall and into the secondary side of the boiler will cause boiling at the nominal prototypical secondary-side temperature of 288°C (550°F) and the associated saturation pressure. The boiling and associated temperature gradients will cause impurity species to concentrate in the crevice region of each tube.

The secondary side of the apparatus forms a natural circulation loop driven by the heat transfer across the seven SG tubes and by the heat removal by a steam condenser external to the boiler. The water will leave the condenser slightly subcooled. Downstream of the condenser, an electrical reheater raises the water temperature to equal that in the secondary side of the boiler. Temperatures and pressures in the boiler can be varied by controlling the heat input at the reflux boiler electrical heater and electrical reheater and the heat removal rate at the steam condenser. The entire apparatus is designed according to the ASME Boiler and Pressure Vessel Code for 20.7 MPa (3000 psi) and 360°C (680°F). All flanges will be in the 2500-lb class, and the piping will be seamless Schedule 160. All pressure boundary components will be fabricated of Type 316 SS. The primary and secondary chambers will have an ID of 257 mm (10.13 in.) and a length of 610 mm (24 in.).

The reflux boiler is driven by a 35-kW electrical heater selected to achieve prototypical heat fluxes across the seven SG tubes for a maximum individual tube heat transfer length of 30 cm (12 in.). It is difficult to use tubes much longer than this, because of the potential for the formation of a falling condensation film/rising vapor flow interference inside the tubes, which would reduce the attainable heat flux. Each of the seven tubes can be fitted with one or more crevice simulators to promote chemical hideout at specific locations on the tubes. The simulators will be of several designs to evaluate the influence of crevice conditions on corrosion behavior.

The multi-tube boiler design also raises concerns about flow interactions/interferences at entrances to the primary-side tubes and on the secondary-side boiling surfaces from the blockages produced by the crevice simulators that fit over the tubes. These interactions can cause differences in the thermal conditions of individual tubes and hence differences in cracking characteristics among the seven tubes. These concerns required that the diameters of primary- and secondary-side chambers to be relatively large to minimize interactions. The tube layout pattern has one tube on center, with six tubes equally spaced on a 76.2-mm (3-in.) radius about the center tube.

The secondary-side natural-circulation circuit is driven by a 40-kW steam condenser, air cooled by a variable-speed-fan, that creates a standing-water driving head of height L relative to the water level in the secondary boiler. This head balances the circuit frictional flow losses. The water leaving the condenser is slightly subcooled and is heated by a 5-kW reheater before entering the boiler. The secondary-side piping diameter of 38.1 mm (1.5 in.) was selected to minimize flow losses and maximize the natural circulation flow for small values of L.

Each of the seven SG tube test specimens is nominally 300 mm (12-in.) long and 19.05 mm (0.750 in.) or 22.23 mm (0.875 in.) in diameter. Each of the seven tubes, sealed on one end with a welded plug, is held in place with Swagelock™ fittings located on a blind flange. This flange is the top flange of the reflux boiler; it is bolted to the bottom flange of the secondary chamber. Access to the tubes is achieved by unbolting the center flange and lifting the secondary chamber upward and away from the lower primary chamber, which is supported by a steel frame.

The crevice simulators that slip over the seven Alloy 600 SG tubes are depicted in Fig. 55. The simulators are of three designs to permit the evaluation of crevice geometry on corrosion behavior. Each simulator is held in place by a wedging action between the simulator and the tube. This wedging action is created by a ring attached to the bottom of the simulator. The crevice annular diametrical gap will be varied in the range of 0.1–1.0 mm (0.004–0.040 in.) with a depth in the range of 2–5 cm (0.8–2 in.). The wall thickness of the crevice simulator is nominally 5 mm (0.2 in.). The crevice in the type a simulator is only open at the top to the secondary bulk water; the crevice in the type b simulator is open both at the top and bottom. The crevice in the type c simulator is instrumented with thermocouples and fitted with tubing for sampling crevice fluid to permit monitoring of crevice conditions. The sampling tube can also be used to inject NaOH locally into a crevice to increase concentration and further promote cracking over that produced by normal crevice boiling. The leads of the crevice instrumentation leave the secondary

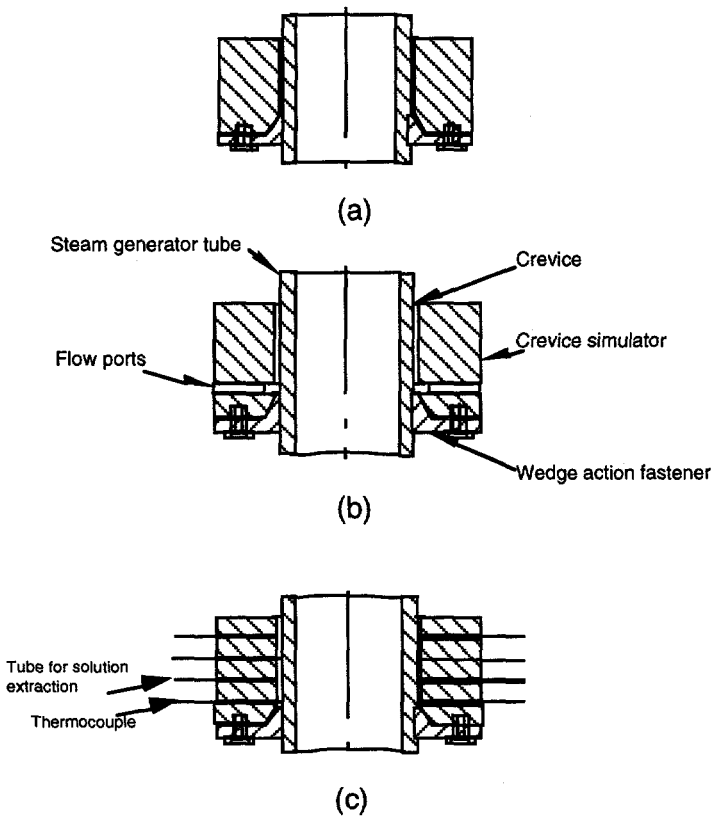

Figure 55.
Types of tube crevice simulators: (a) top open/bottom closed, (b) top open/bottom open, and (c) instrumented with thermocouples and solution sampler.

chamber through a multiported Conax™ fitting in the top flange of the primary reflux chamber.

The crevice thermal-hydraulic conditions that can be achieved in the boiler determine the crevice chemical hideout concentrations that can be achieved and hence influence the ability to produce corrosion-flawed tubes. The likelihood for crevice SCC can be enhanced and varied in this apparatus by increasing the crevice superheat by controlling the primary and secondary saturation conditions and by adding NaOH to the secondary bulk water. The upper limit on secondary bulk concentration is set at 5 mg NaOH/kg H_2O, based on literature that shows an acceptable corrosion performance of Type 316 SS at this level. The concentration of NaOH in the crevices will greatly exceed this limit because of hideout. A metered high-pressure system will be used to inject concentrated NaOH solution into the bulk secondary water, and a chemical monitoring system will be used to track the movement of NaOH from the bulk water to the seven crevices as a function of time. After an initial charge of NaOH to the bulk secondary water migrates into the crevices, additional charges can be injected into the secondary water. Changes in the concentration of NaOH in bulk secondary water over these repeated cycles will be correlated in time with changes in the data from the instrumented crevices.

4.3.2 Crevice Heat Transfer and Chemistry

A primary-to-secondary-side heat transfer model has been developed for predicting tube heat transfer and crevice chemical hideout. The model simulates the coupled falling-

film condensation heat transfer that occurs within the tube because of steam that is generated by the reflux boiler, the heat conduction through the tube and crevice wall, and the boiling that occurs on the outside of the tube. The heat transfer is analyzed as a function of the primary and secondary thermal-hydraulic conditions and the crevice design. It has been demonstrated that by controlling the primary reflux boiler and the secondary condenser, a wide range of heat transfer conditions in the crevice region can be achieved, including prototypical tube wall temperatures.

Results from the model were used to guide the design of the boiler and, with the facility computer control, will be used to guide operation of the facility. The model predicts that the crevice simulators can produce crevice superheats as high as 45°C (80°F) in the presence of heat fluxes in the range of 100,000–250,000 W/m^2 (30,000–79,000 Btu/h-ft^2). Based on these estimates of crevice thermal conditions, chemical concentration factors in the crevices as great as 40,000 are achievable. The meager literature available suggests that the boiler should yield cracked tubes in 10–40 days, depending on conditions. The next two sections present additional details on the heat transfer/crevice model and some performance predictions for the boiler.

4.3.2.1 Heat Transfer Model

A primary-to-secondary-side heat transfer model, shown in Fig. 56, was developed for the boiler tube region. The model represents the coupled falling-film condensation heat transfer that occurs within the tube because of the steam generated by the reflux boiler, the heat condition through the tube wall, and the boiling that occurs on the outside of the tube as a function of primary and secondary thermal-hydraulic conditions.

The reflux boiler (the primary side of the model boiler), when heated electrically, generates saturated steam, which is a condensable vapor in the primary side of the boiler. If the temperature of the tube walls is below the saturation temperature of the vapor, condensation will form on the inner surface of the tubes and, under the action of gravity, will flow down the tube back into the reflux boiler. The inner surfaces of the tubes are blanketed by a smooth condensation film that grows in thickness as it moves down the tube (see Fig. 56). A temperature gradient exists across the film, and the film represents a thermal resistance to heat transfer.

The heat flux through the film condensation can be represented as first proposed by Nusselt[15] by:

$$q = h_v \, (T_{sv} - T_{sw}), \tag{13}$$

where the heat transfer coefficient h_v for film condensation is

$$h_v = 0.943 \left[\frac{\rho_\ell (\rho_\ell - \rho_v) g h'_{fg} k_\ell^3}{\mu_\ell L (T_{sv} - T_{sw})} \right]^{1/4}. \tag{14}$$

In Eq. 14,

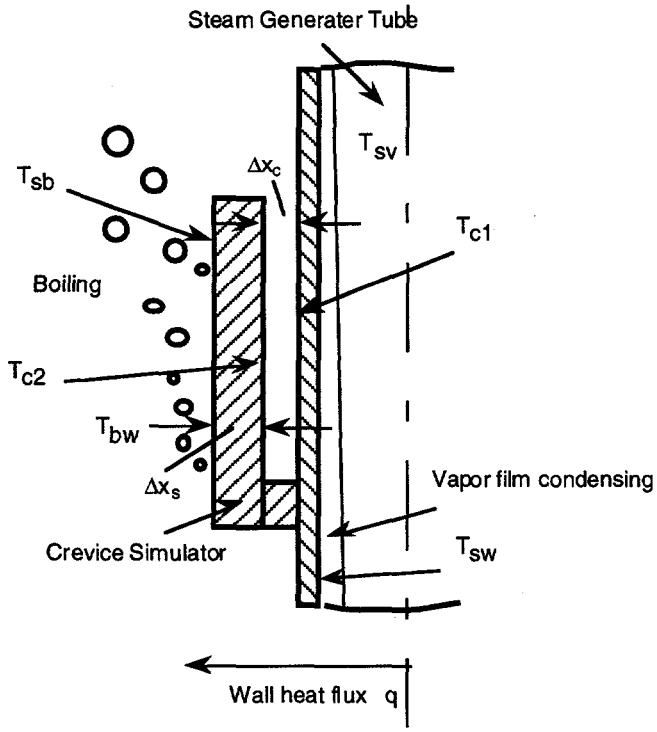

Figure 56.
Crevice heat transfer model

T_{sv} = temperature of vapor,
T_{sw} = temperature on the inner surface of tube wall,
ρ_l = density of liquid in the primary side,
ρ_v = density of vapor in the primary side,
g = acceleration of gravity,
k_l = thermal conductivity of liquid in the primary side,
μ_l = dynamic viscosity of liquid in the primary side,
L = length of tube, and

$$h'_{fg} = h_{fg} + 3/8 c_{pl}(T_{sv} - T_{sw}), \tag{15}$$

where h_{fg} is the enthalpy of vaporization and c_{pl} is the specific heat of the liquid.

If the flow of the condensate is adequate, the condensate film may be turbulent. This turbulence results in higher heat transfer rates. For the condensation film, the Reynolds number, which is the criterion for determining whether the flow is laminar or turbulent, is defined as

$$Re = \frac{4\rho_\ell(\rho_\ell - \rho_v)g\delta_\ell^3}{3\mu_\ell^2}. \tag{16}$$

The thickness of condensate film is defined as

$$\delta_\ell = \left[\frac{4\mu_\ell k_\ell L(T_{sv} - T_{sw})}{g\rho_\ell(\rho_\ell - \rho_v)h_{fg}'} \right]^{1/4}. \quad (17)$$

The parameter δ_ℓ is checked during the calculation to ensure that the film is not blocking the passage of vapor from the reflux boiler into the tube. The flow rate of condensate film on the inside surface of the tube can be written as

$$Q_\ell = \pi\left(d_o - \frac{\delta_\ell}{2}\right)\frac{\rho_\ell(\rho_\ell - \rho_v)g\delta_\ell^3}{3\mu_\ell}. \quad (18)$$

The vapor flow rate is

$$Q_v = \frac{\rho_\ell}{\rho_v} Q_\ell \quad (19)$$

and the vapor flow velocity is

$$V_v = \frac{Q_v}{A_v} = \frac{Q_v}{\frac{\pi}{4}(d_o - \delta_\ell)^2}.$$

Q_v, T_{sv} and P_{sv} can be controlled by the primary electrical heater.

The heat transfer through the tube wall is considered as simple one dimensional heat conduction, and the heat flux is expressed as

$$q = h_w (T_{sw} - T_{bw}), \quad (20)$$

where the heat-transfer coefficient h_w for tube wall is

$$h_w = k_w / \Delta x. \quad (21)$$

Here, k_w is the thermal conductivity of the tube and Δx is the wall thickness. For an Alloy 600 tube k_w = 20.18 W/m·C.

The outer surface of the tube (the secondary side) is considered a nucleate-pool-boiling region where vapor bubbles are generated. The bubbles grow to a certain size, depending on the surface tension at the liquid/vapor interface, the temperature, and the pressure. Depending upon the wall superheat, the bubbles may collapse on the surface, expand and detach from the surface to be dissipated into the body of the liquid, or, at sufficiently high temperatures, rise to the surface of the liquid. In saturated pool boiling, the bubbles break away from the tube surface because of buoyancy and move into the body of the liquid. In this case, the heat transfer rate is influenced by both the agitation caused by the bubbles and the vapor transport of energy into the bulk of the liquid.

A nucleate-pool-boiling model, first proposed by Rohsenow,[16] was used to represent the boiling heat transfer on the tube outer surface as

$$\frac{c_{p\ell}(T_{bw} - T_{sb})}{h_{fg}P_{r\ell}^{1.7}} = C_{sf}\left[\frac{q}{\mu_\ell h_{fg}}\sqrt{\frac{\sigma}{g(\rho_\ell - \rho_v)}}\right]^{0.33}, \quad (22)$$

where T_{sb} = temperature of liquid in the secondary side,
T_{bw} = temperature on the outer surface of tube wall,
c_{pl} = specific heat of saturated liquid in the secondary side,
h_{fg} = enthalpy of vaporization in the secondary side,
P_{rl} = Prandtl number of saturated liquid in the secondary side,
ρ_l = density of liquid in the secondary side,
ρ_v = density of vapor in the secondary side,
g = acceleration of gravity,
μ_l = dynamic viscosity of liquid in the secondary side,
σ = surface tension of liquid/vapor interface (=16.2 N/m), and
C_{sf} = constant, determined from experimental data (≈0.013).

The pool-boiling heat flux can be expressed as

$$q = h_b (T_{bw} - T_{sb}) \quad (23)$$

The heat transfer coefficient in the nucleate pool boiling region h_b is obtained from Eq. 22.

The heat flux through the entire thermal resistance chain is

$$q = h_a (T_{sv} - T_{sb}), \quad (24)$$

where

$$h_a = \frac{1}{\frac{1}{h_v} + \frac{\Delta x}{k_w} + \frac{1}{h_b}}. \quad (25)$$

A computer code based on the preceding heat transfer model has been developed. The code utilizes an iterative scheme to calculate the temperatures of the various zones and the heat flux across the tubes from the primary to the secondary side. The following two calculated cases are for an Alloy 600 tube without a crevice simulator, having an actual heat transfer length of 200 mm (7.9 in.), OD of 19.05 mm (0.750 in.), and a wall thickness of 1 mm (0.040 in.).

Case 1:

T_{sv} = 338°C (640°F),
T_{sw} = 303°C (578°F),
T_{bw} = 295°C (562°F),
T_{sb} = 288°C (550°F),

q = 17,7051 W/m^2 (56,125 Btu/h-ft^2),
h_a = 3,541 W/m^2-°C (623 Btu/h-ft^2-°F),
h_v = 5,167 W/m^2-°C (909 Btu/h-ft^2-°F),
h_w = 20,180 W/m^2-°C (3,552 Btu/h-ft^2-°F),
h_b = 25,437 W/m^2-°C (4,477 Btu/h-ft^2-°F),
δ_l = 0.105 mm (0.0041) in.,
V_v = 0.0492 m/s (9.67 ft./min),
Re = 1085.

Case 2:

T_{sv} = 360°C (680°F),
T_{sw} = 290°C (554°F),
T_{bw} = 278°C (533°F),
T_{sb} = 273°C (525°F),
q = 24,5073 W/m^2 (77,688 Btu/h-ft^2),
h_a = 2,846 W/m^2-°C (501 Btu/h-ft^2-°F),
h_v = 3,527 W/m^2-°C (621 Btu/h-ft^2-°F),
h_w = 20,180 W/m^2-°C (3,552 Btu/h-ft^2-°F),
h_b = 54,450 W/m^2-°C (9,583 Btu/h-ft^2-°F),
δ_l = 0.123 mm (0.0048 in.),
V_v = 0.0356 m/s (7.01 ft./min),
Re = 1483.

These results demonstrate that the tube heat flux can be controlled by adjusting the primary- (T_{sv}) and/or secondary-side temperature (T_{sb}) and that prototypical thermal conditions are achieved. The next section describes the features of the code used to calculate crevice temperature and chemical hideout when a crevice simulator is used.

4.3.2.2 Crevice Superheat and Hideout Concentration

Many of the corrosion problems encountered in nuclear SGs can be attributed to the concentration (hideout) of bulk-water low-concentration, low-volatility ionic impurities in local regions. Hideout is a result of heat-flux-driven boiling processes that occur in semi-isolated locations where access to free circulating bulk water is restricted and within which the temperature is higher than the saturation temperature of the bulk water in the SG. Typical locations are the crevices between tube and tube support plates, crevices within tubesheets, sludge piles that surround active SG tubes, and porous scale deposited on active tubes. The temperature elevation above the secondary-water saturation temperature at these locations is referred to as the local superheat.

Boiling action draws bulk water into crevice locations and expels steam or a mixture of steam and water. Some of the low-volatility dissolved substances that are drawn in with bulk water remain behind to accumulate. If the concentration increases to the solubility limit for a solid substance, the solid will precipitate and block or alter access and escape paths for fluid or vapor. Crevice concentration can increase to the extent that the boiling point of the local fluid is significantly increased over the boiling point of the SG bulk water.

Crevice boiling will stop wherever the concentration increases to the extent that the boiling point elevation equals the local superheat.

Concentrating processes that reach the ultimate concentration at which boiling stops are "thermodynamically limited." The thermodynamic limit on achievable concentration is determined by local superheat, the boiling point elevation characteristics of dissolved substances, and their solubilities. However, the rates of input and output for dissolved substances may become equal at a concentration that is less than the thermodynamic limit; the result is a steady state in which no further net crevice accumulation occurs. This is known as a "kinetically limited" concentrating process. Whether the concentration at a particular location is kinetically limited or thermodynamically limited depends on many factors. These include the geometric configuration of the location itself and of pathways that connect it to the bulk water, the local temperature and heat flux, the boiling point, and other characteristics of the fluid.[17] In our calculations, the hideout amount is estimated from the crevice superheat temperatures at which the boiling is suppressed because of the elevation of boiling point of the solution in the crevice.

In the crevice region, the chemical hideout amount is related to the degree of boiling point elevation, i.e., the crevice boiling point depends on the amount of dissolved species in the crevice fluid. The boiling point of a solution that contains impurities is related to the mole fraction of those impurities by Eq. 26,

$$\mathrm{Ln}\, X_A = \frac{\Delta H_{vap}}{R}\left(\frac{1}{T} - \frac{1}{T_o}\right), \tag{26}$$

where X_A = mole fraction of water,
ΔH_{vap} = molar heat of vaporization of H_2O,
R = universal gas constant, 1.98717 cal/mole-K,
T_o = boiling point of pure H_2O (K), and
T = boiling point of solution (K),

If enough impurities concentrate in the crevices, the boiling point elevation of the resulting mixture will exceed the crevice temperature. The difference between the crevice temperature and boiling point of pure water (both in °C) is often referred to as "available crevice superheat." When the boiling point of the fluid in the crevice exceeds the crevice temperature, boiling will not occur and the fluid will be superheated.

For the heat transfer model of the crevice simulator shown in Fig. 56, the crevice superheat and hideout amount can be estimated by our computer program, in which a solution of dilute sodium hydroxide (NaOH) is assumed to exist in the secondary bulk water and concentrate in the crevice. The heat transfer coefficient through the thermal resistance chain of the model, composed of contributions from the condensate film, tube wall, crevice fluid, simulator wall, and pool boiling at the outer surface of the simulator wall and is given by[18]

$$h_a = \frac{1}{\frac{1}{h_v} + \frac{\Delta x}{k_w} + \frac{1}{h_c} + \frac{\Delta x_s}{k_s} + \frac{1}{h_b}}, \quad (27)$$

where the average temperature in the crevice T_{cc}, and the superheat temperature T_{sh} are defined as

$$T_{cc} = \frac{T_{c1} + T_{c2}}{2} \quad (28)$$

and

$$T_{sh} = T_{cc} - T_{sb}. \quad (29)$$

Results for two crevice cases with the same tube geometry and primary and secondary temperatures as in the two cases described previously are presented below. The calculated heat transfer data, superheat, and NaOH hideout amount (mass percentage) in the crevice fluid are for a crevice simulator with a wall thickness 5.0 mm (0.2 in.) and a diametrical gap of 1.0 mm (0.04 in.).

Case 1

INPUT DATA OF CALCULATION

T_{sv} = 338°C (640°F),
T_{sb} = 288°C (550°F),
Wall Thickness of Simulator, x_s = 5.0 mm (0.2 in.),
Crevice Diametrical Gap, x_c = 1.0 mm (0.04 in.).

OUTPUT DATA OF CALCULATION

q = 2038.4 Btu/h-ft^2,
h_a = 22.58 Btu/h-ft^2-°F,
T_{c1} = 336.8°C (638.3°F),
T_{c2} = 290.5°C (554.9°F),
T_{c1} - T_{c2} = 46.3°C (83.4°F),
Crevice Average Temperature, T_{cc} = 313.7°C (596.6°F),
Crevice Thermal Conductivity, k_c = 0.138 W/m/K,
Crevice Superheat, T_{sh} = 25.9°C (46.6°F),
Hideout Mole Fraction Iron (NaOH) = 22.16%,
NaOH Solution Concentration (mass %) = 27.23%.

Case 2

INPUT DATA OF CALCULATION

T_{sv} = 360°C (680°F),
T_{sb} = 273.9°C (525°F),

Wall Thickness of Simulator, x_s = 5.0 mm (0.2 in.),
Crevice Diametrical Gap, x_c = 1.0 mm (0.4 in.).

OUTPUT DATA OF CALCULATION:

q = 2937.5 Btu/h-ft^2,
h_a = 18.92 Btu/h-ft^2-°F,
T_{c1}= 358.5°C (677.3°F),
T_{c2} = 277.2°C (530.9°F),
T_{c1} - T_{c2} = 81.3°C (146.4°F),
Crevice Average Temperature, T_{cc} = 317.8°C (604.1°F),
Crevice Thermal Conductivity, k_c = 0.114 W/m/K,
Crevice Superheat, T_{sh} = 43.9°C (79.1°F),
Hideout Mole Fraction Iron (NaOH) = 34.82%,
NaOH Solution Concentration (mass %) = 41.26%.

These crevice results indicate that significant superheat, which will cause high levels of NaOH hideout and result in a good environment for stress corrosion cracking to occur, will be established in the crevices of the simulators. Additional calculations have shown that

Crevice superheats in the range of 11–44°C (20–80°F) can be achieved,

Crevice superheat and hideout percentage can be raised by increasing the difference between the primary- and secondary-side temperatures, and

Changes in the crevice diametrical gap will significantly affect the heat flux and heat transfer coefficient because the crevice fluid resistance is a dominating resistance throughout the heat resistance chain. However, changes in the crevice diametrical gap have less effect on the crevice superheat and hideout percentage.

Further model improvements are underway to aid in facility operation and in interpretation of data.

4.3.3 Facility Status

Detailed design of the model boiler multitube corrosion cracking facility has been completed. Detailed hardware specification has been completed for all components and vendor price quotes have been received. Purchase contracts are in place for the major components and vendor fabrication has started. The contract delivery date for the boiler pressure vessel is March 1997. An existing computer control room has been renovated and a new computer system that will be used to control and monitor boiler operations has been purchased and installed. Work continues on refining the boiler performance prediction code, studying operational characteristics, and developing facility operation procedures.

4.4 Pressure Leak-Rate Test Facility

The ANL Pressure Leak-Rate Test Facility will be used to obtain data on failure pressures, failure modes, and leak rates of flawed tubing at temperatures up to 343°C (650°F), pressures of up to 21 MPa (3000 psi), and pressurized-water flow rates up to 760 L/min (200 gal/min). In designing this facility, available information on the design and performance of previous facilities was reviewed. The ANL facility incorporates several features that are necessary to obtain more prototypical data under stable, controlled conditions. In overview, the important features of the facility are a large blowdown vessel water inventory to ensure high, stable, flow rate capability and permit full-range testing of initially stable leaking cracks to instability; piping and valves of a size appropriate to minimize pressure drop in the supply line to a flawed tube and thereby permit high flow rates; the use of a downstream back-pressure regulator valve to control tube secondary-side pressure, thereby minimizing nonprototypical two-phase flow from entering the tube; and computer feedback valve control to allow programmed ramps of the pressure differential across a tube.

A schematic diagram of the facility is shown in Fig. 57. The pressurized and heated blowdown vessel holds ≈760 L (200 gal) of water and thereby provides adequate water inventory for ramping the pressure differential P1-P2 and testing tube specimens that contain preexisting throughwall flaws. The tube specimen is housed in the test module containment vessel. The pressure differential ramp-up is produced through a back-pressure regulator valve (V6) located downstream from the test module containment vessel. The blowdown vessel is maintained at a constant pressure P3 up to 21 MPa (3000 psi) during a test by use of regulated nitrogen cover gas pressurization from a 30-MPa (4400-psi) tank system. The differential pressure P1-P2 across the specimen wall is ramped up in a series of quasi-steady plateau increases through feedback control of Valve V6, which controls pressure P2. The option also exists for linear ramping of P1-P2 at differing rates to simulate more prototypical tube loadings. During the ramp-up of P1-P2, information on flow rate Q, the pressure differential P1-P2, and possibly the jet leak behavior at the flaw (as viewed through an ultra-high-speed 12,000 frames per second video) will be recorded as a function of time.

The ramp-up of the differential pressure P1-P2 will be terminated when the tube crack becomes unstable (i.e., the tube ruptures, causing a dramatic increase in Q) or the water level in the blowdown vessel becomes too low. For large throughwall flaws, the rupture pressure will be considerably <21 MPa (3000 psi) and high flow rates will be required. Under these conditions, short-duration differential pressure plateaus (P1-P2) of 10 s or less will be used, and crack flow rates on the order of 760 L/min (200 gal/min) are achievable and measurable with the water inventory stored in the blowdown vessel. For short throughwall cracks with considerably lower flow rates but higher rupture pressures, the time available for ramping will be considerably longer.

Flawed tubing for testing in this facility can come from three ANL sources: (1) the severe chemistry autoclave cracking facility, (2) the model boiler test facility, and (3) EDM. Flexibility in moving tubes between facilities is achieved by mounting the tubes with identical Swagelock™ fittings. The tubes tested in the present facility can range from

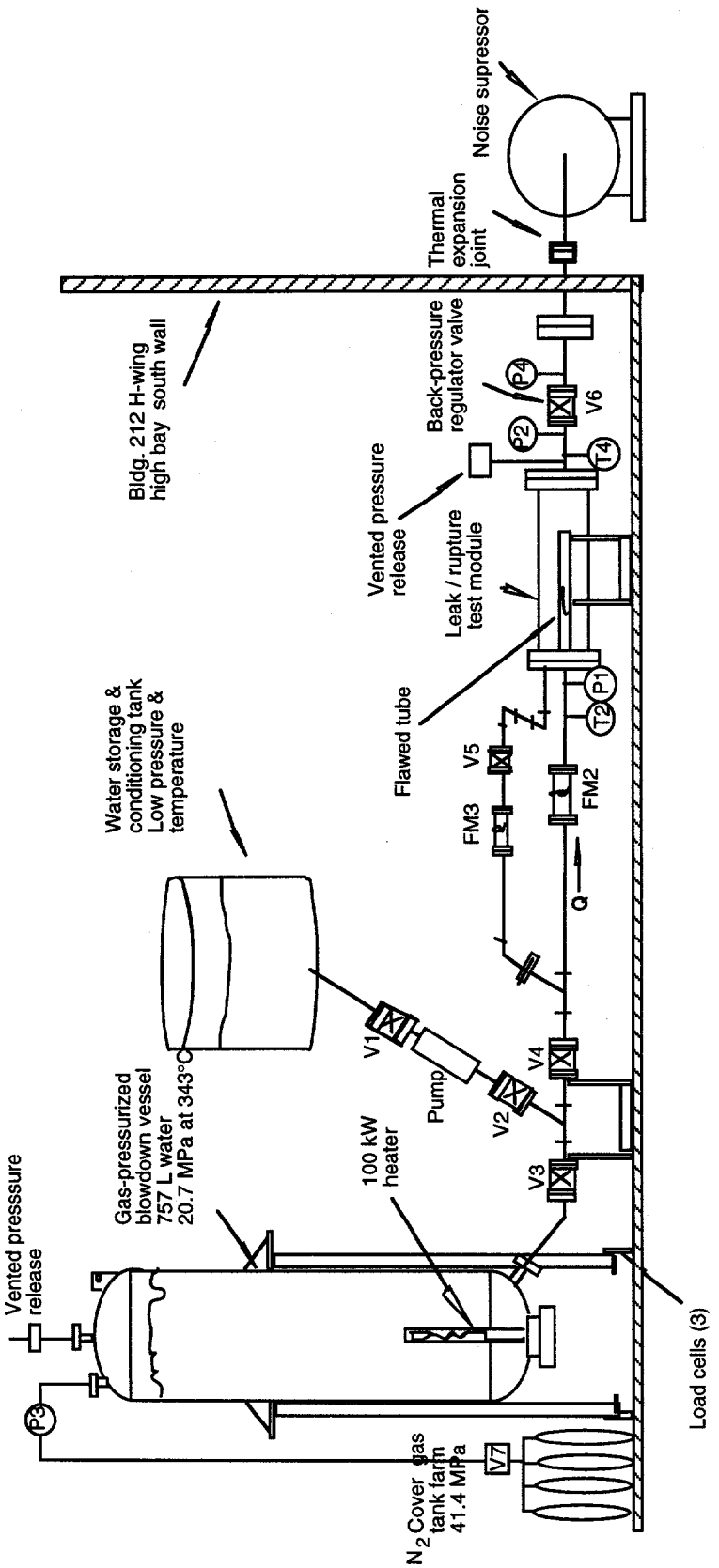

Figure 57. Schematic Diagram of Pressure Leak-Rate Test Facility

several inches in length to ≈1 m (40 in.), which is the length of the test module vessel. The test module will also allow study of the influence of tube support characteristics on rupture pressure through the use of support stings fitted on the inside of the module to simulate support plate constraints on flawed tubes.

4.4.1 Equipment Features

The internal diameter of the blowdown vessel (Fig. 58) is 0.61 m (2 ft.) and its length is 3.7 m (12 ft.). The internal diameter of the test module vessel (Fig. 59) is 0.20 m (8 in.) and its length is 1 m (40 in.). Both vessels are constructed of welded Type 316 SS and are ASME Section VIII, Div. 1 Code designed and stamped for 21 MPa (3000 psi) at 343°C (650°F). Each tank has over-pressurization protection vented to an outside muffler. The 3030-L (800-gal) water storage and conditioning tank will be exposed to only low-pressure service near room temperature and is made of Type 304 SS.

The blowdown vessel is pressurized by a specially designed, regulated nitrogen cover gas pressurization system, which consists of a series of 10 manifold-connected tanks with a total capacity of 34,110 standard ft^3 (SCF) located outside of the laboratory room. Before each test, these tanks are pressurized with nitrogen gas to up to 30 Mpa (4400 psi) by a small compressor. The compressor is fed from an existing low-pressure bulk liquid nitrogen source tank. Full pressurization for a test can be achieved in <6 hours. The gas is piped in by a 50-mm (2-in.) supply line into the blowdown vessel through a flanged port on the top of the vessel. The cover gas pressurization system contains sophisticated controls and valving for maintaining the desired constant cover pressure during a test. The water flow rate out of the blowdown vessel during a test can start at only a few liters per minute and then suddenly increase to as much as 760 L/min (200 gal/min). The pressurization system, which is designed to maintain a constant driving pressure over this wide range in flow conditions, can supply a gas flow rate of 5300 SCF/min to maintain the blowdown vessel pressure at 21 MPa (3000 psig) for a 760-L/min (200 gal/min) water discharge.

The piping that connects the blowdown vessel to the test module is 50-mm (2-in.) Schedule 160, flanged Type 316 SS, to minimize pressure drop under flow conditions of 760 L/min (200 gal/min). The 50-mm (2-in.) Valves V3 and V4 in the main flow path that connects the blowdown and test module vessels are also of a size adequate to pass the 760-L/min (200-gal/min) flow with acceptable pressure drop. Piping downstream of the test module is likewise of a size large enough to minimize back pressure on the test module so that Valve V6 exerts the dominant controlling back pressure. Downstream of Valve V6, the piping size is increased to 0.25 m (10 in.) to improve valve control and permit interfacing with the inlet of the noise suppresser.

The 75-mm (3-in.) back-pressure regulator Valve V6, located downstream of the flawed-tube test module, is used to control and vary the pressure differential across a flawed tube that is being tested. At the start of a test, the pressure differential P1-P2 across the tube wall is zero; it is then ramped up with time in a stepwise fashion under control of Valve V6 to a maximum of 21 MPa (3000 psi), which is the constant cover gas pressure maintained on the water in the blowdown vessel. Specimens with throughwall flaws may leak at the earliest stages of the pressure ramp-up, and a nearly closed Valve V6

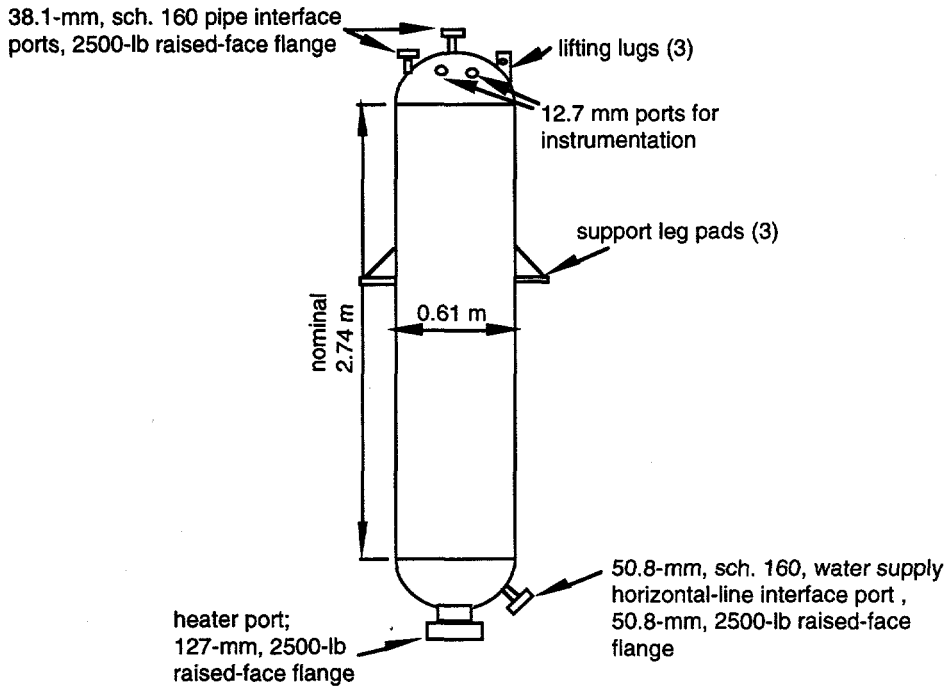

Figure 58. Blowdown vessel for Pressure Leak-Rate Test Facility.

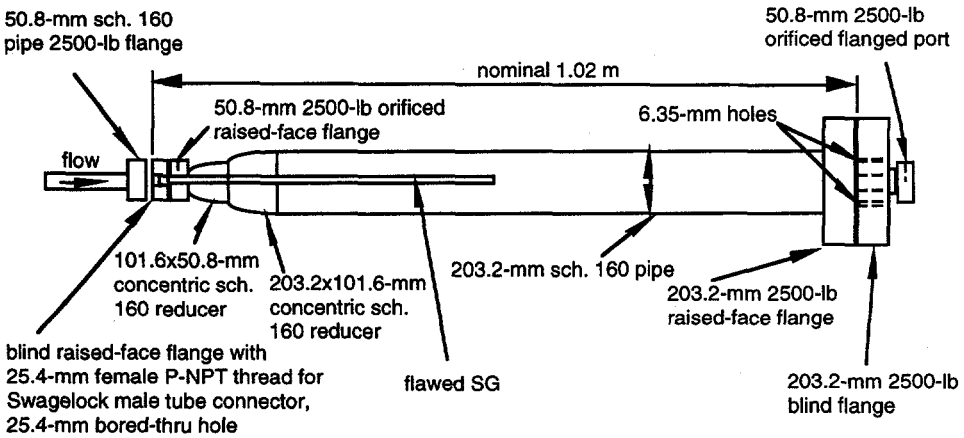

Figure 59. Specimen test module for Pressure Leak-Rate Test Facility.

will cause P2 to nearly equal P1. However, for cases where the flawed tube does not begin to leak until P1-P2 reaches much larger values, water from the pressurized blowdown tank is routed into the test module through a small line under control of Valve V5 at 4-8 L/min (1-2 gal/min) to preheat the test assembly. Valve V6 operates on this flow to regulate P2 or the differential pressure P1 - P2. When the flawed tube begins to leak in response to increasing P1-P2, Valve V6 maintains the desired pressure P2. When the tube leak becomes several times larger than the bleed flow from the blowdown vessel, the bleed flow can be turned off with Valve V5. The facility also allows the option to use gas pressurization of the test module in place of the blowdown vessel bleed to achieve pressurization prior to tube leak. However, this option does not achieve thermal conditioning of the components.

The back-pressure regulator Valve V6 will operate under changing fluid conditions during a test and has been selected because it can provide pressure control under these varying conditions. During the initial stages of the ramp-up of P1 - P2, Pressure P2 in the test module will be above the saturation pressure that corresponds to the water temperature supplied by the blowdown vessel, and the flawed tube will leak pressurized water into the test module. However, when Valve V6 reduces P2 below the saturation pressure, the water leaking from the crack will flash to steam, and Valve V6 will be controlling a steam flow. The facility is designed to accommodate tube leak rates as high as 760 L/min (200 gal/min) of water, which corresponds to 12.6 kg/s (100,000 lb/h) of steam. The 76-mm (3-in.) size of Valve V6 is adequate to pass this steam flow. During typical testing of a flawed tube, the progressive increase of P1 - P2 will cause the crack to gradually open and produce higher flow rates. Some tubes will also reach a point of unstable crack behavior; the tube will rupture and cause a rapid increase in flow rate. The facility is designed to yield information on Q and P1 - P2 for all of these leak regimes, provided $Q \leq 760$ L/min (200 gal/min), P1 - P2 ≤ 21 MPa (3000 psi), and the blowdown vessel has not been emptied. The following describes in more detail the conditions that exist during a test.

This discussion focuses primarily on a flawed tube with an initial throughwall crack. Figure 60 highlights the possible dependence during a test among the pressure P1 inside the flawed tube, the pressure P2 outside the tube, and the mass flow rate M through the crack.

At the beginning of the test depicted in Fig. 60, a flawed tube is in the test module and P2, under control of V6, is nearly equal to P1 (i.e., 21 MPa or 3000 psig), and the through wall flaw is leaking at a low level M. Under facility control (manual or computer) P2 is then reduced by V6 in short interval steps, the pressure differential across the tube P1 - P2 is increased, and the mass flow through the crack increases. At each level of P1 - P2, M is recorded. As P2 is decreased, a point is reached at which the pressure is equal to the saturation pressure for the water temperature supplied to the test, namely 343°C (650°F) for the case being discussed, and the water leak flashes to steam (i.e. P2 = Psat = 15.26 MPa [2,213 psi]). At this point, V6 senses steam and controls steam flow instead of water flow. With further reductions in P2 (or increases in P1 - P2), a point is reached, depending on crack morphology, where the crack flow may become choked. This behavior will be observed for a range of P2 as indicated by Lc in Fig. 60. In this range M is constant.

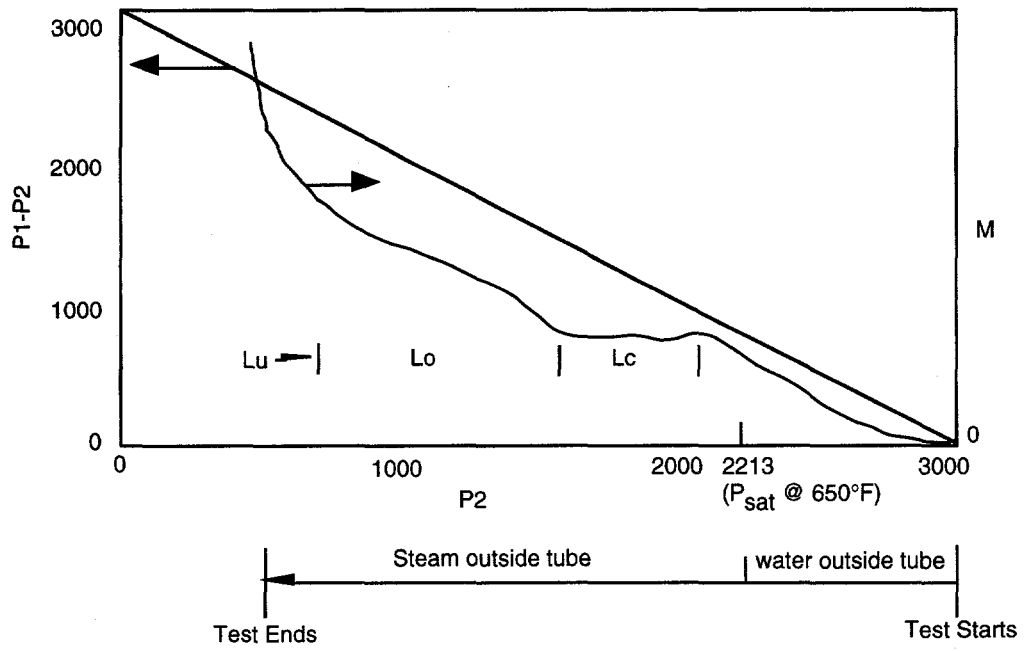

Figure 60. Possible dependence of pressure P1 inside the flawed tube, pressure P2 outside the tube, and mass flow rate M through the crack during a test in the Pressure Leak-Rate Test Facility.

However, as P1 - P2 is increased further, the crack will open up more, and its increasing area will permit a higher mass flow rate M, as shown in the range Lo. Finally, a point Lu is reached where the crack becomes unstable, and its flow area increases dramatically for only a small increase in pressure differential with a large increase in M. Shortly after crack instability, the test would be terminated. Depending on actual tube flaw morphology, a test may never reach point Lu or, for that matter, not even enter the range Lo, because the limit of the facility capability is P1 = 21 MPa (3000 psi). (The failure pressure of an unflawed steam generator tube is of order 63 MPa [9000 psi.])

The preceding discussion refers to a test on a specimen with a crack that is initially throughwall, with a leakage flow that can be controlled with valve V6 at the beginning of the test. For the cases where a throughwall crack is not present initially, Valve V6 can be used to control on a bleed flow that is routed by a small line and control Valve V5 into the test module space that surrounds the outside of the tube being tested. Valve V6 will control P2 by acting on this flow. Actually, the two initial leak cases are quite similar. For the second case, where the test starts with V6 controlling on bleed-line flow, V5 is set at a degree of opening that will give a choked-valve condition with a low flow rate, and V6 operates on the steam outside the tube to reduce P2. The mass flow at choked condition can be preset for a given test by varying the opening of V5.

The capability of controlling P2 with V6 is helped for both types of initial crack morphology by the fact that, for a given M, a large flow resistance (and frequently a choked condition) will exist upstream of V6 in the form of flow through the tube crack or through Valve V5. Hence, a significant pressure drop from the 21-MPa (3000-psi) level of the

blowdown vessel will occur upstream of V6, which reduces the pressure letdown burden on V6 and hence its tendency to choke. Furthermore, as will be discussed later, not only is the pressure upstream of V6 reduced, but this condition occurs at levels of M considerably below the 760 L/min (200 gal/min) level that is the upper boundary for the facility. It should also be noted that, when choking occurs, either at the tube crack or at V5, Valve V6 will be controlling steam flow.

Argonne National Laboratory has made preliminary estimates of the influence of crack morphology on P1 - P2 as a function of flow rate M for flow through an axial crack flaw in tubes of interest to the SG program. Circumferential cracks are also of interest but are not discussed here. This information has helped guide selection of V6, including making tradeoffs in capabilities to give the broadest capability to test a wide variety of flawed tubes. Two limiting-axial-crack-length cases have been identified. The first case is mandated by the facility pressurization limit of 21 MPa (3000 psi), which dictates that the smallest crack that can be driven to instability is ≈20 mm (0.8 in.) long. For this crack length, the flowrate at rupture will be 27 L/min (7 gal/min). The second limiting case is based on a maximum crack length of 64 mm (2.5 in.). For this case, P1 - P2 = 8 MPa (1200 psi) is required to drive the crack to instability, which will result in a flowrate of 380 L/min (100 gal/min). For both limiting cases, valve V6 will be controlling steam at the end of testing when the crack goes unstable. Many flawed tubes that will be tested will go through the entire step increase in pressure differential P1 - P2 from 0 to 21 MPa (3000 psi) with little crack opening and instability never being reached. These tubes will exhibit choked flow for almost the entire test, and only small flows M will exist.

A turbine flow meter FM2 is located just upstream of the test module to monitor the leak rate Q of the flawed tube as a function of P1 - P2. However, to provide a backup and cross check on this vital piece of information, two methods of measuring flow are available in this harsh operating environment. The facility utilizes continuous weighing of the water content of the blowdown vessel as a function of time during the ramping of P1 - P2 by including load cells in each of the three support legs of the vessel. The load cell data provides a second flow rate measurement and a check on turbine flow meter calibration. The accuracy of the flow rate determined from the weight change measurements is potentially greater than that from the turbine flow meter.

All signals for pressure, temperature, flow rate, electrical power for the heaters (for the blowdown vessel and trace heaters on various components), and control valve actuation will provide analog readouts at a master control panel that is shielded from the pressurized components of the facility (see Fig. 61). The shielding consists of stacked concrete slabs on three sides of the blowdown and test chamber vessels and associated piping. When the test system is at temperature and pressure, personnel will not be permitted inside this barrier. All measurement and control signals are also logged into a computerized data acquisition and control system located in an existing renovated air-conditioned control room.

Another important component of the blowdown facility is the muffled noise suppresser on the outside of the south wall of the laboratory space (Fig. 61). This device is designed to handle the maximum anticipated 12.6-kg/s (100,000-lb/h) steam flow from the test

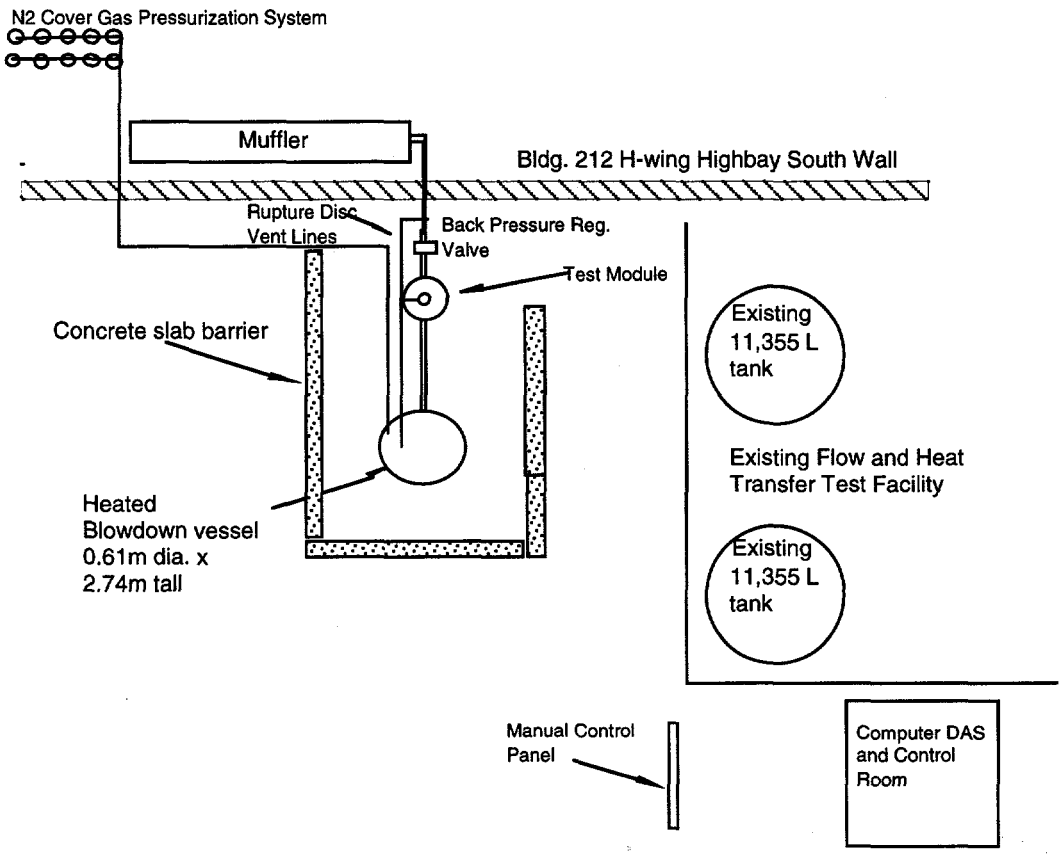

Figure 61. Floor layout of Pressure Leak-Rate Test Facility.

module, as well as possible tank overpressurization steam releases. The unit is 0.91 m (3 ft) in diam and 5.2 m (17 ft) long and is capable of 45-dB noise reduction. To accommodate the outside location of the muffler, a wall penetration for a 0.25-m (10-in.)-diam steam hookup pipe and a concrete base mat are provided. Because the back-pressure regulator Valve V6 and the leaking flawed tube in the test module are also noise sources for a range of the test conditions, they possibly will also require noise suppression.

Because of the elevated temperatures and the batch testing mode associated with recharging the blowdown vessel, thermal shock of the facility components is a design consideration. Thermal shock is minimized by carefully controlling the heatup rate for the blowdown vessel and by using electrical-heat-tape wrap and insulation on all piping and components. The slow bleed of heated water from the blowdown vessel prior to the ramp-up of pressure differential across the flawed tube also facilitates thermal conditioning of downstream components. Thermal expansion of components along the main flow path is accommodated by rigidly anchoring the piping at Valves V3 and V4 and allowing the components to move unconstrained in the axial direction by use of a thermal expansion joint. This expansion joint is at the other end of the flow path, in front of the noise suppressor, in the low-pressure zone.

4.4.2 General Facility Operation

The general philosophy of facility operation is to utilize manual control when bringing the facility to steady-state conditions for the beginning of a test and computer control for actual testing. During the setup period, readings of all instrumentation and the status of controlled hardware is displayed on a control panel on the outside of the protective barrier. All hardware will be controllable from the control panel. During the setup period, the computer will also log all instrumentation data and record controlled hardware configurations; they will display real-time plots of critical safety data and important thermal-hydraulic conditions for tracking the approach to steady state. The computer is a Power Macintosh™ 8500 that utilizes National Instruments Labview™ software, data acquisition, and control boards.

System setup under manual control includes configuring the facility for a particular test, attaining steady-state conditions associated with time zero of the test, and verifying that the computer software is properly configured for the transient portion of the test. Once these conditions are attained, as verified by the facility operator, the test will be switched to computer control, and the transient portion of the test will be initiated under computer control after a short stabilization period to eliminate any switching transients. Once under computer control, a test can terminate in several ways. The first of these is normal termination, in which the flawed tube progresses through stages of increasing leakage to crack instability and tube rupture, with a corresponding rapid increase in leak rate. However, it may be necessary to terminate a test before specimen rupture because the blowdown vessel is low on water, the back-pressure regulator valve fails to stabilize as it is changed under computer control, or the desired ramping of the pressure differential across the cracked tube cannot be achieved for any reason. Finally, the operator can manually override and terminate the test at any time because of safety concerns or any other reason.

The following describes, in detail, a facility operation scenario.

Setup stage (manual control)

(1) Approximately 760 L (200 gal) of room-temperature, conditioned, deionized water are pumped from the 3030-L (800-gal) storage tank to the blowdown vessel to charge it while Valves V1, V2, and V3 are open. Valves V4 and V5 are closed.

(2) Valves V1, V2, and V3 are closed.

(3) Heat-wrap tapes on all downstream piping and components are turned on to bring the structures to the desired operating temperature.

(4) The pressure of the blowdown-vessel cover gas is set to a value slightly above the saturation pressure associated with the desired tank water temperature to prevent boiling during heatup.

(5) The blowdown vessel electrical heater is turned on and the water is brought to temperature at a rate sufficiently low to minimize thermal stressing of the vessel.

(6) When the blowdown vessel has stabilized at the desired operating temperature, the heater is turned off and the pressure of the cover gas is raised to the desired operating value, not to exceed 21 MPa (3000 psi).

(7) The back-pressure regulator Valve V6 is fully closed.

(8) Valve V5 on the bleed line of the blowdown tank is opened slightly.

(9) Valve V3 is opened full and then V4 is slowly opened full.

(10) The flow through the bleed line is set at 4–8 L/min (1–2 gal/min) as it is monitored by flow meter FM3. This may require a slight opening of Valve V6 to facilitate conditioning of downstream components and to provide flow on which Valve V6 can operate. With this valve configuration, the differential pressure P1 - P2 should be near zero.

(11) The system is held in this configuration for several minutes to achieve equilibration.

(12) The computer data acquisition system is readied to acquire flow rate Q, P1 - P2, and other measured quantities vs. time.

Transient stage (computer control)

(13) Back-pressure regulator Valve V6 is put under either computer control or under control of the vendor-supplied valve control module, after ensuring that the initial state of the valve is set in accordance with Step 7 or 10.

(14) Valve V6 is activated for transient control and P1 - P2 is ramped up stepwise to increase the pressure differential across the flawed tube and possibly cause the flaw to progressively open and rupture.

(15) The test is terminated when a tube ruptures or the water level in the blowdown tank becomes too low to continue the test.

(16) All water control valves are shut, the trace heaters are turned off, and the blowdown-vessel cover gas pressure is reduced to just above the saturation pressure of the remaining water, to allow for slow cooldown of the vessel.

4.4.3 Program Status

The design of the Pressure Leak-Rate Test Facility has been completed, and technical specifications for all components have been formulated. A formal ANL safety review of the facility has been conducted, and approval has been granted for facility construction. Purchase order contracts have been issued for all components, instrumentation, and controls. Modifications to the laboratory area are completed, i.e., the required electrical service, blowdown vessel floor load dispersion plates, and concrete pads/wall penetrations for the outside muffler have been installed. An existing computer control room has also been upgraded and a new computer installed.

All procurements have been delivered except for the pressure vessels and the gas pressurization system, which have a long lead time (16–20 weeks) and are currently being manufactured. Installation of instrumentation and control cabinets is ≈60% completed, and the steam muffler has been installed. Upon arrival of the pressure vessels, all hardware installation will be completed and facility shakedown testing will start.

4.5 High-Pressure Test Facility

Steam generator tubes are currently designed with a stress factor of 3 on normal operating condition loadings and/or a factor of 1.4 on postulated design basis accident conditions (e.g., MSLB). As a part of the current experimental program on tube integrity, it is of interest to verify these design margins and to determine flow rates through subcritical throughwall cracks at high pressures. For this reason, a tube-rupture and leak-rate test facility will be constructed to perform tests at pressures up to 52 MPa (7,500 psi) and flow rates up to 45.4 L/min (12 gal/min).

4.5.1 Facility Description and Status

As will be discussed in Section 4.7.1 ("Design Analysis of the Tube Failure Facility"), the critical lengths for throughwall cracks at pressures greater than the 21-MPa (3,000-psi) capability of the Pressure and Leak-Rate Test Facility (see Section 4.4) are rather short, and the corresponding leak rates are relatively small. Therefore, the required maximum flow rate for the high-pressure tube-rupture and leak-rate test facility is only ≈45 L/min (12 gal/min) in order to maintain flow through a subcritical leaking crack and drive it to instability. Ideally, one would like to be able to conduct these high-pressure tests at the nominal SG operating temperature of 300°C (572°F) with superheated water as the fluid. However, we determined that the design and construction of such a facility was impractical and instead opted for room-temperature operation with water as the pressurizing fluid.

The design of the high-pressure test facility is shown schematically in Fig. 62. One of the two key components in the system is the high-pressure positive-displacement triplex pump, which is used to supply water at pressures up to 42 Mpa (7,500 psi) and a fixed flow rate of 45.4 L/min (12 gal/min). The second key component is the test control valve that is used to apportion the flow from the pump either to the specimen or around the bypass loop. The water supply for the system is contained in a 150-L (40-gal) tank, and the internal pressure of the specimen is monitored by a pressure transducer.

The operation of the facility can be illustrated by considering a test on a specimen that initially contains a short nonthroughwall flaw. The test begins with the specimen at zero internal pressure and all of the flow from the pump diverted through the bypass loop. The specimen pressure is gradually ramped up by intermittently directing small amounts of pressurized water to the specimen. At some point, the preexisting flaw may "pop through" the wall without initially becoming unstable. The valve will automatically direct more of the flow through the specimen to maintain the desired internal pressure of the specimen while simultaneously maintaining flow through this subcritical leaking crack. The internal pressure of the specimen can then continue to be ramped upward with the test control valve until unstable rupture of the specimen occurs.

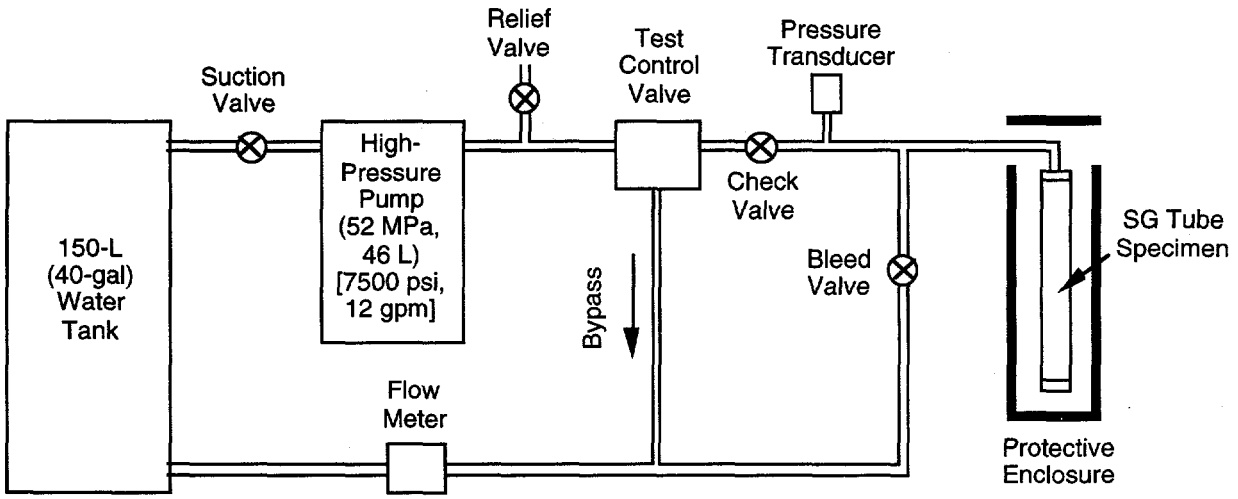

Figure 62. Schematic diagram of high-pressure tube-rupture and leak-rate test facility.

The high-pressure pump, test control valve, and 150-L (40-gal) water tank have been acquired as a skid-mounted "hydro-laser" unit that is used commercially for high-pressure cleaning and paint-removal operations. The remaining components have not yet been acquired. Progress on this facility has been delayed to divert effort to the construction and operation of the high-temperature severe accident test facility, which has been assigned higher priority.

4.6 High-Temperature (Severe-Accident) Test Facility

The Pressure and Leak-Rate Test Facility will be used to determine the rupture behavior and leak rates of flawed tubes under more or less prototypical SG operating conditions ($T \leq 343°C$ [650°F], $p \leq 21$ MPa [3000 psi]). However, the failure pressures of flawed and unflawed tubes at very high temperatures under severe accident conditions are also of interest.

Several hypothetical core-melt-accident scenarios could lead to high-temperature coolant boiloff and the potential for tube rupture at very high temperatures. Of these, the station blackout scenario, with failed auxiliary feedwater and loss of secondary-side integrity, presents one of the most severe challenges to the SG tubes. Under this scenario, the tubes would be exposed to superheated steam from the core in combination with high pressure gradients across the tube wall; hence multiple tube failure, particularly of tubes that contain preexisting flaws, must be considered. A high-temperature facility to determine the failure pressures of unflawed and flawed tubes at very high temperatures has, therefore, been constructed as part of the present program.

4.6.1 Facility Description

A schematic drawing of the high-temperature severe accident test facility is shown in Fig. 63. In simplest terms, it consists of a furnace into which is placed a length of SG tube that is closed off at one end and connected to a high-pressure nitrogen gas bottle through

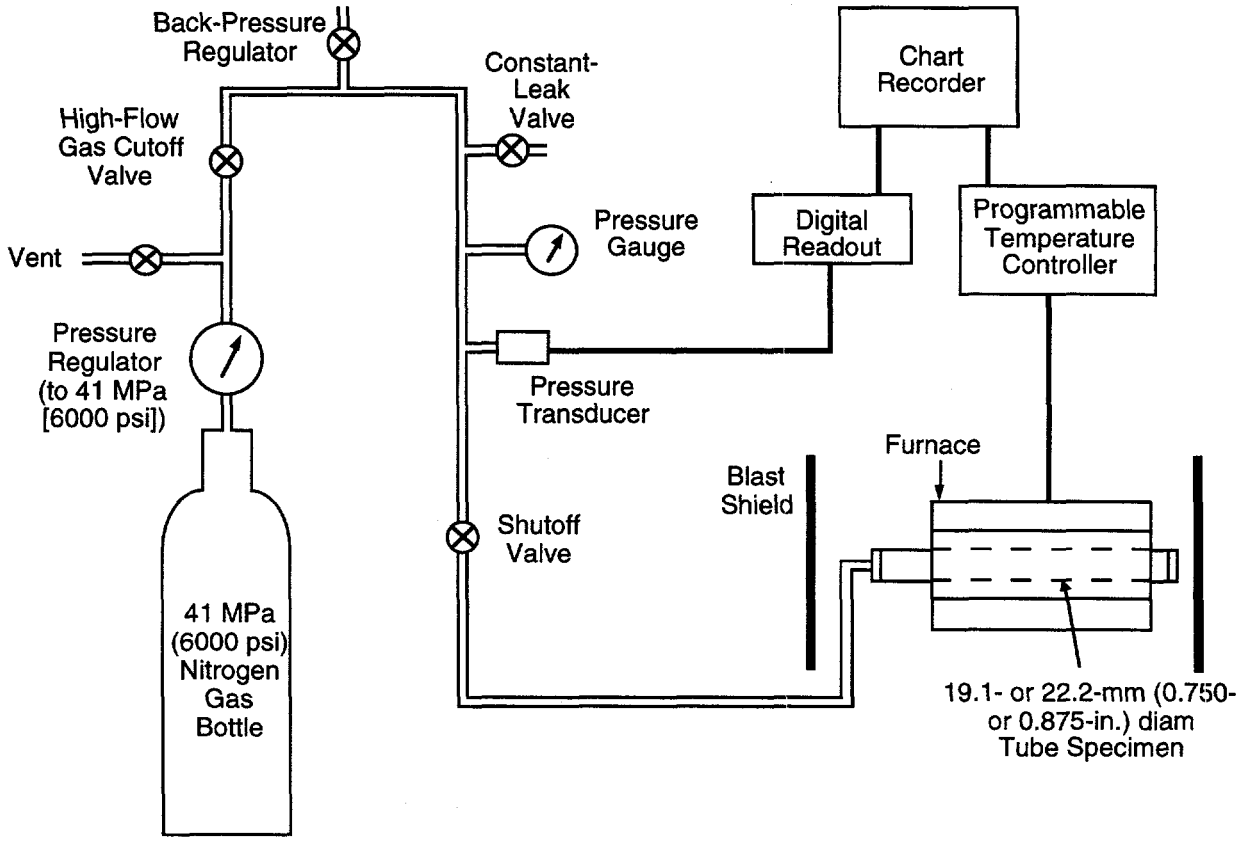

Figure 63. Schematic diagram of high-temperature (severe-accident) tube-rupture facility.

suitable valving at the other end. During a test, the specimen is first stabilized at a nominal SG operating temperature of 300°C (572°F) and a fixed internal pressure. Then, the temperature is ramped up at a predetermined rate until specimen failure occurs.

Constant pressure is maintained during the test by a back-pressure regulator, and the pressure is monitored by a pressure transducer. A constant-leak valve is installed in a position behind the back-pressure regulator as an alternate means of gas pressure control in combination with the pressure regulator on the gas cylinder. A high-flow cutoff valve is also installed in the gas line to automatically stop the flow of nitrogen under high-flow tube-failure conditions. This prevents emptying of the gas bottle when specimen failure occurs during unattended long-term tests. The temperature of the furnace and specimen is controlled with a programmable temperature controller, and both the pressure and temperature outputs are recorded.

The test specimen is ≈0.45 m (18 in.) long, and the furnace is ≈0.33 m (13 in.) long with a uniform temperature zone ≈80 mm (3 in.) long near the center. Welded end plugs close each end of the specimen, and these end plugs are outside of the furnace during testing to avoid failure at the welds. A tapped hole in one end plug permits connection to the gas pressurization system, and a solid mandrel inside the specimen displaces most of the pressurized gas volume to reduce stored energy. The furnace is fitted with heavy-

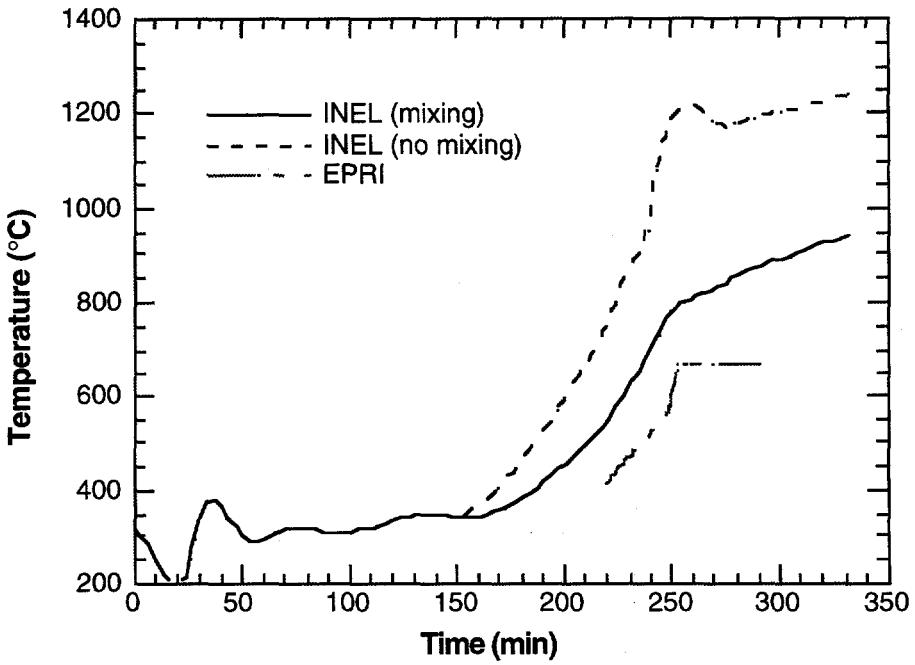

Figure 64. Calculated temperatures of SG tube inlet under hypothesized station blackout core melt conditions, with loss of feedwater and secondary-side depressurization.

metal-plate blast shields at each end to contain any projectiles that may be produced during a tube failure, and the furnace is also fitted with a heavy-wall SS tube to prevent projectile damage to the furnace elements.

4.6.2 Severe-Accident Test Conditions

A detailed analysis of the behavior of the Surry nuclear power plant has been carried out by INEL for several hypothetical core melt scenarios. One of the analyzed scenarios is a total station blackout with a stuck-open SG secondary-side atmospheric dump valve, which results in loss of feedwater and secondary-side depressurization.[19] In this analysis, the temperature histories were calculated with the SCDAP/RELAP5 code for several critical components, including the pressurizer surge line nozzle and the SG tubes at the inlet. Plots of the calculated tube inlet temperatures are shown in Fig. 64, with tube inlet temperature histories shown for the case of complete coolant mixing and for no mixing. Data are needed to characterize tube rupture-behavior under these severe-accident conditions and to determine if the rupture temperatures and pressures can be analytically predicted. Most analysts now feel that the complete mixing case provides the better approximation of actual tube temperatures, and the severe-accident tube rupture tests described in Section 4.7.6 use the INEL mixing case (solid curve in Fig. 64) for one of the temperature histories.

Similar analyses were performed under EPRI sponsorship for a generalized "Zionlike" PWR with the MAAP 4.0.2 computer code.[20] Again, the analyses assumed station blackout conditions with loss of primary feedwater and secondary-side depressurization. These

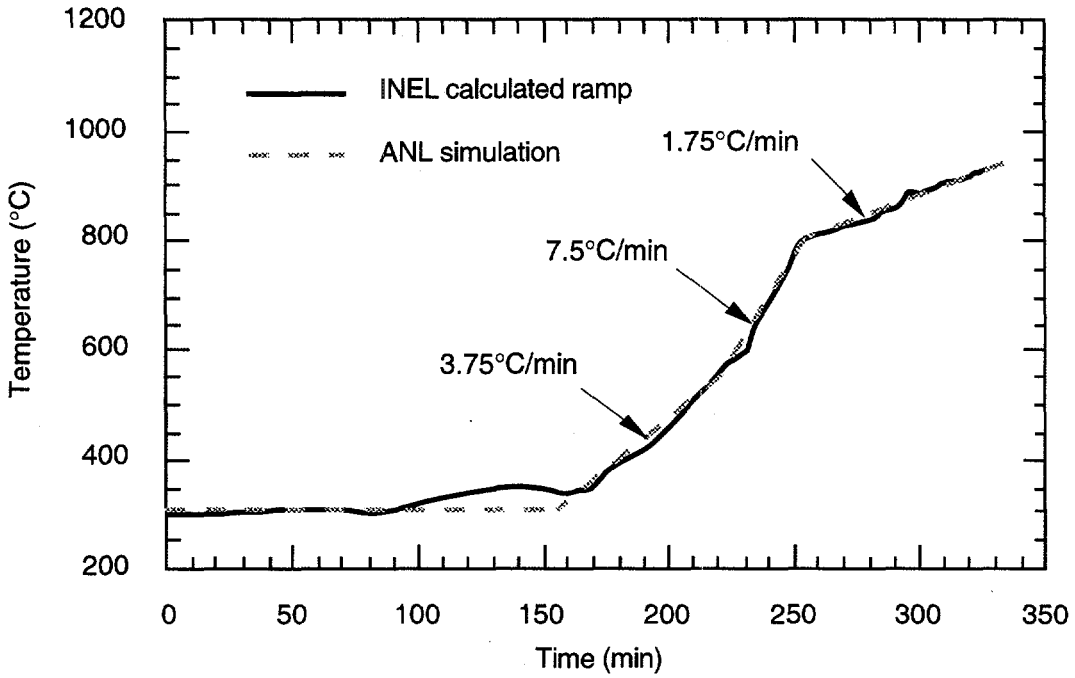

Figure 65. INEL-calculated severe-accident temperature ramp and simulated ramp used in ANL severe-accident tube-rupture tests.

analyses, which calculated the temperature history for the hottest tubes (near the tubesheet on the inlet side), are also shown in Fig. 64. The peak temperature was calculated to be ≈667°C (1230°F) for an assumed primary-to-secondary leak rate of 380 L/min (100 gal/min). The predicted peak tube temperature varied somewhat with leak rate, from 662°C (1224°F) for a zero leak rate to 687°C for a leak rate of 760 L/min (200 gal/min). The analysis predicted rupture of the SG hot-leg nozzle ≈6 min after the SG tubes reached peak temperature; the temperature history in the absence of nozzle failure beyond this point was not calculated.

Both the INEL- and EPRI-calculated temperature ramps shown in Fig. 64 were used in the ANL severe-accident tests described in Section 4.7.6, because these two ramps were felt to bound the conditions expected in an actual severe accident. The mixing-case INEL ramp of Fig. 64 was simulated as a series of linear segments as shown in Fig. 65. In this sequence, the temperature was first stabilized at 300°C (572°F). It was then ramped to 550°C (288°C) at a rate of 3.75°C/min (6.75°F/min), followed by ramping to 800°C (1472°F) at 7.50°C/min (13.5°F/min), and then to specimen failure at a rate of 1.75°C/min (3.15°F/min). As indicated in Fig. 65, this ramp provides as good simulation of the actual INEL ramp, particularly for temperatures above 400°C (750°F), at which measurable creep damage may occur.

The ANL simulation of the EPRI ramp is shown in Fig. 66. In this simulation, the specimen was stabilized at 300°C (572°F), as for the INEL simulation, ramped to 564°C (1047°F) at a rate of 5.37°C/min (9.67°F/min), then to 582°C (1080°F) at 10.6°C/min (19/.1°F/min), to 630°C (1166°F) at 28.24°C/min (50.83°F/min), and to 667°C (1233°F) at 14.80°C/min (26.64°F/min). The calculated temperature history indicates a dropoff in

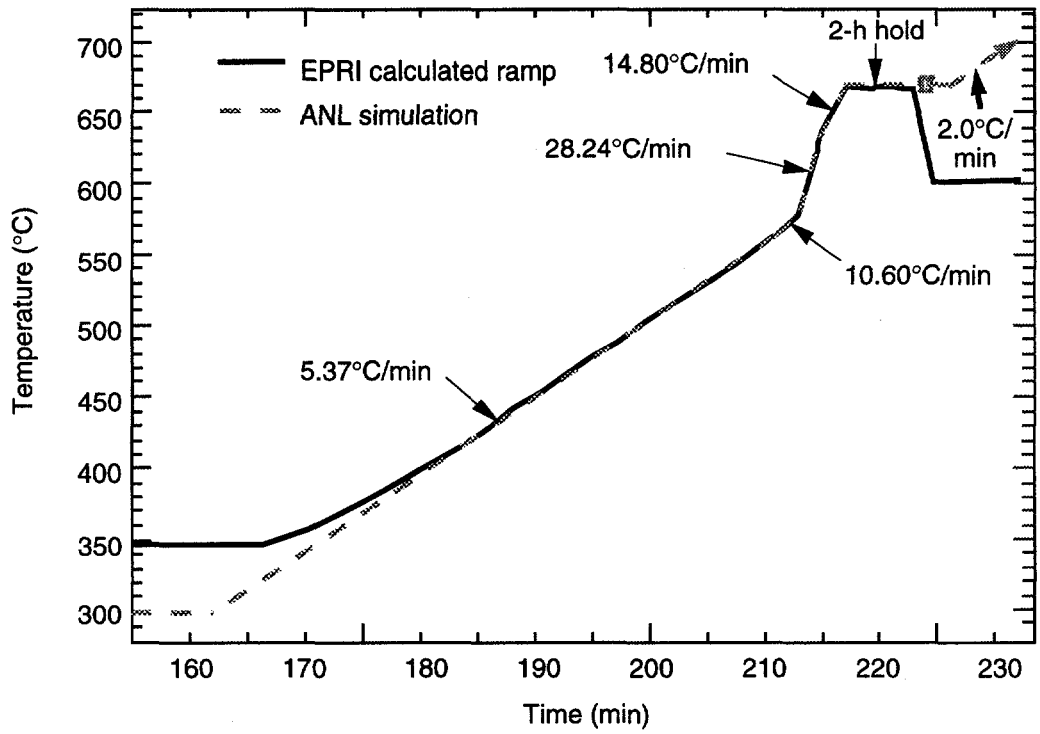

Figure 66. EPRI-calculated severe-accident temperature ramp and simulated ramp simulation used in ANL severe-accident tube-rupture tests. In the ANL simulation, the temperature is held constant at 670°C (1240°F) after ≈217 min rather than following the subsequent drop shown in the calculated curve.

temperature after ≈223 min, corresponding to a predicted rupture of the SG hot leg nozzle. Because the present tests are concerned only with the behavior of the tubes, this event was ignored, and the temperature was, instead, held at 667°C (1233°F). For some of the planned tests, failure was not expected within reasonable times at 667°C (1233°F), and the tests were ramped to failure at a rate of 2°C/min (3.6°F/min) after a 2-h hold time at 667°C (1233°F).

4.6.3 Facility Checkout

The design and construction of the high-temperature severe-accident test facility have been completed, and temperature measurements have been conducted on an instrumented dummy specimen to determine the temperature profiles along the length and through the thickness of the specimen. Under isothermal conditions at 700°C (1400°F), the temperature along the length of the specimen was found to vary ≈6°C (11°F) over a 50-mm (2-in.)-long central portion that corresponds to the maximum flaw length to be tested. During a 400°C/h (720°F/h) constant-temperature ramp, the temperature gradient through the thickness was ≈8°C (14°F), with the temperature of the inner surface being lower, as expected.

Temperature profile tests were subsequently conducted on a dummy specimen using the simulated INEL temperature ramp of Fig. 65. The programming of the temperature controller was adjusted to optimize the temperature response of the specimen, and minor

modifications were made to thermocouple placement and specimen positioning in the furnace. Because of these changes, the temperature of the specimen followed the desired temperature ramp very closely, and the temperature gradient over the central 51 mm (2 in.) of the specimen was reduced to ≈4°C (7°F). The temperature gradient through the specimen thickness was ≈6°C (11°F) during the 7.50°C/min (13.5°F/min) ramp rate, and less for the slower rates.

Finally, a temperature profile test was conducted with the EPRI temperature ramp shown in Fig. 66. The temperature of the specimen followed the desired temperature history very closely during the initial ramp rate of 5.37°C/min (9.7°F/min). However, because of thermal-inertia effects, the specimen could not precisely follow the subsequent higher rate ramps of 10.60, 28.24, and 14.80°C/min (19.1, 40.0, and 26.6°F/min) indicated in Fig. 66. Instead, the specimen heated up at an approximately uniform rate of ≈16-18°C/min (29-32°F/min) over this temperature interval. This rate compares favorably with the average desired heating rate of 17.3°C/min (31.1°F/min) for these three ramp steps. The temperature overshoot at the end of the last ramp step (at 667°C [1233°F]) was ≈8°C (14°F), and the temperature gradient through the thickness of the specimen did not exceed 10°C (18°F) during the fastest ramp.

4.7 Modeling of Crack Behavior

4.7.1 Design Analysis of Pressure and Leak-Rate Test Facility

The Pressure and Leak-Rate Test Facility (Section 4.4) was designed for the study of leakage and failure behavior under normal and design basis accident conditions. To ensure that the flow capacity of the facility is adequate, analytical models were used to estimate critical crack sizes, leak-before-rupture behavior, and expected leak rates for axial and circumferential cracks of various lengths and depths.

The critical pressures and crack sizes for unstable fracture (rupture) of a thin-wall, internally pressurized, cylindrical shell with a throughwall axial crack can be estimated by using the equation

$$p_{cr} = \frac{\bar{\sigma}h}{mR_m} = \frac{p_b}{m}, \tag{30}$$

originally proposed by Hahn et al.[21], where

$$\bar{\sigma} = 0.5(\sigma_y + \sigma_u),$$

$$m = 0.614 + 0.481\lambda + 0.386\exp(-1.25\lambda),$$

$$\lambda = \left[12(1-\nu^2)\right]^{\frac{1}{4}} \frac{c}{\sqrt{R_m h}} = \frac{1.82c}{\sqrt{R_m h}},$$

$$p_b = \frac{\bar{\sigma}h}{R_m} = \text{burst pressure of a virgin tube},$$

R_m and h = mean radius and wall thickness of tube, respectively,

2c = axial crack length,

and

σ_y and σ_u are the yield and ultimate tensile strengths, respectively.

For partthrough axial cracks, the pressure required to rupture the remaining ligament can be calculated with an equation reported by Kiefner et al.[22] (referred to as the BCL equation),

$$p_{sc} = \frac{\bar{\sigma}h}{m_p R_m} = \frac{p_b}{m_p}, \tag{31a}$$

where

$$m_p = \frac{1 - \frac{a}{mh}}{1 - \frac{a}{h}} \tag{31b}$$

and

a = axial crack depth.

It should be emphasized that Eq. 31a gives only the pressure required to produce failure of the remaining ligament. The stability of the resulting throughwall crack can be analyzed by using Eq. 30. If $p_{cr} > p_{sc}$, the throughwall crack is stable. Although the crack will leak, it will not increase in length without a further increase in pressure. If $p_{cr} < p_{sc}$, the resulting crack will be unstable and rapidly increase in length without any additional increase in pressure.

The pressures required to produce failure of a flawed tube were calculated for axial cracks of various dimensions in an internally pressurized tube with an OD of 22 mm (0.875 in.) and a wall thickness of 1.3 mm (0.05 in.). They are plotted in Fig. 67 as a function of crack length for various crack depth to wall thickness (a/h) ratios. The assumed elastic modulus E of 193 GPa (28 x 10^3 ksi) and flow stress σ (flow) of 500 MPa (73 ksi) correspond to the values for mill-annealed Alloy 600 at 288°C (550°F). Short, deep non-throughwall cracks will first break the remaining ligament and go through the wall; a significant pressure increase beyond that necessary to drive them throughwall is required to make them grow in length. For example, a 12.7-mm (0.5-in.) crack with a/h = 0.9 (90% throughwall) will grow throughwall and begin to leak at ≈11 MPa (1.6 ksi). As the pressure is increased from 11 to 30 MPa (1.6 to 4.4 ksi), the crack will open more and leakage will increase, but the crack will not grow in length until the pressure reaches ≈30 MPa (4.4 ksi). At this pressure the crack can grow unstably in length, i.e., "rupture." To make the tube "rupture," the test system must be able to achieve a pressure of 30 MPa (4.4 ksi)

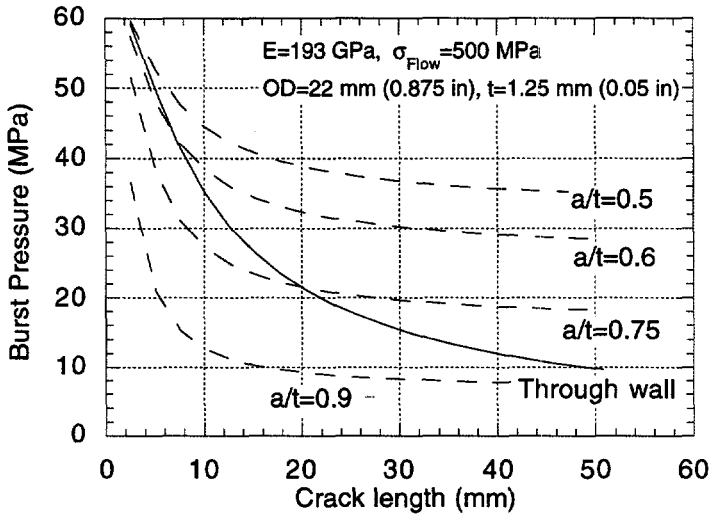

Figure 67. Pressures required for failure of axial cracks. Failure loci that lie above the curve for throughwall cracks correspond to unstable failures ("ruptures"). Failure loci that lie below the curve for throughwall cracks correspond to failure by stable leaks. The resultant throughwall cracks become unstable only after the pressure increases to that required for instability of the throughwall crack.

while the crack is leaking. The initial flow when the crack first goes through the wall (11 MPa or 1.6 ksi) will be ≈3.8 L/min (1 gal/min) (see below). Immediately before instability (30 MPa or 4.4 ksi), the flow through a 12.7-mm (0.5-in.) crack is about 19 L/min (5 gal/min). The total volume of flow necessary depends upon the time required to increase the pressure from 11 to 30 MPa (1.6 to 4.4 ksi).

Shallower, longer cracks will actually rupture without significant prior leakage because they will not break through and leak until the pressure is much higher than that required to cause a throughwall crack of the same length to extend unstably. For example, a 25.4-mm (1-in.) crack with a/h = 0.5 will not leak until p ≈ 37 MPa (5.4 ksi). However, once the remaining ligament tears and the crack extends throughwall, the pressure is well above that required to extend a throughwall 25.4-mm (1-in.) crack, i.e., ≈18 MPa (2.6 ksi).

Under normal operating conditions the pressure across the tube, Δp_{no}, is ≈9 MPa (1.3 ksi); under an MSLB in which the secondary side has dropped to atmospheric pressure the pressure across the tube Δp_{MSLB} is ≈18 MPa (2.6 ksi). These values are also indicated in Fig. 67. Degraded tubes must actually be capable of withstanding $3 \cdot \Delta p_{no}$ ≈27 MPa (3.9 ksi) and $1.4 \cdot \Delta p_{MSLB}$ ≈ 25 MPa (3.7 ksi) to meet requirements for continued operation. An unflawed tube will fail at ≈ 65 MPa (9.4 ksi). Cracks <≈15 mm (0.6 in.) long will never become unstable under any normal or design basis accident scenario. For cracks less than ≈ 51 mm (2 in.) long, only deep cracks (>75% throughwall) would break through and leak

under an MSLB. Throughwall cracks longer than ≈56 mm (2.2 in.) would be unstable even under normal operating pressures.

To obtain estimates of the leak rate through a crack, the area (A) of the crack opening was calculated from Equation 32 proposed by Kastner et al.,[23] which was derived by integrating the equation for elastic crack opening displacement corrected for plasticity by an Irwin-type correction factor (small-scale yielding).

$$A = \frac{32}{3}\frac{K_1}{E\sqrt{2\pi}}\left[(c + r_{pl})^{3/2} - r_{pl}^{3/2}\right]\alpha(\lambda), \tag{32}$$

where

$$r_{pl} = \frac{1}{2\pi}\left(\frac{K_1}{\bar{\sigma}}\right)^2,$$

K_1 = elastic stress intensity factor,

E= Young's modulus,

and

$$\alpha(\lambda) = 1 + 0.1\lambda + 0.16\lambda^2.$$

Crack opening areas calculated using Eq. (32) are close to those calculated by elastic-plastic fracture mechanics equations as long as the bulk of the tube remains elastic at failure. The crack opening area and the pressure difference across the tube at the onset of instability are shown in Fig. 68 as a function of crack length.

For room–temperature, single–phase flows, the flow rate Q through the crack can be estimated as

$$Q = KA\sqrt{2\frac{\Delta p}{\rho}}, \tag{33}$$

where K is a nondimensional constant, A is the crack opening area, Δp is the pressure gradient, and ρ is the fluid density. A review of the literature[24] suggests that K ≈ 0.5 for cracks in tubing. Single–phase flow rates should bound the flow rates for the two–phase flows that will occur at higher temperatures. Two–phase flow calculations are complex, but only rough estimates are needed to estimate the required capacity of the test system. The simplest approximation is to take $\Delta p = \Delta p_{eff} \approx p - p_{sat}$, rather than taking the full pressure drop, where p_{sat} is the saturation pressure at the temperature of interest (at 290°C or 550°F, p_{sat} = 7 MPa or 1 ksi). The estimated flow rate as a function of pressure for an axial crack at the onset of crack instability is shown in Fig. 69. If the test system pressure-vs.-flow characteristic lies above this curve, one can conduct a pressurization test that will determine not only the pressure that produces leakage but also the pressure required to

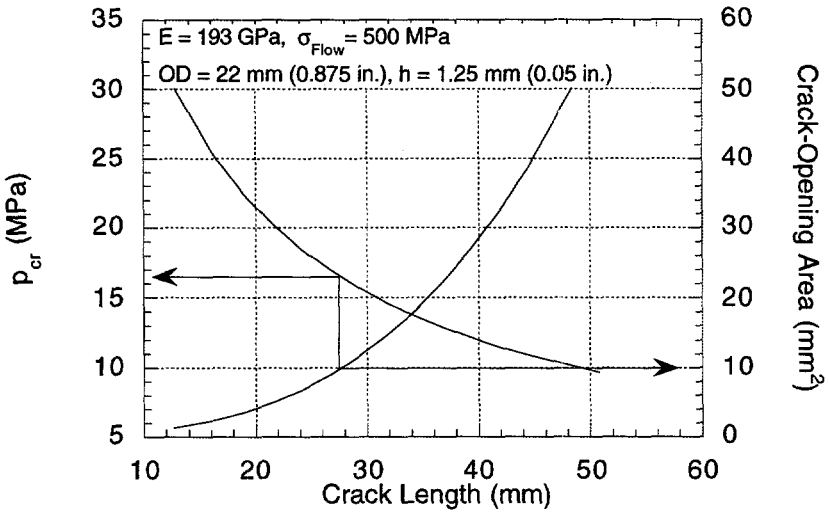

Figure 68. Pressure necessary for crack instability and crack-opening area as a function of crack length at the onset of instability for an axial throughwall crack.

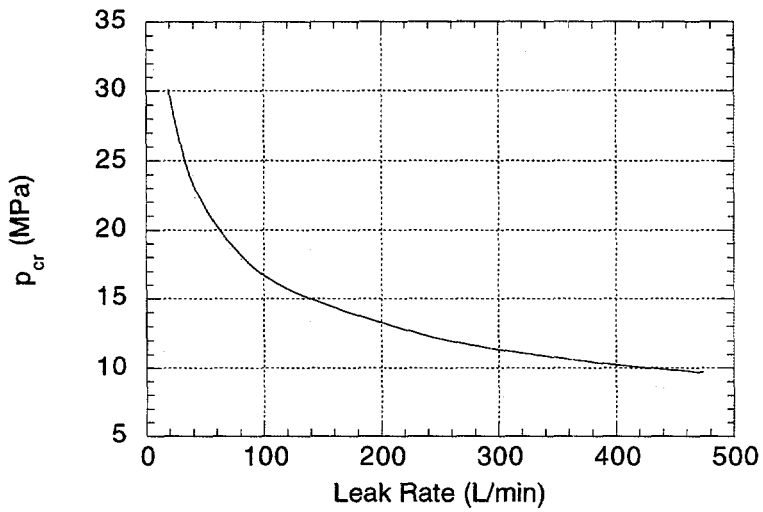

Figure 69. Flow rate as a function of pressure at onset of instability for an axial crack.

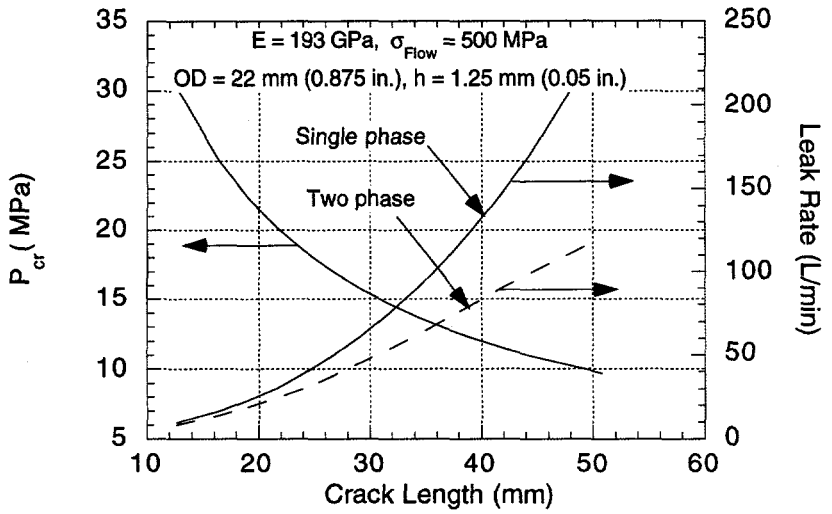

Figure 70. Pressure at crack instability and associated leak rate as a function of crack length for an axial crack.

make the crack grow unstably. The flow rate at which the system characteristic intersects this pressure-vs.-flow characteristic will determine the maximum crack length for which a test to instability can be run.

The maximum flow through the crack and maximum pressure that the tube can withstand without the crack becoming unstable and growing rapidly are shown in Fig. 70 as a function of crack length. Once the crack becomes unstable, it is impossible to predict the leak area, and the resultant flow rates could be close to those for a double ended rupture, i.e., ≈1720 and 2460 L/min (455 and 650 gal/min), respectively, for 19 and 22 mm [0.75 and 0.875 in.] OD tubing). Because cracks longer than ≈56 mm (2.2 in.) would be unstable under normal operating conditions, the maximum flow rate through any stable crack will be ≈300 L/min (80 gal/min) under single-phase flow.

For a given crack length and a pressure less than the critical pressure for crack instability p_{cr}, the flow through the crack will scale roughly like $Q_{max}\cdot(p/p_{cr})^{1.5}$. This can used to estimate the total volume of flow G in a pressure test before the crack becomes unstable in the following equation:

$$G = \frac{Q_{max} t_R}{2.5(1-\alpha)}\left(1-\alpha^{2.5}\right) \qquad (34)$$

where $\alpha = p_l/p_{cr}$ and p_l is the pressure at which the crack first begins to leak, and t_R is the time required to increase the pressure from p_l to p_{cr}, assuming that the pressure increases linearly with time. For a throughwall crack p_l, $\alpha = 0$.

4.7.2 Failure of Tubes with Circumferential Cracks

Although the open literature contains many models and much experimental data on the rupture of SG tubing with axial flaws, the literature on the problem of circumferential cracks in tubing is much more limited. Much has also been written on the failure of piping; however, piping is subjected primarily to bending loads and most of the available test data are for the case of large bending loads. Failure loads for tubing with circumferential cracks can be calculated by using plastic limit load analyses described by Ranganath et al.[25] who based their analyses on earlier work reported by Kanninen et al.[26] If bending is negligible, i.e., the tube is free to deflect in the transverse direction, the failure pressure for a tube with a circumferential throughwall crack of angular length 2θ is

$$p_{cr} = \frac{2\bar{\sigma}h}{R_m}\left(1 - \frac{\theta}{\pi} - \frac{2\beta}{\pi}\right), \tag{35a}$$

where

$$\beta = \sin^{-1}\left(\frac{\sin\theta}{2}\right). \tag{35b}$$

Limit load analyses have also been proposed for part-through circumferential cracks. The analysis of Kurihara et al.[27] uses an empirical correction to account for the difference in stress level between the remaining ligament of the part-through crack and the remainder of the pipe cross section. For the free bending case, an equation for the pressure required to rupture the remaining ligament of a part-through circumferential crack of depth a, is

$$\frac{p_{sc}}{p_b} = \frac{4\gamma}{\pi}\left[\frac{\pi}{2} + \frac{\theta\left(1 - \frac{a}{h} - \gamma\right)}{2\gamma} - \beta\right], \tag{36a}$$

where

$$\beta = \sin^{-1}\left[\frac{\left(\gamma + \frac{a}{h} - 1\right)\sin\theta}{2\gamma}\right] \tag{36b}$$

and

$$\gamma = 1 - \left(\frac{a}{h}\right)^{\kappa}\left(\frac{\theta}{\pi}\right)^{\mu} \tag{36c}$$

Based on comparisons with pipe tests, values for κ and μ of 2.0 and 0.2, respectively, have been suggested.

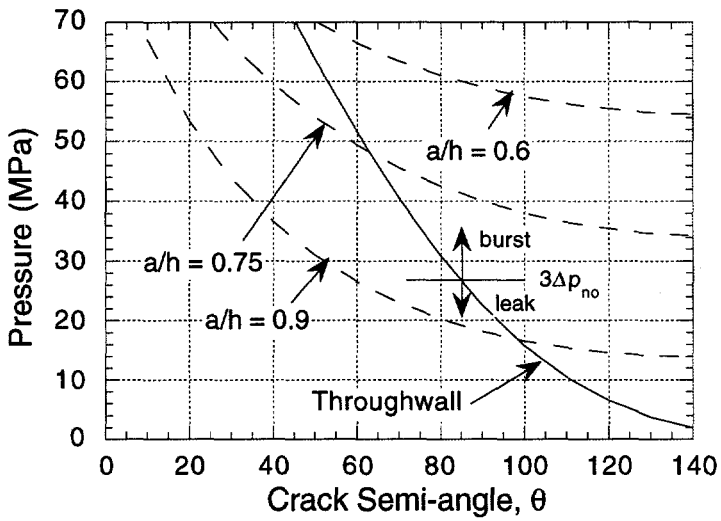

Figure 71. Pressure above which a circumferential crack becomes unstable vs. crack semi-angle for various values of the crack-depth-to-tube-wall-thickness ratios (a/h). A free-bending tube with an OD of 22.23 mm (0.875 in.) and a wall thickness of 1.3 mm (0.05 in.) is assumed.

The stability of circumferential cracks (free-bending) was also analyzed with Eqs. 35a and 36a, and the results are shown in Fig. 71. Because the axial stress in an internally pressurized tube is only one half as large as the circumferential stress, only deep, rather long, circumferential cracks will leak before the tube would fail because of axial stresses even without an axial crack. Even a crack which subtends $2\theta = 90°$ and is 90% throughwall will not leak at $3{\cdot}\Delta p_{no}$.

Free bending is one limiting failure mode for circumferentially cracked tubing. If the lateral deflection of the tube is completely restrained and the tube deforms only axially, another limiting failure occurs. In this case, for the throughwall crack,

$$p_{cr} = \frac{2\bar{\sigma}h}{R_m}\left(1 - \frac{\theta}{\pi}\right). \qquad (36d)$$

It appears that, in most cases, there is sufficient lateral constraint (e.g., by tube support plate) that the failure pressures are much closer to those predicted by Eq. 36d than the pressures predicted for the free bending case. Finite-element analyses are being conducted to verify these results and more accurately characterize the effects of lateral constraint on the failure pressure as well as crack opening area.

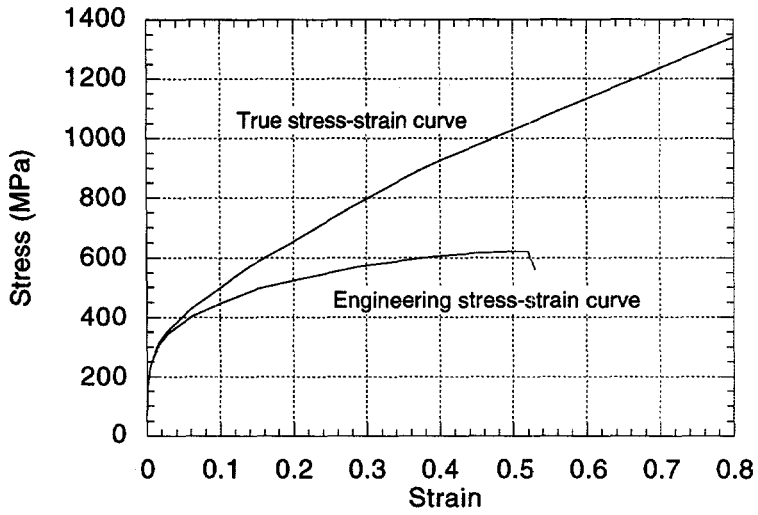

Figure 72. Engineering and true stress/strain curves for Alloy 600 at 288°C.

4.7.2.1 Effects of Lateral Constraint on the Failure Pressure of a Circumferentially Cracked Tube

Elastoplastic finite-element analyses are being conducted to determine the effects of a lateral constraint on the failure pressure of a tube with a single throughwall circumferential crack. The stress-strain curves for Alloy 600 are shown in Fig. 72. Because the analyses included the effects of finite deformation, the true stress/strain curve was used. Initially, two tubes, with 180° and 240° throughwall circumferential cracks, were analyzed. A typical finite-element model and typical displacements for the free-bending case are shown in Figs. 73a and b. Note that the beam bends almost like a rigid body about a hinge at the cracked section. Figure 74a shows the variations of the free-end displacements and the maximum rotation with the normalized failure pressure for 180° and 240° circumferential throughwall cracks. The displacement and rotation curves fall on top of each other confirming that the displacement is of the rigid-body-rotation type. Both cracked tubes reach maximum pressures at a rotation of ≈10°, which is in agreement with the experimental observation by Hernalsteen,[8] that tubes appear to fail at a fixed rotation of the cracked section. Figure 74b compares available failure pressure data reported by the French[29] and predictions by the simple-beam free-bending model (Eq. 35a) and finite-element analysis. The simple model underpredicts the test failure pressures as well as the finite element results slightly.

Preliminary analysis of a transversely supported tube (to simulate the tube support plate) with a 240° crack showed that the maximum pressure capability is increased significantly over that of a free-bending tube (Fig. 75a). The critical pressure for a span of 0.67 m (26 in.) appears to be much closer to the fully constrained case than the free-bending case (Fig. 75b).

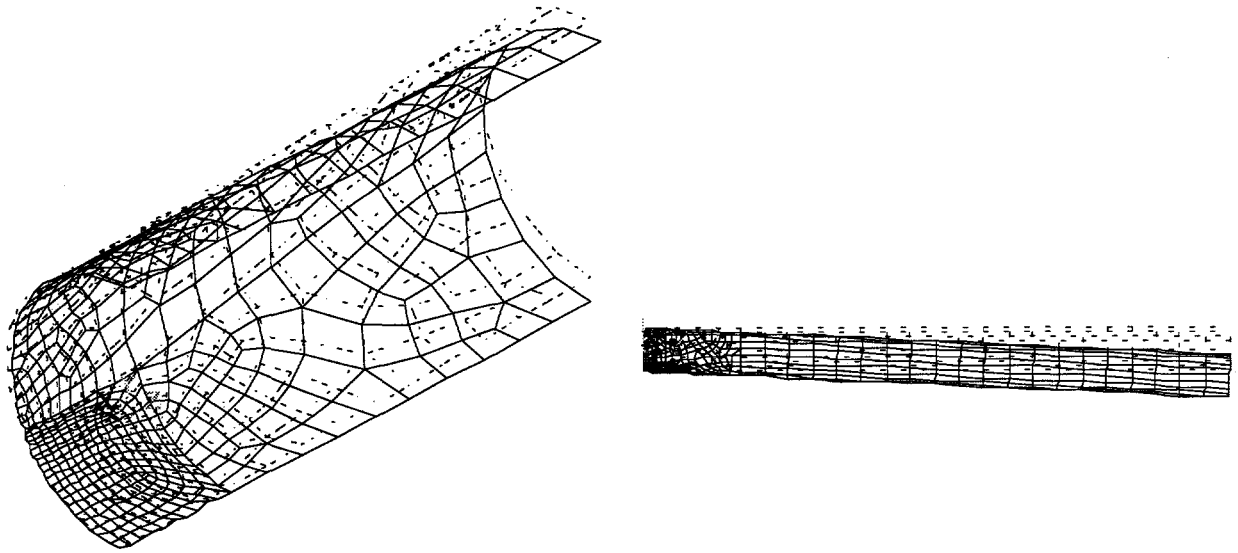

(a) (b)

Figure 73. (a) Typical near-tip finite-element model for a tube with a throughwall circumferential crack. (b) Typical displaced shape of the tube for the free-bending case.

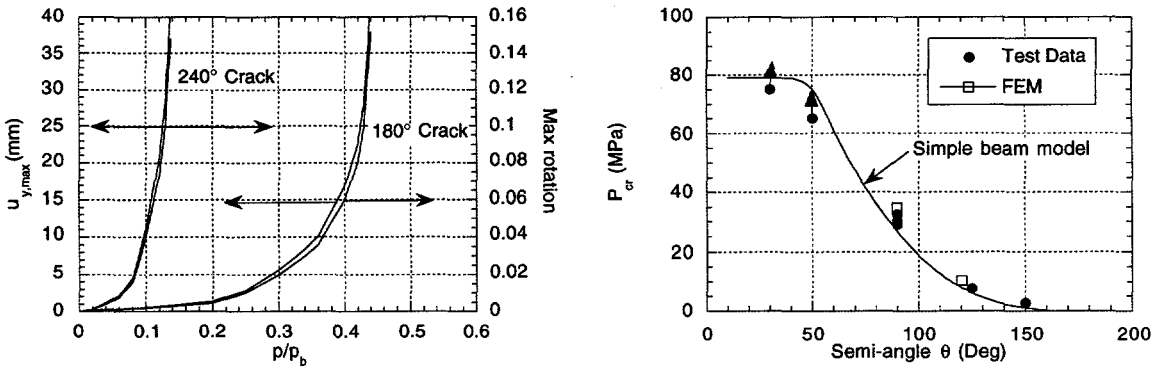

(a) (b)

Figure 74. (a) Variations of free-end displacements and maximum rotations with normalized failure pressure for tubes with 240 and 180° throughwall circumferential cracks. (b) Experimental failure pressure data and failure pressures predicted by a simplified beam model and finite-element method (FEM).

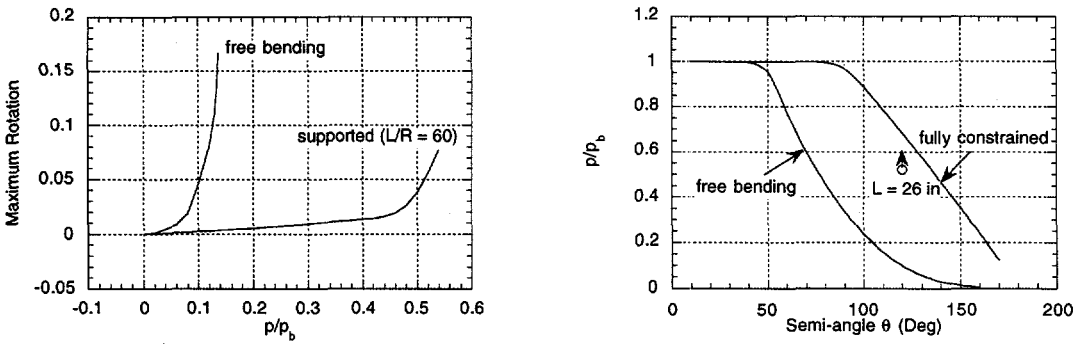

(a) (b)

Figure 75. (a) Maximum rotation of section of 22.23-mm (0.875-in.)-diam tube that contained a 240° circumferential crack, when free to bend and when supported laterally at a span (L/R = 60) of 0.67 m (26 in.) and (b) variation of critical failure pressure with semi-angle of crack for free-bending and fully constrained cases. Arrow represents loading at which the finite-element analysis of the supported tube (Fig. 75b) was discontinued.

4.7.2.2 A Simple Beam Model for the Failure of a Supported Tube with a Circumferential Crack

Consider a tube (Fig. 76) of radius R, wall thickness t, and length L with a throughwall circumferential crack of angular length 2θ subjected to internal pressure p and ignore all hoop stress effects on plastic collapse. By symmetry, only half of the tube from $\alpha = 0$ to $\alpha = \pi$ is considered, with the crack extending from $\alpha = 0$ to $\alpha = \theta$. A vertical restraining force V acts at each support, giving in an externally applied bending moment of M = VL at the section that contains the crack. The bending rotation at the section that contains the crack is given by

$$y' = \frac{VL^2}{3EI} = \frac{VL^2}{3\pi ER^3 h}. \qquad (37)$$

In general, the cross section of the tube that contains the crack will undergo an axial strain ε_o and a curvature κ, so that the axial strain at any location is given by

$$\varepsilon_z = \varepsilon_o + \kappa R \cos\alpha .$$

Two cases may arise.

Case 1: $\varepsilon_o > \kappa R$

In this case, there is no negative yielding in the cracked section. If the section experiences tensile yielding from $\alpha = \alpha_t$ to $\alpha = \theta$, then equilibrium of axial forces gives

$$\sigma_y Rt (\pi - \theta) - E\kappa R^2 h[(\pi-\alpha_t)\cos\alpha_t + \sin\alpha_t] = 1/2p\pi R^2,$$

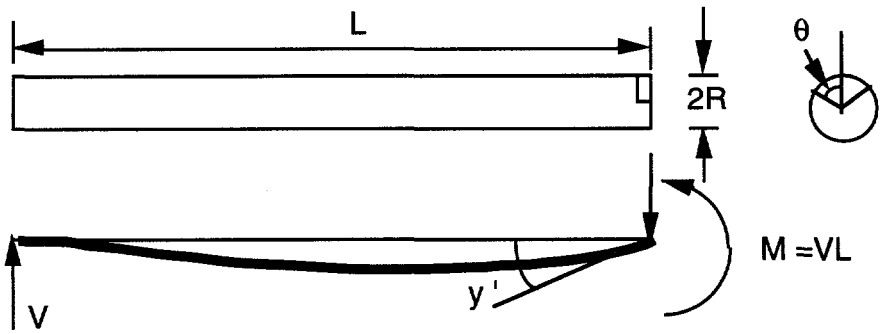

Figure 76. Idealized simple beam model for analysis of rupture of supported tube.

where E is the Young's modulus and σ_y is the flow stress. At collapse, $\alpha_t = \pi$, giving the critical pressure as a fraction of the unflawed failure pressure as

$$\frac{p_{cr}}{p_b} = \frac{2}{\pi}(\pi - \theta). \tag{38}$$

The bending moment at the cracked section at collapse is given by

$$M = VL = 2\sigma_y R^2 h \sin\theta, \tag{39a}$$

which is independent of L. The slope y' at the cracked section is given by Eq. 37 as

$$y' = \frac{2\sigma_y L}{3\pi ER}\sin\theta. \tag{39b}$$

Note that, in this case, the slope at collapse increases linearly with length L.

Case 2: $\varepsilon_o < \kappa R$

In this case, both tensile and compressive yielding will occur at the cracked section. The location of the neutral axis is given by

$$\alpha_n = \cos^{-1}[-\varepsilon_o/\kappa R].$$

As before, axial force equilibrium at collapse gives

$$\frac{p_{cr}}{p_b} = \frac{2}{\pi}(2\alpha_n - \theta - \pi). \tag{40}$$

The bending moment at the cracked section is given by

$$M = VL = 2\sigma_y R^2 h (\sin\theta - 2\sin\alpha_n), \tag{41}$$

which, on solving for α_n, gives

$$\alpha_n = \sin^{-1}\left[\frac{1}{2}\sin\theta - \frac{VL}{4\sigma_y R^2 h}\right]. \tag{42a}$$

Using Eq. 37, one obtains

$$\alpha_n = \sin^{-1}\left[\frac{1}{2}\sin\theta - \frac{3\pi ER}{4\sigma_y L}y'\right]. \tag{42b}$$

Note that as $L \to \infty$, Eqs. 40 and 42b give the failure pressure for the free-bending case. If we make the additional assumption that, for a given crack geometry, y' at collapse is a constant y'_c, independent of L, then, because $\alpha v \le \pi$, a critical length L_{cr} can be defined as a constant for a given crack geometry as follows:

$$L_{cr} = \frac{3\pi ER}{2\sigma_y \sin\theta}y'_c, \tag{43}$$

and Eq. 42b can be rewritten as

$$\alpha_n = \sin^{-1}\left[\frac{1}{2}\left(1 - \frac{L_{cr}}{L}\right)\sin\theta\right]. \tag{42c}$$

Thus, we conclude that

If $L<L_{cr}$, Case 1 is controlling,

If $L>L_{cr}$, Case 2 is controlling.

To solve for the collapse pressure from Eqs. 40 and 42b, a value of y'_c is needed. One option is to obtain this value experimentally by measuring the reactive force V at collapse and then using Eq. 37. In Fig. 77a, the failure pressure is plotted as a function of the length of the tube L for various values of the parameter y'_c. Note that the failure pressure remains constant for $L < L_{cr}$ and drops rapidly with increasing L for $L > L_{cr}$. The variations of the reactive force V and the value of y' at collapse with length L are plotted in Fig. 77b for the cases of $y'_c = 0.03$ and 0.04. The reactive force V decreases with L while the value of y' at collapse first increases with L (Case 1) and then remains constant at y'_c (Case 2).

Although the values of the support reactions at rupture are comparable to those calculated by the finite-element analysis, the values of the rotation are significantly smaller because the model assumes that the tube away from the section that contains the crack remains elastic. The model will be modified in the future to include the effects of plastic deformation in the whole tube.

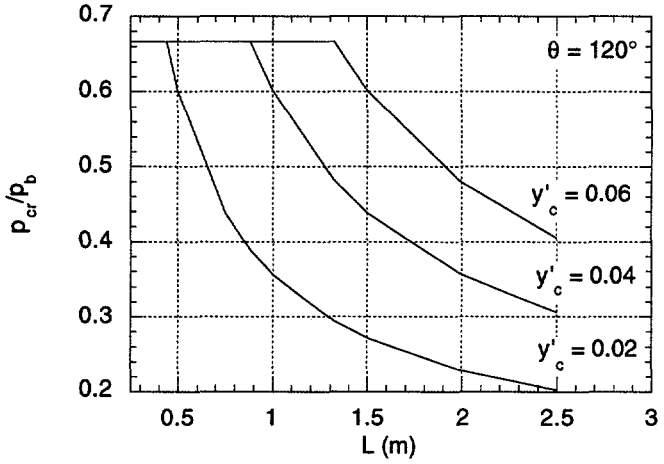

(a)

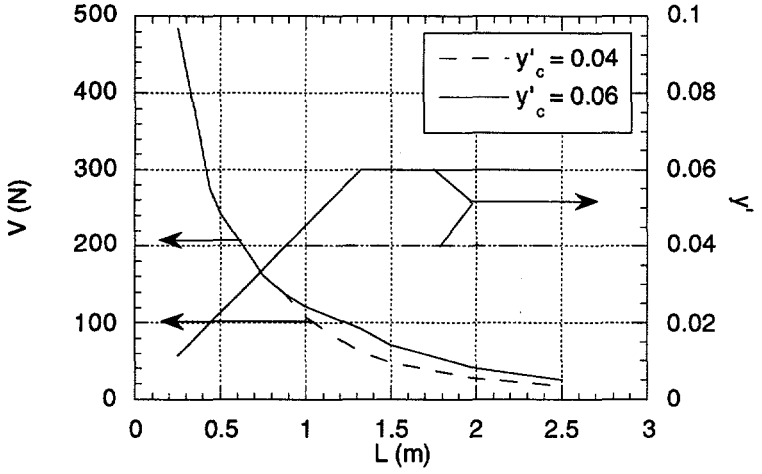

(b)

Figure 77. (a) Variation of calculated rupture pressure with length of tube for various values of critical slope y_c'. (b) Variations of calculated support force and maximum rotation at rupture with the tube length.

4.7.3 Measurement of Flaw Depth in Severe Accident Test Specimens

A series of tests has been carried out using the severe-accident test facility to determine the failure times and temperatures of Alloy 600 tubes of 19.1 mm (3/4 in.) and 22.2 mm (7/8 in.) diam that contained a variety of EDM flaws under simulated severe-accident scenarios. The results of these tests and a description of modeling studies conducted to predict failure pressure in these specimens are described in Sections 4.7.5 and 4.7.6. However, an important aspect of analyzing the results from these tube tests is the characterization of the EDM flaws. The flaw depth and length are critical parameters in calculating the expected failure pressures of the tubes, and these dimensions must be determined as precisely as possible. The accurate determination of the flaw depths, in particular, poses some difficulties. Four methods have been developed to measure the depths of the machined flaws. Two of these methods are applicable to the specimens prior to testing, one is performed after testing, and the fourth method is destructive and thereby precludes subsequent pressure testing of the specimen.

The first technique used to measure flaw depth was posttest fractography. In this method, the fracture surfaces of the failed specimen are photographed at a known magnification after the test, and the contrast between the machined portion of the fracture surface and the region of subsequent ductile fracture in the photograph permits a reasonably accurate determination of flaw depth. This method assumes that the premachined portion of the tube wall does not thin appreciably during the test. This appears to be a reasonable assumption, inasmuch as this portion of the wall cannot support a hoop stress, and the axial deformations observed during pressure testing are on the order of a few percent or less.

The second technique used to measure flaw depth was replication of the pre-machined flaws. In this technique, a plastic replica was made of the flawed region of the specimen prior to testing, and the height of this replica, which corresponds to the depth of the flaw, was then determined by optical microscopy. This technique offers the advantage that the flaw geometry is preserved in time, and reexamination of the flaw is possible even after the test is completed. Accurate measurements require that the replicas do not stretch or tear during extraction from the sample.

A third technique, developed later in the present test series, is to directly measure the flaw depth prior to testing with a traveling optical microscope that gives a digital readout of the x, y, and z positions of the objective lens. The flaw depth can be measured by focusing first on the outer surface of the specimen and then on the bottom of the machined flaw. The flaw depth corresponds to the movement of the microscope objective between these two steps; readings accurate to within ≈±2,500 μm (±0.1 mil) are possible. This technique can also be used to obtain highly accurate measurements of flaw length. Its principal disadvantage is the fact that the measurements cannot be rechecked after the specimen has been tested.

A fourth technique for determining flaw depth is destructive metallography of the flawed tube. The tube is simply sectioned through the flaw, and the depth at that position is determined from a microphotograph. The technique is also highly accurate, but it suffers from the obvious disadvantage that the sectioned tube cannot be subsequently

pressure tested. In addition, the depth is determined at only one position per section along the flaw length.

All four of these techniques have been employed in the present program, and the results are listed in Table 10. Posttest fractography was the first technique used, and data from this procedure are available for all of the tubes. The flaw replication and pretest direct optical measurement techniques were developed later in the program, and values are not available for the early tube tests. Because both of these techniques are applied prior to the test, it is not possible to make these measurements on failed specimens. Only the pretest measurement by optical microscopy (Technique A in Table 10) permitted accurate determination of flaw length, and the values determined by this technique are reported in the table. For those flaws to which this technique was not applied, the nominal flaw length is given. The EDM process is such that the length is not expected to vary significantly from the nominal value, and the observations from Technique A, i.e., pretest measurement by optical microscopy, bear this out.

The last four entries at the bottom of Table 10 represent flaw depth values obtained by three of the four techniques on the same set of flaws. The purpose of these measurements was to compare the flaw depth values determined by the various techniques. Four flaws of various depths were machined into a single 1.27-mm (0.050-in.)-diam tube by the usual procedure. The depths of the flaws along their lengths were then determined by pretest direct optical observation and by replication. The tube was then sectioned through each of the four flaws, and the flaw depth at the point of sectioning was measured metallographically. Because this sectioning made subsequent pressure testing impossible, post-test fractography values for the flaw depths could not be obtained. In addition, the depth measurement obtained by replication from the deepest flaw is not valid because the replica tore, apparently during extraction. This fact was not discovered until after the tube was sectioned, and so a second replica was not made. As indicated in Table 10, aside from this invalid measurement, the agreement among the three techniques for these flaws was quite good. The largest variation in measured flaw depth was 0.02 mm (0.9 mils), or ≈6% variation between the values measured by pretest optical microscopy and posttest metallography.

Table 10 also provides information that can be used to compare the various techniques for tubes that were actually tested to failure. In general, the flaw depth values obtained by replication are slightly greater than those obtained by posttest fractography; the pretest microscopy determinations agree reasonably well with the values obtained by replication. Because the posttest fractography values represent the only consistent set of values for all of the specimens, these are the flaw depth values that have been used in the analysis and modeling of the tests performed to date.

Data on the variation in flaw depth along its length are provided in Table 11 for the nine specimens characterized by pretest optical microscopy (Technique A). Observed depth values are reported at intervals of ≈6.4 mm (0.25 in.) as well as within ≈0.4 mm (0.015 in.) of each end of the flaw. For all of the flaws measured, the variation in depth is 25 μm (1 mil) or less over the central portion of the flaw. This variation represents an improvement over the ≈ 50 μm (2 mil) variability observed in post-test fractography

Table 10. Flaw depth and flaw depth/wall thickness ratio obtained by various techniques[a]

Spec. No.	Tube Diam (in.)	Wall Thick. (mils)	Flaw Length (in.)[b]	Flaw Depth (mils) A	B	C	D	Flaw Depth/Wall Thick. (a/h) A	B	C	D
T-1	0.750	42.3	2.0	-	-	17	-	-	-	0.40	-
T-2	0.750	43.0					unflawed				
T-3	0.750	42.5	2.0	-	-	19	-	-	-	0.45	-
T-4	0.750	42.7	2.0	-	-	8.7	-	-	-	0.20	-
T-5	0.875	49.5	2.0	-	-	8.0	-	-	-	0.16	-
T-6	0.875	49.7	2.0	-	-	18	-	-	-	0.36	-
T-7	0.875	49.4	0.25	-	-	32	-	-	-	0.65	-
T-9	0.875	49.7	1.0	-	-	27	-	-	-	0.54	-
T-10	0.875	50.8					unflawed				
T-11	0.750	42.7	1.0	-	-	26	-	-	-	0.61	-
T-12	0.750	42.6	0.25	-	-	25	-	-	-	0.59	-
T-13	0.750	42.5					unflawed				
T-14	0.750	42.6	2.0	-	-	15	-	-	-	0.35	-
T-15	0.875	49.6	2.0	-	-	15	-	-	-	0.30	-
T-16	0.875	49.1	1.0	-	28.8	28	-	-	0.59	0.57	-
T-17	0.875	49.4	2.0	-	11.8	10	-	-	0.24	0.20	-
T-18	0.875	51.5	0.25	-	34.5	34	-	-	0.67	0.66	-
T-19	0.875	50.6					unflawed				
T-20	0.750	42.6	2.0	-	7.5	5.3	-	-	0.18	0.12	-
T-21	0.750	42.4	2.0	-	18.5	17	-	-	0.44	0.40	-
T-22	0.750	42.5					unflawed				
T-23	0.750	41.9	0.25	-	23.7	24	-	-	0.57	0.57	-
T-24	0.875	51.4	0.25	-	33.4	34	-	-	0.65	0.66	-
T-25	0.875	51.7	2.0	-	12.0	11	-	-	0.23	0.21	-
T-26	0.875	50.8	2.0	-	21.1	21	-	-	0.42	0.41	-
T-27	0.875	50.5	1.0	-	28.4	28	-	-	0.56	0.55	-
T-28	0.875	51.7					unflawed				
T-29	0.750	42.6	1.0	-	24.9	23	-	-	0.58	0.54	-
T-30	0.875	51.9					unflawed				
T-31	0.875	50.1	2.0	-	13.1	11	-	-	0.26	0.22	-
T-32	0.875	51.8	2.0	-	22.6	21	-	-	0.44	0.41	-
T-33	0.875	52.1	1.0	-	30.3	28	-	-	0.58	0.54	-
T-34	0.875	50.2	0.25	-	34.7	31	-	-	0.69	0.62	-
T-35	0.875	51.2					unflawed				
T-36	0.875	50.9					unflawed				
T-37	0.875	51.1	1.010	31.5	31.7	30	-	0.62	0.62	0.59	-
T-38	0.875	51.4	0.997	32.3	32.3	32	-	0.63	0.63	0.62	-
T-39	0.750	-	0.997	27.2	27.3	c	-	-	-	-	-
T-40	0.750	-	0.991	26.6	26.9	c	-	-	-	-	-
T-41	0.875	50.8					unflawed				
T-42	0.875	50.9					unflawed				
T-45	0.875	50.7					unflawed				
T-46	0.875	50.5					unflawed				
T-47	0.875	50.6	0.998	28.3	29.2	28	-	0.56	0.58	0.55	-

Table 10. (Cont'd.)

Spec. No.	Tube Diam (in.)	Wall Thick. (mils)	Flaw Length (in.)[b]	Flaw Depth (mils)				Flaw Depth/Wall Thick. (a/h)			
				A	B	C	D	A	B	C	D
T-48	0.875	50.6	1.010	28.1	28.4	28	-	0.56	0.56	0.55	-
T-55	0.875	50.6	0.25	45.6	44.8	46	-	0.90	0.89	0.91	-
T-56	0.875	50.8	1.0	34.1	34.6	33	-	0.67	0.68	0.65	-
T-57	0.875	50.9	0.244	38.4	38.8	c	-	0.75	0.76	-	-
T-61	0.875	50.5					unflawed				
T-62	0.875	51.0					unflawed				
T-63	0.875	51.0					unflawed				
T-65	0.875	51.1	2.037	45.3	47.3	46	-	0.89	0.93	0.90	-
T-66	0.875	51.0	1.0	46.0	46.0	46	-	0.90	0.90	0.90	-
T-67	0.875	51.0	1.0	33.1	33.7	33	-	0.65	0.66	0.65	-
T-68	0.875	50.7	1.0	32.9	33.0	33	-	0.65	0.65	0.65	-
T-69	0.875	50.7	1.0	33.5	33.4	32	-	0.66	0.66	0.63	-
T-70	0.875	50.5	1.0	33.3	33.3	32	-	0.66	0.66	0.63	-
T-72	0.875	50.0		46.1	c	46	-	0.92	-	0.92	-
T-73	0.875	49.7		46.5	c	46	-	0.94	-	0.93	-
T-74	0.875	49.8	1.0	46.4	46.7	c	-	0.93	0.94	-	-
T-75	0.875	-	1.0	33.3	33.2	c	-	-	-	-	-
T-76	0.875	50.8	0.25	45.1	44.4	c	-	0.89	0.87	-	-
T-77	0.875	50.2	0.25	45.0	45.2	c	-	0.90	0.90	-	-
T-78	0.875	50.3	0.25	46.5	37.2	c	-	0.92	0.74	-	-
T-79	0.875	50.1	2.0	46.0	46.2	c	-	0.92	0.92	-	-
T-80	0.875	50.2	2.0	46.2	46.5	c	-	0.92	0.93	-	-
T-81	0.875	50.0	2.0	46.5	46.3	c	-	0.93	0.93	-	-
T-82	0.875	50.6					unflawed				
T-83	0.875	50.5					unflawed				
T-84	0.875	50.7	1.0	45.9	46.2	46	-	0.91	0.91	0.91	-
T-85	0.875	50.8					unflawed				
T-86	0.875	50.4					unflawed				
T-87	0.875	50.3					unflawed				
STD-1A	0.875	50	1.990	10.2	10.2	-	10.6	0.20	0.20	-	0.21
STD-1B	0.875	50	1.993	15.4	16.0	-	16.3	0.31	0.32	-	0.33
STD-1C	0.875	50	1.998	24.4	24.3	-	24.7	0.49	0.49	-	0.49
STD-1D	0.875	50	0.264	32.0	27.6[d]	-	32.7	0.64	0.55[d]	-	0.65

[a] A = Pre-test measurement by non-destructive optical microscopy.
B = Pre-test measurement by replication.
C = Post-test measurement by fractography.
D = Measurement by destructive metallography (specimen not pressure tested).

[b] Nominal flaw lengths except for those specimens characterized by technique A (see footnote b) for which actual values are reported.

[c] Not yet measured.

[d] Replica torn.

Table 11. Variation of flaw depth along length of various specimens as determined by pretest optical microscopy.

Position along Flaw Length (in.)	Flaw Depth for Specimen Indicated (mils)								
	T-37	T-38	T-39	T-40	T-47	T-48	T-57	T-58	T-59
0.0089	-	-	-	26.5	-	-	-	-	-
0.0120	-	-	19.2	-	-	-	-	-	-
0.0132	-	23.6	-	-	-	-	-	-	-
0.0150	-	-	-	-	26.3	22.4	33.3	38.1	36.8
0.0159	30.6	-	-	-	-	-	-	-	-
0.0800	-	-	-	-	-	-	38.0	-	-
0.1400	-	-	-	-	-	-	38.0	-	-
0.2100	-	-	-	-	-	-	39.1	-	-
0.2287	-	-	-	-	-	-	35.4	-	-
0.250	31.8	32.0	27.2	26.7	28.2	27.9	-	40.2	39.9
0.500	32.4	31.3	27.3	26.5	28.5	28.3	-	40.2	-
0.750	32.8	31.3	27.1	26.6	28.3	28.1	-	40.6	40.6
0.9803	-	31.7	-	26.1	-	-	-	-	-
0.9834	-	-	-	-	28.9	-	-	-	-
0.9919	-	-	26.0	-	-	-	-	-	-
0.9947	18.4	-	-	-	-	-	-	-	-
0.9954	-	-	-	-	-	27.4	-	-	-
1.000	-	-	-	-	-	-	-	-	40.5
1.0181	-	-	-	-	-	-	-	35.4	-
1.250	-	-	-	-	-	-	-	-	40.1
1.500	-	-	-	-	-	-	-	-	39.8
1.750	-	-	-	-	-	-	-	-	40.2
2.0472	-	-	-	-	-	-	-	-	17.0
Flaw Length (in.)	1.0104	0.9972	0.9974	0.9905	0.9984	1.0104	0.2437	1.0331	2.0622
Ave. Depth (mils)	32.3	31.5	27.2	26.6	28.3	28.1	38.4	40.3	40.2

measurements on specimens before improvements in flaw fabrication procedures were instituted. However, several of the flaws still show substantial variation in depth near the ends, with rounding of the corners indicated. The average values for flaw depth reported in Tables 10 and 11 for these specimens were obtained by ignoring the measurements at each end, because the depths at these locations were nonrepresentative in many cases.

4.7.4 Verification of Flaw Depths in Specimens Pressure Tested at PNNL

The posttest fractography technique was also used to verify the depth of EDM flaws in SG tube specimens tested at PNNL in the late 1970s (Ref. 30). Several types of artificial defect geometries were evaluated in the PNNL tests, but the present analysis is concerned

with those specimens in which part-throughwall EDM notches of various lengths and depths were introduced, followed by pressure testing to failure. These test specimens have been obtained by ANL as a part of the present program, and the verifications were carried out as a part of a reanalysis of the PNNL tube failure data in conjunction with the ANL experimental and analytical study of tube failure behavior under severe accident conditions.

The results of the flaw depth measurements are summarized in Table 12. In this table, the flaw depths originally determined by PNNL with replication techniques are compared with the remeasured values obtained by ANL with posttest fractography. The Table also includes flaw depths estimated at PNNL by EC testing. Where the original flaw was 100% throughwall, no remeasured value is given, and, in some cases, the specimen fracture surface was of such poor quality that an accurate remeasurement could not be performed. In addition, a substantial number of the specimens listed as tested in NUREG/CR-0718 were not among the specimens provided to ANL. For the most part, the remeasured depths agree reasonably well with the values reported by PNNL, but significant discrepancies exist for several specimens, including C-03-9, C-19-5, C-34-1, C-34-3, C-36-7, C-41-3 and C-41-5. The values for these specimens will be rechecked, and the remeasured flaw depths obtained by ANL will be used to reanalyze the PNNL data on tube rupture behavior. Despite these discrepancies in flaw depth for several of the specimens, this reanalysis is not expected to significantly alter the correlation obtained by PNNL in terms of mean rupture behavior.

4.7.5 Models for Predicting Failure under Severe-Accident Conditions

During design basis accidents, the temperature of the SG tubing is <350°C. In this temperature range, creep effects are negligible in Alloy 600. However, in severe accidents much higher temperatures are possible. At these higher temperatures plastic deformation is likely to be much more extensive than it is at normal reactor operating temperatures, and creep effects may no longer be negligible. The behavior of flawed SG tubing during severe accidents has recently been considered in reports by INEL[19] and EPRI.[20] In these reports, the failure of unflawed tubing and other components, such as the surge line nozzle, is described in terms of creep damage failure. In contrast, both analyses assume that failure of flawed SG tubing in severe accidents can be predicted by a flow stress model by taking the flow stress to be a function of temperature. With this assumption, the failure pressure of a flawed tube depends only on the flaw geometry and temperature, and is independent of the detailed time/temperature history.

Intuitively, one would expect flow stress to control failure if the temperature ramps are sufficiently rapid so that there is insufficient time for creep to influence the deformation or damage of the tube. At the other extreme, if the temperature ramps are sufficiently slow (in the limit, a constant-temperature hold), failure should be controlled by creep processes. In loading histories at intermediate rates, the damage processes are more complex and difficult to analyze.

Recent tests conducted at ANL have shown that pressure and temperature ramp rates significantly influence failure pressure (Fig. 78a) and failure temperature (Fig. 78b),

Table 12. PNNL and ANL measurements of depth of machined flaws in specimens used in PNNL pressure tests.

Specimen Number	PNNL Measurements			ANL Measurements	
	Flaw Length (in.)	Flaw Depth (% throughwall)	ECT Depth (% throughwall)	Flaw Depth (in.)	Flaw Depth (% throughwall)
B-06-9	0.496	25.3	Undetectable	0.014	28
B-07-1	0.495	100.0	100	-	-
B-07-3	1.485	29.8	Undetectable	-	-
B-08-7	0.500	100.0	100	-	-
B-12-3	0.996	100.0	100	-	-
B-13-9	0.255	30.2	Undetectable	0.012	24
B-16-1	0.500	30.7	Undetectable	0.015	30
B-19-1	0.255	100.0	100	-	-
B-19-5	0.485	100.0	100	-	-
B-21-1	0.495	100.0	100	-	-
B-21-9	1.480	26.6	Undetectable	0.013	26
B-22-1	0.255	25.9	Undetectable	0.013	26
B-27-9	0.255	100.0	100	-	-
B-28-5	0.247	100.0	100	-	-
B-35-9	0.245	100.0	100	-	-
B-38-3	0.250	25.0	48	-	-
B-39-5	0.487	100.0	100	-	-
B-41-3	1.503	100.0	100	-	-
B-41-7	0.500	100.0	100	-	-
B-43-1	0.502	100.0	100	-	-
B-56-5	1.009	100.0	100	-	-
B-70-1	0.999	84.0	76	0.044	88
C-03-9	0.250	88.9	49	0.019	44
C-14-9	1.500	100.0	100	-	-
C-18-7	1.500	53.8	5	-	-
C-19-5	1.500	26.1	Undetectable	0.006	14
C-21-09	1.495	77.5	67	0.038	88
C-21-10	1.495	89.2	77	0.036	84
C-24-5	1.500	56.3	60	0.019	44
C-27-1	0.240	29.6	Undetectable	0.013	30
C-31-7	1.480	100.0	100	-	-
C-34-1	0.500	27.9	Undetectable	0.005	12
C-34-3	0.500	53.5	5	0.016	37
C-36-3	0.250	58.7	53	0.021	49
C-36-7	0.500	56.3	8	0.015	35
C-37-1	1.490	86.9	74	0.039	91
C-40-3	0.500	100.0	100	-	-
C-41-3	0.500	28.3	Undetectable	0.006	14
C-41-5	1.500	28.4	Undetectable	0.006	14
C-44-5	0.495	100.0	100	-	-
D-03-5	0.495	29.6	Undetectable	0.015	30
D-11-5	1.495	58.6	60	0.028	56
D-12-1	0.245	87.0	69	0.041	82
D-12-3	0.265	31.2	51	-	-
D-12-9	1.495	29.6	Undetectable	0.010	20

Table 12. (Cont'd.)

Specimen Number	PNNL Measurements			ANL Measurements	
	Flaw Length (in.)	Flaw Depth (% throughwall)	ECT Depth (% throughwall)	Flaw Depth (in.)	Flaw Depth (% throughwall)
D-17-3	0.255	84.3	73	0.040	80
D-17-7	1.525	84.0	69	0.040	80
D-19-5	0.495	86.6	70	0.040	80
D-23-3	0.500	84.6	70	0.039	78
D-25-1	0.247	30.9	Undetectable	0.016	32
D-25-5	0.245	27.0	Undetectable	0.015	30
D-31-1	1.515	84.3	63	0.041	82
D-31-7	1.495	27.7	Undetectable	-	-
D-31-8	1.500	27.0	Undetectable	0.012	24
D-31-9	0.490	57.8	62	-	-
D-35-3	0.490	64.3	58	0.033	66
D-41-9	1.490	59.2	57	0.026	52
D-45-3	0.250	67.6	67	0.034	68
E-03-7	0.496	28.3	Undetectable	0.013	26
E-04-1	0.505	89.1	77	-	-
E-04-5	0.500	26.3	Undetectable	0.013	26
E-04-9	0.505	91.1	75	-	-
E-05-7	0.495	58.7	63	-	-
E-09-9	0.505	100.0	100	-	-
E-15-7	0.498	100.0	100	-	-
F-03-9	0.499	89.7	77	-	-
F-04-1	0.495	100.0	100	-	-
F-06-1	0.504	85.0	68	0.042	84
F-06-7	0.501	57.3	52	-	-
F-07-9	0.497	100.0	100	-	-
F-09-3	0.496	27.7	Undetectable	0.012	24
F-09-9	0.498	27.7	Undetectable	-	-
F-10-3	0.500	57.5	55	0.028	56
G-05-1	0.250	29.9	Undetectable	0.010	29
G-05-9	1.503	57.4	65	0.020	59
G-07-1	1.503	80.9	64	0.025	74
G-07-3	0.249	59.2	54	0.025	74
G-07-9	1.500	85.3	64	0.028	82
G-14-7	0.497	28.4	43	-	-
G-15-3	0.497	28.6	51	-	-
G-15-7	0.496	89.9	67	0.030	88
G-18-9	0.251	58.8	65	-	-
G-22-5	0.499	88.8	61	0.030	88
G-22-9	0.250	26.5	53	-	-
G-28-9	0.500	56.2	55	-	-
G-30-3	1.495	27.8	42	0.009	26
G-30-9	0.247	87.7	53	0.027	79
G-34-1	1.495	62.5	61	-	-
G-35-1	0.499	61.4	48	0.019	56
G-35-7	1.495	34.0	44	0.011	32
G-35-9	0.249	86.8	53	0.024	71

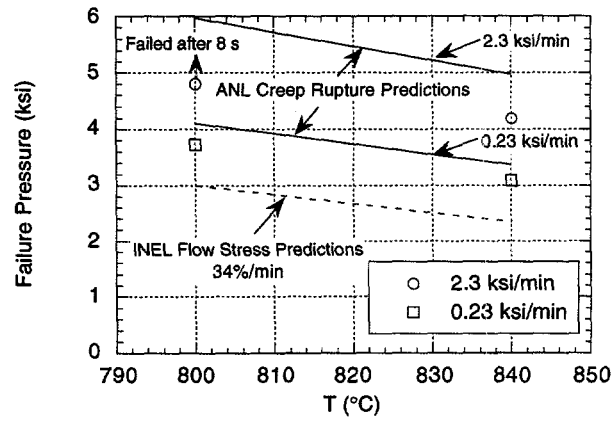

(a)

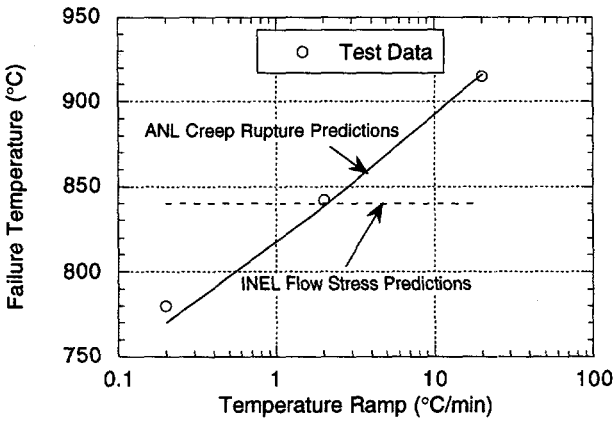

(b)

Figure 78. Effects of (a) loading rate on failure pressure in isothermal pressurization test and (b) temperature ramp on failure temperature in pressurization test at a constant pressure of 16 MPa (2.35 ksi) on unflawed 22.23-mm (0.875-in.)-diam Alloy 600 tube. Also shown are failure pressures and temperatures predicted by flow stress model (dashed lines) that used INEL flow stress curve and by ANL creep rupture model (solid lines).

respectively. Therefore, a creep rupture model for predicting failure of flawed and unflawed tubes was developed. For the high-temperature tests conducted at ANL under a variety of loading histories, predictions based on this model are in much better agreement with the test results than predictions based on flow stress models. However, for completeness, the flow stress models are also discussed in this report.

Consider a tube with a flaw subjected to a temperature history T(t) and nominal hoop stress history $\sigma(t)$. To analyze the behavior of a tube with such a general loading history with either the flow stress or the creep rupture model, the following assumptions are usually made:

(1) The failure time and temperature of a flawed tube are the same as those of an unflawed tube subjected to a nominal hoop stress history $m_p\sigma(t)$ and the same temperature history T(t).

(2) The values of the magnification factor m_p determined from pressurization tests of flawed tubes at low temperatures are also applicable at high temperatures.

These assumptions can be shown to be valid for certain classes of creep and plasticity problems.[31] They are not strictly valid for the problem considered here, but the test program at ANL has shown that they can provide a reasonable approximation.

4.7.5.1 Flow stress models

In the flow stress models, it is assumed that, for any arbitrary history of hoop stress $\sigma(t)$ and temperature T(t), failure occurs at a temperature T and hoop stress σ whenever the following failure equation is satisfied, independent of stress/temperature history:

$$\sigma = \frac{\overline{\sigma(T)}}{m_p}, \tag{44}$$

where $\overline{\sigma(T)}$ is the flow stress at temperature T and m_p is a hoop stress magnification factor that accounts for the crack. The original BCL equation for m_p (Eq. 31b) was based on tests with large diameter pipes. Since then, several other empirical equations, based on tests of SG tubes, have been proposed.

Under the auspices of an NRC-sponsored SG integrity program, PNNL[32] conducted a series of tests on tubes that contained part-through axial cracks. Based on these tests, PNNL developed an empirical formula for the failure pressure of a tube that contained a part-through axial crack. This formula, referred to as the PNNL equation, is of the same form as Eq. 31a but where Eq. 31b is replaced by

$$m_p = \left[1 - \frac{a}{h} + \frac{a}{h}\exp(-0.41\lambda)\right]^{-1}, \tag{45a}$$

Chavez et al.[33] re-analyzed the PNNL data and proposed that the value of k (0.5 in the definition of $\bar{\sigma}$ below Eq. 30) should be taken as 0.5973 and that Eq. 45a, referred to as the INEL equation, should be modified to

$$m_p = \left[1 - \frac{a}{h} + \frac{a}{h}\exp(-0.51\lambda)\right]^{-1}. \qquad (45b)$$

Based on pressurization tests on tubes, Flesch and Cochet[34] recommended the use of Eqs. 31a and b for flaw depths greater than 85% of the wall thickness. However, to reduce the degree of conservativeness, they used σ_u instead of $\bar{\sigma}$. To predict failure of the remaining ligament by plastic instability of tubes with flaw depths between 20 and 85% of wall thickness, they recommended that Eq. 31b be replaced by the following empirical equation (referred to as the EdF equation):

$$m_p = \left(1 - \frac{\frac{c}{h}\frac{a}{h}}{1 + \frac{c}{h}}\right)^{-1} \text{ for } 0.2 < a/h < 0.85, \qquad (46a)$$

and

$$m_p = \frac{1 - \frac{a}{mh}}{1 - \frac{a}{h}} \frac{\bar{\sigma}}{\sigma_u} \text{ for } a/h > 0.85. \qquad (46b)$$

Improved correlation for m_p

As the crack depth approaches 100% of the thickness (i.e., a/h = 1), Eqs. 31a and b and Eq. 46b predict that p_{sc} approaches 0, as would be expected, whereas Eqs. 45a and b predict that $p_{sc} > 0$, even for throughwall cracks.. Hence, Eqs. 45a and b must eventually become unconservative for very deep cracks. To develop a more satisfactory expression for m_p, the results of the tube pressurization tests performed at PNNL[32] were reexamined. The tube failure data and all of the available tube pressurization specimens were sent by PNNL to ANL. The crack depths of the specimens were remeasured at ANL as described in Section 4.7.4 by examining the fracture surface of the failed specimens. The crack depths for the PNNL tube pressurization tests were updated with the values determined at ANL for the tests for which specimens were available. The PNNL values for the crack depths were used in cases where specimens could not be remeasured.

The results of the pressurization tests performed by PNNL are compared with the predictions of the respective models in Figs. 79–81. The results are given in terms of the relative error in the predicted failure pressure,

$$\varepsilon = \frac{p_{f_{exp}} - p_{f_{pred}}}{p_{f_{exp}}}, \qquad (47)$$

where $p_{f_{exp}}$ is the observed failure pressure and $p_{f_{pred}}$ is the failure pressure predicted by the model. The errors for unflawed tubes ($1/m_p = 1$) are very small. There is much more scatter in the results for cracked tubes; this is true both for relatively shallow cracks and deep cracks, but the scatter does seem to increase with crack depth ($1/m_p \rightarrow 0$). One

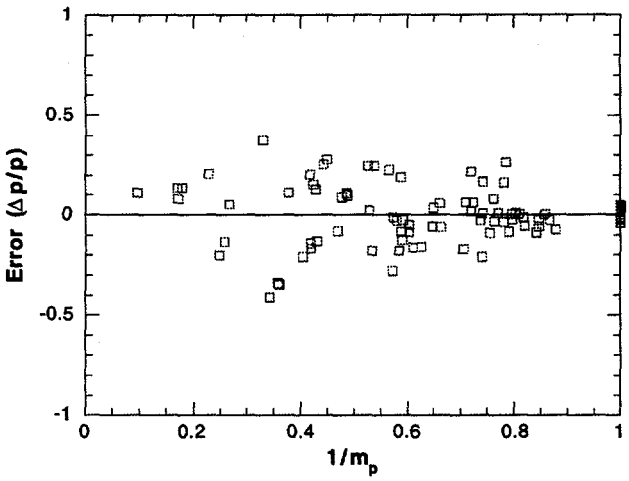

Figure 79.
Errors in failure pressures predicted by PNNL model (average error = –0.01, RMS error = 0.13

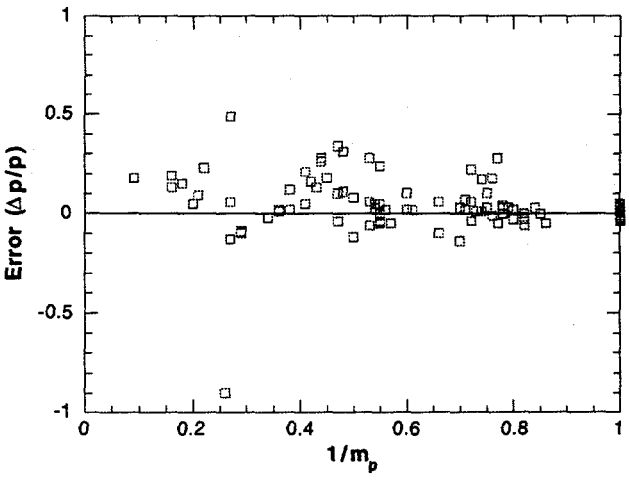

Figure 80.
Errors in failure pressures predicted by INEL model (average error = 0.04, RMS error = 0.11)

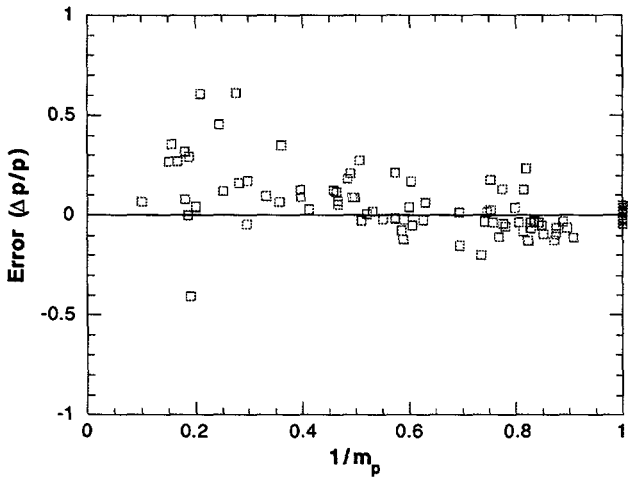

Figure 81.
Errors in failure pressures predicted by BCL model (average error = 0.05, RMS error = 0.13)

outlier in the PNNL data set at −1.3 is not shown on the graph. The RMS error is somewhat smaller for the INEL fit when compared with that developed by PNNL, but the average or mean error is also larger. The RMS error for the model of Kiefner et al.[22] is approximately the same as that of the PNNL and INEL models. However, the errors are larger for deep cracks (small $1/m_p$). The tendency for the BCL model to overpredict the stress magnification associated with deep cracks has been noted by other researchers.[34]

To eliminate the mean error for deep cracks, modifications to the Kiefner expression for m_p were sought. Several alternate expressions were examined, and it was proposed that Eq. 31b be modified to read as follows:

$$m_p = \frac{1-\alpha\frac{a}{mh}}{1-\frac{a}{h}}, \qquad (31c)$$

where $\alpha\left(\frac{a}{h}\right) = 1 + 0.9\left(\frac{a}{h}\right)^2\left(1-\frac{1}{m}\right)$.

Except for short deep cracks, Eq. 31c, which is referred to as the ANL equation, predicts failure pressures that are similar to those predicted by Eq. 31b.

The errors associated with Eq. 31c are shown in Fig. 82. The RMS error is somewhat smaller than that associated with the other correlations and the bias observed in the BCL model for deep crack has been eliminated. There are three significant outliers in the data set. They are all associated with deep cracks ($a/h > 0.85$) for which the results are quite sensitive to errors in the measurement of a. Unfortunately, these specimens were not among those shipped to ANL (they may have been sectioned for examination) and there is no way to check the measurements.

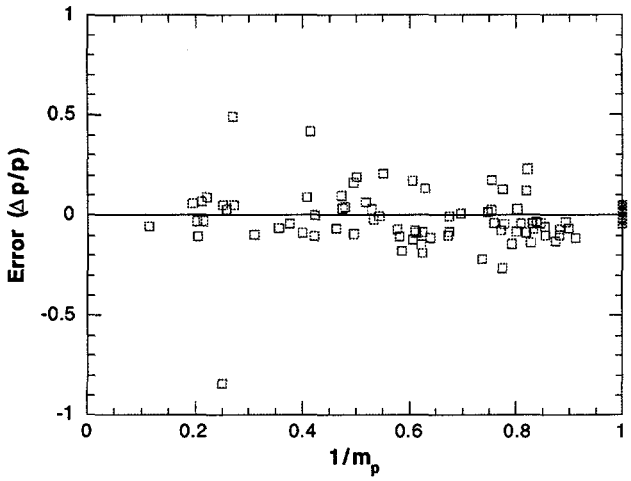

Figure 82.
Errors in failure pressures predicted by ANL model (average error = –0.02, RMS error = 0.09)

Values of m_p predicted by various models, and the results of pressurization tests performed at PNNL[30] are summarized in Table 13. The errors are expressed in terms of the RMS errors for the entire test series and in terms of the RMS errors associated with a range of cracks depths. The number of tests in each crack depth range is roughly equivalent. The Flesch and Cochet[34] correlation (referred to in Table 13 as the EdF model) is also included for comparison, but because it involves a material characteristic (the ultimate tensile stress) as well as geometric factors, it would be an unsatisfactory choice for high temperatures, where creep damage is significant.

The errors are smaller for unflawed tubes than for flawed tubes even for those with relatively shallow cracks. The PNNL and BCL models seem to have significantly larger errors for deep (a/h > 0.75) cracks than shorter cracks. The INEL and ANL models have a more uniform distribution of errors with flaw depth. Although the errors associated with the predictions from Eq.31c (with k = 0.5) for the PNNL data set are slightly smaller than with the other correlations, the INEL correlation describes the PNNL tests almost as well. However, as will be discussed in Section 4.6.4.4, the ANL correlation is in better agreement with the high-temperature creep–dominated tube failures.

A comparison of the values of stress magnification factor m_p, as computed by the various equations, is shown in Figs. 83a and b. Note that, although the values of m_p as computed by the various equations are within 20-30% of each other for shallow cracks (a/h = 0.5), they can differ by as much as a factor of 2 for short, deep cracks (≈0.25 in. [6.4 mm], a/h = 0.9). Failure tests on tubes that contain deep cracks (to be discussed later) have shown that the m_p values are more in accord with the ANL equation (Eq. 31c) than the BCL equation (Eq. 31b). To verify this analytically, detailed elastoplastic finite-element analyses were conducted for a 22-mm (7/8-in.)-diam tube with a 25-mm (1-in.)-long and 50% deep axial crack and a 6-mm (0.25 in.)-long and 90% deep axial crack, both subjected to rapidly increasing internal pressure at 300 and 750°C (572 and 1382°F). The stress-

Table 13. Error for failure pressures observed in PNNL tests as predicted by various m_p models.[a]

Error	m_p model				
	PNNL	INEL	EdF	BCL	ANL
Mean Error	-0.01	0.05	0.08	0.04	-0.02
RMS all	0.13	0.11	0.12	0.13	0.09
RMS (a/h = 0)	0.03	0.03	0.03	0.03	0.03
RMS (0.25<a/h≤0.45)	0.09	0.09	0.09	0.09	0.09
RMS (0.45<a/h≤0.75)	0.14	0.14	0.14	0.11	0.12
RMS (0.75<a/h)	0.21	0.11	0.17	0.22	0.08

[a] Errors may differ from estimates in original reports because they are based on new measurements of a/h made at ANL. Three outlier PNNL tests (C-03-5, C-15-5, and C-44-3) were not included in the calculation of the errors.

strain curves at these temperatures are shown in Fig. 84a. The results presented in Fig. 84b show that the maximum hoop stress magnification in the ligament for the shallower crack is independent of the stress-strain curve of the material. Furthermore, the hoop stress magnification factor (defined as the ratio of the average hoop stress in the ligament and the average hoop stress in an unflawed tube) changes very little with internal pressure and its variation with crack depth is more in agreement with the ANL equation than with the BCL equation.

The errors reported in Table 13 include both errors in the models for m_p and experimental errors. The primary source for experimental error would appear to be the determination of crack depths. To obtain an estimate of just the model error, efforts were made to estimate the portion of the error that attributable to errors in the crack depth measurements. For the low-temperature tests, the error in the predicted failure pressure Δp due to an error in crack depth measurement Δa is

$$\frac{\Delta p}{p} = m_p \frac{d\left(\frac{1}{m_p}\right)}{d\left(\frac{a}{h}\right)} \frac{\Delta a}{h}. \tag{48}$$

If one assumes that the variance in a is independent of crack size, the total variance for the test series due to errors in the measurement of a can be estimated from:

$$\sigma_p^2 = \left[\sum \left(m_p \frac{d\left(\frac{1}{m_p}\right)}{d\left(\frac{a}{h}\right)} \frac{1}{h} \right)^2 \right] \sigma_a^2. \tag{49}$$

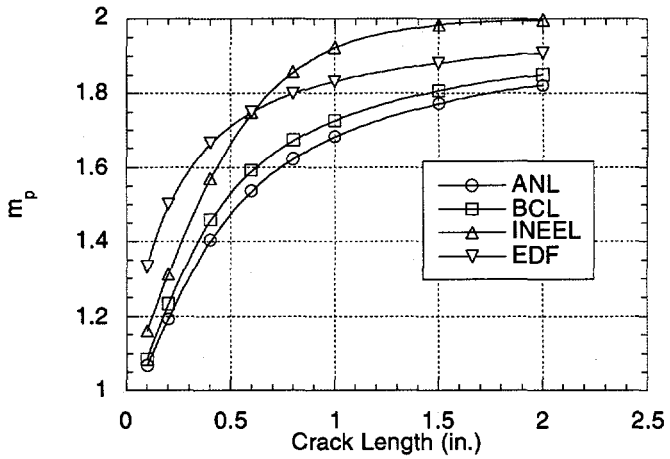

(a)

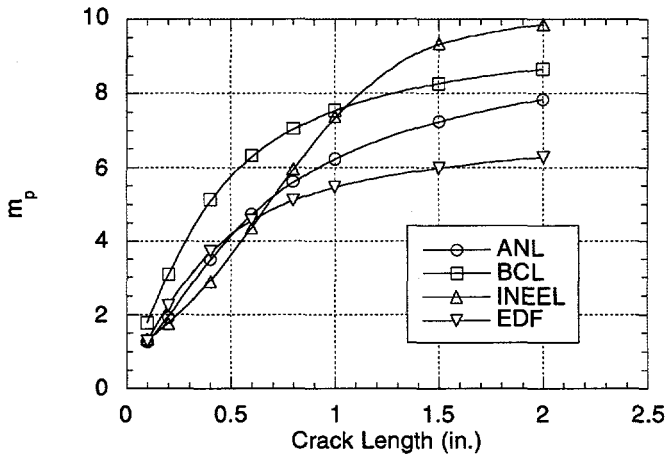

(b)

Figure 83. Magnification factor m_p as computed by BCL Eq. 31b, ANL Eq. 31c, INEL Eq. 45b, and the EdF Eqs. 46a-b as a function of crack length for crack depth-to-thickness ratios (a) a/h = 0.5 and (b) a/h = 0.9.

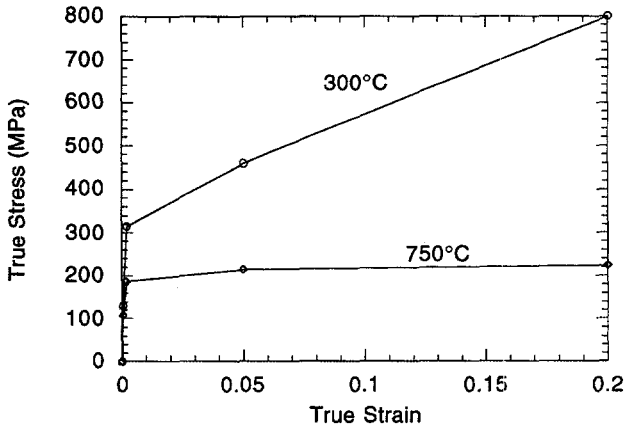

(a)

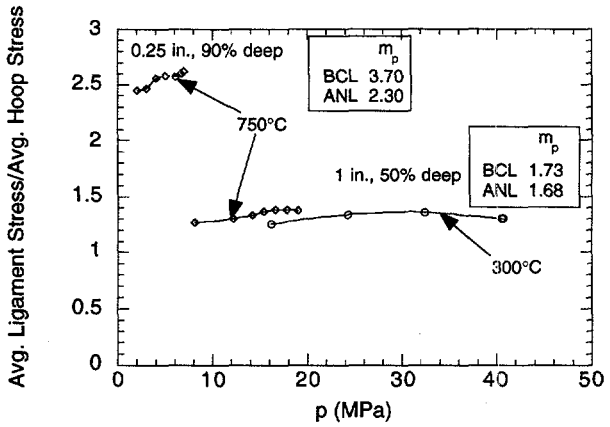

(b)

Figure 84. (a) True stress-strain curve used in finite-element analysis and (b) variation of calculated hoop stress enhancement factor in the ligament with pressure for a tube 22.23 mm (0.875 in.) in diam with two axial part-through cracks at 300 and 750°C (572 and 1382°F).

For estimates of σ_a based on the uncertainty of the depth measurements originally reported by PNNL (±1.5 mils [38 μm] or σ_a = 0.75 mils [19 μm]), the estimate of σ_p obtained from Eq. 49 represents only a small portion of the observed error. However, in the 20 samples that have been re-examined by ANL to date, the standard deviation of the differences between the ANL measurement and the previous PNNL measurement is >56μm (2.2 mils). This suggests that the uncertainty in the depth measurements is much larger than previously assumed, and that most of the observed scatter in the values observed for m_p in the tests can be attributed to uncertainties in the crack size measurements. In many cases, it is desirable to account for crack size uncertainties explicitly; hence, it is of interest to try to estimate the "model error," i.e., the error in the predicted m_p, given that

the crack size is known exactly. The mean value of the observed m_p is a much better measure of the "true" m_p and uncertainty estimates on the mean should provide a good estimate of the model error. Such estimates can be obtained by standard statistical techniques.[35] The standard error of the mean estimate of the fitted variable is given by

$$\sigma_m = s\left\{\frac{1}{n} + \frac{(x - \bar{x})^2}{\sum_k (x_k - \bar{x})^2}\right\}^{1/2},$$

where n is the total number of data points, $\bar{x}$ is the mean value of the x_k values at which observations are available, s is the estimated variance about the regression

$$s^2 = \frac{\sum_k (y_k - \hat{y}_k)^2}{n - 2},$$

y_k represents the observed values of the variable, and $\hat{y}_k$ represents the values predicted by the regression equation. The standard error of the predicted values then is

$$\sigma_m = s\left\{1 + \frac{1}{n} + \frac{(x - \bar{x})^2}{\sum_k (x_k - \bar{x})^2}\right\}^{1/2}.$$

These limits are larger than those for the value of the mean value of y for a given x.

Although the actual uncertainty estimates are nonlinear, the simple linear expression

$$m_p = \frac{1 - \alpha\frac{a}{mh}}{1 - \frac{a}{h}}(1 \pm 0.06) \qquad (50)$$

can be shown to bound the estimates of the 95% confidence interval on the mean.

Flow stress of Alloy 600

To use the flow stress models rigorously for predicting the failure temperatures of SG tubes, the tensile properties of Alloy 600 tubes in the hoop direction as functions of temperature must be known. Although fairly extensive tensile-property data for tubing are available at room temperature,[32] only limited data are currently available at higher temperatures. Tensile properties of Alloy 600 rod as a function of temperature were reported by Rempe et al.[36] Chavez et al.[33] expressed the sum of the yield and ultimate tensile strengths of Alloy 600 bar (in MPa) as a function of temperature as follows:

$$\sigma_y + \sigma_u = \begin{cases} 564.4 - 0.4546T + 1.5055\text{x}10^{-3}T^2 - 1.9907\text{x}10^{-6}T^3 & \text{for } 20°C \le T \le 727°C \\ 4308.9 - 11.381T + 1.030\text{x}10^{-2}T^2 - 3.1734\text{x}10^{-6}T^3 & \text{for } 727°C < T \le 1100°C \end{cases} \quad (51a)$$

To estimate the variation of the flow stress of Alloy 600 tubes with temperature, Chavez et al. multiplied Eq. 51a by a factor of 0.9, which is the factor by which the sum of the yield and ultimate tensile strengths of Alloy 600 bars[36] at room temperature must be multiplied to obtain the sum of the yield and ultimate tensile strengths for Alloy 600 tubes at room temperature.[32,33]

Tensile data on hot-rolled Alloy 600 bar as a function of temperature are also reported in Ref. 37. In this case the sum of the yield and ultimate tensile strengths (in MPa) of hot rolled Alloy 600 bar was given as a function of temperature by the equation:

$$\sigma_y + \sigma_u = 1780 - 9.84T + 0.0352T^2 - 5.08\text{x}10^{-5}T^3 + 2.4\text{x}10^{-8}T^4 \quad (51b)$$

for $200°C \le T \le 870°C$

Flow stresses for hot-rolled Alloy 600 computed from above data (with k = 0.5), together with flow stresses for other forms of Alloy 600 from various sources, are plotted in Fig. 85. Most of these tests were conducted under stroke-control at a nominal strain rate of 34%/min. Data from room-temperature tensile tests on the tubing being tested at ANL are also shown in Fig. 85. The flow stress decreases markedly with temperature above 600°C (1112°F). Note from Fig. 85, that, although there may be a wide variation in the flow stress at low temperatures, the variations in flow stress from heat-to-heat and with product form diminish rapidly with increasing temperature. Therefore, the INEL flow stress curve, which covers the widest range of temperature, is used to predict failure.

Although the flow stress model is a straight forward extension of a model that has been well verified at normal operating temperatures, conceptual difficulties are encountered when such a model is used at high temperatures. For example, the flow stress at elevated temperatures is a function of not only temperature but also of strain rate. In Fig 86, the results from isothermal pressure ramp tests at two ramp rates are used to define "effective" flow stresses; with the flow stress curve based on the INEL tensile tests is also presented in the figure. Note that, as expected, higher ramp rate leads to a higher flow stress. Conceptually, it is possible to include rate effects within the framework of a flow stress model by developing a constitutive equation that expresses the flow stress as a function of both strain rate and temperature. Several such constitutive relations based on the so-called equation-of-state theory are available. However, in addition to being quite complex, they are not easily applied to the problem of predicting failure of SG tubes, particularly those that contain flaws and are subjected to typical temperature and pressure histories expected during severe accidents. In this report, the term flow stress models is used exclusively to denote simple rate-independent flow stress models that have been used successfully at low temperatures.

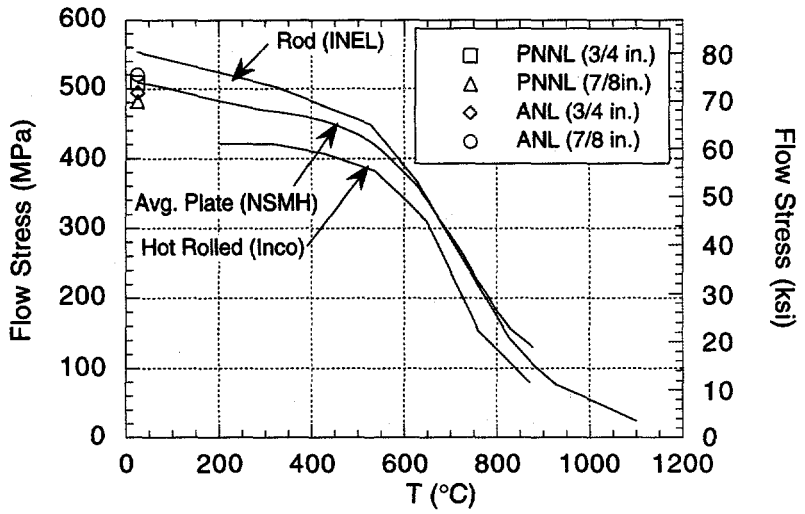

Figure 85. Flow stress curves (with k = 0.5) for various product forms of Alloy 600 and data from room-temperature tensile tests conducted at ANL.

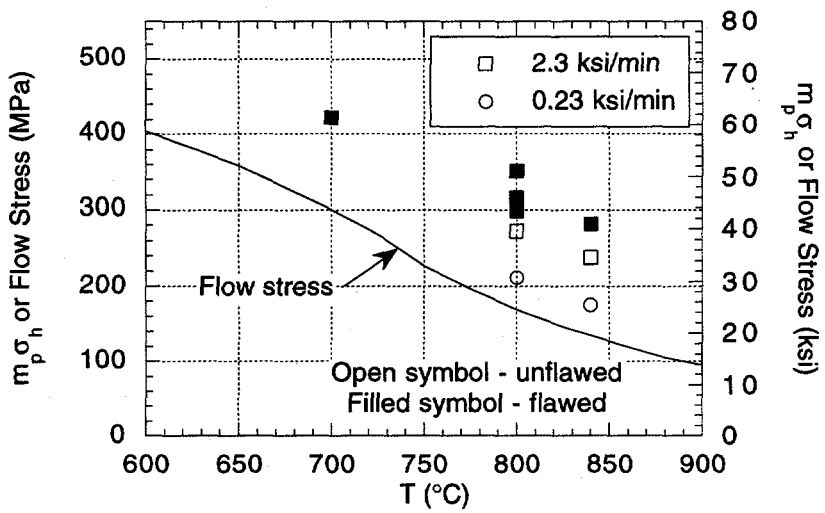

Figure 86. Flow stress curve based on INEL tensile tests and data obtained experimentally by pressure ramp tests on flawed and unflawed tubes.

4.7.5.2 Creep rupture model

Creep failure of an unflawed tube under varying stress and temperature conditions, based on a linear time-fraction damage rule such as the one used in Code Case N 47 of the ASME Code, Section III, can be predicted by a relatively straight-forward analysis[12] as follows:

$$\int_0^{t_f} \frac{dt}{t_R(T,\sigma)} = 1, \quad (52a)$$

where t_R is the time to creep rupture for a uniaxial specimen under a stress σ and temperature T, both of which may be functions of time, and t_f is the time to failure of the tube.

A rigorous analysis of flawed tubes under similar loading would be very complex. Therefore, the creep failure model was extended to flawed tubing with the assumptions referred to earlier, i.e., it was assumed that failure can be predicted by the equation

$$\int_0^{t_f} \frac{dt}{t_R(T, m_p\sigma)} = 1. \quad (52b)$$

Creep Rupture Properties of Alloy 600

To use the creep rupture model for predicting failure under severe-accident conditions, creep rupture properties (particularly at short lives) of Alloy 600 tubes in the hoop direction are needed. The available literature data on the creep rupture properties of Alloy 600 was reviewed. A compilation of the available data (233 data points) is shown in Fig. 87 in terms of the stress and the Larson–Miller parameter. These data represent both cold-worked and annealed materials. However, a preliminary examination of the data revealed no apparent clustering of the data due to the different thermomechanical treatment and data corresponding to both types of materials were included in the fits. A least–squares bilinear best fit is shown in Fig. 87, along with estimated 95% confidence limits. The best–fit curves for the Larson–Miller parameter P_{lm} are

$$\log_{10}\sigma = 4.31\pm0.10 - 1.43 \times 10^{-4} P_{lm} \quad \sigma \le 39.3 \text{ MPa}$$
$$\text{and} \quad \log_{10}\sigma = 5.03\pm0.13 - 1.81 \times 10^{-4} P_{lm} \quad \sigma > 39.3 \text{ MPa}, \quad (53a)$$

where the time to rupture t_R is

$$t_R = 10^{\frac{P_{lm}}{T} - 15} \quad (53b)$$

where t is expressed in h and T is expressed in K.

For actual calculations, the inverse of the expressions is more useful. In English units

$$P_{lm} = (24.3\pm0.7 - 3.0 \ln\sigma) \times 10^3 \quad \sigma \le 5.7 \text{ ksi}$$
$$\text{and} \quad P_{lm} = (23.2\pm0.7 - 2.4 \ln\sigma) \times 10^3 \quad \sigma > 5.7 \text{ ksi}, \quad (53c)$$

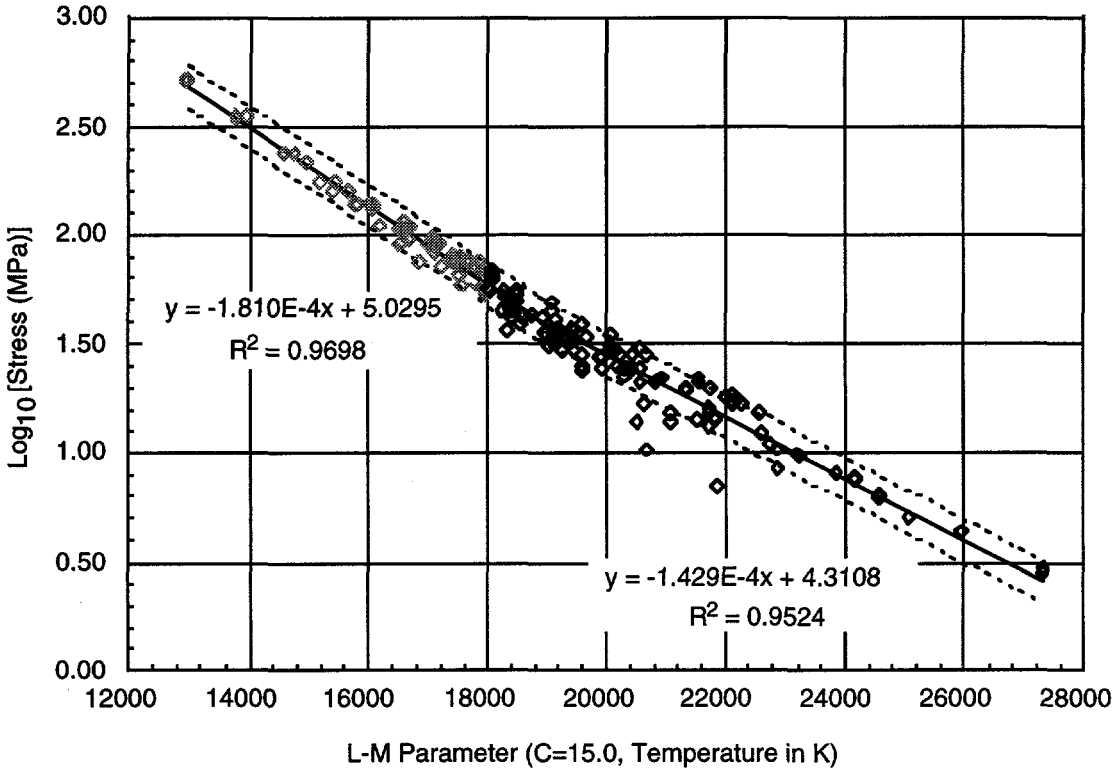

Figure 87. Bilinear fit to existing creep data for Alloy 600. The three low outliers were not included in the analysis; 95% confidence interval = 0.1009.

where lnσ is the natural log. The uncertainty in the Larson–Miller parameter reflected in Eqs. 53a and c is due primarily to differences in the heat–to–heat behavior of the materials.

The "breakpoint" in the bilinear fit occurs at a stress that is relatively low when compared with stresses of interest in SG tube failures. Even the nominal stress in an SG tube when the secondary system is depressurized is >130 MPa (19 ksi)—$\log_{10}\sigma \approx 2.1$. In the crack ligament the stress is even higher. Hence, for these applications, only the second Eq. 53c is actually used. The variance has been assumed to be the same for all stress levels; this is unlikely to be true. We expect that the variance will be less at the higher stresses of actual interest, but, as noted, very few data are available at higher stresses and it is difficult to quantify this judgment. The bounds predicted by Eq. 53c are expected to be conservative at the stress levels that are typical of flawed tubes.

Figure 88 shows the Larson–Miller correlation currently used in the SCDAP analysis along with the data. It is a reasonable fit to the data, but there clearly is some change in slope that is not reflected in the correlation. In particular, the slope departs from the data at the high stress levels (low LMP values) of interest in the present analyses.

To establish the applicability of Eqs. 53b and c to our tubing material, constant-pressure creep-rupture tests were conducted on unflawed 22-mm (7/8-in.)-diam tubes with both isothermal and constant-temperature-ramp loading. In Fig. 89, the experimental results are plotted against times to rupture predicted from Eqs. 53b and c. In all cases,

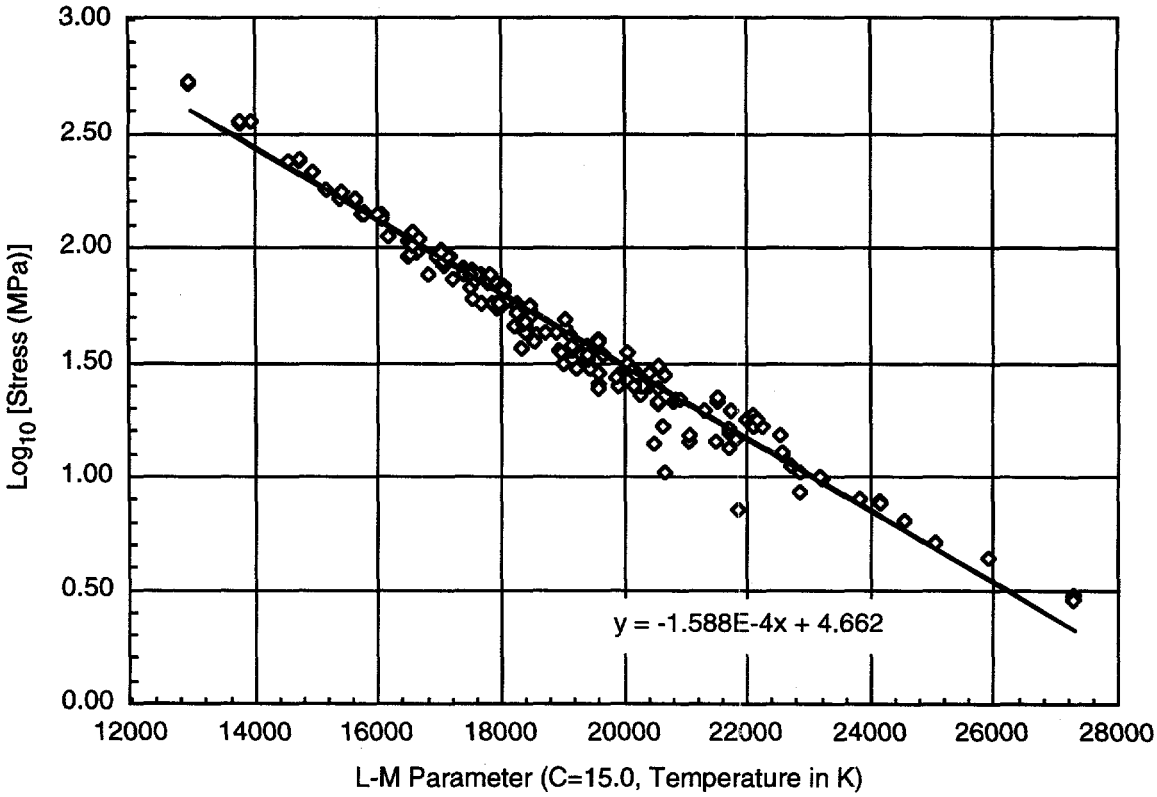

Figure 88. Current correlation used in SCDAP analysis and existing creep data.

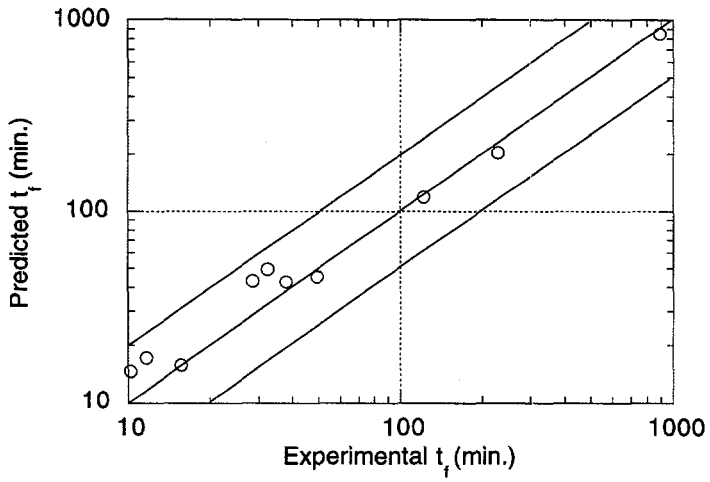

Figure 89. Experimental and predicted times to rupture of unflawed Alloy 600 tubing under constant internal pressure. Tests were conducted isothermally and under constant-temperature ramps of 0.2°C/min (0.36°F/min), 2°C/min (3.6°F/min), and 20°C/min (36°F/min).

the predicted rupture times are well within a factor of two of the experimental times, thus indicating that the above Larson-Miller representation of the data is adequate for our material.

Creep Rupture Properties of Type 316 Stainless Steel

Literature data on the creep rupture properties of Type 316 SS have also been reviewed. These data, as well as data for A508, Class 2 low-alloy steel (discussed in the next section), are of interest in the analysis of SG components other than the tubes under severe-accident conditions. For example, the piping for the secondary system coolant is fabricated of Type 316 SS, and the SG pressure vessel and nozzles are made of A508, Class 2 steel. It is of interest in the overall analysis of a SG in a hypothetical severe-accident scenario to determine the failure temperatures and times of these components relative to those of the Alloy 600 SG tubes.

The available data for Type 316 SS, expressed in terms of the Larson–Miller parameter and the stress is shown in Figs. 90 and 91. Least–squares linear and bilinear fits and the associated estimated 95% confidence limits are also shown. The best–fit curves for the Larson–Miller parameter P_{lm} are

$$\begin{aligned} &\log_{10}\sigma = 5.70 \pm 0.05 - 1.64 \times 10^{-4}\, P_{lm} && \sigma \le 122 \text{ MPa} \\ \text{and}\quad &\log_{10}\sigma = 5.16 \pm 0.05 - 1.40 \times 10^{-4}\, P_{lm} && \sigma > 122 \text{ MPa}, \end{aligned} \tag{54}$$

where the time-to-rupture t_R is

$$t_R = 10^{\frac{P_{lm}}{T} - 20.2}, \tag{55}$$

where t_R is expressed in h and T is expressed in K.

For actual calculations, the inverse of the expressions is more useful. In English units

$$\begin{aligned} &P_{lm} = (29.65 \pm 0.63 - 2.65 \ln\sigma) \times 10^3 && \sigma \le 17.70 \text{ ksi} \\ \text{and}\quad &P_{lm} = (30.97 \pm 0.74 - 3.10 \ln\sigma) \times 10^3 && \sigma > 17.70 \text{ ksi} \end{aligned} \tag{56}$$

where $\ln\sigma$ is the natural log.

The linear fit is

$$\log_{10}\sigma = 5.50 \pm 0.11 - 1.55 \times 10^{-4}\, P_{lm}, \tag{57}$$

where σ is expressed in MPa.

The corresponding inverse expression is

$$P_{lm} = (30.02 \pm 0.71 - 2.80 \ln\sigma) \times 10^3, \tag{58}$$

where σ is now expressed in ksi.

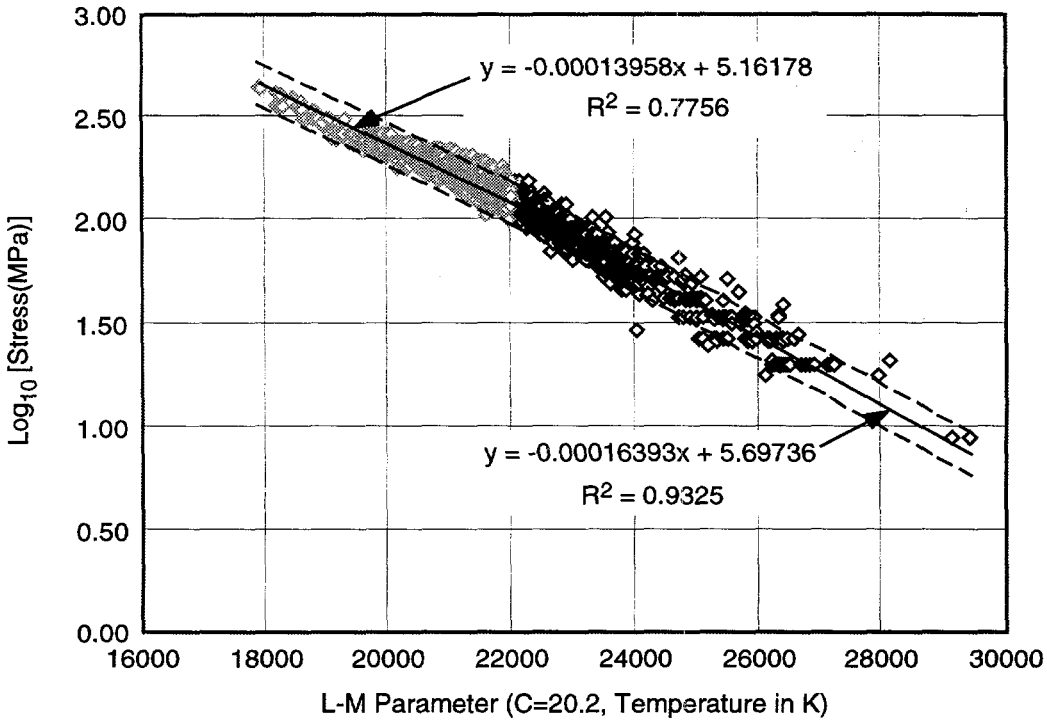

Figure 90. Bilinear fit to existing creep data for Type 316 SS; 95% confidence interval = 0.1043.

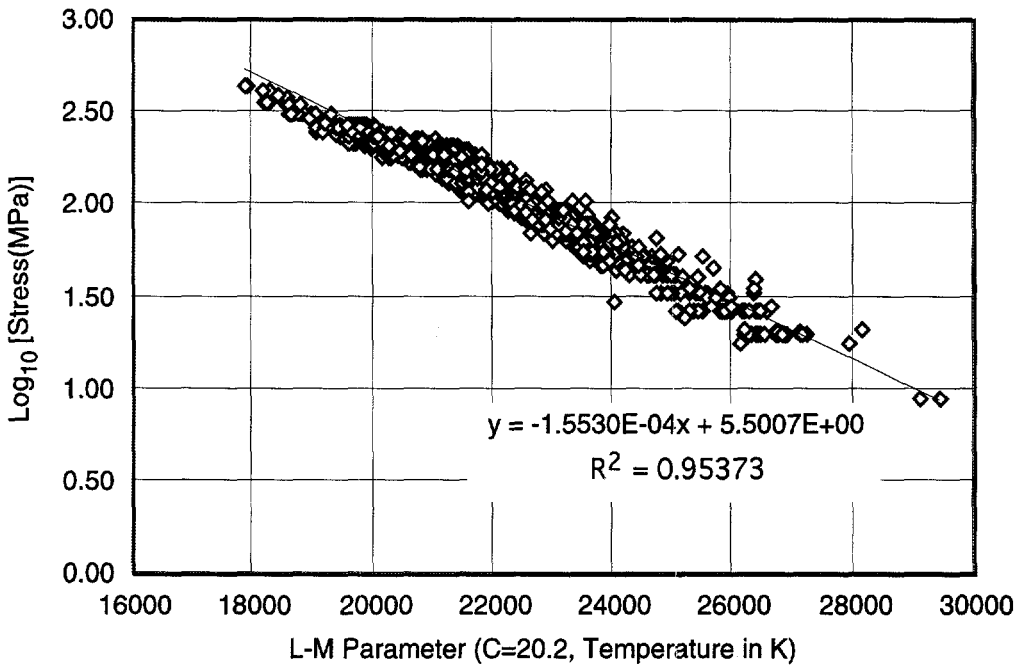

Figure 91. Linear fit to existing creep data for Type 316 SS.

The uncertainty bounds on the lives are approximately a factor of 5, i.e., the lower limit is ≈1/5 of the average, the upper limit is ≈5 times the average.

The predicted lives for the bilinear fit at 1050, 950, and 850 K are shown in Figs. 92–94, along with the lives predicted by the current SCDAP correlation.[19] The current SCDAP correlations predict lives that are very short when compared to the proposed correlation. At most stress levels, the SCDAP predictions lie almost on the estimated lower 95% confidence limit. The break in the SCDAP lives at 359 MPa (52 ksi) is significant only at lower temperatures, and physically represents a transition from creep type behavior to flow stress type behavior.

Figure 95 compares the stress-rupture lives of Type 316 SS and Alloy 600 at 650, 700, and 750°C. The curves shown in the figure for Type 316 SS were calculated from the Larson-Miller parameter fit described here, and the curves for Alloy 600 were calculated from Eq. 53c. At all three temperatures, the Type 316 SS is more resistant to stress rupture than Alloy 600.

Creep Rupture Properties of A508 Steel

Literature data on the creep rupture properties of A508, Class 2 low-alloy steel have also been reviewed and found to be quite limited. Although it is A508, Class 2 that is of interest, data for A508, Class 3 are included, because they seemed comparable and inclusion of these data effectively doubled the available data. The data, expressed in terms of the Larson–Miller parameter and the stress are shown in Fig. 96. A least–squares linear fit and the associated estimated 95% confidence limits are also shown. The best–fit curves for the Larson–Miller parameter P_{lm} are

$$\log_{10}\sigma = 4.91 \pm 0.20 - 1.78 \times 10^{-4} P_{lm}, \tag{59}$$

where σ is expressed in MPa.

The time to rupture t_R is

$$t_R = 10^{\frac{P_{lm}}{T} - 16.4}, \tag{60}$$

where t_R is expressed in h and T is expressed in K.

For actual calculations the inverse of Eq. 59 is more useful. In English units

$$P_{lm} = (22.85 \pm 1.13 - 2.44 \ln\sigma) \times 10^3, \tag{61}$$

where σ is expressed in ksi and $\ln\sigma$ is the natural log.

The bounds on the lives are approximately a factor of 14, i.e., the lower bound is ≈1/14 of the average, the upper bound is ≈14 times the average. The uncertainty bounds were computed from the standard deviation of the residuals. The actual 95% confidence bounds

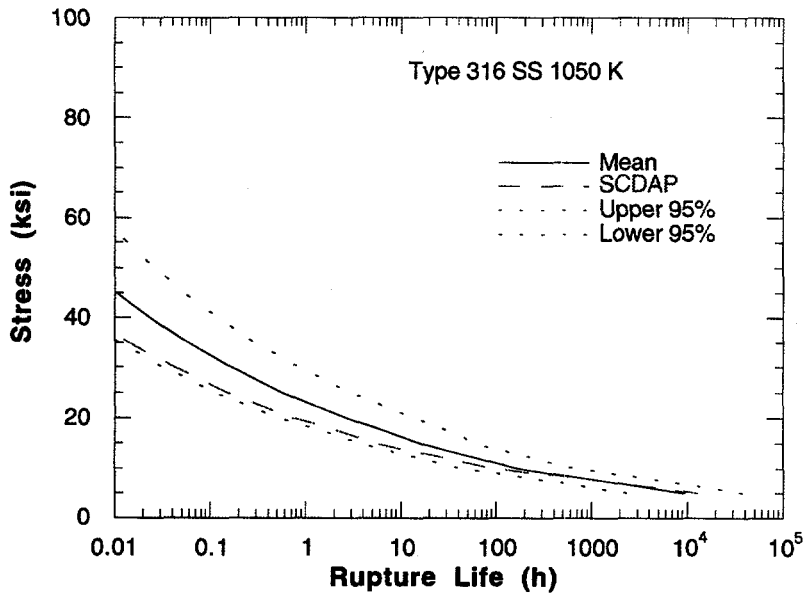

Figure 92. Estimated time to rupture for Type 316 SS at 1050 K.

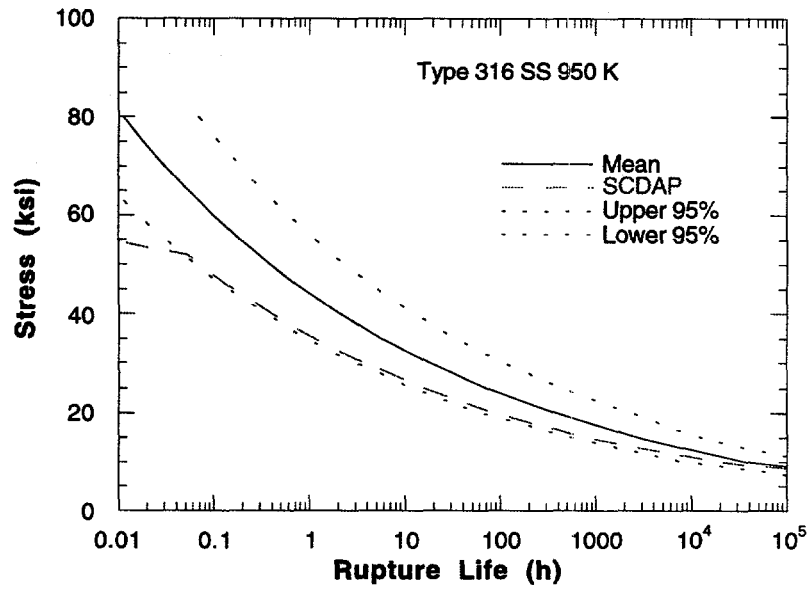

Figure 93. Estimated time to rupture for Type 316 SS at 950 K.

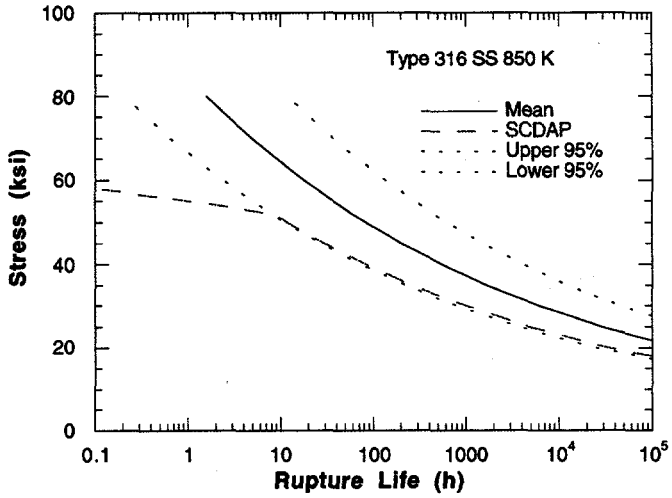

Figure 94. Estimated time to rupture for Type 316 SS at 850 K.

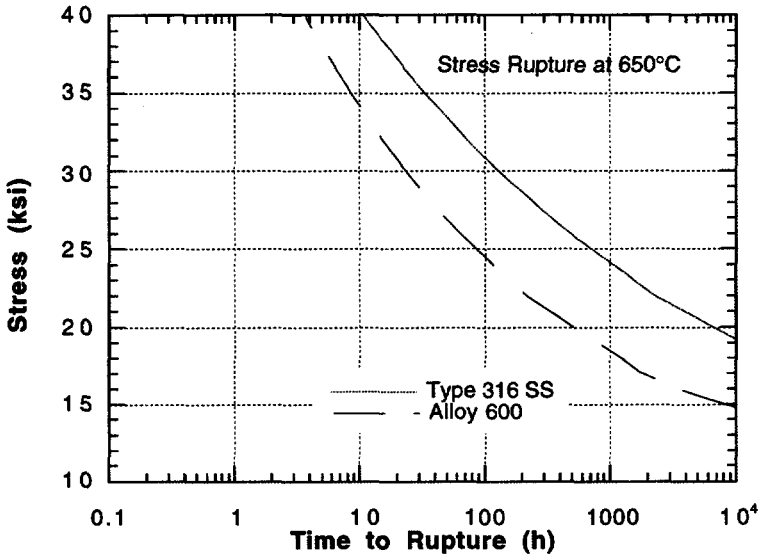

(a)

Figure 95. Stress-rupture properties of Alloy 600 and Type 316 SS at (a) 650°C, (b) 700°C, and (c) 750°C.

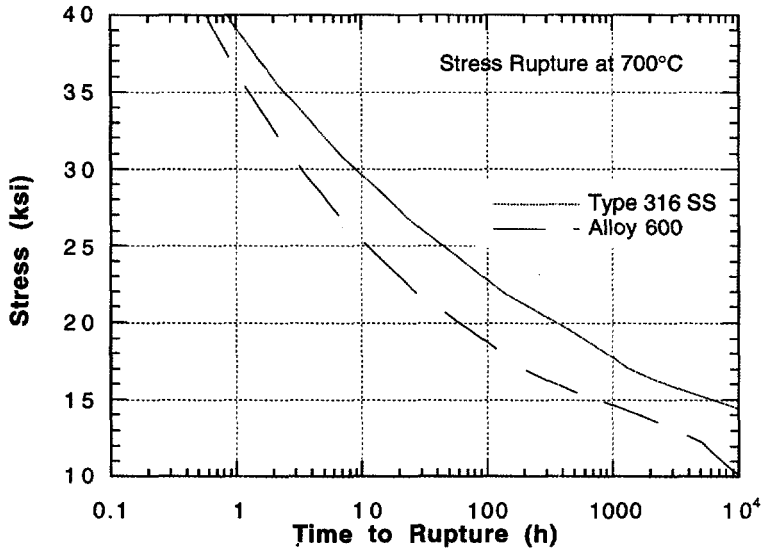

(b)

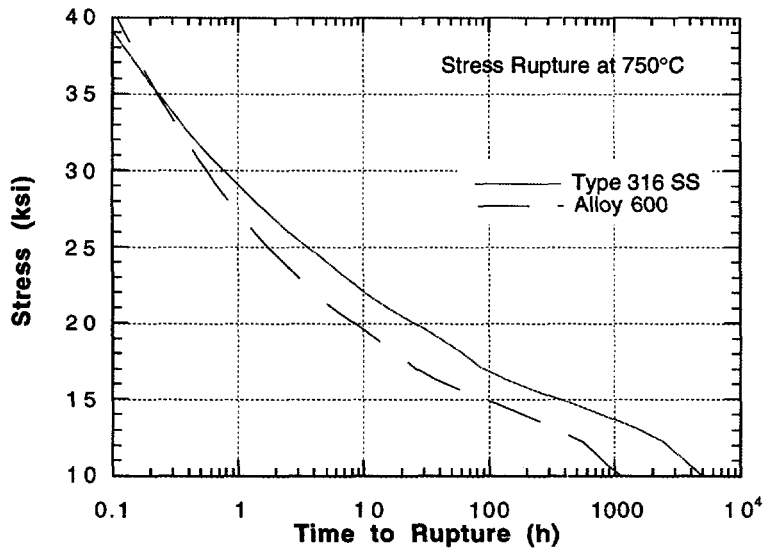

(c)

Figure 95. (Cont'd.).

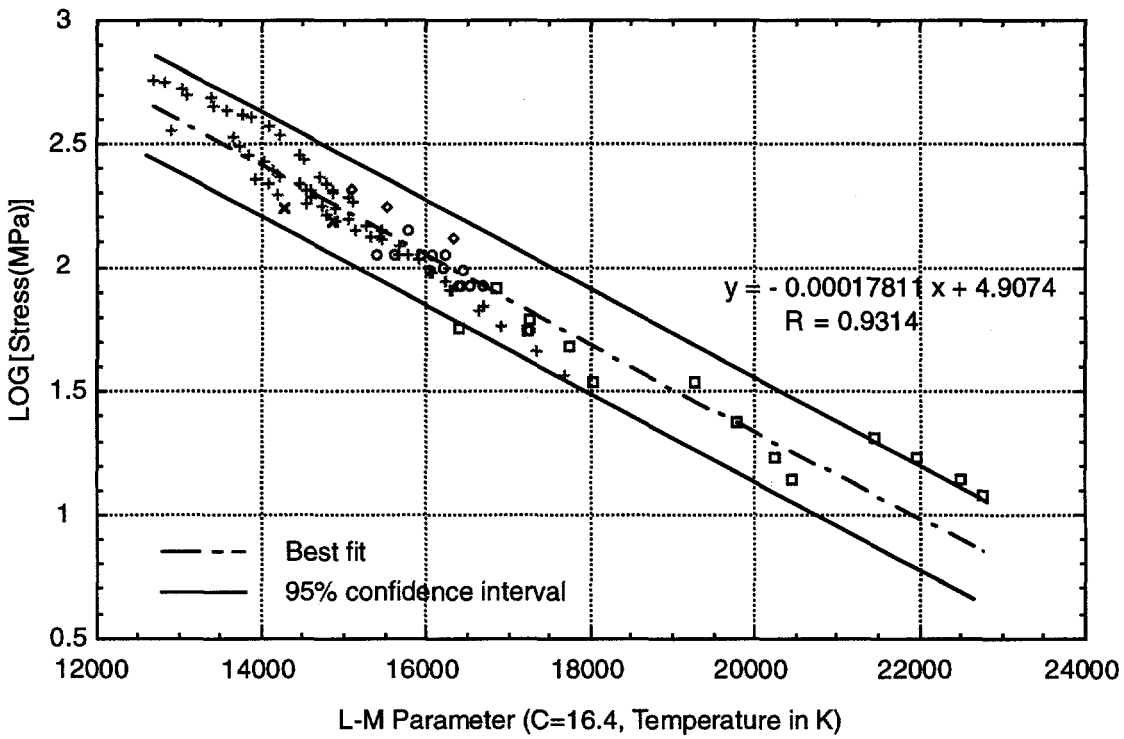

Figure 96. Linear fit to A508, class 2 creep data; 95% confidence interval = 0.2015.

should also include the uncertainty on the mean, which gives the well-known hour glass shape to the bounds away from regions for which large amounts of data are available. However, in this case the uncertainty on the mean is so small when compared with that associated with the residuals that it could be neglected to simplify the calculations. These bounds are roughly three times as large as those for Alloy 600 and Type 316 SS and reflect the relative paucity of data. It was hoped that this uncertainty could be reduced by comparing the uncertainty bounds for 2-1/4 Cr–1 Mo steel, which is a related low-alloy steel for which many more creep data are available. However, examination of these data lead to the conclusion that they are not comparable, and that the results for 2-1/4 Cr–1 Mo steel were not applicable to A508 Class 2 low-alloy steel.

The Larson-Miller parameter in the situations of interest in severe-accident analysis will probably be ≈15,000, a region in which there is a relatively large amount of data.

The correlations in the SCDAP documentation appear to be incorrect as given. Our best guess at the intended correlations are as follows:

$$t_r = 10^{\left[\left(\frac{T-1503.69}{P}\right)+3.499\right]} \qquad (62)$$

$$P = 158.233\log_{10}(\sigma) - 255.346 \qquad 0 \le \sigma < 14 \quad \text{(ksi)},$$

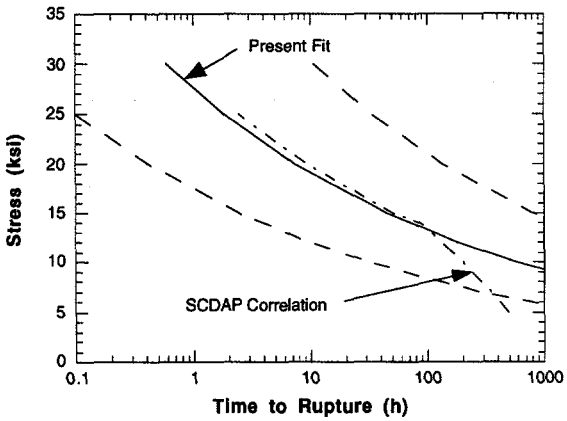

Figure 97. Time to rupture as a function of stress at 900K for the SCDAP correlation and the present fit. Dashed lines are 95% confidence limits.

and $t_r = 10^{\frac{P}{T}-20}$

$$P = -9603.0 \log_{10}(\sigma) + 46454 \qquad 14 \leq \sigma,$$

where T is expressed in degrees Rankine. The time to rupture as a function of stress for the SCDAP correlation and the present fit are compared in Fig. 97. Given the limited data that are available, the basis for introducing the break in slope at σ = 97 MPa (14 ksi), which corresponds to ≈2 on the log stress plot of Fig. 97, is unclear. The original INEL report that is referenced (EGG–EA–7431), gives a Larson Miller plot [Fig. 6 of the report] very similar to Eq. 59, and no break is shown at 97 Mpa (14 ksi).

4.7.6 Validation Tests for Creep Rupture Model

To validate the creep rupture model, several types of tests were conducted on both flawed and unflawed SG tubes. The tests were conducted in a single-zone furnace, using programmable temperatures and high-pressure nitrogen gas to apply internal pressures on the tubes. A temperature profile determined under both transient and steady-state conditions showed a maximum 5°C (9°F) axial variation within a 50-mm (2-in.) central section, with the center being the hottest. The maximum through thickness temperature gradient was <1°C (1.8°F).

4.7.6.1 Isothermal failure tests

Tests were conducted on flawed tubes by subjecting them to isothermal constant-pressure loading. The flaws were created in the specimens by EDM. Such notches are not as sharp as real cracks, but previous tests at lower temperatures have shown that crack tip geometry has very little effect on the failure loads.[32] At higher temperatures, the effect of the crack tip geometry would be expected to be even less significant. A summary of the tests is given in Table 14. The predicted failure times obtained for four different values of m_p are plotted against the experimental failure times in Fig. 98a for tubes that contained a

Table 14. Constant-pressure failure tests at various temperatures on specimens with and without flaws to validate m_p approach proposed by ANL. Also shown are the failure times predicted by the ANL creep rupture model.

Test No.	Crack Geometry 2c (in.)	a/h	m_p	Loading History[a] max. T (°C)	p (psi)	Failure Conditions T_f (°C)	p_f (psi)	t_f (min)	Pred. t_f (min)
T-37	1	0.59	1.96	667	2350	667	2350	336	128
T-56[b]	1	0.65	2.21	667	2350	667	2350	74	62
T-38	1	0.62	2.07	700	1915	700	1915	28	88
T-41	Unflawed		1	700	4500	700	4500[c]	38	42
T-61[d]	Unflawed		1	700	4450	700	4450	49	45
T-47	1	0.55	1.82	750	1400	750	1400	186	176
T-60	Unflawed		1	750	3290	750	3290	29	43
T-48	1	0.55	1.82	800	1400	800	1400	26	32
T-42	Unflawed		1	800	2350	800	2350	33	50

[a] Specimen pressure was first ramped to the indicated pressure at room temperature at a rate of 15.9 MPa/min (2300 psi/min) and held constant. The temperature was then increased following the EPRI ramp (Fig. 66) to the indicated temperature.

[b] Duplicate of test listed immediately above.

[c] Pressure decreased gradually from 4750 psi to 4250 psi during hold.

[d] Duplicate of test listed immediately above, but with pressure held constant at 4450 psi during hold.

crack that was ≈60% throughwall and 25 mm (1 in.) long. Except for a test at 667°C (1232°F), the failure lives predicted by the ANL m_p (Eq. 31c) are within a factor of 2 of the experimental lives. The predicted lives obtained with m_p values as determined by the BCL (Eq. 31b) and EdF (Eq. 46a) equations are also reasonable, but those obtained with the INEL equation (Eq. 45b) differ significantly in most cases. It should be noted that the flow stress model is incapable of predicting time to failure for tests of this type and, in fact, would predict that none of the tubes should have failed.

4.7.6.2 Failure tests of specimens with deep cracks

Some experimental data[34] indicate that the numerical values of m_p computed by the BCL equation for short and deep cracks are too high for tests conducted at low temperatures, where a flow stress model is valid. Results from tests, summarized in Table 15 and shown in Fig. 98b, confirm that this is also true at high temperatures. All of the test specimens in this figure contained cracks that were ≥90% throughwall. The BCL equation grossly overestimates the damaging influence (i.e., underestimates the time to rupture) of these cracks. The predictions obtained with the INEL and ANL equations are in better agreement with the results than predictions obtained with the BCL model. The

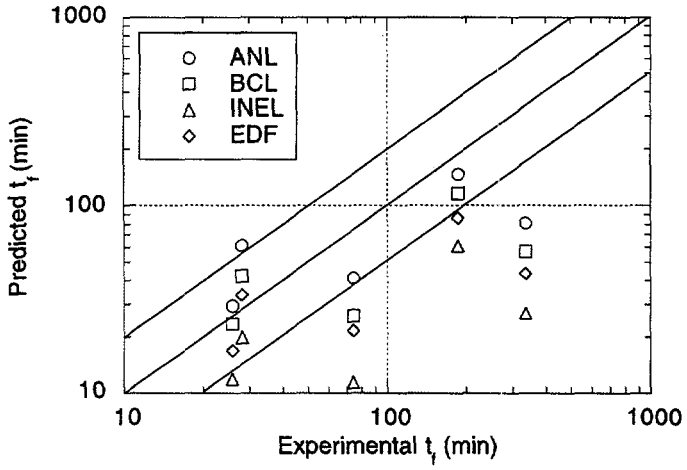

(a)

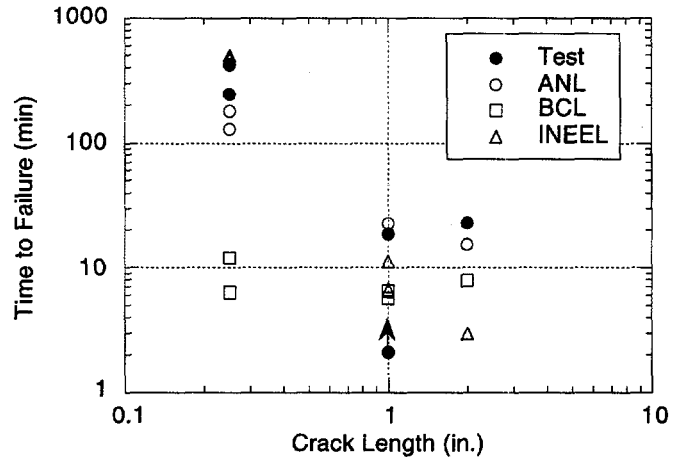

(b)

Figure 98. (a) Experimental and predicted times to rupture of flawed Alloy 600 tubing tested isothermally under constant internal pressure, for shallow flaws 25 mm (1 in.) long and 56–65% throughwall at temperatures between 667 and 800°C (1232 and 1472°F); and (b) relationship of crack length to time to failure for flaws that were between 90 and 92% throughwall at 800°C (1472°F). Arrow indicates pin hole failure in which pressure was undiminished after failure, but the test was interrupted.

Table 15. Constant-pressure failure tests on specimens with deep flaws to validate the new m_p correlation proposed by ANL. Also shown are the failure times predicted by the ANL creep rupture model.

Test No.	Crack Geometry 2c (in.)	a/h	m_p	Loading History[a] max. T (°C)	p (psi)	Failure Conditions T_f (°C)	p_f (psi)	t_f (min)	Pred. t_f (min)
T-55	0.25	0.91	2.45	800[a]	750	800	750	420	180
T-78[b]	0.25	0.92	2.61	800	750	800	750	246	130
T-83	Unflawed		1	800	1800	800	1800	228	202
T-72	1	0.92	7.62	800	356	800	356	19	23
T-84	1	0.91	6.85	800	450	800	450	2	18
T-87	Unflawed		1	800	2910	800	2910	12	15
T-66	2	0.90	7.83	800	300	800	300	23	15
T-85	Unflawed		1	800	3000	800	3000	10	13

[a] The temperature of the specimens was first increased from room temperature to 800°C in 1 h with no internal pressure. The pressure was then ramped at 15.9 Mpa/min (2300 psi/min) to the indicated value.

[b] Duplicate of test listed immediately above.

predictions obtained with the EdF equation are not shown in Fig. 98b because, at high temperatures, they are essentially the same as the BCL predictions. At low temperatures, the EdF model[34] predicts a smaller m_p for cracks that are >85% throughwall than the BCL model because the flow stress in the BCL equation is replaced by the ultimate tensile strength (see Eq. 46b). However, there is little difference between the flow stress and the ultimate tensile strength at high temperatures because strain hardening is greatly reduced. Overall, as in the low-temperature case, the ANL equation for m_p gave the best predictions for failure lives of specimens with shallow as well as deep cracks and was used for the analysis of the high-temperature tests.

4.7.6.3 Pressure and temperature ramp tests

To evaluate the importance of loading rates on the failure conditions and compare the predictive capabilities of the creep rupture and the flow stress models, two additional types of tests were conducted. In the first type, the specimens were heated to a given temperature and then pressurized isothermally at a constant pressure ramp until failure. In the second type, the specimens were first pressurized at low temperature and then, with the pressure held constant, they were subjected to a constant temperature ramp until failure. Test conditions and the results obtained are summarized in Tables 16 and 17. Results from both types of tests, plotted in Figs 99a and b, show that the loading rate (pressure or temperature), which is ignored in a simple flow stress model, significantly

Table 16. Constant-pressure temperature ramp tests to validate creep rupture model. Also shown are the failure temperatures predicted by the ANL creep rupture model.

Test No.	Crack Geometry			Loading History[a]		Failure Conditions	
	2c (in.)	a/h	m_p	Ramp rate (°C/min)	p (psi)	T_f (°C)	Pred. T_f (°C)
T-62	Unflawed		1	20	2350	913	916
T-63	Unflawed		1	2	2350	843	838
T-71	Unflawed		1	0.2	2350	779	770
T-67	1	0.65	2.21	20	1065	892	916
T-68	1	0.65	2.21	0.2	1065	770	778
T-74	1	0.93	8.60	0.2	270	860	918
T-73	1	0.93	8.60	0.2	1065	612	604
T-76	0.25	0.89	2.22	20	1090	915	911
T-77	0.25	0.9	2.32	0.2	1040	778	766
T-59	2	0.79	3.93	2	750	810	801
T-79	2	0.92	9.68	0.2	245	815	914
T-80[b]	2	0.92	9.68	0.2	245	859	914
T-81	2	0.93	10.99	0.2	217	678	768

[a] The specimens were first pressurized to the indicated value, and the temperature was then ramped to 600°C in 1 h, followed by the indicated temperature ramp to failure.

[b] Duplicate of test listed immediately above.

influences the failure, even for unflawed tubes. Figure 99, which shows results from pressure ramp tests on flawed and unflawed tubes, clearly indicates that the flow stress model would grossly underpredict the failure pressures for the higher ramp rate tests if the INEL flow stress curve were used. The failure pressures are much closer to those predicted by the creep rupture model; see Fig. 99a. The pressures in the temperature ramp tests on flawed specimens were selected so the products of m_p and the nominal hoop stresses were approximately equal for two crack geometries. Thus, the predicted failure temperatures for both geometries fall approximately on a single line for either the creep rupture or flow stress models, as shown in Fig. 99b. The experimental results are in much better agreement with the predictions of the creep rupture model and confirm that the effect of flaws on failure can be characterized by the m_p approach. Therefore, the creep rupture model can be expected to more reliably predict failure under varying

Table 17. Isothermal pressure ramp tests to establish the maximum flow stress curve. Also shown are the failure pressures and times predicted by the ANL creep rupture model.

	Crack Geometry			Loading History[a]		Failure Conditions			
Test No.	2c (in.)	a/h	m_p	T (°C)	Ramp rate (psi/min)	p_f (psi)	t_f (min)	Pred.p_f (psi)	Pred. t_f (min)
T-35	Unflawed		1	840	2300[b]	3000	3.3	3000	5.8
T-36	Unflawed		1	840	2300[b]	4000	1.8	4000	2.8
T-46	Unflawed		1	840	2300	4190	1.8	4987	2.2
T-45	Unflawed		1	840	230	3090	13	3390	15
T-86	Unflawed		1	800	230	3730	16	4115	18
T-82	Unflawed		1	800	2300[b]	4800	2.2	4800	3.4
T-57	0.25	0.75	1.58	800	2300	3520	1.5	3520	1.8
T-58	1	0.79	3.32	800	2300	1590	0.7	2194	0.9
T-70	1	0.65	2.21	840	2300	2250	1.0	2570	1.1
T-69	1	0.65	2.21	800	2300	2740	1.2	3020	1.3
T-75	1	0.65	2.21	700	2300	3370	1.5	4860	2.1

[a] Specimen temperatures were ramped following the INEL ramp (Fig. 65) to the indicated temperatures and held constant, with no internal pressure. The pressure was then ramped at the indicated rate to the final value.
[b] Held at maximum pressure.

temperature and pressure histories during severe accidents than a simple rate-independent flow stress model.

4.7.6.4 Tests under simulated severe accident time-temperature histories

Tests were performed at ANL to determine the behavior of flawed tubes under time/temperature histories similar to those projected to occur under severe accident conditions. The purpose of the tests was to further validate the creep rupture model to support its use to determine the time to failure of flawed tubes under projected time/temperature histories in which temperatures could rise to as high as 850°C (1562°F).

In all of the tests, the internal pressure was held constant at 16.2 MPa (2350 psi). Tests were conducted on tubes with ODs of both 19 mm (3/4 in.) and 22 mm (7/8 in.) and wall thicknessess of 1 mm (0.043 in.) and 1.3 mm (0.050 in.), respectively. Four nominal flaw geometries with axial lengths of 6 mm (0.25 in.), 25 mm (1 in.), and 50 mm (2 in.) and depths varying from 20 to 65% throughwall were tested. The actual flaw depths were determined by fractography after the tests. In many cases, they were also measured prior

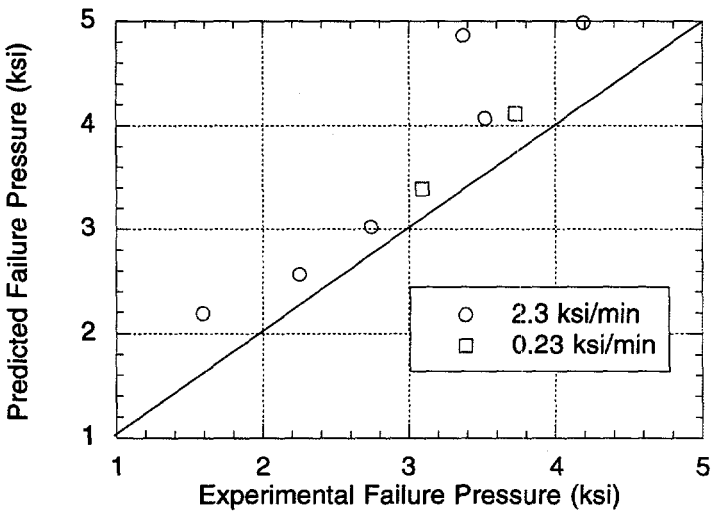

(a)

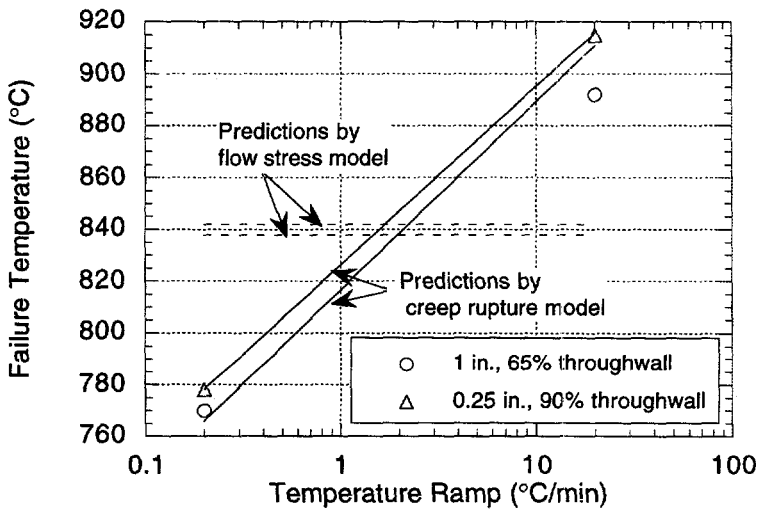

(b)

Figure 99. (a) Experimental and predicted failure pressures of flawed and unflawed tubes subjected to two pressure ramps isothermally at 700-840°C (1292-1472°F) and (b) relationship of failure temperature to temperature ramp rate for flawed tubes subjected to two temperature ramps with constant internal pressures chosen so that the product of m_p and nominal hoop stress were kept approximately constant.

to the tests by a replication technique. The differences between the two measurements, when available, were not large. Duplicate tests were run for all 22-mm (7/8-in.)-diam tubes.

For the tests to date, two time/temperature histories have been considered. Both are based on preliminary analyses of an accident sequence that involved total station blackout with a stuck-open SG secondary-side atmospheric dump valve, resulting in loss of feedwater and secondary-side depressurization. One history, which is referred to as the "INEL ramp," is based on a preliminary analyses by INEL;[19] the other, referred to as the "EPRI ramp," is based on a preliminary analysis reported by EPRI.[20] These two time/temperature scenarios are shown in Fig. 64; Figs. 65 and 66 show the time-temperature histories used in the ANL tests. In both series of tests, the specimens were first heated rapidly to 300°C (572°F), equilibrated at 300°C (572°F), and then subjected to the test ramps. Both analyses also predict depressurization of the system due to the failure of the surge line. Because the primary purpose of our tests was to help develop a failure model, the tests have ignored the predicted depressurization. The EPRI analysis also predicts a reduction in temperature after a short 5-min hold at 667°C (1232°F). To increase the contribution of creep damage in the tests, the EPRI temperature history was arbitrarily modified to include a 2-h hold time at 667°C (1232°F) and ignored the predicted reduction of temperature after the hold. If the specimen did not fail in 2 h of constant temperature hold, it was subjected to a temperature ramp of 2°C/min (3.6°F/min) until failure. Neither ramp chosen for the tests was intended to be an accurate representation of a particular sequence, but together they can represent a range of histories for which a failure model would be needed. Thus, although the INEL and EPRI analyses predict that failure of the surge line nozzle and consequent depressurization of the system will occur prior to the failure of the SG tubes, the tests at ANL were continued with full pressure until failure occurred.

Thirty two ramp tests have been performed using the INEL and EPRI time/temperature histories. Results from these tests are summarized in Tables 18 and 19 and Figs. 100a and b. In addition to failure data, Tables 18 and 19 also include crack depths measured by posttest fractography. The predicted failure temperatures and times in Figs. 68a and b were calculated with the creep rupture model and the ANL correlation for m_p, Eq 31c. The test results are replotted in Figs. 101a and b to show the dependence of the time to failure on m_p. The numbers on the abscissa of Figs. 101a and b are the stress magnification factors m_p, as calculated by Eq. 31c; m_p can be considered a measure of crack severity that takes into account both the length and the depth of the crack. The difference between failure temperature of a flawed tube and that of an unflawed tube increases with increasing m_p. The failure temperature depends on the time/temperature history. The EPRI ramp, which includes a 2-h hold time, leads to lower failure temperatures than the INEL ramp, which does not include such a constant temperature hold. The deleterious effect of the 2-h constant-temperature hold of the EPRI ramp increases with increasing severity of the crack. For the unflawed tubes there is little difference between the failure temperatures for the two histories, but for the most severe flaw geometries, there are significant reductions in the temperatures at which failure occurs with the EPRI ramp. This observation confirms that for time-temperature histories that are characteristic of severe-accident sequences, the particular history can significantly influence the failure temperature.

Table 18. Flaw sizes and temperatures at failure for INEL ramp tests. Also shown are the failure temperatures predicted by the ANL creep rupture model.

	19.05-mm (0.750-in.)-Diam Tube				22.34-mm (0.875-in.)-Diam Tube			
2c (in.)	Test No.	a/h	T_f (°C)	Pred. T_f (°C)	Test No.	a/h	T_f (°C)	Pred. T_f (°C)
Unflawed	T-2	Unflawed	823	837	T-10	Unflawed	835	844
Unflawed	T-13	Unflawed	826	837	T-30	Unflawed	843	844
0.25	T-12	0.59	798	806	T-7	0.65	803	806
0.25	-	-	-	-	T-34	0.62	802	809
1	T-11	0.61	758	752	T-9	0.54	768	784
1	-	-	-	-	T-33	0.54	778	792
2	T-3	0.45	774	788	T-6	0.36	808	805
2	T-14	0.35	805	803	T-32	0.41	800	803
2	T-4	0.2	808	816	T-5	0.16	825	824
2	-	-	-	-	T-31	0.22	817	818

Table 19. Flaw sizes and temperatures at failure for EPRI ramp tests. Also shown are the failure temperatures predicted by the ANL creep rupture model.

	19.05-mm (0.750-in.)-Diam Tube				22.34-mm (0.875-in.)-Diam Tube			
2c (in.)	Test No.	a/h	T_f (°C)	Pred. T_f (°C)	Test No.	a/h	T_f (°C)	Pred. T_f (°C)
Unflawed	T-22	Unflawed	828	833	T-19	Unflawed	839	842
Unflawed	-	-	-	-	T-28	Unflawed	843	842
0.25	T-23	0.57	767	772	T-18	0.66	779	786
0.25		-	-	-	T-24	0.66	781	782
1	T-29	0.54	726	702	T-16	0.57	724	692
1	-	-	-	-	T-27	0.55	724	727
2	T-21	0.40	760	745	T-15	0.30	794	786
2	-	-	-	-	T-26	0.41	770	762
2	T-20	0.12	814	814	T-17	0.20	816	802
2	-	-	-	-	T-25	0.21	817	811

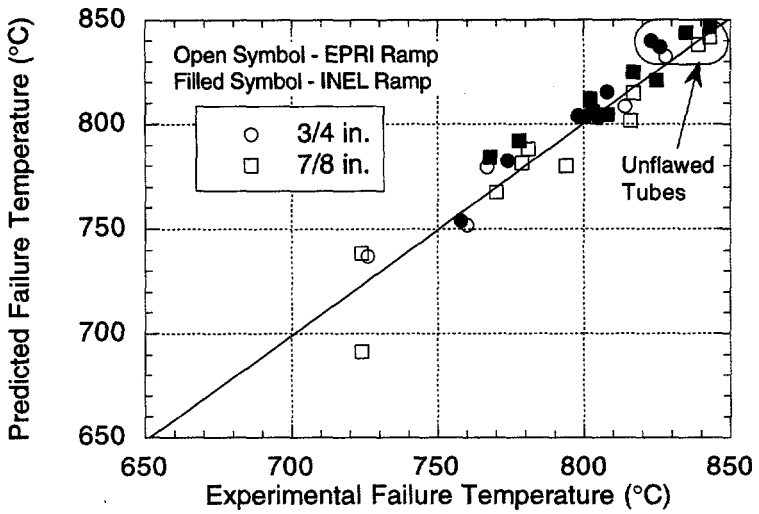

(a)

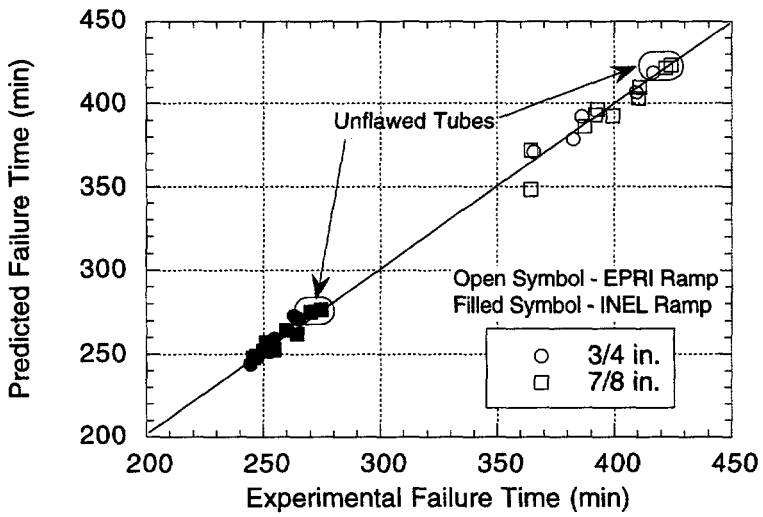

(b)

Figure 100. Predicted (by creep rupture model) versus experimental (a) failure temperatures and (b) times to failure for high-temperature rupture tests conducted with INEL and EPRI temperature ramps.

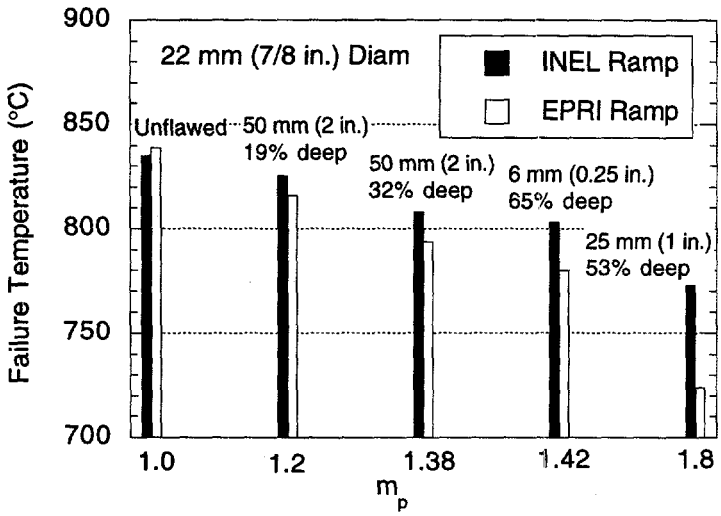

(a)

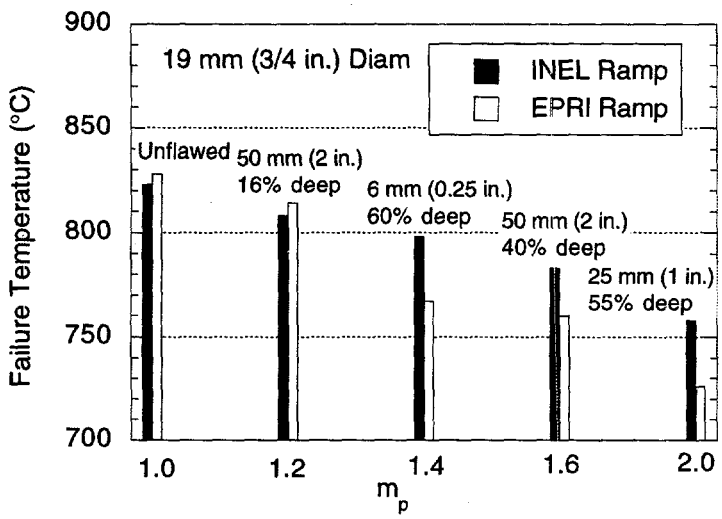

(b)

Figure 101. Summary of experimentally observed failure temperatures for severe accident tests on (a) 22.23-mm (0.875-in.)-diam tubes and (b) 19.05-mm (0.750-in.)-diam tubes. The abscissa shows average magnification factors (Eq. 31c) m_p for each crack configuration.

Table 20. Errors in failure temperatures (°C) obtained when INEL and EPRI ramp test data were analyzed with various models for m_p.

Errors	Models			
	ANL	BCL	PNNL	INEL
Mean	2.5	7.5	11.6	14.5
RMS	9.7	14.2	18.9	18.8
Maximum	24.7	48.4	59.0	59.0

Evaluation of Stress Magnification Factor m_p in Flawed Tubes for High-Temperature Tests

The various m_p models were evaluated using the low-temperature tube failure results obtained at PNNL,[32] as reported in Table 13. The high temperature INEL and EPRI ramp tests were also analyzed with ANL, BCL, PNNL, and INEL correlations for m_p. Table 20 presents the errors in failure temperature (relative to PNNL results[32]) that were obtained when INEL and EPRI ramp tests were analyzed with the ANL, BCL, PNNL, and INEL models. Although the m_p models were based on the low-temperature tests, they appear capable of accurately predicting high-temperature situations, where creep damage is predominant, i.e., m_p seems to depend primarily on geometric factors not material characteristics. The ANL and BCL models give significantly better results than the PNNL and INEL models in these tests. Considering the relatively small differences in the predicted values of m_p for most crack depths and sizes, the differences are somewhat surprising. However, the matrix for these tests was heavily weighted towards cracks with $a/h \approx 0.6$, where the differences between the BCL type models and the PNNL, INEL type models are relatively large. The test results suggest that the ANL and BCL models are more accurate in this range. Additional isothermal creep failure tests (discussed in an earlier section on validation tests) performed with deep cracks ($a/h \approx 0.9$) showed that either the ANL or the INEL correlation for m_p was appropriate for this geometry. The results from these tests confirmed that the original BCL model overestimates m_p for such deep cracks, a finding consistent with the behavior observed in the low-temperature tests at EdF and PNNL, and that either the ANL or the INEL model gives much better predictions for such deep cracks. However, when both shallow and deep cracks are included, the ANL model gives the best overall predictions.

Predictions by Flow Stress Models

The times to failure for the INEL and EPRI ramp tests were also predicted with the flow stress models. The predictions of the flow stress models are compared with experimental results in Figs. 102a and 70b. The predicted values were calculated with the INEL flow stress curve (Fig. 85, Eq. 60a) and the ANL stress magnification factor (Eq. 31c). Although the predictions for the tests with the EPRI ramp are reasonably good, the failure temperatures and times for the tests that used the INEL ramp were significantly underpredicted. The accurate prediction of the EPRI ramp tests is probably a fortuitous

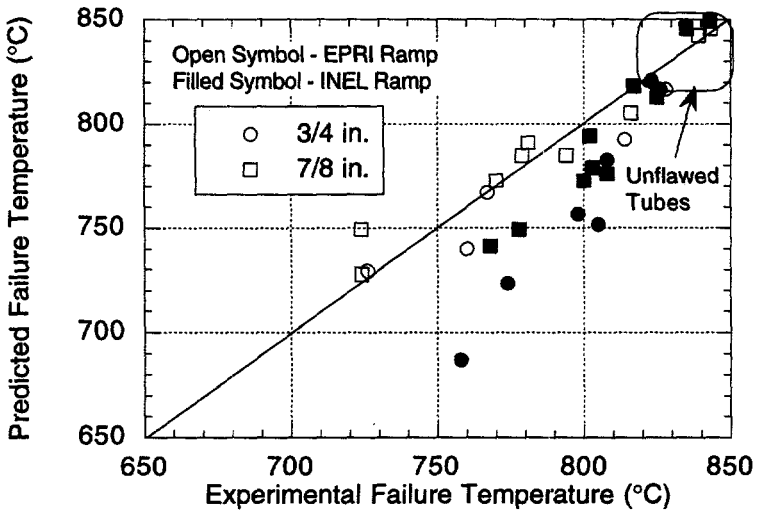

(a)

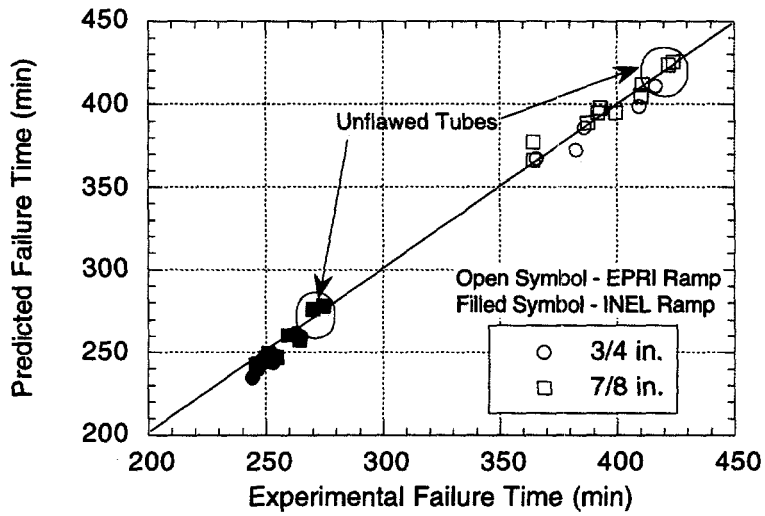

(b)

Figure 102. Predicted (by flow stress model) vs. experimentally observed (a) failure temperatures and (b) times to failure for high-temperature rupture tests conducted with the INEL and EPRI temperature ramps.

consequence of the average strain rates in the ligament being close to the strain rate used in the tensile tests from which the flow stress curve was derived. Overall the agreement is much better with the predictions of the creep rupture model.

4.7.7 Uncertainty in Predictions

As mentioned earlier, the uncertainty in the Larson–Miller parameter reflected in Eq. 62c is due primarily to differences in heat–to–heat behavior of materials. For the tubes used in the validation tests at ANL, the best fit to the experimental data is obtained when the constant in Eq. 62c is taken to be 23.1, i.e., the tubes seem to represent fairly "average" heats of material. In "sampling" from the population represented by Eq. 62c when computing damage, a single member of the population represented by Eq. 62c is selected and used for the entire history; the sampling is performed once for each history not for each time step. The variability observed in replicate tests on the same heat of material could be taken into account by assuming that the accumulated damage at failure is distributed, i.e., at failure, $D = 1 + \beta$, where β is a random variable that could be estimated from the variability observed in replicate tests. This variability, however, is small when compared with that observed in heat–to–heat variations. For tubes with flaws, it is assumed that failure is controlled by Eq. 61b, where the effective stress is given by the nominal hoop stress multiplied by the magnification factor m_p, which is a function of crack geometry. For a given time/temperature history, the time to failure is a function only of m_p and the creep properties.

4.7.8 Discussion of Models

At high temperatures (>700°C), the simple rate-independent flow stress model cannot account for the rate effects observed in isothermal pressure ramp tests or constant-pressure temperature ramp tests. The flow stress model predicts failure at constant pressure and constant failure temperature, respectively, for these two types of tests, independent of the ramp rates, contrary to the test results. Furthermore, the flow stress model incorrectly predicts no failure for the isothermal constant pressure failure tests that experienced time-delayed failure. To develop a flow stress model that can account for the effects of rate on failure of flawed SG tubes, some major theoretical developments would be required. The semi-empirical creep rupture model developed at ANL can account for the rate effects reasonably well in all of the tests conducted to date by relatively simple calculations. It can also predict the time to failure for the isothermal constant-pressure failure tests reasonably well.

In general, the failure temperatures and times predicted by the flow stress models are closer to the experimentally measured values for the EPRI ramp than to the values for the INEL ramp. The flow stress models tend to underestimate the failure temperatures of the most severe cracks by ≈60°C (108°F) for the INEL ramp tests. However, they appear to predict the failure temperatures for the EPRI ramp tests, which include a 2-h constant-temperature hold, much better.

Independent of any model, the EPRI ramp produced more damage than the INEL ramp (see Fig. 101). For a given crack geometry, the flow stress prediction for the failure temperature is nominally independent of the temperature ramp history. In reality, the

values obtained for flow stress at high temperatures are quite sensitive to the strain rates at which the flow stress is measured, and the flow stress models would not be expected to give good results for histories that produced strain rates too different from those in the test used to determine the flow stress. Thus, the flow stress models might be expected to be more applicable to the loading history that did not contain a constant-temperature hold. That the agreement is better for the EPRI ramp is probably fortuitous. Conservatism in the flow stress model that may be associated with the stress analysis or the strain rates used in the tensile tests to determine the flow stress are balanced by the additional damage associated with the 2 h hold of the EPRI ramp. It is likely that predictions obtained with the flow stress models would not be as favorable if the hold time for the EPRI ramp were at a lower temperature (≤500°C [932°F]) where creep is negligible, or if the hold time was at a higher temperature, where creep damage would be more extensive.

The creep rupture model correctly predicts the EPRI ramp to be more damaging than the INEL ramp. Also, it predicts the failure times and temperatures for both ramps more accurately than the flow stress model.

4.7.9 Conclusions

Available flow stress models for predicting failure of flawed SG tubing under normal operating conditions and design basis accidents have been reviewed. All of the models predict similar failure rupture pressure for shallow axial cracks, but give failure rupture pressures that differ significantly when the cracks are deep. A new correlation developed under this study using the PNNL data from earlier studies appears to correlate data for all flaw depths better than the existing ones. The new correlation is supported by detailed finite-element analysis.

The failure pressure for tubes that contain unsymmetrical circumferential cracks has recently been observed experimentally to increase in the presence of lateral constraint. Detailed finite-element analyses show that such behavior is to be expected and that a tube support plate spacing of 0.65 m (26 in.) or less should increase the failure rupture pressure to almost that of a fully constrained tube.

Tests conducted on unflawed and flawed specimens at the high temperatures postulated for severe accidents show that the failure pressure at a constant temperature is dependent on the pressure ramp rate and that the failure temperature at a constant pressure is dependent on the temperature ramp rate. Whereas the rate-independent flow stress model cannot predict such a behavior, the creep rupture model developed in this study can do so.

The creep rupture model has been validated with failure tests on flawed specimens with various loading histories. While the flow stress model is incapable of predicting the time to failure of flawed specimens under isothermal, constant-pressure loading, the creep rupture model can do so. Finally, the creep rupture model can predict failure times and temperatures of both flawed and unflawed tubes that have been subjected to varying temperature and pressure histories more accurately than the flow stress models. Therefore, it is recommended that the creep rupture model be used to evaluate failure of SG tubes under severe accidents scenarios.

5 Tube Removals from Steam Generators (W. J. Shack and D. R. Diercks)

This new task was created in July 1996, and its objective is to remove and obtain tubes and sections from retired SG(s) for use in the other research tasks in this program. The work to be performed under this task may be divided into three activities: (1) review of inspection records and other plant data to determine which tubes to remove; (2) arranging for necessary on-site support services, such as radiation control, health physics support and monitoring, and area power; and (3) arranging for access to the tubes, the actual cutting and removal of tubes and sections that contain tubes and portions of the tube sheet and tube support plates, and packaging and shipment of the removed tubes and sections to ANL.

The possible acquisition of tubes from one or more of the Salem Units 1 and 2 SGs that have been scheduled for replacement in late 1996 and early 1997 has been discussed extensively with Public Service Electric and Gas (PSE&G), the utility that owns and operates Salem 1. Initially, PSE&G had been considering the option of having the old SGs disassembled for recycling, in which case tubes could be made available without great difficulty. However, the utility has, instead, decided to dispose of the SGs by burial at Barnwell, and tube sampling is not possible at that site. Other options are currently being explored for the possible sampling of one of the Salem SGs, but no decision has been reached.

Discussions are simultaneously in progress with Duke Power Company about obtaining tubes from one of the McGuire Unit 1 SGs, which are to be replaced between January and May 1997. Duke has indicated a willingness to permit ANL (or its contractor) to perform sampling on site in the mausoleum that has been constructed for long-term storage. Duke has provided ANL with records from the most recent NDE of the present SGs to permit ANL to begin to select possible tubes and sections for recovery. The details of an agreement with Duke Power Company are currently being negotiated.

Contacts have also been made with Florida Power and Light about the recovery of tubes from the Combustion Engineering SGs being replaced at St. Lucie, and with South Carolina Electric and Gas about obtaining tubes from the Westinghouse D-3 units at Virgil Summer. All of these discussions are now at an early stage, and no commitments have been made.

References

1. Voltage–Based Interim Plugging Criteria for Steam Generator Tubes, U.S. Nuclear Regulatory Commission Report NUREG–1477 (Draft), June 1993.

2. D. Dobbeni, D. Degreve, J. P. Roussseaux, and M. Zavadsky, NDE of Sleeved Tubes: Belgian Approach, EPRI 14th Steam Generator Workshop, Seattle, Aug. 7-9, 1995.

3. H. Houserman, R. Warlick, and R. Vollmer, Using Satellite Technology to Improve SG Eddy Current Inspections, *Nucl. Eng. Int.*, Vol. 37, No. 456, July 1992, pp. 37–38.

4. D. L. Atherton, D. D. Mackintosh, S. P. Sullivan, J. M. S. Dubois and T. R. Schmidt, Remote–Field Eddy Current Signal Representation, *Mater. Eval.*, July 1993, pp. 782–789.

5. C. V. Dodd and J. R. Pate, Advancement in Eddy–Current Test Technology for Steam Generator Tube Inspection, in Proc. Twentieth Water Reactor Safety Information Meeting, NUREG/CP–0126, Vol. 3, March 1993, pp. 267–276.

6. S. J. Norton and J. R. Bowler, Theory of Eddy Current Inversion, *J. Appl. Phys.*, Vol. 73, No. 2, Jan. 15, 1993, pp. 501-512.

7. J. M. Mann, L. W. Schmerr and J. C. Moulder, Neural Network Inversion of Uniform–Field Eddy Current Data, *Mater. Eval.*, Jan. 1991, pp. 34–39.

8. K. Satake, M. Tanaka, N. Shimizu, Y. Araki, and K. Morimoto, Three–Dimensional Analysis on Eddy Current Testing for S/G Tubes, *IEEE Transactions on Magnetics*, Vol. 28, No. 2, March 1992, pp. 1466–1468.

9. T. Stepinski and N. Maszi, Conjugate Spectrum Filters for Eddy Current Signal Processing, *Mater. Eval.*, Vol. 51, July 1993, pp. 839–844.

10. J. L. Rose, K. M. Rajana, and F. T. Carr, "Ultrasonic Guided Wave Inspection Concepts for Steam Generator Tubing," *Mater. Eval.*, Vol. 52, Feb. 1994, pp. 307–311.

11. J. R. Pate, and C. V. Dodd, "Computer Programs for Eddy-Current Defect Studies," Oak Ridge National Laboratory, NUREG/CR-5553,1990.

12. S. Bakhtiari, and D. S. Kupperman, Modeling of Eddy Current Probe Response for Steam Generator Tubes, in Proc. 24th Water Reactor Safety Information Meeting, October 21-23, 1996, Bethesda, MD, NUREG/CP-0157, Vol. 2, Feb. 1997, pp. 323-342.

13. Dodd, C.V., Data Analysis for Steam Generator Tube Samples, Oak Ridge National Laboratory, NUREG/CR-6455, ORNL/TM-13206, July 1996.

14. R. A. Clark and R. L. Burr, A Method for Controlled Stress Corrosion Cracking in Nonsensitized Inconel 600 Tubing, Corrosion, Vol. 36, July 1980, pp. 382-383.

15. F. Kreith, Principles of Heat Transfer, 3rd Ed., Dun-Donnelley Publisher, New York, 1976, pp. 524-534.

16. W. M. Rohsenow, A Method For Correlating Heat-Transfer Data for Surface Boiling Liquids, Trans. ASME, Vol. 74, 1954, pp. 969-975.

17. P. J. Millett and J. M. Fenton, A Modelling Study of Parameters Controlling Local Concentration Processes In Pressurized Water Reactor Steam Generators, Nucl. Technol., Vol. 108, Nov. 1994, pp. 256-265.

18. D. B. Scott and C. L. Glaves, Production of Intergranular Attack of Alloy 600, Alloy 690 and Alloy 800 Tubing In Tubesheet Crevices, EPRI NP-5263, Electric Power Research Institute, Palo Alto, CA, July 1987.

19. P. G. Ellison, L. W. Ward, C. Dobbe. S. A. Chavez, C. L. Atwood, C. L. Smith, L. M. Wolfram, J. L. Jones, L. N. Haney, and W. J. Reece, The Risk Significance of Induced Steam Generator Tube Rupture, INEL-95/0641, Rev. 1, Lockheed Martin Idaho Technologies, Inc., Idaho National Engineering Laboratory, Dec. 15, 1995.

20. E. L. Fuller, M. A. Kenton, M. Epstein, R. E. Henry, and N. G. Cofie, Risks from Severe Accidents Involving Steam Generator Tube Leaks or Ruptures, draft EPRI TR-106194, Electric Power Research Institute, Palo Alto, CA.

21. G.T. Hahn, M. Sarrate, and A.R. Rosenfield, Criteria for crack extension in cylindrical pressure vessels, *Int. J. Fracture Mech.*, Vol. 5, No. 3, 1969, pp. 187-210.

22. J. F. Kiefner, W. A. Maxey, R. J. Eiber, and A. R. Duffy, Failure stress levels of flaws in pressurized cylinders, in *Progress in Flaw Growth and Fracture Toughness Testing*,, Kaufman, J. G., Ed., Sixth National Symp. on Fracture Mechanics, American Society for Testing and Materials, ASTM Special Technical Publication 536, Philadelphia 1973.

23. W. Kastner, E. Röhrich, W. Schmitt, and R. Steinbuch, Critical crack sizes in ductile piping, *Int. J. Pres. Ves. Piping*, Vol. 9, 1981, pp 197-219.

24. E. Gillot, B. Cochet, P. Richard, and C. F. Faidy, Validation of leak before break analysis for steam generator tubes, SMIRT-9, Vol. D, A. A. Balkema Publisher, 1987, pp. 405-411.

25. S. Ranganath and H. S. Mehta, Engineering Methods for the Assessment of Ductile Fracture Margin in Nuclear Power Plant Piping, Elastic Plastic Fracture Second Symposium, Vol. 2, Fracture Resistance Curves and Engineering Applications, American Society for Testing and Materials, ASTM Special Technical Publication 803, Philadelphia 1973.

26. M. F. Kanninen, A. Zahoor, G. M. Wilkowski, I. Abou-Sayed, C. Marschall, D. Broek, S. Sampath, C. Rhee, J. Ahmad, Instability Predictions for Circumferentially Cracked Type 304 Stainless Steel Pipes under Dynamic Loading, EPRI NP-2347 (Vol. 1: Summary; Vol. 2: Appendices), Electric Power Research Institute, Palo Alto, CA, April 1982.

27. R. Kurihara, S. Ueda, and D. Sturm, Estimation of the Ductile Unstable Fracture of Pipe with a Circumferential Surface Crack Subjected to Bending, *Nucl. Eng. and Design*, Vol. 106, 1988, pp. 265-273.

28. P. Hernalsteen, Structural and Leakage Integrity of Tubes Affected by Circumferential Cracking, in Proc. CNRA/CSNI Workshop on Steam Generator Tube Integrity in Nuclear Power Plants, NUREG/CP-0154, ANL-96/14, NEA/CNRA/R(96)1, Feb. 1997, pp. 233-257.

29. B. Cochet and B. Flesch, Crack stability criteria in steam generator tubes, SMIRT-9, Vol. D, A. A. Balkema Publisher, 1987, pp. 413-419.

30. J. M. Alzheimer, R. A. Clark, C. J. Morris, and M. Vagins, Steam Generator Tube Integrity Program, Phase I Report, NUREG/CR-0718, PNL-2937, Pacific Northwest Laboratory, Sept. 1979.

31. I. Finnie and W. R. Heller, Creep of Engineering Materials, McGraw-Hill, New York, 1959.

32. R. J. Kurtz, R. A. Clark, L. R. Bradley, W. M. Bowen, P. G. Doctor, R. H. Ferris, and F. A. Simonen, Steam Generator Tube Integrity Program/Steam Generator Group Project, Final Project Summary Report, NUREG/CR-5117, PNNL, Richland, WA, May 1990.

33. P. G. Ellison, L. W. Ward, C. A. Dobbe, S. A. Chavez, C. L. Atwood, L. N. Haney, W. G. Reece, and H. S. Blackman, Steam Generator Induced Rupture from Operating Transients, Design-Basis Accidents, and Severe Accidents, INEL-95/0641, Idaho National Engineering Laboratory, Aug. 1996.

34. B. Flesch and B. Cochet, Application of the leak before break concept to steam generator tubes, Proc. Int. Cong. on Pressure Vessel Technology, Beijing, Sept. 1988.

35. N. R. Draper and H. Smith, Applied Regression Analysis, 2nd Edition, John Wiley and Sons, New York, 1981.

36. J. L. Rempe, S. A. Chavez, G. L. Thinnes, C. M. Allison, G. E. Korth, R. J. Witt, J. J. Sienicki, S. K. Wang, L. A. Stickler, C. H. Heath, and S. D. Snow, Light Water Reactor Lower Head Failure Analysis, NUREG/CR-5642, EGG-2618, Idaho National Engineering Laboratory, Idaho Falls, ID, Oct., 1993.

37 International Nickel Co., Engineering Properties of Inconel Alloy 600, Tech. Bull. T-7, Huntington, WV, 1964.

Appendix A: ORNL Computer Codes[a]

Program Name	Brief Description	Reference
ABBORAR	Defect impedance change for boreside coil	A-1
ABENCAR	Defect impedance change for encircling coil	A-1
AIRCO	Computes the air inductance of a coil	A-2
AIRMAG	Computes the magnetic field of an air coil	A-2
APUFIT	Fits readings from a pulsed instrument	A-3
APULG	Takes readings from a pulsed instrument	A-3
BIGFIT	Fits computed or experimental readings	A-4,A-5
BIGRDG	Makes experimental readings and stores data	A-4,A-5
BODEDF	Makes a Bode difference plot	A-6
BODEPL	Makes an absolute Bode plot	A-6
CIR.DAT	Data file for ORNL boreside/encircling coils	A-7
CLADT	Calculates impedance for a clad conductor	A-2
CONDTF	Measures conductivity (through transmission)	A-4,A-8
DATGEN	Generates multiple property data file	A-4
DBDSF	Defect sensitivity factor for differential boreside	A-1
DBDSFPLT	Generates a contour plot from DBDSF data	A-1
DEFBOR	Absolute boreside coil	A-1
DEFBORDF	Differential boreside coil	A-1
DEFBORDG	Differential boreside coil	A-1
DEFENC	Absolute encircling coil	A-1
DEFENCDF	Differential encircling coil	A-1
DEFPLA	Defect in a plate	A-1
DEFRDG	Makes readings on the impedance analyzer	A-6
DEFBORAR	Defect impedance change, averaged over depth	A-1
DEFENCAR	Defect impedance change, averaged over depth	A-1
DFPLARY	Defect impedance change, averaged over depth	A-1
DFPLVOL	Defect impedance change, averaged over volume	A-1
DFRFPARY	Defect voltage change, averaged over depth	A-1
DFRFPLA	Defect voltage change, single value of r	A-1
DFRFRSTP	Defect voltage change, step in r direction	A-1
DIFBOR	Differential boreside coil	A-1
FINDFIT	Fits multiple-frequency data, saves best	
FITANA	Fitting program for the impedance analyzer	A-6
GETKY	Utility to get the value of typed key	
INVDEF	Inversion program for a defect in a plate	A-1,A-9
INVPLA	Inversion program for a defect in a plate	A-1,A-9
MAGSCN	Calculates magnetic field at different points	
MULDEF	Multilayer defect program for the reflection probe	
MULIMP	Multilayer defect program for the coil impedance	A-4
MULPUL	Multilayer program for pulsed calculation	
MULRFD	General multilayer design program for reflection probe	A-4
MULTIC	Multilayer, reflection probe, conductivity changes	A-10
MULTID	Multilayer, reflection probe, defects	A-10
MULTIT	Multilayer, reflection probe, thickness changes	A-10
NORIMP	Measures normalized impedance	A-6
PAN.DAT	ORNL pancake coil data file	
PCAVVSCN	Average defect (over volume) for pancake coil	A-1
PCAVZSCN	Average defect (over depth) for pancake coil	A-1
PCBLDF	Builds a magnitude and phase lookup file	A-1
PCDSF	Calculates DSF for a PC	A-1

PCDSFPLT	Generates a contour plot of the magnitude of DSF	A-1
PCGRAPH	Plots two sets of data on same graph	A-1
PCINV	Inverts scan of PC data	A-1
PCRTSCAN	Converts raw voltage readings to impedance change	A-1
PERMCON	Permeability from through-transmission readings	
PHNWRK	Calculates voltage for calibrator network	A-5
PULFIT	Fits pulse data to properties	A-3
PULRDG	Makes readings on pulsed EC instrument	A-3
RDGANA	Makes readings on impedance analyzer	A-6
REF.DAT	Data file for ORNL reflection probes	A-4
RESFIT	Fits resistivity to readings	
RFAVZSCN	Defect voltage, average over depth	A-1
RFBLDF	Builds a lookup file of magnitude and Phase of DSF	A-1
RFCLAD	Magnitude and phase for reflection probe, clad conductor	A-10
RFDSF	Magnitude and phase of DSF a for lattice of points	A-1
RFDSFL	Magnitude and phase of DSF a for lattice of points	A-1
RFDSFPLT	Generates a contour plot of magnitude of DSF	A-1
RFGRAPH	Plots two sets of data on same graph, rf probe	A-1
RFINV	Inverts scan of defect using reflection coil data	A-1
SUBMLRF	Subroutines for reflection coil	A-10
SUBTUB	General subroutines	
TICOIL	Calculates RLC for low-temperature drift reflection coil	A-10

*Programs with a date (listed in each code) after 4/23/87 have been written on the PC-AT. Most of the programs are written in Ryan McFarland FORTRAN, but will run on Microsoft and NDP FORTRAN with only slight modifications. The programs that read from an instrument or send data to a controller use IEEE-488 bus, which will have to be configured to a particular board. Some of the programs also use Graphmatic and Printmatic routines.

References for Appendix A

A-1. J. R. Pate and C. V. Dodd, Computer Programs For Eddy-Current Defect Studies, NUREG CR/ORNL TM-5553, Oak Ridge National Laboratory, June 1990.

A-2. W. A. Simpson, C. V. Dodd, J. W. Luquire, and W. G. Spoeri, Computer Programs for Some Eddy-Current Problems - 1970, ORNL-TM-3295, Oak Ridge National Laboratory, June 1971.

A-3. C. V. Dodd, et al., Pulsed Eddy Current Inspection of Thin- Walled Stainless Steel Tubing, ORNL-6408, Martin Marietta Energy Systems, Oak Ridge National Laboratory, Sept. 1987.

A-4. W. E. Deeds, C. V. Dodd, and G. W. Scott, Computer-Aided Design of Multifrequency Eddy-Current Tests for Layered Conductors with Multiple Property Variations, ORNL/TM-6858, Oak Ridge National Laboratory, Oct. 1979.

A-5. C. V. Dodd and L. D. Chitwood, Three-Frequency Eddy-Current Instrument, ORNL/TM-10663, Martin Marietta Energy Systems, Oak Ridge National Laboratory, Oak Ridge, Tenn., May 1988.

A-6. C. V. Dodd, L. M. Whitaker, and W. E. Deeds, An Eddy-Current Laboratory Test System Using Commercial Equipment, ORNL-6366, Martin Marietta Energy Systems, Oak Ridge National Laboratory, April 1987.

A-7. W. E. Deeds, and C. V. Dodd, Multiple Property Variations in Coaxial Cylindrical Conductors Determined with Multiple-Frequency Eddy Currents, NUREG/CR-0967; NUREG/TM-335, Martin Marietta Energy Systems, Oak Ridge National Laboratory, Nov. 1979.

A-8. C. V. Dodd, and W. E. Deeds, Absolute Eddy-Current Measurement of Electrical Conductivity, in Review of Progress in Quantitative Nondestructive Evaluation, (Proc. AF/DARPA Rev. Progr. Quant. NDE, 1981) Vol. 1, D. O. Thompson and D. E. Chimenti, eds., Plenum, New York, 1982, pp. 387-394.

A-9. C. V. Dodd, C. D. Cox, and W. E. Deeds, Experimental Verification of Eddy-Current Flaw Theory, in Review of Progress in Quantitative Nondestructive Evaluation, Vol. 4A, Proc. 11th Annual Review of Progress in Quantitative Nondestructive Evaluation, D. O. Thompson and D. E. Chimenti, eds., Plenum, New York, 1985, pp. 359-364.

A-10. C. V. Dodd, C. C. Cheng, W. A. Simpson, D. A. Deeds, and J. H. Smith, The Analysis of Reflection Type Coils for Eddy-Current Testing, ORNL-TM-4107, Oak Ridge National Laboratory, April 1973.

APPENDIX B: Coil, Tube, and Measurement Parameters

Using an absolute-bobbin coil SN480A, we conducted experimental measurements on a large aluminum cylinder. The coil, tube, and defect dimensions are a follows:

SN480A 2 RDGS AVGD TIME: 7:33:28 DATE: 3/9/94

Coil Dimensions[a]

Mean radius = 35.0 mm (1.3775 in.)
Coil inner radius = 31.75 mm (1.25 in.), nor = 0.9074
Coil outer radius = 38.23 mm (1.505 in.), nor = 1.0926
Coil length = 6.6 mm (0.26 in.), nor = 0.1887
1836 turns of #36 wire; cal ind = 380.7 mH; cal res = 550 Ω

Tube Dimensions[a]

Tube outer diameter = 88.9 mm (3.5 in.), nor outer rad = 1.2704;
Tube wall thickness = 5.6 mm (0.220 in.), nor = 0.1597
Tube inner radius = 38.9 mm (1.53 in.), nor = 1.1107
Radial clearance = 0.64 mm (0.0250 in.), nor = 0.0181
Coil form rad clr = 0.25 mm (0.010 in.), nor = 0.00726
ρ = 3.88 μΩ-cm

Defect Dimensions (4 each)[a]

11.2-mm (0.440-in.)-diam hole; nor = 0.3194
29.0-mm (1.420-in.)-long notch; nor = 1.031
8.76-mm (0.345-in.)-diam hole; nor = 0.250

---

[a] *nor* refers to the value normalized with respect to the coil mean radius $\bar{r} = \frac{r_i^c - r_o^c}{2}$.

The coil parameters in air are listed in Table B.1.

Table B.1. Coil parameters in air at frequencies of 500, 1200, and 7500 Hz[a]

Parameter	Frequency (Hz)		
	500	1200	7500
wusr2[b]	124.6	298.9	1,868.4
Inductance, air (mH)	380.0	382.2	497.4
Resistance, air (Ω)	565.0	573.0	1,050.0
Reactive component, air (Ω)	1,196.0	2,884.0	23,440.0
Resistance, normal meas. (Ω)	0.1120	0.0794	0.026
Resistance, normal calc. (Ω)	0.1200	0.0867	0.375
Reactance, normal meas. (Ω)	0.549	0.506	0.375
Reactance, normal calc. (Ω)	0.530	0.485	0.414

[a] Readings are the average of nine measurements, each made in a different circumferential orientation. Each throughwall artifact was repeated every 90° around the tube.

[b] *wusr2* is the characteristic parameter; $wusr2 = \bar{r}^2 \omega \mu_r \sigma$.

In Table B.2, we present the values for resistance and reactance obtained at the peak of the defect and the nominal value obtained from the tube away from the defects.

Table B.2. Values of resistance and reactance obtained at defect peak and nominal value obtained from tube away from defects

Distance	500 Hz		1200 Hz		7,500 Hz	
[(mm (in.)]	Resist (Ω)	React. (Ω)	Resist (Ω)	React. (Ω)	Resist (Ω)	React. (Ω)
23.1 (0.91)	700.67	688.01	804.12	1,527.25	1,681.75	9,330.12
99.6 (3.92)	724.50	746.58	867.12	1,620.62	2,024.31	9,503.94
175.0 (6.90)	701.09	676.02	804.75	1,500.12	1,681.56	9,104.94
nom.	698.94	657.15	802.10	1,460.30	1,662.40	8,793.40

NRC FORM 335 (2-89) NRCM 1102, 3201, 3202

U. S. NUCLEAR REGULATORY COMMISSION

BIBLIOGRAPHIC DATA SHEET

(See instructions on the reverse)

1. REPORT NUMBER *(Assigned by NRC. Add Vol., Supp., Rev., and Addendum Numbers, if any.)*
NUREG/CR-6511, Vol. 2
ANL-97/3

2. TITLE AND SUBTITLE
Steam Generator Tube Integrity Program:
Annual Report August 1995—September 1996

3. DATE REPORT PUBLISHED
MONTH: February
YEAR: 1998

4. FIN OR GRANT NUMBER
W6487

5. AUTHOR(S)
D. R. Diercks, S. Bakhtiari, K. E. Kasza, D. S. Kupperman
S. Majumdar, J. Y. Park, and W. J. Shack

6. TYPE OF REPORT
Technical; Annual

7. PERIOD COVERED *(Inclusive Dates)*
Aug. 1995—Sept. 1996

8. PERFORMING ORGANIZATION – NAME AND ADDRESS *(If NRC, provide Division, Office or Region, U.S. Nuclear Regulatory Commission, and mailing address; if contractor, provide name and mailing address.)*

Argonne National Laboratory
9700 South Cass Avenue
Argonne, IL 60439

9. SPONSORING ORGANIZATION – NAME AND ADDRESS *(If NRC, type "Same as above": if contractor, provide NRC Division, Office or Region, U.S. Nuclear Regulatory Commission, and mailing address.)*

Division of Engineering Technology
Office of Nuclear Regulatory Research
U. S. Nuclear Regulatory Commission
Washington, DC 20555

10. SUPPLEMENTARY NOTES
J. Muscara, NRC Project Manager

11. ABSTRACT *(200 words or less)*

This report summarizes work performed by Argonne National Laboratory on the Steam Generator Tube Integrity Program from the inception of the program in August 1995 through September 1996. The program is divided into five tasks: (1) Assessment of Inspection Reliability, (2) Research on ISI (in-service-inspection) Technology, (3) Research on Degradation Modes and Integrity, (4) Tube Removals from Steam Generators, and (5) Program Management. Under Task 1, progress is reported on the preparation of facilities and evaluation of nondestructive evaluation techniques for inspecting a mock-up steam generator for round-robin testing, the development of better ways to correlate failure pressure and leak rate with eddy current (EC) signals, the inspection of sleeved tubes, workshop and training activities, and the evaluation of emerging NDE technology. Results are reported in Task 2 on closed-form solutions and finite-element electromagnetic modeling of EC probe responses for various probe designs and flaw characteristics. In Task 3, facilities are being designed and built for the production of cracked tubes under aggressive and near-prototypical conditions and for the testing of flawed and unflawed tubes under normal operating, accident, and severe-accident conditions. Crack behavior and stability are also being modeled to provide guidance for test facility design, develop an improved understanding of the expected rupture behavior of tubes with circumferential cracks, and predict the behavior of flawed and unflawed tubes under severe accident conditions. Task 4 is concerned with the acquisition of tubes and tube sections from retired steam generators for use in the other research tasks. Progress on the acquisition of tubes from the Salem and McGuire 1 nuclear plants is reported.

12. KEY WORDS/DESCRIPTORS *(List words or phrases that will assist researchers in locating this report.)*
Steam Generator
Tubes
Stress Corrosion Cracking
Eddy Current Testing
Nondestructive Evaluation
In-service Inspection
Pressure Testing
Tube Burst
Leak Rate
Alloy 600, Incoloy 600

13. AVAILABILITY STATEMENT
Unlimited

14. SECURITY CLASSIFICATION
(This Page)
Unclassified
(This Report)
Unclassified

15. NUMBER OF PAGES

16. PRICE